



Weakly Collisional and Collisionless Astrophysical Plasmas

Thomas Berlok

Supervisors:

Martín E. Pessah, Troels Haugbølle and Tobias Heinemann

This thesis has been submitted to the PhD School of the Faculty of Science,
University of Copenhagen

Weakly Collisional and Collisionless Astrophysical Plasmas
PhD thesis in Theoretical Astrophysics

Thomas Berlok

Supervisors:

Martín E. Pessah, Troels Haugbølle and Tobias Heinemann

Niels Bohr International Academy
Niels Bohr Institute
Faculty of Science
University of Copenhagen

Submitted October 6, 2017.

Abstract

Weakly collisional and collisionless astrophysical plasmas are not well described by ideal magnetohydrodynamics (MHD) whose validity depends on a high collision frequency. This thesis aims to address this issue by moving beyond ideal MHD and the scope of the thesis is twofold. Firstly, we investigate helium mixing in the weakly collisional intracluster medium of galaxy clusters using Braginskii MHD. Secondly, we present a newly developed Vlasov-fluid code which can be used for studying fully collisionless plasmas such as the solar wind and hot accretions flows.

The equations of Braginskii MHD are used to study weakly collisional, stratified atmospheres which offer a useful model of the intracluster medium of galaxy clusters. Using linear theory and computer simulations, we study instabilities that feed off thermal and compositional gradients. We find that these instabilities lead to vigorous mixing of the composition and discuss the potential consequences for X-ray observations of galaxy clusters.

Collisionless plasmas can be subject to microscale velocity-space instabilities which are not well-described by Braginskii MHD. In contrast, Vlasov-fluid theory captures all the kinetic phenomena associated with the ions and is thus well suited for studying collisionless plasmas. We have developed a new 2D-3V Vlasov-fluid code which works by evolving the phase-space density distribution of the ions while treating the electrons as an inertialess fluid. The code uses the particle-in-cell (PIC) method and several options for particle interpolation (cloud-in-cell and triangular-shaped-cloud) and several methods for updating the equations in time (the predictor-corrector and the Horowitz method) are provided. The programming language Python has been chosen for its usability but high performance is nevertheless maintained and the code is MPI-enabled. The Vlasov-fluid code

has been tested and is able to convincingly reproduce results from linear theory. The tests include one-dimensional simulations of plasma instabilities such as the firehose instability, the ion-cyclotron instability and the ion beam instability and simulations of waves, such as the ion-acoustic, ion Bernstein, ion-cyclotron and whistler waves. The thesis also contains a general introduction to the PIC method including a discussion of aliasing due to the numerical grid and the finite grid instability. We furthermore study ion-cyclotron damping and Landau damping of ion-acoustic waves and present a two-dimensional simulation of the parallel firehose and oblique firehose instability. We conclude the thesis by pointing to possible future applications of the Vlasov-fluid code.

Resume

Svagt kollisionale og kollisionsløse, astrofysiske plasmaer er ikke velbeskrevne inden for ideel magnetohydrodynamik (MHD), da denne teori beror på en høj kollisionsfrekvens. Denne afhandling har derfor to dele, der benytter to forskellige teorier, der ligger udover ideel MHD. De to teorier er Braginskii MHD, som er en fluid-model, der kan benyttes når plasmaet er svagt kollisionalt og Vlasov-fluid teori, som kan benyttes når ionerne er kollisionsløse og dynamikken på elektron-skala ikke er essentiel. De to dele udgøres af *i)* et studie, der benytter Braginskii MHD til at undersøge blanding af heliumindholdet i det svagt kollisionale intergalaktiske medium i galaksehobe og *ii)* en præsentation af en nyudviklet Vlasov-fluid kode, der kan benyttes til at studere helt kollisionsløse plasmaer såsom solvinden eller massetilvækstsskiver rundt om sorte huller.

Braginskii MHD-ligningerne benyttes til at studere svagt kollisionale atmosfærer, der udgør en brugbar model til at studere det intergalaktiske medium i galaksehobe. Ved at benytte lineær teori og computersimuleringer undersøges plasmainstabiliteter, der drives af gradienter i temperatur og plasmasammensætning. Det konkluderes at disse plasmainstabiliteter kan medføre en effektiv blanding af plasmasammensætningen og konsekvenserne for røntgenobservationer af galaksehobe diskuteres.

Kollisionsløse plasmaer kan undergå instabilitet på mikrofysisk skala, hvis der er anisotropi i hastighedsfordelingen af partikler. Sådanne instabiliteter er ikke velbeskrevne inden for Braginskii MHD. Vlasov-fluid teori beskriver derimod alle de kinetiske fænomener, der er associerede med ionerne og er derfor velegnet til at studere et kollisionsløst plasma. Vi har udviklet en ny kode, der kan løse Vlasov-fluid ligningerne ved at beregne tidsudviklingen af ionernes faserums-

densitet, mens elektronerne behandles som en væske uden inertie. Koden benytter partikel-i-celle (PIC) metoden og har flere forskellige valgmuligheder for interpolation (CIC og TSC) samt flere forskellige valgmuligheder for opdatering i tid (predictor-corrector- og Horowitzmetoden). Det dynamiske og fortolkede programmeringssprog Python er blevet valgt for dets brugervenlighed, men ikke desto mindre kan koden køre på mange processorer ved hjælp af MPI og den udviser god performance. Vlasov-fluid koden er blevet testet og kan på overbevisende vis reproducere resultater fra lineær teori. Testene inkluderer endimensionelle simuleringer af plasmainstabiliteter såsom brandslange-, ion-cyklotron- og ion-stråleinstabiliteten samt simuleringer af bølger såsom ion-akoustisk, ion Bernstein, ion-cyklotron, og fløjtebølger. Afhandlingen indeholder også en introduktion til PIC-metoden og herunder en diskussion af hvordan en begrænset rumlig opløsning kan føre til såkaldt aliasing og numerisk instabilitet. Derudover behandles ion-cyklotron dæmpning samt Landau dæmpning af ion-akoustiske bølger. Til sidst præsenteres en todimensionel simulering af brandslangeinstabiliteten og afhandlingen afsluttes med en gennemgang af fremtidige anvendelsesmuligheder af Vlasov-fluid koden.

Publications

The following publications were published during the PhD study and are appended the thesis. A summary of our findings can be found in Chapter 3.

- Thomas Berlok and Martin E. Pessah (2015). *Plasma Instabilities in the Context of Current Helium Sedimentation Models: Dynamical Implications for the ICM in Galaxy Clusters*. The Astrophysical Journal, 813, 22.
- Thomas Berlok and Martin E. Pessah (2016a). *Local Simulations of Instabilities Driven by Composition Gradients in the ICM*. The Astrophysical Journal 824, 32.
- Thomas Berlok and Martin E. Pessah (2016b). *On Helium Mixing in Quasi-global Simulations of the Intracluster Medium*. The Astrophysical Journal 833, 164.



Acknowledgments

First and foremost, I would like to thank my main advisor, Martin Pessah. I have had the pleasure of working with Martin since 2013, first as a Master's student, and, since November 2014, as his PhD student. Throughout this time, Martin has always supported my development as a researcher and has always found the time to advice and encourage me. I would like to use this opportunity to express my gratitude for his guidance and the many interesting discussions we have had during the last 4 years. I would like to thank my advisor Tobias Heinemann for sharing with me his knowledge of plasma physics and for teaching me what attention to detail and a pursuit of perfectionism really is. The development of the hybrid code presented in this thesis was done in close collaboration with Toby and I would like to thank him for introducing me to Cython and object-oriented programming in Python. I would like to thank my advisor Troels Haugbølle for his enthusiasm and positive attitude, his help with the PhotonPlasma code, and for sharing with me his expertise on particle-in-cell simulations. My PhD position was financed by a grant from the European Research Council awarded to Martin Pessah with one year of salary paid by the Niels Bohr Institute (NBI). I would like to thank the European and Danish taxpayers who gave me the freedom to pursue my interests for the last three years. I am also grateful to Andrew Jackson and Niels Kahlke for awarding me the Lørup scholar stipend which helped me transition from Master's to PhD student. I am grateful to Eliot Quataert for hosting me at the Theoretical Astrophysics Center during the fall of 2016 and for interesting discussions of the problem that we are currently working on. I would also like to thank: Daisuke Nagai, for giving me the resources to reproduce all the data in his helium sedimentation model and for interesting discussions in Copenhagen

and Minneapolis; Matthew Kunz for providing me with additional details about technical issues related to the linear theory in Latter and Kunz (2012) and the simulations in Kunz et al. (2012); Gareth Murphy, for his aid with recognizing the finite grid instability and Oliver Gressel, for suggesting quasi-periodic boundary conditions. Furthermore, I would like to thank Martin and Toby, for their careful scrutiny of the present manuscript. I would also like to thank the NBI librarians, Lisbeth Dilling and Kader Ahmad, the group secretary at the Niels Bohr International Academy (NBIA), Anette Studsgård, and the NBI IT Support, Björn Nilsson, for all their help and assistance during my time at the NBI. I would like to thank all the (somewhat) junior staff at NBI and Starplan, i.e., Yuri Fujii, Pablo Benitez-Llambay, Philipp Weber, Leonardo Krapp, Farrukh Nauman, Michael Küffmeier, Troels Frostholt, Andrius Popovas, Gareth Murphy, Gopakumar Mohandas, Neil Vaytet, Jonathan Ramsey and Tommaso Grassi for fun at workshops, schools and conferences abroad and in Denmark. I am thankful to Andrew Jackson and Chris Pethick for making NBIA pleasant by providing tea, interesting conversations and a broader (physics) perspective. I would like to thank Gopakumar Mohandas, my office mate and contemporary PhD student at NBI, for his help and advice, both with the present thesis and in general. During my studies, I had the privilege of living for four years at Collegium Mediceum (in Danish: Borchs Kollegium). I would like to thank the founder, Ole Borch, for granting me this privilege and the other residents, too many to name here, for making my time at Borchs Kollegium very rewarding and enjoyable. Finally, I would like to thank my parents and Line for always supporting me.

Contents

1	Introduction	1
1.1	Plasma astrophysics	4
1.2	The solar wind	10
1.3	Hot accretion flows	13
1.4	The intracluster medium	15
1.5	Outline of the thesis	17
2	Plasma frameworks	19
2.1	Vlasov-fluid equations	19
2.2	Hall MHD	23
2.3	Braginskii MHD	25
3	On the distribution of helium in the intracluster medium	29
3.1	Paper I	32
3.2	Paper II	35
3.3	Paper III	39
4	The Hall dispersion relation	45
4.1	Perpendicular propagation	47
4.2	Parallel propagation	48
4.2.1	Polarization	50
4.3	Conclusion	51
5	Derivation of the Vlasov and Vlasov-fluid dispersion relations	53
5.1	Vlasov-fluid dispersion relation	54

5.2	Vlasov dispersion relation	59
5.3	Relativistic dispersion relation	59
6	Derivation of the conductivity tensor	61
6.1	The conductivity tensor	61
6.2	Velocity space integrals	64
7	Solutions to the Vlasov and Vlasov-fluid dispersion relations	69
7.1	Transverse Vlasov-fluid dispersion relation	70
7.1.1	Parallel firehose instability	74
7.1.2	Ion-cyclotron instability	75
7.1.3	Ion-cyclotron damping	77
7.2	General Vlasov-fluid dispersion relation	77
7.2.1	Oblique firehose instability	79
7.2.2	Ion-cyclotron and mirror instabilities	80
8	Introduction to particle-in-cell simulations	85
8.1	Particle mover	87
8.2	Interpolation	89
8.3	Field solver	91
8.4	A few implementation details	92
9	Numerical methods	97
9.1	Staggering	97
9.1.1	Finite difference scheme	99
9.1.2	Divergence of B	101
9.2	Time stepping procedures	103
9.2.1	Predictor-corrector method	105
9.2.2	Horowitz method	106
10	Particle loading	109
10.1	Inverse transform sampling	110
10.2	Non-uniform density	111
10.3	Maxwellian with low noise	113

11 Landau damping, aliasing and the finite grid instability	117
11.1 Landau damping	118
11.2 Numerical dispersion relations	122
11.3 The finite grid instability	125
12 Hybrid code experiments	129
12.1 Whistler and ion-cyclotron waves	130
12.2 Ion-cyclotron damping	131
12.3 Ion-cyclotron instability	132
12.4 Parallel firehose instability	133
12.5 Oblique firehose instability	134
12.6 Ion Bernstein modes	135
12.7 Ion beam instability	138
12.8 Firehose instability in 2D	142
13 Conclusion and future prospects	145
A Various derivations	165
A.1 Integrals in perpendicular velocity	165
A.2 Integrals in parallel velocity	167
A.3 Bessel function sums	171
A.4 Ichimaru's plasma dispersion function	172
A.5 Linearized Hall MHD equations	173
A.6 Hall conductivity tensor	174
A.7 Divergence of \mathbf{B}	176

List of Figures

- 3.1 Figure 7 in Paper I. The mean molecular weight profile (blue line) in a 11 Gyr-old galaxy cluster and the temperature profile (red dashed line) used in the model of Peng and Nagai (2009). The dashed black line indicates the primordial composition. 30
- 3.2 Figure 11 in Paper I. Contour plots of the growth rate in Gyr^{-1} for the outer ICM ($r/r_{500} = 0.5$ where $r_{500} = 1.63$ Mpc). This region is unstable to the MTI at $t = 0$ Gyr (left panel) or the MTCI and the conduction modes at $t = 11$ Gyr (right panel). The most unstable modes are found at intermediate parallel wavenumbers at which heat conduction is effective. Magnetic tension stabilizes the instability at higher parallel wavenumbers. The maximum growth rate is decreased by 15% with respect to the homogeneous case. The magnetic field, indicated with a red solid line, is assumed to be inclined at angle of 45 deg with respect to the direction of gravity. 34
- 3.3 Figure 14 in Paper I. The maximum growth rates as a function of radius in the cluster model of Peng and Nagai (2009) at $t = 11$ Gyr in the limit where magnetic tension is neglected (dashed lines) and when it is taken into account (solid lines). 35

3.4	Figure 15 in Paper I. The maximum growth rate as a function of radius in the cluster model of Peng and Nagai (2009) at $t = 0$ (dashed) and $t = 11$ Gyr (solid) for a field with $\theta = 90^\circ$ (red) and $\theta = 0^\circ$ (blue) inclination with respect to the direction of gravity. The effects of a finite β are included. The sedimentation increases (decreases) the theoretically predicted growth rates in the inner (outer) cluster.	36
3.5	Figure 2 in Paper II. Evolution of box-averaged quantities for the MTCI with $\chi_{\parallel} = 3 \times 10^{-3}$ and $\beta_0 = 2 \times 10^8$. The perturbed quantities grow exponentially with a growth rate $\sigma = 0.40$	37
3.6	Figure 6 in Paper II. Growth rates at $r/r_{500} = 0.02$ as a function of $k = k_x = k_z$ (left panel) and growth rates at $r/r_{500} = 0.5$ as a function of $k = k_x$. Theoretical values (blue solid lines) and values obtained from simulations (green crosses) are seen to agree. . . .	38
3.7	Figure 1 in Paper III. Equilibrium atmosphere inspired by the sedimentation model of Peng and Nagai (2009) and the radial temperature profile of Vikhlinin et al. (2006). The temperature (blue) and the mean molecular weight (green) increase with radius while pressure (red) and density (magenta) decrease with radius at this radial distance in the cluster model. The derivative of the entropy (purple) is positive, indicating stability according to the Schwarzschild criterion.	40
3.8	Figure 3 in Paper III. Growth rates as a function of the horizontal wavenumber, $k_x H_0$, for the 10 fastest growing modes in units of $\sigma_0 = t_0^{-1}$ where $t_0 = H_0/v_{0,th} = 45$ Myr. The solid blue lines were obtained using the pseudo-spectral method. Each cross corresponds to a simulation where the eigenmodes were used for initial conditions. The numerical growth rate was found from the subsequent exponential evolution.	41

3.9	Figure 5 in Paper III. Evolution of the HPBI as a function of time in units of $t_0 = H_0/v_{0,th} = 45$ Myr. The size of the box is $H_0 \times 2H_0$ with $H_0 = 40$ kpc. The bottom of the atmosphere has $T_0 = 5.8$ keV and $c_0 = 0.52$ while the top of the atmosphere has $T = 9.6$ keV and $c = 0.62$, values found at $r_0 = 160$ kpc and $r = r_0 + 2H_0 = 240$ kpc in the model of Peng and Nagai (2009). The top row of panels include anisotropic heat conduction and the middle and bottom rows also include Braginskii viscosity. The middle row uses limiters. Solid lines indicate magnetic field lines and green (purple) corresponds to a high (low) helium content.	43
4.1	Dispersion of whistler, ion-cyclotron and Alfvén waves.	49
7.1	Growth rate and frequency of the parallel firehose instability for $\beta_{\parallel} = 4$ and $\beta_{\perp} = 1$ ($\Delta = -3/4$).	75
7.2	Growth rate of the ion-cyclotron instability with $\beta_{\parallel} = 1$ and $\beta_{\perp} = 4$ ($\Delta = 3$). Blue solid lines found using Vlasov-fluid theory and the dashed orange lines found using Vlasov ions and electrons. . .	76
7.3	Ion-cyclotron damping for $\beta = 5$	77
7.4	Contour plot of the growth rates for a plasma with $\beta_{\parallel} = 2.8$ and $\beta_{\perp} = 0.4\beta_{\parallel}$. The two instabilities are the whistler (parallel) firehose instability and the Alfvén (oblique) firehose instability. The maximum growth rate of the latter is indicated with a red cross. .	80
7.5	Contour plot of the growth rates for a plasma with $\beta_{\parallel} = 1$ and $\beta_{\perp} = 4$. The mode with maximal growth rate with $k = k_{\parallel}$ is recognized as the ion-cyclotron instability by comparing with Figure 7.2. The other mode is the mirror instability which has its maximum growth rate indicated with a red cross.	81
8.1	Flowchart for the PIC method.	87
8.2	Illustration of the leapfrog method. The particle positions, \mathbf{x} , and velocities, \mathbf{v} , are defined at integer and half-integer time steps, respectively.	89

8.3	Comparison of performance between a C version and a Python version of the skeleton code made available by Decyk (1995). <i>Upper panel:</i> The execution time of the particle move. <i>Lower panel:</i> The ratio of the Python execution time to the C execution time.	94
9.1	The grid layout with crosses (solid circles) indicating cell centers (corners). Blue symbols are active cells and orange symbols are guard layers. The thick black solid line indicates the grid boundaries. In the x -direction this is always equivalent to the physical boundaries while the boundaries in the y -direction are MPI boundaries.	99
10.1	Density profile generated using 1024 particles per cell and 128 cells. The orange (blue) solid line was found by calculating the particle positions x_j by numerically solving equation 10.7 using random numbers (regularly spaced values) for y_j	112
10.2	Histograms of velocities generated using equation 10.12 with a quiet method (blue) and a noisy method (orange) for $N = 2^8, 2^{10}, 2^{12}$ and 2^{14} numbers. The probability distribution function, $f(v)$, given by equation 10.8 is shown with a black solid line for reference.	114
11.1	Landau damping of ion-acoustic waves.	121
11.2	Aliasing of ion-acoustic waves in a cold plasma with CIC (left panel) and TSC (right panel) interpolation. We find agreement with the theoretical predictions given in Equations 11.24 and 11.25.	124
11.3	Warm plasma with $\lambda_D/\Delta x = 1$ which is numerically stable at all wavelengths (upper row) and warm plasma with $\lambda_D/\Delta x = 1/10$ which is numerically unstable (lower row).	125
11.4	Warm Vlasov fluid with $T_i/T_e = 1/10$ which is numerically stable at all wavelengths (upper row) and very cold Vlasov fluid with $T_i/T_e = 10^{-3}$ which is numerically unstable at short wavelengths (lower row).	126

12.1	Dispersion relation for whistler and ion-cyclotron waves. The frequencies measured in simulations agree with the Hall MHD linear dispersion relation given by Equations 4.14 and 4.15.	131
12.2	Second order convergence of whistler waves with $k_x v_a / \Omega = 1$	132
12.3	Ion-cyclotron damping for a plasma with $\beta = 5$	133
12.4	Evolution of the transverse magnetic field for the ion-cyclotron instability.	134
12.5	Evolution of the transverse magnetic field for the parallel firehose instability with $\beta_{\parallel} = 4$ and $\beta_{\perp} = 1$	135
12.6	Growth rates for the whistler and Alfvén firehose instabilities as a function of the inclination, θ , between \mathbf{k} and \mathbf{B} for $\beta_{\parallel} = 4$ and $\beta_{\perp} = 1$	136
12.7	Power spectrum of \hat{E}_x . Theoretical curves for ion Bernstein modes shown with long-dashed solid lines and for the magnetosonic wave with a short-dashed solid line for the $k_{\perp} > 0$ modes. The power spectrum is symmetric around $k_{\perp} = 0$	137
12.8	Resonant ($k > 0$) and non-resonant ($k < 0$) ion beam instability.	139
12.9	Evolution of B_y as a function of time for the resonant ion beam instability.	140
12.10	The particle phase-space at $\Omega t = 40$. The core (beam) ions are shown in the upper (lower) panel. Notice the difference in axis limits.	141
12.11	The change in velocity space distribution between the initial ($\Omega t = 0$) and the one at $\Omega t = 400$, produced by subtracting the normalized histograms.	142

List of Tables

- 1.1 Characteristic temperatures, number densities and magnetic field strengths for the solar wind, Sgr A* and the ICM (Quataert, 2003; Vikhlinin et al., 2006; Borovsky and Gary, 2011). The characteristic lengths are chosen to be 1 AU, 0.04 pc and 100 kpc, respectively. 11

- 9.1 Finite difference approximations to the derivative of a quantity depend on the staggering of the quantity. Here we show the 8 versions of the first order derivatives. Due to the interlaced grid only the upper and lower row are used in our hybrid code. 100

Chapter 1

Introduction

The radiative component of many astrophysical systems are in the plasma state, i.e., it consists of a highly ionized gas in which the electrons are dissociated from the ions. Understanding the dynamics of plasmas is therefore of prime importance for astrophysics and a variety of methods to study plasmas have been developed during the last century (see, e.g., Chen 2012). Collisional plasmas can be studied by using ideal magnetohydrodynamics (MHD, see, e.g., Freidberg 2014) which regards the plasma as a highly conducting fluid subject to the Lorentz force due to magnetic fields. While MHD is a highly successful theory, and forms the basis for astrophysical fluid dynamics (Pringle and King, 2007) its validity depends on particle collisions establishing local thermodynamic equilibrium. For collisionless plasmas, where this does not happen, a different set of tools is required. A basic distinction for a plasma, which depends on the collisionality, is thus whether it can be described with a fluid theory such as MHD or whether it is necessary to use a refined theory.

In this thesis, we employ two different methods for describing fully collisionless or weakly collisional plasmas *i)* the Vlasov-fluid framework (Freidberg, 1972), which uses the Vlasov equation to describe the evolution of the phase-space distribution of the ions, thereby capturing all kinetic effects associated with the ions in a collisionless plasma and *ii)* the Braginskii MHD framework (Braginskii, 1965) which is an extension to ideal MHD in which weakly collisional effects are included as anisotropic diffusion of heat and momentum. These frameworks will be

1. Introduction

described in more detail in Chapter 2.

The intracluster medium (ICM) of galaxy clusters, hot accretion flows in disks around compact objects, and the solar wind have characteristic length scales that differ by many orders of magnitude. The sphere of influence of the solar wind, called the Heliosphere, has a length scale of ~ 100 AU (Zurbuchen, 2007), the hot accretion flow at the center of our galaxy has an estimated length scale of ~ 0.04 pc (Quataert, 2003; Yuan and Narayan, 2014) and the ICM has a size of \sim Mpc (McNamara and Nulsen, 2007). Despite the disparity in length scales, these astrophysical systems all consist of highly ionized plasmas. Furthermore, due to their high temperatures and low densities, the plasmas are believed to be weakly collisional or collisionless, meaning that the mean-free-path characterizing particle collisions is not small compared to the characteristic sizes of the systems. Consequently, ideal MHD is not an appropriate theory for describing these systems.

Another property that these astrophysical systems have in common is that they have weak magnetic fields such that the thermal pressure exceeds the magnetic pressure. If the plasmas were collisional and could be described by ideal MHD, the weak magnetic field strengths would therefore be predicted to be energetically unimportant. A weak magnetic field can however be dynamically important in a collisionless plasma. The underlying reason is that even a weak magnetic field limits the motion of charged particles in the direction perpendicular to the magnetic field while allowing them to stream freely along the magnetic field. This leads to transport of heat and momentum which is preferentially along the magnetic field direction.

For stratified, weakly collisional, magnetized environments, such as the ICM, the anisotropic properties of the medium lead to stability properties which differ markedly from the collisional case (Balbus, 2000, 2001; Quataert, 2008; Pessah and Chakraborty, 2013). The instabilities found in Pessah and Chakraborty (2013) are the focus of the three papers that have been published during the PhD study. A detailed study of the stability properties of atmospheres with gradients in temperature and composition was performed using the Braginskii MHD equations. This was made possible by building upon the publicly available MHD code Athena (Stone et al., 2008). We present a summary of the findings of Berlok and Pessah (2015), Berlok and Pessah (2016a), and Berlok and Pessah (2016b) (hereafter Paper

I, Paper II, and Paper III, respectively) in Chapter 3.

Besides the change in transport properties, which can lead to instabilities on a macrophysical scale, collisionless plasmas with a weak magnetic field can also be subject to microscale instabilities. These microscale instabilities arise due to the way charged particles respond to changes in magnetic field strength. Because the magnetic moment is an adiabatic invariant, slow changes in magnetic field strength go hand-in-hand with the development of anisotropic velocity space distributions. When the plasma is collisionless this almost inevitably leads to velocity space instabilities.

We review the linear theory for some of the prominent velocity space instabilities in Chapter 7 and note that these instabilities are not well described within the framework of Braginskii MHD (Schekochihin et al., 2005). In order to study the non-linear evolution of these instabilities computer simulations using a kinetic code are thus required. Kinetic codes that use the particle-in-cell (PIC) method can be roughly divided into two classes: Full PIC codes (Hockney and Eastwood, 1988; Birdsall and Langdon, 1991) which treat both ions and electrons as particles and hybrid PIC codes (Byers et al., 1978; Harned, 1982; Winske et al., 2003) which treat the ions as particles and the electrons as a fluid by solving the Vlasov-fluid equations.¹

While there are presently a number of MHD codes (e.g. *Athena* by Stone et al. 2008 and *Pluto* by Mignone et al. 2007) and full PIC codes (e.g. *TRISTAN-MP* by Spitkovsky 2005 and the *Photon-Plasma* code by Haugbølle, Frederiksen, and Nordlund 2013) which benefit the astrophysical community by being publicly available, it seems that there is not yet a corresponding code that solves the Vlasov-fluid equations. To the best of our knowledge, the hybrid PIC codes used in the astrophysics and space plasma physics communities are *CAMELIA* (Matthews, 1994), *DHybrid* (Gargaté et al., 2007), the code by Brecht and Ledvina (2007), the code by Holmström (2010), *AIKEF* (Müller et al., 2011), *Pegasus* (Kunz, Stone, and Bai, 2014), *CHIEF* (Muñoz et al., 2016) and *AMITIS* (Fatemi et al., 2017).

As far as we are aware, none of the codes listed above are publicly available and we have therefore resorted to developing a new Vlasov-fluid code in order to

¹A proper introduction to the Vlasov-fluid equations is given in Chapter 2 and an introduction to the particle-in-cell method is given in Chapter 8.

1. Introduction

be able to study the microscale physics of collisionless astrophysical systems. The development of the Vlasov-fluid code is the topic of Chapters 8-12 of the thesis.

The rest of this chapter is organized as follows: in Section 1.1 we introduce key concepts from plasma physics which will be used throughout the thesis. In Section 1.2, 1.3, and 1.4 we give a brief introduction to the collisionless plasma physics of the solar wind, hot accretion flows and the ICM in galaxy clusters. These introductions are by necessity highly simplified and incomplete but are nevertheless provided in order to give context to the tools that we have developed for studying collisionless plasmas. We finish the chapter by providing an outline for the remainder of the thesis in Section 1.5.

1.1 Plasma astrophysics

In order to quantitatively understand when collisions are important (and when they are not) we summarize some concepts from plasma physics (see, e.g., Hazeltine and Waelbroeck 2004). This also serves to introduce the notation used throughout the thesis. We note that we work exclusively in SI units.

We consider a completely ionized plasma which consists of electrons and ions. We introduce the electron plasma frequency, ω_p , given by

$$\omega_p^2 = \frac{n_e e^2}{\epsilon_0 m_e}, \quad (1.1)$$

where n_e is the electron number density, e is the fundamental charge such that $-e$ is the electron charge, m_e is the electron mass and ϵ_0 is the vacuum permittivity. The plasma frequency gives the inverse time scale for quasi-neutrality to be achieved after a perturbation of the electron charge density.

We can use the plasma frequency to define two length scales of interest. First we define the electron skin depth, also known as the electron inertial length, as

$$d_e = \frac{c}{\omega_p}, \quad (1.2)$$

where c is the speed of light. The electron skin depth is the length scale on which an electromagnetic wave with frequency, $\omega < \omega_p$, is attenuated as it tries to pene-

trate into the plasma. Secondly, we define the electron thermal velocity as

$$v_{e,t} = \sqrt{\frac{T_e}{m_e}}, \quad (1.3)$$

where T_e is the electron temperature² in order to define the electron Debye length as

$$\lambda_D = \frac{v_{e,t}}{\omega_p}. \quad (1.4)$$

Deviations from neutrality are screened on distances larger than the Debye length and the plasma is said to be quasi-neutral. This terminology refers to the fact that the particles comprising the plasma are charged and that deviations from neutrality do occur at scales below the Debye length.

At a microscopic level, a plasma consists of a myriad of charged particles which all generate magnetic and electric fields while being subject to the Lorentz force arising due to the fields of all the other particles. The Lorentz force acting on particle species s is given by

$$m_s \mathbf{a}_s = e_s (\mathbf{E} + \mathbf{v} \times \mathbf{B}), \quad (1.5)$$

where \mathbf{a}_s is the acceleration of a particle of species s with mass m_s and charge e_s . The acceleration arises due to the electric field, \mathbf{E} and the magnetic field, \mathbf{B} . These fields are in general functions of time and space, i.e., $\mathbf{E}(x, y, z, t)$ and $\mathbf{B}(x, y, z, t)$ where t denotes the time and x, y and z are spatial coordinates in a Cartesian coordinate system with unit vectors $\mathbf{e}_x, \mathbf{e}_y$, and \mathbf{e}_z . Some insight can however be gained by considering the following, much simpler, scenario. For a single particle in a constant magnetic field of strength B , the Lorentz force predicts simple gyromotion with a frequency

$$\Omega_s = \frac{e_s B}{m_s}, \quad (1.6)$$

which is known as the cyclotron frequency (or gyrofrequency). The associated

²We measure temperature in units of energy by setting Boltzmann's constant to unity, $k_B = 1$.

1. Introduction

thermal gyroradius is given by

$$r_s = \frac{v_{s,t}}{\Omega_s} . \quad (1.7)$$

The ratio of the thermal gyroradius to the characteristic length scale of the system, L , is called the magnetization parameter and is given by (Hazeltine and Waelbroeck, 2004)

$$\delta_s = \frac{r_s}{L} , \quad (1.8)$$

such that plasmas with $\delta_s \ll 1$ ($\delta_s \gtrsim 1$) are said to be magnetized (unmagnetized).

When additional forces enter the picture (due to an electric field, a gradient in the magnetic field strength, curvature of the magnetic field lines, gravity, density and/or temperature gradients, etc.) these can often be modeled as gyromotion around a guiding center that drifts due to the additional forces (see, e.g., Chen 2012). A lot of progress can thus be made by treating a plasma as a collection of particles with fast gyration around a guiding center. Averaging out the fast gyration yields the framework of gyrokinetics (Howes et al., 2006).

Particles can also collide, although the plasmas we will consider are too dilute to undergo collisions in the literal sense of the word. Instead, collisions for a weakly coupled plasma are really events of close approach with another particle that lead to a small change in the direction of the particle. A Coulomb 'collision' is then defined to be a collection of such events which change the direction of the particle by 90 degrees. We define the collision frequency for species s as (Hazeltine and Waelbroeck, 2004)

$$\nu_s = \sum_{s'} \nu_{ss'} , \quad (1.9)$$

where the sum extends over all species s' and the Coulomb collision frequency between species s and s' is approximated by (Braginskii, 1965)

$$\nu_{ss'} = \frac{4\sqrt{2}\pi}{3} \frac{e_s^2 e_{s'}^2}{(4\pi\epsilon_0)^2} \frac{m_{ss'}^{1/2}}{m_s} \ln \Lambda_{ss'} \frac{n_{s'}}{T^{3/2}} . \quad (1.10)$$

Here $\ln \Lambda_{ss'}$ is the Coulomb logarithm and

$$m_{ss'} = \frac{m_s m_{s'}}{m_s + m_{s'}} , \quad (1.11)$$

is the reduced mass. We observe from Equation 1.10 that the collision frequency is proportional to the density but decreases sharply with temperature. Dilute, hot plasmas will thus have low collision frequencies.

We can use the collision frequency to define a mean-free-path for collisions given by

$$\lambda_{s,\text{mfp}} = \frac{v_{s,t}}{\nu_s} , \quad (1.12)$$

in order to obtain a quantitative measure for what it means for a plasma to be collisionless. If the mean-free-path of collisions, $\lambda_{s,\text{mfp}}$, is much smaller than the characteristic size of the system, L , then the plasma is said to be collisional. In the opposite limit, $\lambda_{s,\text{mfp}} \gtrsim L$, the plasma is said to be collisionless. We define a collisionality parameter

$$\text{Kn}_s = \frac{\lambda_{s,\text{mfp}}}{L} , \quad (1.13)$$

called the Knudsen number, such that plasmas with $\text{Kn}_s \ll 1$ are collisional and plasmas with $\text{Kn}_s \gtrsim 1$ are effectively collisionless.

In analogy with the electron inertial length, the ion inertial length is given by

$$d_i = \frac{c}{\omega_{pi}} , \quad (1.14)$$

where the ion plasma frequency is

$$\omega_{pi}^2 = \frac{e^2 n_i}{\epsilon_0 m_i} . \quad (1.15)$$

We will exclusively consider non-relativistic plasma models in this thesis. This limit is formally found by setting the speed of light to infinity. Equation 1.2 and 1.14 seem to indicate that the inertial lengths go to infinity in this limit. This is, of course, not the case. Using that the speed of light is given by $c = 1/\sqrt{\epsilon_0 \mu_0}$,

1. Introduction

where μ_0 is the vacuum permeability, it is straightforward to show that the inertial length of species s is given by

$$d_s = \sqrt{\frac{m_s}{\mu_0 e_s^2 n_s}}. \quad (1.16)$$

We will often consider a pure hydrogen plasma consisting of electrons and a single ion species with mass, m_i , charge, e , and number density, n_i , for which the Alfvén velocity is given by³

$$v_a^2 = \frac{B^2}{\mu_0 n_i m_i}. \quad (1.18)$$

The ion inertial length can in this case be written in terms of the Alfvén velocity and the ion cyclotron frequency as

$$d_i = \frac{v_a}{\Omega_i}. \quad (1.19)$$

The ion inertial length is the scale at which the ion motion decouples from the electrons. It is also the scale at which the ion velocity space microscale instabilities grow (see Chapters 7 and 12). Notice that while both the Alfvén speed (Equation 1.18) and the ion cyclotron frequency (Equation 1.6) depend on the magnetic field strength, the ion inertial length (Equation 1.19) does not.

We have already mentioned that the solar wind, hot accretion flows and the ICM can have thermal energies that exceed the magnetic energies. This ratio defines the plasma- β , given by

$$\beta_s = \frac{2n_s T_s \mu_0}{B^2}, \quad (1.20)$$

³In general, we define the Alfvén velocity, v_a , as

$$v_a^2 = \frac{B^2}{\mu_0 \varrho}, \quad (1.17)$$

where $\varrho = \sum_s m_s n_s$ is the mass density of the plasma.

for species s . The total β is then defined as⁴

$$\beta = \sum_s \beta_s . \quad (1.22)$$

From Equation 1.7, 1.16 and 1.20, we observe that the gyroradius and the inertial length differ by a factor of $\sqrt{\beta_s/2}$ as $r_s = \sqrt{\beta_s/2} d_s$. For high β plasmas the inertial lengths are thus shorter than the gyroradii.

The final parameter, that we introduce, is the plasma coupling parameter⁵, Γ . This parameter is given by the ratio of the characteristic electrostatic potential energy to the characteristic kinetic energy per particle (Piel, 2010). The kinetic energy is given by $E_{\text{kin}} = m_s v_{s,t}^2/2 = T_s/2$ and, assuming a mean inter-particle distance of $n_s^{-1/3}$, the potential energy is given by

$$E_{\text{pot}} = \frac{e_s^2 n_s^{1/3}}{4\pi\epsilon_0} . \quad (1.23)$$

The plasma coupling parameter is thus given by

$$\Gamma = \frac{E_{\text{pot}}}{E_{\text{kin}}} = \frac{2e_s^2 n_s^{1/3}}{4\pi\epsilon_0 T_s} \sim \frac{n_s^{1/3}}{T_s} , \quad (1.24)$$

When $\Gamma \ll 1$ the kinetic energy of the plasma greatly exceeds the potential energy associated with the Coulomb potential. A particle does not continuously feel the influence of the other particles in this limit and the plasma is said to be weakly coupled. The Vlasov equation, introduced in Chapter 2, is only valid⁶ when the

⁴For a fluid description the total β is given by

$$\beta = 2 \frac{c_s^2}{v_a^2} , \quad (1.21)$$

where v_a^2 is given by Equation 1.17, the sound speed is $c_s = \sqrt{p/\rho}$ and p is the fluid pressure. This agrees with Equation 1.22 as $p = \sum_s p_s$.

⁵Not to be confused with the plasma parameter, $\Lambda = 4\pi\lambda_D^3$, or the Debye number, $N_D = \Lambda/3$, which is the number of particles in a Debye sphere. These parameters are however related such that $\Lambda \gg 1$ corresponds to $\Gamma \ll 1$ and vice versa.

⁶The derivation of the Vlasov equation truncates the BBGKY hierarchy by assuming that the one-particle distribution function does not depend on two-particle correlations and this assumption is only valid if the interactions are short-ranged, i.e., if the plasma is weakly coupled. See e.g. Bartelmann (2013) and Hazeltine and Waelbroeck (2004).

1. Introduction

plasma is weakly coupled. Most astrophysical plasmas and all of the plasmas considered in this thesis have $\Gamma \ll 1$. Examples of strongly coupled plasmas include dusty plasmas and laboratory plasmas that are not quasi-neutral (Piel, 2010).

The various plasma parameters introduced above can be estimated for the astrophysical systems of interest. The information required is the plasma temperature, density and the magnetic field strength. In order to estimate the magnetization, δ , and the Knudsen number, Kn , we also need an estimate for the characteristic length scale of the system. We have found rough estimates for T , n , B and L in the literature, i.e., in Borovsky and Gary (2011) for the solar wind, in Quataert (2003) for Sgr A* and in Carilli and Taylor (2002) and Vikhlinin et al. (2006) for the ICM⁷. A summary of the resulting parameters are presented in Table 1.1. We observe that the solar wind is the least collisional ($\text{Kn} \approx 3$) followed by the accretion flow in Sgr A* with $\text{Kn} \approx 0.6$. The ICM has $\text{Kn} \approx 0.01$ which is small but collisions might have a role to play here, i.e., the ICM is weakly collisional. We also note that all three astrophysical systems are magnetized with $\delta \ll 1$ and that they are weakly coupled $\Gamma \ll 1$ (or equivalently Λ , $N_D \gg 1$). The plasma β is greater than one for hot accretion flows and the ICM. This implies that these systems are very likely to be subject to velocity-space microscale instabilities. While the Solar wind has $\beta \approx 0.4$ with the values used here, the solar wind is also thought to be subject to microscale instabilities. We discuss this in the following.

1.2 The solar wind

The fast solar wind consists of a stream of charged particles traveling at a velocity of $\sim 400 - 800$ km/s (Schwenn, 2001). The existence of this low density (5 cm^{-3}) and high temperature (10 eV) plasma was deduced by L. Biermann who interpreted observations of ion tails in comets as being due to acceleration by a "corpuscular radiation" from the sun, i.e., a solar wind (Biermann, 1951; Biermann, 1957). Using ideal MHD the solar wind was predicted by (Parker, 1958) to

⁷We note that we have assumed $T_i = T_e$ for simplicity and that the values used here are merely meant to illustrate the difference in the magnitudes of the various parameters.

	Solar wind at 1 AU	Sgr A*	ICM
T (eV)	10	2×10^3	5×10^3
n (m^{-3})	5×10^6	10^8	10^4
B (T)	10^{-8}	10^{-7}	10^{-10}
L (m)	10^{11}	10^{15}	3×10^{21}
ω_p (s^{-1})	10^5	6×10^5	6×10^3
$v_{t,i}$ (m/s)	4×10^4	6×10^5	10^6
v_a (m/s)	10^5	2×10^5	2×10^4
Ω_i (s^{-1})	1	10	0.01
ν_{ii} (s^{-1})	10^{-7}	9×10^{-10}	3×10^{-14}
λ_D (m)	10	50	7×10^3
r_i (m)	5×10^4	6×10^4	10^8
$\lambda_{\text{mfp},i}$ (m)	4×10^{11}	7×10^{14}	3×10^{19}
β	0.4	20	4×10^3
δ_i	3×10^{-7}	5×10^{-11}	3×10^{-14}
Kn	3	0.6	0.01
Γ	5×10^{-8}	7×10^{-10}	10^{-11}

Table 1.1: Characteristic temperatures, number densities and magnetic field strengths for the solar wind, Sgr A* and the ICM (Quataert, 2003; Vikhlinin et al., 2006; Borovsky and Gary, 2011). The characteristic lengths are chosen to be 1 AU, 0.04 pc and 100 kpc, respectively.

have an associated magnetic field of the form (see, e.g., Fitzpatrick 2014)

$$\mathbf{B} = B_0 \left[\left(\frac{r_0}{r} \right)^2 \mathbf{e}_r - \frac{\Omega_\odot r_0}{u_{\text{SW}}} \frac{r_0}{r} \sin \theta \mathbf{e}_\phi \right]. \quad (1.25)$$

Here u_{SW} is the solar wind speed, Ω_\odot is the solar rotation rate and B_0 is the magnetic field strength at the reference point, $r = r_0$ and $\theta = 0$.

The dipolar magnetic field of the Earth impedes the solar wind resulting in a bow shock and a distortion of the Earth's magnetic field, giving it an elongated shape (Baumjohann and Treumann, 1996). Some of the solar wind particles are reflected at the bow shock, forming the foreshock region. This region has particle populations with different drift velocities which can give rise to the ion beam instability that we discuss in Chapter 12 (Treumann and Baumjohann, 1997).

We can use the magnetic field given by Equation 1.25 to estimate how an ini-

1. Introduction

tially isotropic velocity space distribution will change as a function of radius (Matteini et al., 2006). If we completely ignore collisions then it is possible to derive the CGL-equations (Chew, Goldberger, and Low, 1956) given by (see, e.g., Baumjohann and Treumann 1996 or Berlok 2014 for a discussion of these equations by the present author)

$$\frac{d}{dt} \left(\frac{p_{\perp}}{n_s B} \right) = 0, \quad (1.26)$$

$$\frac{d}{dt} \left(\frac{p_{\parallel} B^2}{n_s^3} \right) = 0, \quad (1.27)$$

where the parallel and perpendicular pressures are related to the parallel and perpendicular temperatures by the equation of state for an ideal gas, i.e., $p_{\parallel} = n_s T_{\parallel}$ and $p_{\perp} = n_s T_{\perp}$. The CGL-equations describe how a changing magnetic field and/or density will lead to changes in the parallel and perpendicular pressures (temperatures). The derivation of these equations assumes that the pressure tensor, \mathbf{P} , can be written as (Baumjohann and Treumann, 1996)

$$\mathbf{P} = p_{\perp} \mathbf{1} + (p_{\parallel} - p_{\perp}) \mathbf{b}\mathbf{b}, \quad (1.28)$$

where $\mathbf{1}$ is the identity matrix and \mathbf{b} is a unit vector in the direction of the local magnetic field.

From mass continuity in the solar wind we can assume that $n_s u_{\text{SW}} r^2$ is constant such that the number density of the plasma will scale as $n_s \propto r^{-2}$. If we ignore the azimuthal component of the magnetic field (Equation 1.25), the magnetic field strength will scale as $B \propto r^{-2}$. The CGL equations (Equations 1.26 and 1.27) then predict that (Matteini et al., 2006)

$$T_{\parallel} \propto n_s^2 / B^2 \propto \text{const.}, \quad (1.29)$$

$$T_{\perp} \propto B \propto r^{-2}, \quad (1.30)$$

such that the ratio of parallel to perpendicular temperature will vary as $T_{\parallel}/T_{\perp} \propto r^2$. In Chapters 7 and 12 we will see that temperature anisotropies can lead to microscale instabilities that are driven by the anisotropy in the velocity space dis-

tribution. In particular, the firehose instability is expected to go unstable for a temperature anisotropy with $T_{\parallel} > T_{\perp}$. For the solar wind, Marsch, Zhao, and Tu (2006) and Bale et al. (2009) have presented data from observations that show that the velocity space distribution is confined to the region of stability for the mirror and firehose instabilities. This indicates that the microscale instabilities saturate by driving the temperature anisotropy back to marginal stability. A similar behavior is also observed in simulations of microscale instabilities. For instance, studies using "expanding box" Vlasov-fluid simulations, which imitate the solar wind expansion by continuously driving the temperature anisotropy have been performed by Matteini et al. (2006, 2012) and Hellinger et al. (2015). Similarly, Sironi and Narayan (2015) employed a 'compressing box' to study compressive motions in hot accretion flows. We will use these observations as motivation for limiting the temperature anisotropy in our implementation of Braginskii MHD (Chapter 2).

In the preceding discussion we considered a stationary description of the solar wind. In reality, the solar wind is a dynamic system which should be understood through its coupling to the sun and its internal dynamics (see, e.g., Zurbuchen 2007). More information about plasma physics in the solar system, i.e., space plasma physics, can be found in, e.g., Baumjohann and Treumann (1996) and Treumann and Baumjohann (1997).

1.3 Hot accretion flows

Radiatively inefficient accretion flows (RIAFs) are believed to take place in accretion disks around compact objects. These hot accretion flows accrete at a rate much smaller than the Bondi accretion rate and have been reviewed by Quataert (2003) and Yuan and Narayan (2014). The prime candidate for a RIAF is the radio (and X-ray) source at the center of our galaxy, Sagittarius (Sgr) A*. As heat escapes slowly, this makes the accretion disk very hot and gives rise to a geometrically thick and optically thin disk. The estimated temperature and density at the Bondi radius of the black hole candidate are shown in Table 1.1. The estimated value of the Knudsen number is $\text{Kn} = 0.6$, i.e., the plasma is collisionless and the time scale for Coulomb collisions is much longer than the time scale for accretion. This also means that the timescale for thermal equilibration between ions and electrons is

1. Introduction

long compared to the accretion time scale. As electrons cool more efficiently than ions (by emitting radiation) this could give rise to a two-temperature flow with the electron temperature being a fraction of the ion temperature. Counteracting the cooling, however, the ions and electrons are also thought to be heated by other mechanisms such as turbulence and magnetic reconnection (Yamada, Kulsrud, and Ji, 2010). Understanding the relative efficiency of heating of electrons and ions is therefore important for determining whether the plasma has a two-temperature structure. Studies of electron heating have been performed by, e.g., Sharma et al. (2007) and Sironi and Narayan (2015). We note that the thermodynamics of the electrons is especially interesting because of its impact on the emitted radiation.

The magneto-rotational instability (MRI, Velikhov 1959; Chandrasekhar 1960; Balbus and Hawley 1991, see also Balbus and Hawley 1998 for a review) is considered a promising mechanism for transport of angular momentum leading to accretion in astrophysical disks. This instability was originally found using ideal MHD but has since then been extended to the collisionless case using kinetic MHD (Quataert, Dorland, and Hammett, 2002). A study of the transition from collisional MRI to collisionless MRI was presented by Sharma, Hammett, and Quataert (2003) using a Krook operator for the collisions. A treatment of the problem using an anisotropic viscosity tensor can be found in Balbus (2004). These initial analytical studies found that the growth rate of the collisionless MRI can exceed the growth rate of the collisional MRI. Ferraro (2007) also included a Braginskii ion gyroviscosity and found that this can stabilize even long wavelength modes of the MRI. The complete dispersion relation for a collisionless plasma using Vlasov theory has more recently been obtained by Heinemann and Quataert (2014) and solved in the hot electron limit in Quataert, Heinemann, and Spitkovsky (2015).

Shearing box simulations of the MRI have been performed by using the CGL-equations with a Landau fluid closure (Sharma et al., 2006) and stratified shearing box simulations have been performed by Hirabayashi and Hoshino (2017). Particle-in-cell simulations of the MRI with kinetic ions and electrons have also been presented by Riquelme et al. (2012) and Hoshino (2013, 2015). More recently, a shearing box simulation of the MRI using the Vlasov-fluid equations was presented by Kunz, Stone, and Quataert (2016).

We have highlighted that the application of ideal MHD to hot accretion flows is suspect due to the low degree of collisionality. This is, however, not the only reason. Due to the proximity with a super massive black hole with mass $\sim 10^6 M_\odot$, general relativity should also be taken into account. General relativistic MHD (GRMHD) simulations of hot accretion flows have been performed for some time (see, e.g., Gammie, McKinney, and Toth 2003 and references therein). More recently, GRMHD simulations have directly incorporated the effects of low collisionality as diffusion terms which model anisotropic heat flow and momentum (Ressler et al., 2015; Foucart et al., 2016; Ressler et al., 2016; Chandra, Foucart, and Gammie, 2017). This general relativistic version of Braginskii MHD has the same limitation as non-relativistic Braginskii MHD in that it does not describe velocity-space instabilities from first principles (see also Chapter 2).

1.4 The intracluster medium

The intracluster medium (ICM) is a hot, dilute plasma which permeates the space between galaxies in galaxy clusters. Typical galaxy cluster masses are $10^{14} - 10^{15} M_\odot$ of which the primary component is dark matter with the ICM contributing roughly 10% and the galaxies themselves only contributing around 1% of the total mass (Andreon, 2010). Galaxy cluster sizes are of order Mpc (Vikhlinin et al., 2006) and galaxy clusters are the largest gravitationally bound objects in the Universe both by volume and mass. While we will only concern ourselves with the plasma physics of the ICM, we note that galaxy clusters are also useful astrophysical systems in cosmology (Voit, 2005; Mantz et al., 2014).

The ICM is a diffuse X-ray source, the emission mechanism being thermal Bremsstrahlung (Sarazin, 1986). Since this emission mechanism is well understood the underlying temperature and density of the plasma can be deduced from X-ray observations⁸. Such observations reveal that the ICM is often approximately spherically symmetric and in hydrostatic equilibrium (McNamara and Nulsen, 2007). Assuming that the gas is in hydrostatic equilibrium can be used to estimate the total cluster mass. Although such an estimate is limited by this assumption, general consensus is found with estimates from weak lensing or velocity dispersion

⁸Bearing in mind the caveat outlined in Chapter 3.

1. Introduction

of galaxies (McNamara and Nulsen, 2007).

The magnetic field strength of the ICM can be measured using Faraday rotation, synchrotron emission or inverse Compton scattering and values are found to be of order⁹ μG (Carilli and Taylor, 2002). A radial profile for the magnetic field in the Coma cluster has been estimated by Bonafede et al. (2010) and is used to estimate β in Chapter 3. As observed in Table 1.1, the value of β can be quite high. This implies that the ICM will be subject to microscale instabilities (see, e.g., Schekochihin et al. 2005).

A proper description of the physics of the ICM contains a lot of elements and is not within the scope of this thesis. We refer the interested reader to Markevitch and Vikhlinin (2007) for a review of shocks and cold fronts; to McNamara and Nulsen (2007) for a review of the role of heating by active galactic nuclei (AGN), radio lobes and the absence of a cooling flow; and to Voit (2005) for a general overview of galaxy clusters which includes how they form and the role of dark matter and cosmology on their evolution.

It is computationally demanding to perform global simulations of the ICM (see however, e.g., Parrish, Quataert, and Sharma 2009 for an example) but important insight can also be gained by studying simplified models that retain the most relevant physics. In this thesis we consider an idealized model, i.e., a plane-parallel atmosphere which is weakly collisional ($\text{Kn} = 0.01$) and stratified in temperature and composition. The motivation for considering this model is that stratification in temperature is found in observations (Vikhlinin et al., 2006) and that stratification in composition is found in theoretical sedimentation models (see Chapter 3).

A weakly collisional, magnetized atmosphere as outlined above has stability properties that differ from those expected from the Schwarzschild criterion which governs the stability of stars (Schwarzschild, 1958). The new stability properties arise as a consequence of anisotropic transport of heat, in which the heat flow is directed along the local magnetic field. This anisotropic transport has been modeled by using Braginskii MHD (Braginskii, 1965) in which the heat flow vector,

⁹Where $1 \mu\text{G} = 10^{-4} \text{ T}$.

Q , is given by

$$Q = -\chi_{\parallel} \mathbf{b}\mathbf{b} \cdot \nabla T, \quad (1.31)$$

where T is the temperature of the plasma and χ_{\parallel} is the heat conductivity (Spitzer, 1962).

Two widely studied instabilities that can arise due to anisotropic transport of heat given by Equation 1.31, are the magneto-thermal instability (MTI, Balbus 2000, 2001) and the heat-flux-driven buoyancy instability (HBI, Quataert 2008). The MTI (HBI) can be active for stratified atmospheres in which the temperature decreases (increases) with height and is maximally unstable when the magnetic field is horizontal (vertical) with respect to gravity. These instabilities have been studied by, e.g., Parrish and Stone (2005), Parrish, Stone, and Lemaster (2008), Kunz (2011), Kunz et al. (2012), and Parrish et al. (2012a,b) and a review is given by Balbus and Potter (2016).

Generalizations of the MTI and the HBI to a setting where composition is stratified are discussed in Chapter 3 as well as Pessah and Chakraborty (2013), Paper I, Paper II, Paper III and Sadhukhan, Gupta, and Chakraborty (2017).

1.5 Outline of the thesis

The outline of the remainder of the thesis is as follows. In the next chapter we introduce three frameworks used to model weakly collisional and collisionless plasmas. We present the Vlasov-fluid equations (Freidberg, 1972; Cerfon and Freidberg, 2011) which assume that the ions are completely collisionless and that the electrons are an inertialess fluid in Section 2.1. We also introduce Hall MHD which can be regarded to be the cold ion limit of the Vlasov-fluid theory in Section 2.2 and Braginskii MHD which assumes that the plasma is weakly collisional in Section 2.3.

Part two of the thesis, i.e., Chapter 3, provides a summary of Paper I, Paper II, Paper III where we use the Braginskii MHD framework to study the stability properties of the ICM when both temperature and composition gradients are present.

1. Introduction

Part three of the thesis, i.e., Chapters 4-7, describes the linear theory for a magnetized plasma. We consider some of the linear waves that arise in Hall MHD in Chapter 4 and derive the linear dispersion relation for the Vlasov-fluid equations in Chapter 5. This dispersion relation depends on the conductivity tensor of the ions which we present in Chapter 6. Solutions of the dispersion relation are then presented in Chapter 7.

Part four of the thesis, i.e., Chapters 8-12, describes the development of a new Vlasov-fluid code which uses the particle-in-cell (PIC) method. We provide an introduction to this method in Chapter 8 followed by a discussion of staggering in time and space in Chapter 9. Methods for initializing particle positions and velocities are described in Chapter 10. A discussion of aliasing in PIC codes and the finite grid instability is presented in Chapter 11 along with its relation to Landau damping. We present a variety of computer simulations of plasma waves and instabilities in order to illustrate the physics and show that the code is working as intended in Chapter 12.

Finally, Chapter 13 provides a discussion of our results and future prospects.

Chapter 2

Plasma frameworks

This chapter provides a brief introduction to the Vlasov-fluid equations (Freidberg, 1972), Hall MHD and Braginskii MHD (Braginskii, 1965). Braginskii MHD is employed in our study of the ICM in Chapter 3. Vlasov-fluid theory forms the basis for the new code presented in Chapters 8-12 and the linear theory presented in Chapters 5-7. Some of the waves present in Hall MHD, which can be considered to be the cold ion limit of the Vlasov-fluid equations, are derived in Chapter 4 as they have been found to be useful for testing purposes of the Vlasov-fluid code.

2.1 Vlasov-fluid equations

We introduce the Vlasov-fluid model, also often referred to as a hybrid model as it is a hybrid between a fully kinetic model and a fluid description. This system of equations treats the ions kinetically and the electrons as an inertialess, i.e., massless, fluid. In this model, the evolution of the ensemble-averaged phase space density of the ions, $f_s(\mathbf{x}, \mathbf{v}, t)$, is given by (Hazeltine and Waelbroeck, 2004)

$$\frac{df_s}{dt} = 0, \quad (2.1)$$

where

$$\frac{d}{dt} = \frac{\partial}{\partial t} + \mathbf{v} \cdot \nabla + \mathbf{a}_s \cdot \frac{\partial}{\partial \mathbf{v}}, \quad (2.2)$$

2. Plasma frameworks

is the convective derivative in 6-dimensional phase space and the acceleration \mathbf{a}_s is given in Equation 1.5. Equation 2.1 highlights that the phase space volume is conserved when there are no collisions.

We can write out Equations 1.5, 2.1 and 2.2 in order to obtain the Vlasov equation

$$\frac{\partial f_s}{\partial t} + \mathbf{v} \cdot \nabla f_s + \frac{e_s}{m_s} (\mathbf{E} + \mathbf{v} \times \mathbf{B}) \cdot \frac{\partial f_s}{\partial \mathbf{v}} = 0, \quad (2.3)$$

which describes the evolution of the phase space distribution function in a 6-dimensional phase space consisting of three spatial and three velocity dimensions. In this equation $f_s(\mathbf{x}, \mathbf{v}, t)$ is the smooth one-particle phase space distribution function for an ion species s which is subject to the acceleration felt by an ion with charge e_s and mass m_s in the presence of a magnetic field, \mathbf{B} , and an electric field, \mathbf{E} .

Fluid quantities such as ion number density, n_s , and bulk velocity, \mathbf{u}_s , are found by taking moments, i.e., performing integrals over velocity space, of the distribution function. The phase space distribution function is normalized such that

$$n_s = \int d^3v f_s, \quad (2.4)$$

and

$$\mathbf{u}_s = \frac{1}{n_s} \int d^3v \mathbf{v} f_s. \quad (2.5)$$

The ion charge density is given by $\rho_s = e_s n_s$ and the ion current density is given by $\mathbf{J}_s = n_s e_s \mathbf{u}_s$.

The total ion charge density and current¹ are then given by

$$\rho_i = \sum_s \rho_s = \sum_s e_s n_s, \quad (2.6)$$

$$\mathbf{J}_i = \sum_s \mathbf{J}_s = \sum_s n_s e_s \mathbf{u}_s, \quad (2.7)$$

¹Current densities will often simply be referred to as currents.

where the sum extends over all ion species.

An essential ingredient in the Vlasov-fluid framework is the assumption of charge neutrality. Charge neutrality implies that the electron charge density is given by $\rho_e = -en_e = -\rho_i$. The relevant frequency for charge separation is the electron plasma frequency. The assumption of quasi-neutrality thus effectively corresponds to ω_p being infinite, i.e., as the electrons are massless they will immediately respond to any deviation from charge neutrality and erase it.

The equations governing the evolution of the magnetic and electric fields are Faraday's law

$$\frac{\partial \mathbf{B}}{\partial t} = -\nabla \times \mathbf{E}, \quad (2.8)$$

and the pre-Maxwell, i.e., non-relativistic, Ampère's law

$$\nabla \times \mathbf{B} = \mu_0 \mathbf{J}. \quad (2.9)$$

The latter equation gives the total current as the curl of the magnetic field. This means that electromagnetic waves propagating at the speed of light are not included in the model. In simulations, this has the advantage that we do not have to adhere to the severe limits on the timestep that these fast-moving waves would impose.

The total current, \mathbf{J} , is given by the sum of ion and electron currents

$$\mathbf{J} = \mathbf{J}_e + \sum_s \mathbf{J}_s, \quad (2.10)$$

and the relation between the electron fluid velocity and the electron current is $\mathbf{J}_e = -en_e \mathbf{u}_e$.

For an electrostatic PIC code, the electric field is found from

$$\mathbf{E} = -\nabla \Phi, \quad (2.11)$$

where Φ is the potential determined from the solution to Poisson's equation

$$\nabla^2 \Phi = -\rho / \epsilon_0, \quad (2.12)$$

2. Plasma frameworks

and ρ is the total charge density. In the Vlasov-fluid code $\rho = 0$ and the electric field is instead found from the electron momentum equation. This equation can be derived by taking the 1st moment of the Vlasov equation for the electrons. One finds (see, e.g., page 13 in Berlok 2014 or most books on plasma physics/MHD)

$$m_e n_e \frac{d\mathbf{u}_e}{dt} = -\nabla p_e - n_e e (\mathbf{E} + \mathbf{u}_e \times \mathbf{B}), \quad (2.13)$$

where it was assumed that the electron pressure is scalar².

Invoking the Vlasov-fluid framework assumption that the electron mass is zero, i.e., $m_e = 0$ removes the time dependence of the electron momentum equation. This enables us to write an expression for the electric field

$$\mathbf{E} = -\frac{\nabla p_e}{en_e} - \mathbf{u}_e \times \mathbf{B}. \quad (2.14)$$

Equation 2.14 is also known as the generalized Ohm's law.

For future reference we note that we can also write Ohm's law as

$$\mathbf{E} = \frac{\nabla p_e}{\rho_e} - \frac{\mathbf{J}_e \times \mathbf{B}}{\rho_e}, \quad (2.15)$$

where the electron current

$$\mathbf{J}_e = \mathbf{J} - \sum_s \mathbf{J}_s, \quad (2.16)$$

is found by subtracting the sum of the ion currents from the total current.

The magnetic field is tied to the electron fluid in Vlasov-fluid theory. We can show this by combining Ohm's law (Equation 2.14) and Faraday's law (Equation 2.8)

$$\frac{\partial \mathbf{B}}{\partial t} = \nabla \times \left(\frac{\nabla p_e}{en_e} + \mathbf{u}_e \times \mathbf{B} \right) = \nabla \times (\mathbf{u}_e \times \mathbf{B}), \quad (2.17)$$

²The pressure tensor is given by the 2nd moment of the distribution function. We instead truncate the scheme by assuming an equation of state for the electrons, i.e., $p_e = p_e(n_e, T_e)$.

yielding a, from MHD familiar-looking, induction equation³. The well-known proof showing that the magnetic field is moving with the fluid in MHD (see, e.g., Hazeltine and Waelbroeck 2004) can be used to see that the magnetic field is tied to the electron fluid in the Vlasov-fluid model.

The main computational advantage of the Vlasov-fluid framework is that the electron plasma frequency, ω_p , and the Debye length, λ_D , do not enter in the model. This provides a significant simplification both analytically and computationally. The Vlasov-fluid approach significantly eases the computational burden compared to simulations where both the ions and electrons are treated kinetically. For particle in cell (PIC) methods this alleviation of the computational burden comes from not having to resolve the electron time and length scales which are a factor of m_i/m_e shorter. The cost of this simplification is that electron scale phenomena are not included in the model. The Vlasov-fluid model will, for instance, not be useful for studying electron Landau damping, electron scale magnetic reconnection and acceleration of electrons in various astrophysical collisionless systems.

2.2 Hall MHD

The key difference between Hall MHD and the Vlasov-fluid approach is in the way the ions are treated. For Hall MHD the ions are treated as a fluid, i.e., it is the 0th and first order moments of the Vlasov equation that are evolved. We consider for simplicity a fully ionized hydrogen plasma⁴. The mass continuity equation is then

$$\frac{\partial \rho}{\partial t} + \nabla \cdot (\rho \mathbf{u}_i) = 0, \quad (2.19)$$

³Note that

$$\nabla \times \frac{\nabla p_e}{en_e} = 0, \quad (2.18)$$

for a barotropic electron fluid.

⁴The derivation can be generalized by defining the fluid velocity to be a mass weighted sum.

2. Plasma frameworks

where ρ is the mass density of ions, and the ion momentum equation is

$$\rho \frac{d\mathbf{u}_i}{dt} = -\nabla p_i + n_i e (\mathbf{E} + \mathbf{u}_i \times \mathbf{B}) . \quad (2.20)$$

The electric field in Equation 2.20 can be found from the generalized Ohm's law (Equation 2.14). This expression depends on the electron fluid velocity, \mathbf{u}_e , but we can express the electron velocity in terms of the total current and the ion velocity, \mathbf{u}_i , by using the definition of the total current (Equation 2.10). We find

$$\mathbf{u}_e = -\frac{\mathbf{J}_e}{en_e} = -\frac{\mathbf{J}}{en_e} + \frac{\mathbf{J}_i}{en_e} = -\frac{\mathbf{J}}{en_e} + \mathbf{u}_i , \quad (2.21)$$

which upon substitution into Equation 2.14 yields Ohm's law in the form

$$\mathbf{E} = -\frac{\nabla p_e}{en_e} + \frac{\mathbf{J}}{en_e} \times \mathbf{B} - \mathbf{u}_i \times \mathbf{B} . \quad (2.22)$$

The first term in Equation 2.22 is known as the ambipolar electric field, the second term is the Hall electric field and the last term is the electric field also found in ideal MHD. Note that last term contributing to the electric field is zero in a frame moving with the plasma (Parker, 2007).

Combining Equation 2.20 and Equation 2.22 we obtain

$$\rho \frac{d\mathbf{u}_i}{dt} = -\nabla(p_i + p_e) + \mathbf{J} \times \mathbf{B} , \quad (2.23)$$

where charge neutrality, $n_i = n_e$, was assumed. The ion momentum equation can then be written as

$$\rho \frac{d\mathbf{u}_i}{dt} = -\nabla p + \mathbf{J} \times \mathbf{B} , \quad (2.24)$$

if we define the total (thermal) pressure as $p = p_e + p_i$.

Summarizing, the equations of Hall MHD are the ion mass continuity equation (Equation 2.19), the ion momentum equation (Equation 2.24) with the current given by Ampère's law (Equation 2.9) and Faraday's law (Equation 2.8) with the electric field given by Ohm's law (Equation 2.22).

2.3 Braginskii MHD

Braginskii MHD is a fluid model which includes diffusion terms in order to model transport of heat and momentum in a weakly collisional plasma (Braginskii, 1965).

A derivation of Braginskii MHD can be found in Fitzpatrick (2014) and a derivation of the equations of Braginskii MHD for a binary mixture of hydrogen and helium has previously been presented by the present author in Berlok (2014). The latter set of equations was used by Pessah and Chakraborty (2013) and a discussion of their derivation can also be found in Appendix B in Paper I. We do not re-derive these results here but simply note that the basic idea is that collisions can be included by adding a collisional term on the right hand side of the Vlasov equation (Equation 2.3), yielding the Boltzmann equation.

The equations of Braginskii MHD are found to be the mass continuity equation

$$\frac{\partial \varrho}{\partial t} + \nabla \cdot (\varrho \mathbf{u}) = 0, \quad (2.25)$$

the momentum equation

$$\frac{\partial(\varrho \mathbf{u})}{\partial t} + \nabla \cdot \left(\varrho \mathbf{u} \mathbf{u} + p_{\text{T}} \mathbf{1} - \frac{\mathbf{B} \mathbf{B}}{\mu_0} \right) = -\nabla \cdot \mathbf{\Pi} + \varrho \mathbf{g}, \quad (2.26)$$

the induction equation

$$\frac{\partial \mathbf{B}}{\partial t} = \nabla \times (\mathbf{u} \times \mathbf{B}), \quad (2.27)$$

and the energy equation

$$\frac{\partial E}{\partial t} + \nabla \cdot \left[(E + p_{\text{T}}) \mathbf{u} - \frac{\mathbf{B}(\mathbf{B} \cdot \mathbf{u})}{\mu_0} \right] = -\nabla \cdot \mathbf{Q} - \nabla \cdot (\mathbf{\Pi} \cdot \mathbf{u}) + \varrho \mathbf{g} \cdot \mathbf{u}. \quad (2.28)$$

In these equations \mathbf{u} is the fluid velocity, $p_{\text{T}} = p + B^2/2\mu_0$ is the total pressure

2. Plasma frameworks

(gas plus magnetic) and

$$E = \frac{1}{2}\varrho u^2 + \frac{B^2}{2\mu_0} + \frac{p}{\gamma - 1}, \quad (2.29)$$

is the total energy density. We take $\gamma = 5/3$ and

$$p = \frac{\varrho T}{m_{\text{H}}\mu}, \quad (2.30)$$

where m_{H} is the proton mass and μ is the mean molecular weight. Gravity is included in the momentum and energy equations where the gravitational acceleration is given by $\mathbf{g} = -g\mathbf{e}_z$, g being a constant.

For a hydrogen-helium plasma we amend these equations with a continuity equation for the helium mass

$$\frac{\partial(c\varrho)}{\partial t} + \nabla \cdot (c\varrho\mathbf{u}) = 0, \quad (2.31)$$

where c is the helium mass concentration

$$c \equiv \frac{\varrho_{\text{He}}}{\varrho_{\text{H}} + \varrho_{\text{He}}} = \frac{\varrho_{\text{He}}}{\varrho}, \quad (2.32)$$

which is related to the mean molecular weight by

$$\mu = \frac{4}{8 - 5c}. \quad (2.33)$$

This generalizes the Braginskii MHD equations to describe systems where the composition is not constant (Pessah and Chakraborty, 2013).

The anisotropic heat flux, \mathbf{Q} , present in the energy equation, is given by

$$\mathbf{Q} = -\chi_{\parallel}\mathbf{bb} \cdot \nabla T, \quad (2.34)$$

where χ_{\parallel} is the Spitzer heat conductivity given by (Spitzer, 1962)

$$\chi_{\parallel} = \frac{5p_e}{2m_e\nu_e}, \quad (2.35)$$

and ν_e is obtained from Equations 1.9 and 1.10.

A pressure anisotropy, $\Delta p_s = p_{\perp,s} - p_{\parallel,s}$, for species s , enters in both the momentum and entropy equation through the viscosity tensor

$$\mathbf{\Pi} = - \sum_s \Delta p_s \left(\mathbf{bb} - \frac{1}{3} \mathbf{1} \right), \quad (2.36)$$

Within the framework of Braginskii-MHD (Braginskii, 1965), this pressure anisotropy can be calculated from⁵

$$\Delta p_s = \frac{p_s}{\nu_s} \frac{d \ln B^3 n_s^{-2}}{dt} = \frac{p_s}{\nu_s} (3\mathbf{bb} : \nabla \mathbf{u} - \nabla \cdot \mathbf{u}), \quad (2.37)$$

where ν_s is the Coulomb collision frequency of species s (Equation 1.9 and 1.10). The last equality can be shown to be true by using the continuity equation and the induction equation, i.e., Equations 2.25 and 2.27. We see from Equation 2.37 that a pressure anisotropy naturally arises in a weakly collisional or collisionless plasma because changes in magnetic field strength or plasma density will, in general, lead to a non-zero pressure anisotropy. The resulting magnitude of the pressure anisotropy depends inversely on the collision frequency.

The Braginskii viscosity tensor can also be written as

$$\mathbf{\Pi} = -3\rho\nu_{\parallel} \left(\mathbf{bb} - \frac{1}{3} \mathbf{1} \right) \left(\mathbf{bb} - \frac{1}{3} \mathbf{1} \right) : \nabla \mathbf{u}, \quad (2.38)$$

where the Braginskii viscosity coefficient is defined as

$$\nu_{\parallel} = \frac{T}{\rho} \left(\frac{n_{\text{H}}}{\nu_{\text{H}}} + \frac{n_{\text{He}}}{\nu_{\text{He}}} \right). \quad (2.39)$$

Only the ion pressure anisotropy is included because the electron viscous flux due to electrons will be lower by a factor of $\sim \sqrt{m_e/m_i}$, where m_e (m_i) is the electron (ion) mass.

While Braginskii MHD can capture some aspects of low collisionality, i.e., anisotropic transport of heat and momentum, it does not correctly describe the

⁵The notation $:$ has the following meaning $\mathbf{bb} : \nabla \mathbf{u} = \sum_i \sum_j b_i b_j \partial_i u_j$ which is equivalent to the trace of the matrix product between the matrices \mathbf{bb} and $\nabla \mathbf{u}$.

2. Plasma frameworks

microscale instabilities (Schekochihin et al., 2005). Using Braginskii MHD, the growth rates found for the firehose and mirror instabilities are proportional to the wavenumber which leads to a UV-catastrophe (see also Chapter 7). For computer simulations this means that the growth rate will depend on the numerical resolution. Since the microscale instabilities do not saturate correctly the pressure anisotropy can in principle grow to very large values. This would make the simulations more viscous than expected in a simulation where the microscale instabilities are correctly described.

Motivated by observations in the solar wind and PIC simulations (see also Section 1.2) Sharma et al. (2006) limited the pressure anisotropy in their shearing box simulations of the MRI to be within the thresholds set by marginal stability of microscale instabilities. A similar approach has been used to study the MTI and the HBI in Kunz et al. (2012) and to study the MTCI and the HPBI in Paper III (see also Chapter 3).

We consider two important microscale instabilities for the ions, namely the firehose and the mirror instability (see Chapter 7 for discussion of these instabilities). The firehose instability is unstable if

$$\frac{p_{\perp}}{p_{\parallel}} - 1 < -\frac{2}{\beta_{\parallel}}, \quad (2.40)$$

and the mirror instability is unstable if

$$\frac{p_{\perp}}{p_{\parallel}} - 1 > \frac{1}{\beta_{\parallel}}, \quad (2.41)$$

where $\beta_{\parallel} = 2\mu_0 p_{\parallel}/B^2$ and $\beta_{\perp} = 2\mu_0 p_{\perp}/B^2$. Note that these criteria for instability can be rewritten into a criterion for stability

$$-\frac{B^2}{\mu_0} < \Delta p < \frac{B^2}{2\mu_0}. \quad (2.42)$$

In the simulations where we use limiters, the pressure anisotropy is calculated using Equation 2.36 but its value is limited to lie in the interval given by Equation 2.42.

Chapter 3

On the distribution of helium in the intracluster medium

This chapter provides a summary of our work on the stability properties of the ICM which resulted in the publications Berlok and Pessah (2015), Berlok and Pessah (2016a), and Berlok and Pessah (2016b), hereafter referred to as Paper I, Paper II, and Paper III, respectively. The work leading to these publications was initiated during the M.Sc. study and some of the material in the publications has previously been presented in Berlok (2014). In this chapter we summarize our findings with an emphasis on the results that were obtained during the PhD study.

The work presented here is a generalization of previous studies on weakly collisional atmospheres which are stratified in temperature but have a constant composition. These studies found that a weakly collisional atmosphere can be unstable to the magneto-thermal instability (MTI, Balbus 2000, 2001) when the temperature decreases with height and to the heat-flux-driven buoyancy instability (HBI, Quataert 2008) when temperature increases with height. The criteria for instability for the MTI and the HBI are such that they could be present in the outer and inner regions of cool core clusters. The reason is that the temperature in such clusters increases (decreases) with radius in the inner (outer) regions. A typical temperature distribution is shown with a red dashed line in Figure 3.1 (Vikhlinin et al., 2006). These instabilities have been the subject of intensive research and a review can be found in Balbus and Potter (2016). Many references to the literature

3. On the distribution of helium in the intracluster medium

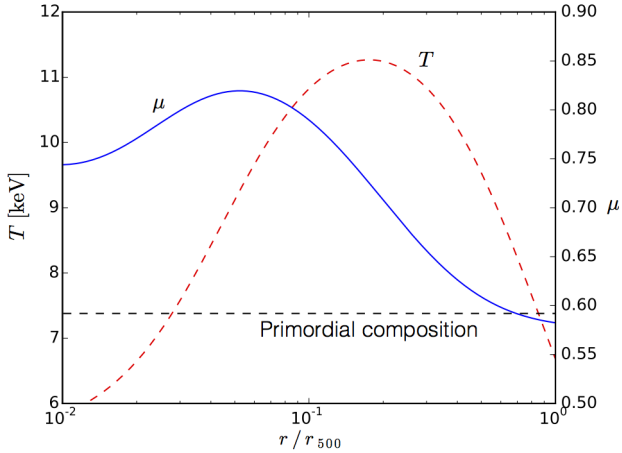


Figure 3.1: Figure 7 in Paper I. The mean molecular weight profile (blue line) in a 11 Gyr-old galaxy cluster and the temperature profile (red dashed line) used in the model of Peng and Nagai (2009). The dashed black line indicates the primordial composition.

on the MTI and the HBI can also be found in Paper I, Paper II and Paper III.

The motivation for including a composition gradient is that 1D sedimentation models predict its existence (Fabian and Pringle, 1977; Gilfanov and Syunyaev, 1984; Chuzhoy and Nusser, 2003; Chuzhoy and Loeb, 2004; Peng and Nagai, 2009; Shtykovskiy and Gilfanov, 2010) and that X-ray measurements might be biased as a consequence (Markevitch, 2007; Peng and Nagai, 2009).

We have used the model by Peng and Nagai (2009) extensively in Paper I, Paper II and Paper III. Their model for a 11 Gyr old intracluster medium, in which helium has been sedimenting towards the core, is shown in Figure 3.1. In this figure the mean molecular weight, μ , is seen to have a positive (negative) gradient in the inner (outer) ICM. Correspondingly, the temperature profile, which is given by Vikhlinin et al. (2006), is seen to have positive (negative) gradient in the inner (outer) ICM. The similarity between the temperature and composition profiles arises due to the assumed temperature dependence of the friction between hydrogen and helium ions as the helium ions sediment (Peng and Nagai, 2009). The black dashed line shows the initial distribution of composition in their model,

given by a constant primordial value of $\mu = 0.59$.

The 1D sedimentation models have not been compared directly with observations because the amount of helium in the hot ICM cannot be inferred directly from X-ray measurements. The problem is that helium is completely ionized at the > 1 keV temperatures characteristic of the ICM such that line emission from helium is not emitted. The helium composition will however effect the X-ray continuum (Bremsstrahlung) emission as the intensity of Bremsstrahlung emission depends on the charge of the ion species. We briefly outline the arguments put forward in Markevitch (2007) in order to show how this can lead to biases in X-ray observations if the composition is not constant.

If we assume that all ion species and electrons have the same temperature then the emissivity is given by (Bartelmann, 2013)

$$j(\omega) = \frac{16\pi^2}{3\sqrt{3}} \frac{e^6}{m_e^2 c^3} e^{-\hbar\omega/T} \sqrt{\frac{2m_e}{\pi T}} \sum_s e_s^2 n_s n_e, \quad (3.1)$$

where \hbar is the reduced Planck constant. From this equation we see that the emissivity of a binary mixture of hydrogen and helium is proportional to

$$j(\omega) \propto \sum_s e_s n_s n_e = 4e^2 n_{\text{He}} n_e + e^2 n_{\text{H}} n_e = e^2 (2n_{\text{He}} + n_{\text{H}})(4n_{\text{He}} + n_{\text{H}}) = e^2 n_{\text{H}}^2 (2x + 1)(4x + 1), \quad (3.2)$$

where we used that the electron number density $n_e = 2n_{\text{He}} + n_{\text{H}}$ (one electron per hydrogen ion and two per helium ion) and defined $x = n_{\text{He}}/n_{\text{H}}$ to be the ratio of the helium and hydrogen number densities. As x cannot be determined spectroscopically a common assumption is that the helium composition is primordial, i.e. $x = 0.083$ (Markevitch, 2007). This assumption is seen to lead to an error in the estimate of n_{H} if helium has sedimented such that $x > 0.083$. Such an error can propagate into the estimate for the gas density of the ICM, the total mass of the ICM and the gas mass fraction of the cluster (Markevitch, 2007).

In the helium sedimentation model of Peng and Nagai (2009) the composition profile, shown in Figure 3.1 with a blue solid line, leads to an error of 20 % in the

3. On the distribution of helium in the intracluster medium

predicted value of the Hubble constant if a primordial composition is assumed¹.

As originally shown in Pessah and Chakraborty (2013), the model of Peng and Nagai (2009) is however unstable to generalizations of the MTI and HBI due to the temperature and composition gradients. The most important² of these generalizations are called the magneto-thermo-compositional instability (MTCI) and the heat- and particle-flux-driven buoyancy instability (HPBI) (Pessah and Chakraborty, 2013). If these instabilities are able to mix the composition gradient on a fast time scale then the concerns about biases in X-ray observations raised above would be severely alleviated. Attempting to answer this question has been the aim of Paper I, Paper II and Paper III.

3.1 Paper I

In the first paper we used the Braginskii-MHD equations (Equations 2.25-2.31) to perform a local, linear mode analysis of plane-parallel atmospheres that are stratified in composition and temperature. The dispersion relation was solved for a number of ideal cases, i.e., strictly isothermal atmospheres with varying signs of the composition gradient and magnetic field inclination with respect to gravity. The main conclusions found from this idealized setting was that *i*) isothermal atmospheres comprised of weakly collisional plasmas in which the composition increases with height are unstable regardless of whether the magnetic field is horizontal (the MTCI) or vertical (the HPBI). Furthermore, when the magnetic field is inclined both the MTCI and the HPBI can be present at the same time. This is in contrast to the temperature driven instabilities, i.e., the MTI and the HBI will never be present at the same time as they require temperature gradients pointing in opposite directions. *ii*) the HPBI has its most unstable wavelength at a length scale longer than the scale height of the atmosphere when the effect of Braginskii viscosity is taken into account. This feature of the HPBI calls into question the lo-

¹Conversely, independent measurements of the Hubble constant could in principle be used to constrain the amount of helium sedimentation present (Markevitch, 2007). This requires that other sources of error are so small that the bias introduced by assuming a constant composition is dominant.

²Several other instabilities, such as diffusion modes driven by anisotropic diffusion of helium composition, are introduced in Pessah and Chakraborty (2013). Some of these are also discussed in Paper I and Paper II.

cal, linear analysis that was performed as it assumed that the wavelengths are much smaller than the scale height of the atmosphere. A similar problem has previously been found for the HBI (Kunz, 2011) and consequently remedied by extending the linear analysis to be quasi-global (Latter and Kunz, 2012).

We have similarly extended the linear analysis of the HPBI in Paper III. These conclusions have also been presented in Berlok (2014). Similarly, both Pessah and Chakraborty (2013) and Berlok (2014) applied local, linear stability analysis to current state-of-art models for the distribution of composition and temperature in the intracluster medium. The main extension to the work presented in Pessah and Chakraborty (2013) and Paper I during the PhD study was a much more detailed application of the linear stability analysis to the cluster model of Peng and Nagai (2009). In Paper I, the model of Peng and Nagai (2009) is used to estimate gradients of temperature and composition (along with other physical quantities) as a function of radius. Given this knowledge, the growth rates of the instabilities at any given radius can be found by solving the dispersion relation as a function of wave number. An example of the resulting growth rate contours is presented in Figure 3.2. In this figure the growth rates have been calculated for both models without (left panel) and with (right panel) a composition gradient. The values used to create this figure were taken at $r/r_{500} = 0.5$, i.e., in the outskirts where both the temperature and composition decrease with radius in the model of Peng and Nagai (2009). The growth rates in the left panel are due to the MTI and the growth rates in the right panel are due to its generalization, the MTCI. We see that the presence of a composition gradient reduces the maximal growth rate of the instability by roughly 15%.

The dispersion relation presented in Paper I provides an extension to the dispersion relation previously derived in Pessah and Chakraborty (2013) by retaining the terms responsible for magnetic tension. By also assuming a radially decreasing dependence of the magnetic field strength as found by Bonafede et al. (2010) this enabled us to study the effect of magnetic tension. We found that magnetic tension can inhibit growth rates and provide a cut-off above which parallel wavenumbers are stabilized. The latter effect is clearly seen in Figure 3.2 while the former is illustrated in Figure 3.3. In order to produce this figure the maximum growth

3. On the distribution of helium in the intracluster medium

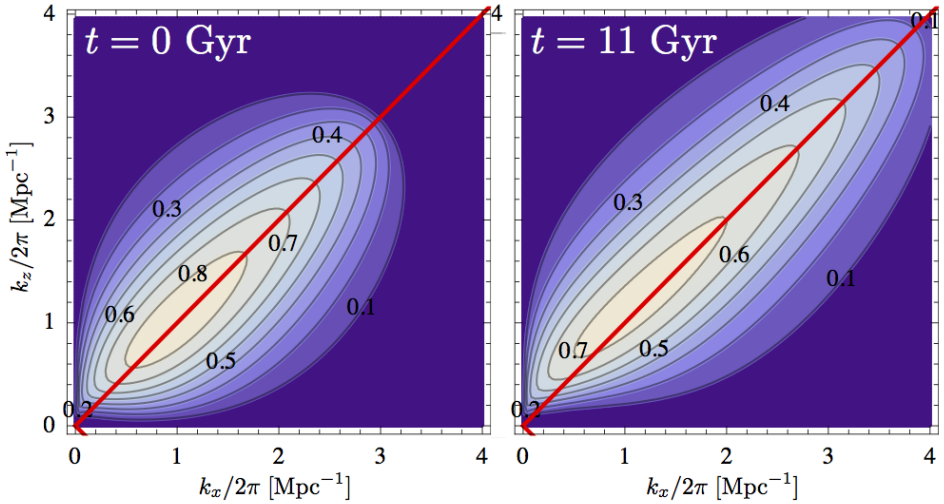


Figure 3.2: Figure 11 in Paper I. Contour plots of the growth rate in Gyr^{-1} for the outer ICM ($r/r_{500} = 0.5$ where $r_{500} = 1.63$ Mpc). This region is unstable to the MTI at $t = 0$ Gyr (left panel) or the MTCI and the conduction modes at $t = 11$ Gyr (right panel). The most unstable modes are found at intermediate parallel wavenumbers at which heat conduction is effective. Magnetic tension stabilizes the instability at higher parallel wavenumbers. The maximum growth rate is decreased by 15% with respect to the homogeneous case. The magnetic field, indicated with a red solid line, is assumed to be inclined at angle of 45 deg with respect to the direction of gravity.

rate³ has been calculated at each radii by using the dispersion relation in Pessah and Chakraborty (2013) (dashed lines) and the dispersion relation that includes magnetic tension (solid lines). The red (blue) lines in Figure 3.2 assume a vertical (horizontal) magnetic field for which only the inner (outer) ICM is unstable. The growth rates are decreased at all radii when magnetic tension is included.

The application of the local, linear, stability analysis to the ICM model of Peng and Nagai (2009) and the influence of composition gradients, is summarized in Figure 3.4. In this figure we have calculated the maximum growth rate as a function of radius for a cluster model with the composition profile given by Peng

³The maximum growth rate is largest growth rate found when calculating the growth rates as a function of wave number, as in Figure 3.2.

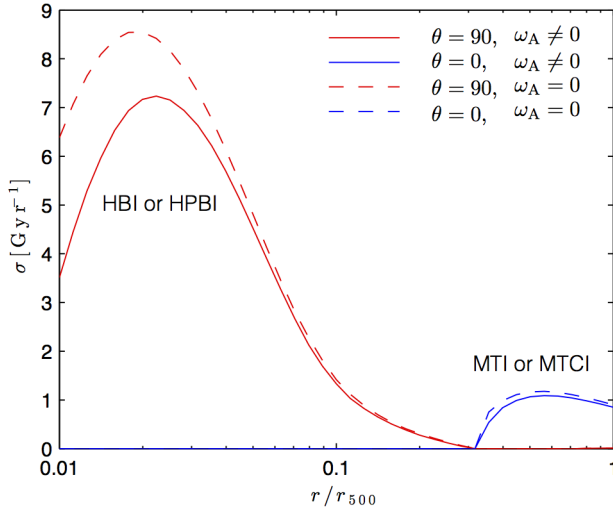


Figure 3.3: Figure 14 in Paper I. The maximum growth rates as a function of radius in the cluster model of Peng and Nagai (2009) at $t = 11$ Gyr in the limit where magnetic tension is neglected (dashed lines) and when it is taken into account (solid lines).

and Nagai (2009) model at $t = 11$ Gyr (solid lines) and a cluster model with constant composition (dashed lines, their model at $t = 0$ Gyr). From this figure we conclude that the composition gradients in the model of Peng and Nagai (2009) will increase (decrease) the growth rates in the inner (outer) regions with respect to the constant composition scenario. We also observe that the model is unstable at all radii.

3.2 Paper II

In the second paper we presented the first simulations of some of the instabilities that are driven by gradients in composition in weakly collisional, magnetized atmospheres. The most interesting of the simulations considered the nonlinear evolution of isothermal atmospheres in which the mean molecular weight increases with height. This is the physical setup that in Paper I was found to be unstable regardless of the magnetic field inclination (to either the MTCl or the HPBI or

3. On the distribution of helium in the intracluster medium

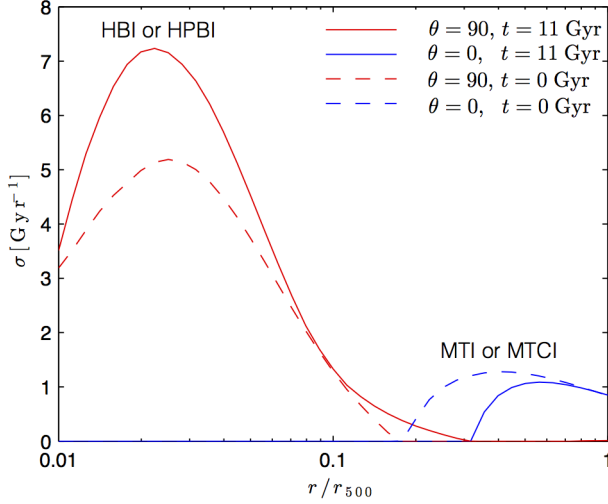


Figure 3.4: Figure 15 in Paper I. The maximum growth rate as a function of radius in the cluster model of Peng and Nagai (2009) at $t = 0$ (dashed) and $t = 11$ Gyr (solid) for a field with $\theta = 90^\circ$ (red) and $\theta = 0^\circ$ (blue) inclination with respect to the direction of gravity. The effects of a finite β are included. The sedimentation increases (decreases) the theoretically predicted growth rates in the inner (outer) cluster.

potentially both instabilities) due to the weakly collisional nature of the plasma. The evolution of the magnetic field structure and composition for these instabilities was presented in figure 7 in Paper II for the case of an initial horizontal and vertical magnetic field. In both cases the instabilities were shown to lead to mixing of the composition (i.e., the instabilities act to erase the helium gradient) and to saturate with a magnetic field inclination of approximately 45 deg.

In order to perform the simulations, a modification of the MHD code Athena (Stone et al., 2008) was required. This modification entailed including the value of the mean molecular weight in the calculation of the temperature of the plasma. Anisotropic diffusion of the helium composition along magnetic field lines was also implemented along with the tests presented in the appendix of Paper II. Furthermore, the transport coefficients for anisotropic diffusion of composition, heat and momentum (D , χ_{\parallel} and ν_{\parallel}) were made spatially dependent⁴, a feature that

⁴The public version Athena (v. 4.2) assumes constant coefficients for χ_{\parallel} and ν_{\parallel} .

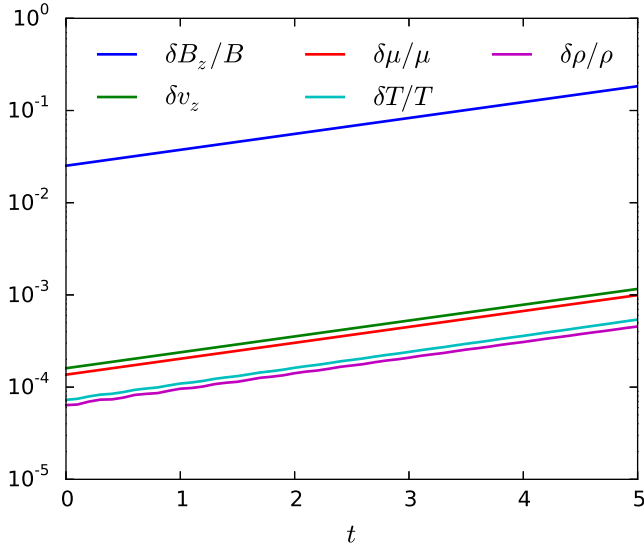


Figure 3.5: Figure 2 in Paper II. Evolution of box-averaged quantities for the MTCI with $\chi_{\parallel} = 3 \times 10^{-3}$ and $\beta_0 = 2 \times 10^8$. The perturbed quantities grow exponentially with a growth rate $\sigma = 0.40$.

was necessary to perform the quasi-global simulations appearing in Paper III. The changes to Athena also included implementing custom boundary conditions that satisfy hydrostatic equilibrium in the vertical direction. The changes were tested by comparing the local, linear theory with the results from simulations.

Most of the code changes described above were implemented during the M.Sc. study and have also been presented in Berlok (2014). During the PhD study a method for exciting all the components of the eigenmodes of the system exactly was developed. This improvement, compared to the previous efforts in which only the velocity components were excited, enabled a much more clean study of the linear evolution of the instabilities. In Figure 3.5 we present an example of the exponential evolution for the MTCI. It is evident that the instability grows cleanly from $t/t_0 = 0$ compared with, e.g., figure 6.7 in Berlok (2014), i.e., without an initial transient.

The comparisons between local simulations and local, linear theory presented in Berlok (2014) only considered isothermal atmospheres. In contrast we showed

3. On the distribution of helium in the intracluster medium

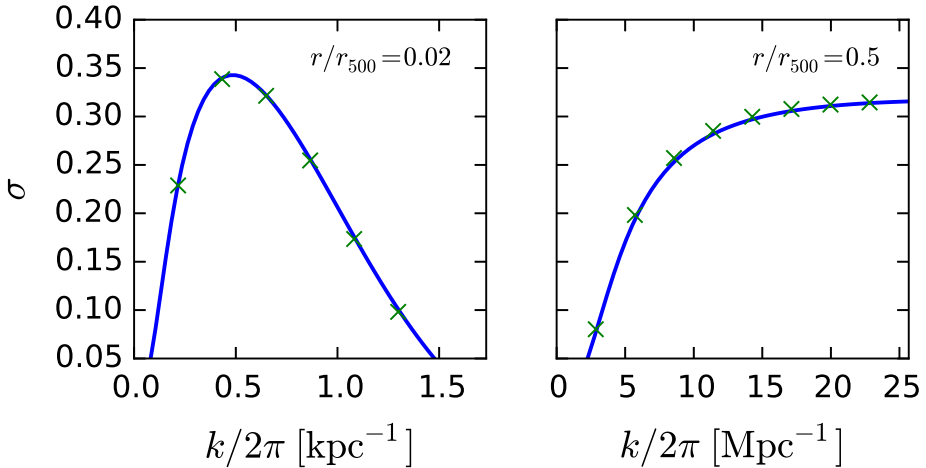


Figure 3.6: Figure 6 in Paper II. Growth rates at $r/r_{500} = 0.02$ as a function of $k = k_x = k_z$ (left panel) and growth rates at $r/r_{500} = 0.5$ as a function of $k = k_x$. Theoretical values (blue solid lines) and values obtained from simulations (green crosses) are seen to agree.

explicitly in Paper II that growth rates found for atmospheres that are stratified in both temperature and composition agree with the local linear theory developed in Paper I and Pessah and Chakraborty (2013). This is illustrated in Figure 3.6 in which the left (right) panel shows the growth rates as a function of wavenumber for the HPBI (MTCI). The parameters used to perform these simulations were found by using values from the model of Peng and Nagai (2009) at $r/r_{500} = 0.02$ and $r/r_{500} = 0.5$ for the left and right panels, respectively. Details can be found in section 4.4 in Paper II.

The nonlinear simulations presented in Paper II made a number of assumptions that limited the applicability of the results to the ICM. These include *i*) assuming locality, i.e., the simulation had a size of $H_0/10 \times H_0/10$ where H_0 is the pressure scale height, and the heat conductivity was set to be a constant, *ii*) assuming isothermality, i.e., neglecting the temperature gradient known to be present in the ICM, *iii*) using a background composition gradient with a significantly larger value than the value expected in the sedimentation model of Peng and Nagai (2009) and *iv*) ignoring the effect of Braginskii viscosity. The neglect of

Braginskii viscosity was necessary for consistency with the local approximation as the fastest growing modes for the HPBI would otherwise not have fit inside the simulation domain (Paper I). Although the simulations were thus highly idealized compared to the properties expected in the ICM, they uncovered basic properties of the instabilities, i.e., their ability to eliminate radial gradients in composition, which motivated further studies in which we were able to relax some of these assumptions.

3.3 Paper III

In Paper III we presented the first quasi-global simulations of the MTCI and the HPBI with gradients in composition and temperature taken from the model of Peng and Nagai (2009). We also developed a quasi-global linear theory for the HPBI and applied it to their model. In this short summary of Paper III we limit the discussion to the theory for, and simulations of, the HPBI.

We consider the model atmosphere, illustrated in Figure 3.7, in which both temperature and composition increase with height. The magnetic field is assumed to be initially vertical. The profiles for temperature, mean molecular weight, density and pressure satisfy hydrostatic equilibrium and the heat flux has the property that $\nabla \cdot \mathbf{Q} = 0$ such that this model atmosphere is an equilibrium solution to Equations 2.25-2.31. This equilibrium is stable according to the Schwarzschild (1958) and Ledoux (1947) criteria. Nevertheless, due to the weakly collisional nature of the plasma, the equilibrium is unstable according to the dispersion relations derived in Pessah and Chakraborty (2013) and Berlok and Pessah (2015).

The atmosphere shown in Figure 3.7 has a vertical extent of two scale heights (where $H_0 = 40$ kpc). In order to calculate the growth rates and eigenmodes for such a system a local stability analysis does not suffice. We have instead derived a quasi-global theory in which the perturbations are not assumed to be periodic in the vertical direction (Berlok, 2014). This results in a coupled set of partial differential equations for the perturbations which can be expressed and solved as a generalized eigenvalue problem using pseudo-spectral methods (Boyd, 2000). In Paper III, we applied this theory to the model atmosphere shown in Figure 3.7 in order to calculate the relevant growth rates. These are shown as a function of the

3. On the distribution of helium in the intracluster medium

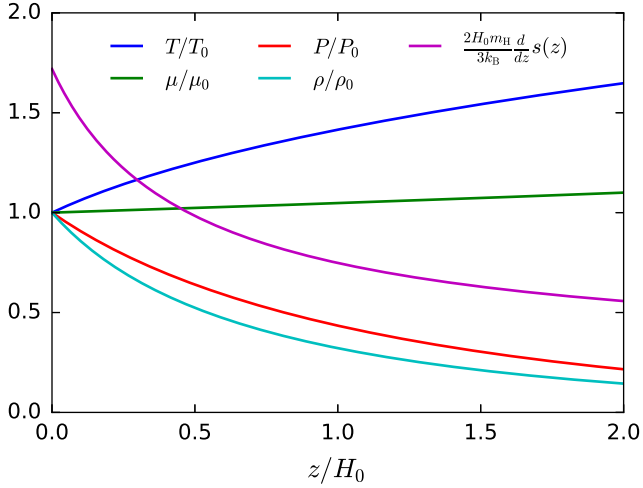


Figure 3.7: Figure 1 in Paper III. Equilibrium atmosphere inspired by the sedimentation model of Peng and Nagai (2009) and the radial temperature profile of Vikhlinin et al. (2006). The temperature (blue) and the mean molecular weight (green) increase with radius while pressure (red) and density (magenta) decrease with radius at this radial distance in the cluster model. The derivative of the entropy (purple) is positive, indicating stability according to the Schwarzschild criterion.

horizontal wavenumber in Figure 3.8. In this figure, the blue solid lines represent the theoretical predictions and the crosses represent results from linear simulations in which eigenmodes were excited. The maximum growth rate is found to be roughly 10 Gyr^{-1} , slightly higher than what was found using local linear theory in Paper I. We included Braginskii viscosity and took into account the temperature dependence of the coefficients for heat conductivity and Braginskii viscosity, χ_{\parallel} and ν_{\parallel} for this calculation. The radial dependence of these parameters in the model of Peng and Nagai (2009) was presented in figure 17 in Paper I.

The evolution of the model atmosphere, seeded with subsonic Gaussian velocity perturbations, is shown in Figure 3.9 on page 43. In this figure, each row of panels shows the time evolution of the composition and the initially vertical magnetic field in a simulation of the HPBI. Three different simulations were performed in order to quantify how Braginskii viscosity influences the evolution of the instability. The first row of panels does not include Braginskii viscosity, the middle

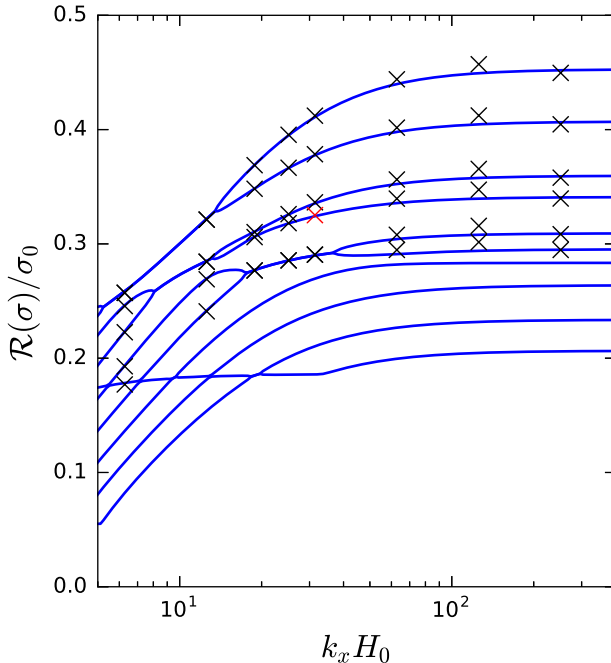


Figure 3.8: Figure 3 in Paper III. Growth rates as a function of the horizontal wavenumber, $k_x H_0$, for the 10 fastest growing modes in units of $\sigma_0 = t_0^{-1}$ where $t_0 = H_0/v_{0,th} = 45$ Myr. The solid blue lines were obtained using the pseudo-spectral method. Each cross corresponds to a simulation where the eigenmodes were used for initial conditions. The numerical growth rate was found from the subsequent exponential evolution.

row employs Braginskii viscosity but uses limiters on the pressure anisotropy (see discussion of this approach in Section 2.3) and the bottom row employs Braginskii viscosity without any modifications to the pressure anisotropy. Helium mixing is observed in all three simulations with the most vigorous mixing happening in the simulation without Braginskii viscosity.

The quasi-global linear theory can be used to predict that the instability will grow faster at the bottom of the atmosphere. This is illustrated in figure 2 in Paper III which shows that the fastest growing eigenmodes have their highest amplitudes in the lower part of the atmosphere. This is also observed in the second panels in the second and third rows in Figure 3.9.

3. On the distribution of helium in the intracluster medium

The purpose of Paper I was to provide the basic theoretical framework for instabilities present in weakly collisional plasmas stratified in temperature and composition and Paper II sought to document our modifications to the MHD code Athena in order to show that it can now reliably model such atmospheres. In Paper III we have made a more serious attempt to apply the methods that we have developed to the cluster model of Peng and Nagai (2009). This was done in order to better understand whether the instabilities discussed in Pessah and Chakraborty (2013), Paper I and Paper II can lead to helium mixing on astrophysically relevant time scales. If mixing does indeed happen on a fast time scale, this would call into question the 1D sedimentation models which do not include mixing by plasma instabilities (Fabian and Pringle, 1977; Gilfanov and Syunyaev, 1984; Chuzhoy and Nusser, 2003; Chuzhoy and Loeb, 2004; Peng and Nagai, 2009; Shtykovskiy and Gilfanov, 2010). As our models do not include helium sedimentation, such a conclusion would motivate further work on developing a model that self-consistently includes the combined influence of plasma instabilities and helium sedimentation. As observational evidence for gradients in the concentration of helium is so far unattainable due to the high temperatures of the ICM, such a model would be needed in order to indicate whether helium composition gradients, with their potential for causing biases in the estimates of cluster properties, should be a concern for precision cosmology, or not (Markevitch, 2007; Peng and Nagai, 2009).

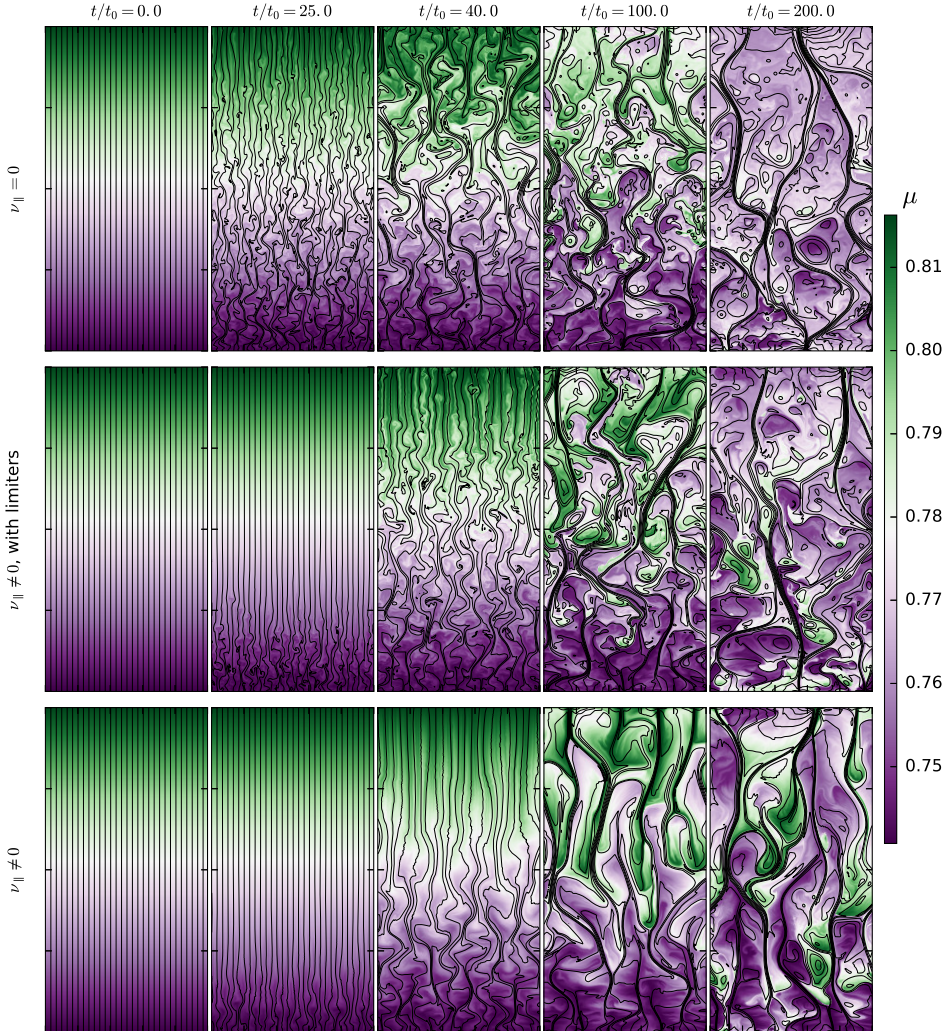


Figure 3.9: Figure 5 in Paper III. Evolution of the HPBI as a function of time in units of $t_0 = H_0/v_{0,th} = 45$ Myr. The size of the box is $H_0 \times 2H_0$ with $H_0 = 40$ kpc. The bottom of the atmosphere has $T_0 = 5.8$ keV and $c_0 = 0.52$ while the top of the atmosphere has $T = 9.6$ keV and $c = 0.62$, values found at $r_0 = 160$ kpc and $r = r_0 + 2H_0 = 240$ kpc in the model of Peng and Nagai (2009). The top row of panels include anisotropic heat conduction and the middle and bottom rows also include Braginskii viscosity. The middle row uses limiters. Solid lines indicate magnetic field lines and green (purple) corresponds to a high (low) helium content.

3. On the distribution of helium in the intracluster medium

Chapter 4

The Hall dispersion relation

The equations of Hall MHD presented in Section 2.2 corresponds to a two-fluid model of ions and electrons in which the electron fluid is considered inertialess. This is the cold ion limit of the Vlasov-fluid equations which implies that Hall MHD describes the Vlasov-fluid code simulations when the ions are cold. Consequently, a good understanding of Hall MHD is useful for testing the Vlasov-fluid code. In this chapter we derive the Hall MHD dispersion relation as in Pandey and Wardle (2008) and solve it in order to describe the waves that are present in Hall MHD. We also present some analytical results for the eigenvalues, i.e., wave-frequencies, and the eigenmodes. These results are used to initialize many of the tests presented in Chapter 12.

The equations of Hall MHD (see Section 2.2) describing the plasma are the continuity equation

$$\frac{\partial \varrho}{\partial t} + \nabla \cdot (\varrho \mathbf{u}) = 0, \quad (4.1)$$

the momentum equation

$$\varrho \frac{d\mathbf{u}}{dt} = -\nabla p + \mathbf{J} \times \mathbf{B}, \quad (4.2)$$

Faraday's law (Equation 2.8) with the electric field given by

$$\mathbf{E} = -\mathbf{u} \times \mathbf{B} + \eta \mathbf{J} + \eta_H \mathbf{J} \times \mathbf{b}, \quad (4.3)$$

4. The Hall dispersion relation

and the current given by Ampère's law (Equation 2.9). In these equations \mathbf{u} is the fluid velocity, $d/dt = \partial/\partial t + \mathbf{u} \cdot \nabla$ is the Lagrangian derivative and $p = c_s^2 \rho$ is the pressure where c_s is the sound speed. Here we have defined the Hall coefficient as (Pandey and Wardle, 2008)

$$\eta_H = \frac{B}{en_e}, \quad (4.4)$$

and η is the Ohmic resistivity which arises due electron-ion collisions (Baumjohann and Treumann, 1996). The latter is thus zero in a strictly collisionless plasma.

We linearize the equations and assume perturbations of the form $\exp(-i\omega t + i\mathbf{k} \cdot \mathbf{x})$. We also assume, without loss of generality, that $\mathbf{B} = B\mathbf{e}_z$ and $\mathbf{k} = k_\perp \mathbf{e}_x + k_\parallel \mathbf{e}_z$. The details of this derivation can be found in Appendix A.5. The resulting eigenvalue problem is given by

$$\mathbf{A} \cdot \delta \mathbf{x} = \omega \delta \mathbf{x}, \quad (4.5)$$

where

$$\mathbf{A} = \begin{bmatrix} 0 & k_\perp & 0 & k_\parallel & 0 & 0 & 0 \\ k_\perp c_s^2 & 0 & 0 & 0 & -k_\parallel v_a^2 & 0 & k_\perp v_a^2 \\ 0 & 0 & 0 & 0 & 0 & -k_\parallel v_a^2 & 0 \\ k_\parallel c_s^2 & 0 & 0 & 0 & 0 & 0 & 0 \\ 0 & -k_\parallel & 0 & 0 & -ik_\parallel^2 \eta / \mu_0 & -ik_\parallel^2 \eta_H / \mu_0 & ik_\perp k_\parallel \eta / \mu_0 \\ 0 & 0 & -k_\parallel & 0 & ik_\parallel^2 \eta_H / \mu_0 & -ik_\parallel^2 \eta / \mu_0 & -ik_\perp k_\parallel \eta_H / \mu_0 \\ 0 & k_\perp & 0 & 0 & ik_\perp k_\parallel \eta / \mu_0 & ik_\perp k_\parallel \eta_H / \mu_0 & -ik_\perp^2 \eta / \mu_0 \end{bmatrix}, \quad (4.6)$$

ω is the eigenvalue and

$$\delta \mathbf{x} = \left(\delta \rho / \rho, \delta u_x, \delta u_y, \delta u_z, \delta b_x, \delta b_y, \delta b_z \right)^T, \quad (4.7)$$

is the eigenvector of Fourier amplitudes. In the Vlasov-fluid code, this eigenvalue

problem is solved numerically when initializing tests¹. Physical insight can however be gleaned by solving the eigenvalue problem analytically for a few special cases as we do in the following sections.

As mentioned in the beginning of this chapter, Hall MHD corresponds to setting the temperature to zero for the ions. An interesting question is therefore what happens when the temperature of the ions is not zero. This is the realm of Vlasov-fluid theory. We anticipate some of the results of Vlasov-fluid theory found in Chapter 7 by commenting on the influence of hot ions and/or temperature anisotropies on the various modes.

4.1 Perpendicular propagation

We start out by considering perpendicular propagation, i.e. $\mathbf{k} = k_{\perp} \mathbf{e}_x$. We also assume that Ohmic resistivity is negligible, $\eta = 0$, and obtain the eigenvalues

$$\omega = \pm k_{\perp} \sqrt{c_s^2 + v_a^2}, \quad (4.8)$$

with corresponding eigenmode given by $\delta \rho / \rho = 1$, $\delta u_x = \pm \omega / k_{\perp}$ and $\delta b_z = 1$. This eigenmode is longitudinal and we recognize it as the compressional Alfvén wave (also called the fast magnetosonic wave) known from ideal MHD. It is an acoustic wave which travels in the direction perpendicular to the background field with its wave frequency modified by the background magnetic field. We see that the compressional Alfvén wave is not influenced by the Hall term. The reason is that the perturbed current and the background magnetic field are aligned. Ohmic resistivity will however lead to exponential decay of the wave. When the ions are hot Vlasov-fluid theory predicts ion Bernstein modes for this orientation of the wavevector. These are discussed in more detail in Chapter 12.

¹This can be an advantage, especially if $\eta \neq 0$ as the eigenmodes are complicated in this case. We use the eigenvalue solver in Numpy to calculate the eigenvalues and eigenmodes of \mathbf{A} .

4. The Hall dispersion relation

4.2 Parallel propagation

We then consider parallel propagation with $\mathbf{k} = k_{\parallel} \mathbf{e}_z$. The first set of eigenvalues we find are

$$\omega = \pm k_{\parallel} c_s, \quad (4.9)$$

with eigenmodes $\delta\rho/\rho = 1$ and $\delta u_z = \pm c_s$. These are simply sound waves which are unaffected by the magnetic field because of the parallel propagation. In plasma theory, these sound waves are referred to as ion-acoustic waves (Ichimaru, 1973). They are subject to Landau damping when the ions are hot. In hybrid PIC codes they are also subject to a numerical instability known as the finite grid instability (Rambo, 1995). Both Landau damping and the finite grid instability are discussed in more detail in Chapter 11.

The four other eigenvalues are the frequencies of transverse waves

$$\omega_{\pm}^2 = \frac{k_{\parallel}^2}{4} \left(\sqrt{\eta_H^2 k_{\parallel}^2 + 4v_a^2} \pm \eta_H k_{\parallel} \right)^2, \quad (4.10)$$

where the \pm correspond to whistler waves (+) and ion-cyclotron waves (-). When the ions are hot these waves can be subject to damping (e.g. ion cyclotron damping) and when the temperature distribution is anisotropic various instabilities such as the ion-cyclotron and firehose instabilities can arise. More information on this will be given in Chapter 7 and 12.

The whistler and ion-cyclotron waves arise due to the Hall term in the induction equation and replace the Alfvén wave found in ideal MHD which has frequency

$$\omega = \pm k_{\parallel} v_a. \quad (4.11)$$

Equation 4.11 is recovered when $\eta_H = 0$ in Equation 4.10.

We now consider a plasma with a single ion species with mass m and ion

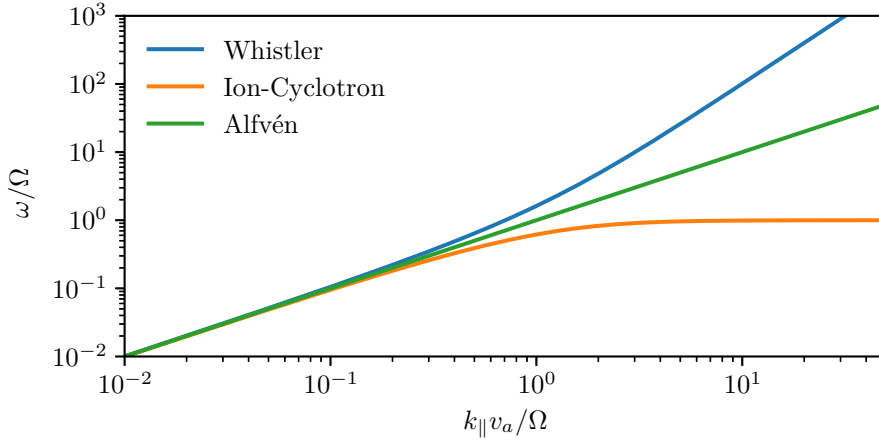


Figure 4.1: Dispersion of whistler, ion-cyclotron and Alfvén waves.

cyclotron frequency,

$$\Omega = \frac{eB}{m} . \quad (4.12)$$

The Hall parameter introduced is then given by $\eta_H = v_a^2/\Omega$ where v_a is the Alfvén speed given by

$$v_a^2 = \frac{B^2}{\mu_0 m n} , \quad (4.13)$$

and $n = n_e$ is the ion number density. We can then write the eigenvalues for the whistler waves as

$$\omega_{\pm}^{(r)} = \pm \frac{k_{\parallel} v_a}{2\Omega} \left(\sqrt{k_{\parallel}^2 v_a^2 + 4\Omega^2} + k_{\parallel} v_a \right) , \quad (4.14)$$

and the eigenvalues for the ion-cyclotron waves as

$$\omega_{\pm}^{(l)} = \pm \frac{k_{\parallel} v_a}{2\Omega} \left(\sqrt{k_{\parallel}^2 v_a^2 + 4\Omega^2} - k_{\parallel} v_a \right) . \quad (4.15)$$

The r and l superscripts will be explained in section 4.2.1. The frequencies for whistler, ion-cyclotron and Alfvén waves are shown in Figure 4.1 as a function

4. The Hall dispersion relation

of wavenumber. We observe that both whistler and ion-cyclotron waves have the same frequency as the Alfvén wave in the limit $k_{\parallel}v_a/\Omega \ll 1$. The Hall term is not important in this limit where the wavelengths considered are much longer than the ion inertial length, $d = v_a/\Omega$ (Birn et al., 2001). In the opposite limit, $k_{\parallel}v_a/\Omega \gg 1$, the whistler frequency is given by

$$\omega_{\pm}^{(r)} \approx \pm \frac{k_{\parallel}^2 v_a^2}{\Omega}, \quad (4.16)$$

and the frequency of the ion-cyclotron wave asymptotes to the ion-cyclotron frequency $\omega_{\pm}^{(l)} \approx \pm\Omega$. We also conclude from Equations 4.14 and 4.15 that both the whistler and the ion-cyclotron waves are dispersive, i.e., their phase-speed depends on the wavenumber. For the whistler waves the phase-speed keeps increasing² with k_{\parallel} . This results in a very severe time step constraint in simulations with the Hall effect as the Courant–Friedrichs–Lewy (CFL) condition (Courant, Friedrichs, and Lewy, 1967; Durran, 2010) needs to be fulfilled on the shortest scale in the system in order to avoid numerical instability. In our simulations of the whistler wave we thus require

$$\Delta t < \frac{C}{|\omega(k_{\max})|}, \quad (4.17)$$

where $C < 1$ is the Courant number, $\omega(k_{\max})$ is estimated from Equation 4.14 and $k_{\max} = \pi/\Delta x$ is the maximum wavenumber that can be resolved on the grid (assuming the grid distance to be uniform, $\Delta x = \Delta y$ for simplicity).

4.2.1 Polarization

The eigenvectors for whistler and ion-cyclotron waves are incompressible ($\delta\varrho/\varrho = 0$) and transverse ($\delta u_z = \delta b_z = 0$). The transverse components are given by

$$(\delta u_x, \delta u_y, \delta b_x, \delta b_y) = (\pm i\omega_{\pm}^{(l)}/k_{\parallel}, -\omega_{\pm}^{(l)}/k_{\parallel}, \mp i, 1), \quad (4.18)$$

²In a treatment where the electrons are also treated kinetically, the whistler waves are electron cyclotron waves whose frequency asymptotes to the electron cyclotron frequency, eB/m_e . This is in complete analogy with the behavior of the ion-cyclotron waves, see, e.g., Fitzpatrick (2014). As the electron cyclotron frequency does not enter in Hall MHD the whistler frequency grows unbounded.

for whistler waves with frequency $\omega_{\pm}^{(r)}$ and by

$$(\delta u_x, \delta u_y, \delta b_x, \delta b_y) = (\mp i \omega_{\pm}^{(r)} / k_{\parallel}, -\omega_{\pm}^{(r)} / k_{\parallel}, \pm i, 1). \quad (4.19)$$

for ion-cyclotron waves with frequency $\omega_{\pm}^{(l)}$. The x and y components are seen to be out of phase by $\pi/2$. We can determine their polarization by using the definition in Gary (1993) where the polarization, P , is defined as³

$$P \equiv -i \frac{\delta E_y}{\delta E_x} \frac{\text{Re}(\omega)}{|\text{Re}(\omega)|} = i \frac{\delta b_x}{\delta b_y} \frac{\text{Re}(\omega)}{|\text{Re}(\omega)|}, \quad (4.20)$$

and $P = -1$ ($P = 1$) corresponds to left-hand (right-hand) circularly polarized waves.

Whistlers with frequency $\omega_{\pm}^{(r)}$ have $\delta \mathbf{b} = (\mp i, 1, 0)$ and ion-cyclotron waves with $\omega_{\pm}^{(l)}$ have $\delta \mathbf{b} = (\pm i, 1, 0)$. We find $P = -1$ for the ion-cyclotron waves (left-hand circularly polarized) and $P = 1$ for the whistler waves (right-hand circularly polarized). This agrees with the l and r superscripts which are revealed to be abbreviations for left and right.

4.3 Conclusion

In this chapter we have derived and solved the dispersion relation for Hall MHD in order to obtain expressions for the frequencies and eigenmodes of the whistler wave, the ion-cyclotron wave, the fast magnetosonic wave and the ion-acoustic wave (i.e., sound wave). These expressions will be used for testing purposes in Chapter 12. We only considered $k = k_{\parallel}$ and k_{\perp} but the Hall MHD dispersion solver that we have implemented in Python can also handle general orientations of the wave vector.

³The latter equality was found using the linearized version of Faraday's law, i.e. Equation A.67 in Appendix A.5.

Chapter 5

Derivation of the Vlasov and Vlasov-fluid dispersion relations

We derived the dispersion relation and found the corresponding eigenmodes for Hall MHD in the previous chapter. These will be useful for testing the hybrid code in Chapter 12. As pointed out, however, Hall MHD corresponds to the cold ion limit of the Vlasov-fluid equations. The main purpose of developing a hybrid code is to be able to study plasmas in which the ions are hot. Proper testing of the hybrid code should therefore involve the eigenmodes and frequencies of a hot plasma. The dispersion relation for a hot plasma turns out to be significantly more complicated than the Hall MHD dispersion relation. And while the Hall MHD frequencies were all real, the frequencies are often complex for a hot plasma. With our convention for the complex exponential, complex frequencies correspond to damping when $\text{Im}(\omega) < 0$ or instability when $\text{Im}(\omega) > 0$. We will sometimes use the shorthand $\gamma = \text{Im}(\omega)$.

In this chapter we derive the dispersion relation for a hot, uniform, magnetized plasma in terms of the conductivity tensor, σ . This tensor is defined to be the linear relationship between the perturbed electric field, $\delta\mathbf{E}$, and the perturbed total current, $\delta\mathbf{J}$, i.e.,

$$\delta\mathbf{J} = \sigma \cdot \delta\mathbf{E}. \tag{5.1}$$

5. Derivation of the Vlasov and Vlasov-fluid dispersion relations

All the complexity that arises from dealing with a hot plasma is contained in σ . This makes the derivations of the dispersion relation in this chapter surprisingly simple. The expression for σ , on the other hand, is very complicated. It depends on the specific form of the equilibrium phase-space distribution function, f_s , for each plasma species. For the Vlasov-fluid approach we only want to treat the ions kinetically while the electrons are treated as a fluid. We can define the species dependent conductivity

$$\delta \mathbf{J}_s = \boldsymbol{\sigma}_s \cdot \delta \mathbf{E}, \quad (5.2)$$

which, due to the linearity of the problem is such that the ion conductivity tensor can be written as $\boldsymbol{\sigma}_i = \sum_s \boldsymbol{\sigma}_s$, the sum extending only over ion species. The kinetic expression for $\boldsymbol{\sigma}_s$, which is necessary to evaluate the ion conductivity tensor, is derived in Chapter 6, see Equation 6.5. The total conductivity tensor can then be written as $\boldsymbol{\sigma} = \boldsymbol{\sigma}_i + \boldsymbol{\sigma}_e$ where $\boldsymbol{\sigma}_e$ is given by a fluid expression in the Vlasov-fluid framework (Equation 5.23).

5.1 Vlasov-fluid dispersion relation

We consider Faraday's law (Equation 2.8)

$$\frac{\partial \mathbf{B}}{\partial t} = -\nabla \times \mathbf{E}, \quad (5.3)$$

Ampère's law (Equation 2.9)

$$\nabla \times \mathbf{B} = \mu_0 \mathbf{J}, \quad (5.4)$$

where the total current (Equation 2.10)

$$\mathbf{J} = \mathbf{J}_e + \sum_s \mathbf{J}_s, \quad (5.5)$$

is given by the sum of the electron and ion currents. We also consider the electron continuity equation

$$\frac{\partial n_e}{\partial t} + \nabla \cdot (n_e \mathbf{u}_e) = 0, \quad (5.6)$$

and the generalized Ohm's law for the electric field (Equation 2.14)

$$en_e(\mathbf{E} + \mathbf{u}_e \times \mathbf{B}) + \nabla p_e = 0. \quad (5.7)$$

We perturb these equations and assume a dependence $\exp(-i\omega t + i\mathbf{k} \cdot \mathbf{x})$ and find

$$-i\omega \delta \mathbf{B} = -i\mathbf{k} \times \delta \mathbf{E}, \quad (5.8)$$

$$i\mathbf{k} \times \delta \mathbf{B} = \mu_0 \delta \mathbf{J}, \quad (5.9)$$

$$-i\omega \frac{\delta n_e}{n_e} + i\mathbf{k} \cdot \delta \mathbf{u}_e = 0, \quad (5.10)$$

$$en_e(\delta \mathbf{E} + \delta \mathbf{u}_e \times \mathbf{B}) + \frac{dp_e}{dn_e} i\mathbf{k} \delta n_e = 0, \quad (5.11)$$

where

$$\delta \mathbf{J} = \delta \mathbf{J}_e + \sum_s \delta \mathbf{J}_s. \quad (5.12)$$

Combining Equation 5.8 and 5.9 we find

$$(\mathbf{k}\mathbf{k} - k^2 \mathbf{1}) \cdot \delta \mathbf{E} = -i\omega \mu_0 \delta \mathbf{J}, \quad (5.13)$$

which, using Equation 5.12 with $\delta \mathbf{J}_e = -en_e \delta \mathbf{u}_e$ and

$$\delta \mathbf{J}_i = \sum_s \delta \mathbf{J}_s = \boldsymbol{\sigma}_i \cdot \delta \mathbf{E}, \quad (5.14)$$

gives

$$(\mathbf{k}\mathbf{k} - k^2 \mathbf{1}) \cdot \delta \mathbf{E} = -i\omega \mu_0 (\boldsymbol{\sigma}_i \cdot \delta \mathbf{E} - en_e \delta \mathbf{u}_e). \quad (5.15)$$

5. Derivation of the Vlasov and Vlasov-fluid dispersion relations

We can find an expression relating $\delta \mathbf{u}_e$ and $\delta \mathbf{E}$ using the linearized electron continuity equation and the generalized Ohm's law (Equations 5.10 and 5.11)

$$\delta \mathbf{E} = \mathbf{B} \times \delta \mathbf{u}_e + \frac{1}{i\omega e} \frac{dp_e}{dn_e} \mathbf{k} \mathbf{k} \cdot \delta \mathbf{u}_e = \left(\mathbf{B} \times \mathbf{1} + \frac{1}{i\omega e} \frac{dp_e}{dn_e} \mathbf{k} \mathbf{k} \right) \cdot \delta \mathbf{u}_e . \quad (5.16)$$

Defining the matrix

$$\mathbf{M} = \mathbf{B} \times \mathbf{1} + \frac{1}{i\omega e} \frac{dp_e}{dn_e} \mathbf{k} \mathbf{k} , \quad (5.17)$$

such that

$$\delta \mathbf{E} = \mathbf{M} \cdot \delta \mathbf{u}_e , \quad (5.18)$$

it is evident that

$$\delta \mathbf{u}_e = \mathbf{M}^{-1} \cdot \delta \mathbf{E} . \quad (5.19)$$

Here \mathbf{M}^{-1} can be written explicitly as

$$\mathbf{M}^{-1} = \begin{bmatrix} 0 & \frac{1}{B} & 0 \\ -\frac{1}{B} & 0 & \frac{1}{B} \frac{k_{\perp}}{k_{\parallel}} \\ 0 & -\frac{1}{B} \frac{k_{\perp}}{k_{\parallel}} & \left(\frac{dp_e}{dn_e} \right)^{-1} \frac{i\omega e}{k_{\parallel}^2} \end{bmatrix} , \quad (5.20)$$

when the wavevector is given by $\mathbf{k} = k_{\perp} \mathbf{e}_x + k_{\parallel} \mathbf{e}_z$ and the magnetic field is in the z -direction, $\mathbf{B} = B \mathbf{e}_z$.

The dispersion relation can then be written as

$$\mathbf{D}_E \cdot \delta \mathbf{E} = 0 , \quad (5.21)$$

where the dispersion tensor is given by

$$\mathbf{D}_E = \mathbf{k}\mathbf{k} - k^2\mathbf{1} + i\omega\mu_0(\boldsymbol{\sigma}_i - en_e\mathbf{M}^{-1}). \quad (5.22)$$

This suggests that we define an electron conductivity as

$$\boldsymbol{\sigma}_e = -en_e\mathbf{M}^{-1}, \quad (5.23)$$

such that Equation 5.22 has the natural interpretation that the effective conductivity is simply the sum of the ion and electron conductivities, i.e., the Vlasov-fluid dispersion relation is

$$\mathbf{D}_E = \mathbf{k}\mathbf{k} - k^2\mathbf{1} + i\omega\mu_0(\boldsymbol{\sigma}_i + \boldsymbol{\sigma}_e). \quad (5.24)$$

Equation 5.24 is in a way the expected result. As the difference between a full Vlasov treatment and the Vlasov-fluid treatment is that the electrons are treated as a fluid instead of kinetically it seems very reasonable that the only change in the dispersion relation should be in the electron conductivity. Unfortunately, this way of writing the dispersion tensor is not well-posed in the limit $dp_e/dn_e = 0$, nor is it if $B = 0$, as can be seen from the expression for the inverse of \mathbf{M} in Equation 5.20. In fact, in either of these limits the inverse cannot be determined as the determinant of the matrix \mathbf{M} is zero. It turns out that this issue disappears in the limit $k_\perp = 0$, i.e., parallel propagation, and Equation 5.24 is useful in this limit (see Chapter 7).

Nevertheless, it would be advantageous to have a general dispersion relation more suitable for numerical implementation. That is, it would be useful to have a general plasma dispersion solver which can handle the limit of zero electron temperature.

The close resemblance between Equation 5.24 and the full Vlasov dispersion relation (to be derived later, see Equation 5.30) arises because we derived the dispersion relation in terms of the perturbed electric field as

$$\mathbf{D}_E \cdot \delta\mathbf{E} = 0, \quad (5.25)$$

5. Derivation of the Vlasov and Vlasov-fluid dispersion relations

where D_E is the dispersion tensor. It is however possible to write down the dispersion relation in terms of other perturbed quantities.

Cerfon and Freidberg (2011) state that it is most natural to work in terms of $\delta \mathbf{u}_e$ in the Vlasov-fluid framework. This will lead to a different expression for the dispersion tensor which turns out to be more well-behaved.

In order to derive the dispersion relation in terms of $\delta \mathbf{u}_e$ we go back to Equation 5.15 and substitute for $\delta \mathbf{E}$ by using Equation 5.16. This yields

$$\begin{aligned} & \left(\mathbf{k}\mathbf{k} - k^2 \mathbf{1} \right) \cdot \left(\mathbf{B} \times \mathbf{1} + \frac{1}{i\omega e} \frac{dp_e}{dn_e} \mathbf{k}\mathbf{k} \right) \cdot \delta \mathbf{u}_e = \\ & -i\omega\mu_0 \left(\boldsymbol{\sigma}_i \cdot \left[\mathbf{B} \times \mathbf{1} + \frac{1}{i\omega e} \frac{dp_e}{dn_e} \mathbf{k}\mathbf{k} \right] \cdot \delta \mathbf{u}_e - en_e \delta \mathbf{u}_e \right), \end{aligned} \quad (5.26)$$

or, after some rearrangement and simplifications

$$\begin{aligned} & \left(\mathbf{k}\mathbf{k} - k^2 \mathbf{1} + i\omega\mu_0 \boldsymbol{\sigma}_i \right) \cdot (\mathbf{B} \times \mathbf{1}) \cdot \delta \mathbf{u}_e + \\ & \mu_0 \boldsymbol{\sigma}_i \cdot \left(\frac{1}{e} \frac{dp_e}{dn_e} \mathbf{k}\mathbf{k} \cdot \delta \mathbf{u}_e \right) - i\omega\mu_0 en_e \delta \mathbf{u}_e = 0, \end{aligned} \quad (5.27)$$

In this case we can write the dispersion relation as

$$\mathbf{D}_u \cdot \delta \mathbf{u}_e = 0, \quad (5.28)$$

where the dispersion tensor is

$$\mathbf{D}_u = \left(\mathbf{k}\mathbf{k} - k^2 \mathbf{1} + i\omega\mu_0 \boldsymbol{\sigma}_i \right) \cdot (\mathbf{B} \times \mathbf{1}) + \mu_0 \boldsymbol{\sigma}_i \cdot \left(\frac{1}{e} \frac{dp_e}{dn_e} \mathbf{k}\mathbf{k} \right) - i\omega\mu_0 en_e \mathbf{1}. \quad (5.29)$$

Equation 5.29 is well-behaved in various limits such as $B = 0$ and $dp_e/dn_e = 0$. It is thus advantageous to use this expression for the dispersion tensor although the contributions from electron and ion physics is not as clearly interpreted as for the dispersion tensor given in Equation 5.24. We use the dispersion relation given by Equation 5.29 in the general dispersion solver that we introduce in Chapter 7.

5.2 Vlasov dispersion relation

For a standard Vlasov dispersion relation both ions and electrons are treated using the Vlasov equation. This actually makes the dispersion relation appear simpler although the physics is richer, as kinetic electron physics is now included. The dispersion relation is simply Equation 5.24 with the expression for the electron conductivity, σ_e , given by a kinetic expression (to be derived in Chapter 6, see Equation 6.5) instead of the fluid expression in Equation 5.23. That is, the dispersion relation is found by combining Equations 5.12 and 5.13 without using the electron fluid equations. We find

$$\left(\mathbf{k}\mathbf{k} - k^2\mathbf{1} + i\omega\mu_0\boldsymbol{\sigma} \right) \cdot \delta\mathbf{E} = 0, \quad (5.30)$$

with

$$\boldsymbol{\sigma} = \sum_s^{e+i} \boldsymbol{\sigma}_s, \quad (5.31)$$

where the sum in this equation extends over all species (both ions and electrons).

5.3 Relativistic dispersion relation

In this section we derive the version of the dispersion relation that is most often found in plasma physics text books. This dispersion relation is not used in the rest of the thesis but is included here in order to elucidate how the Vlasov-fluid approach differs from the standard textbook dispersion relation. The main difference is that the displacement current is retained in Ampère's law and that electrons are treated kinetically. This makes the general dispersion relation derived contain the eigenmode for electromagnetic waves. The relativistic version of Ampère's law is given by

$$\nabla \times \mathbf{B} = \mu_0\mathbf{J} + \mu_0\epsilon_0 \frac{\partial \mathbf{E}}{\partial t}, \quad (5.32)$$

5. Derivation of the Vlasov and Vlasov-fluid dispersion relations

and we find for the linearized version that

$$i\mathbf{k} \times \delta\mathbf{B} = \mu_0\delta\mathbf{J} - i\omega\mu_0\epsilon_0\delta\mathbf{E} , \quad (5.33)$$

which upon substitution of Equation 5.8 and $\delta\mathbf{J} = \boldsymbol{\sigma} \cdot \delta\mathbf{E}$ becomes

$$\left(\mathbf{k}\mathbf{k} - k^2\mathbf{1}\right) \cdot \delta\mathbf{E} = \left(-i\omega\mu_0\boldsymbol{\sigma} - \omega^2\mu_0\epsilon_0\mathbf{1}\right) \cdot \delta\mathbf{E} . \quad (5.34)$$

Since $c^{-2} = \mu_0\epsilon_0$ where c is the speed of light we have

$$\left(\mathbf{k}\mathbf{k} - k^2\mathbf{1}\right) \cdot \delta\mathbf{E} = -\frac{\omega^2}{c^2} \left(\frac{i}{\epsilon_0\omega}\boldsymbol{\sigma} + \mathbf{1}\right) \cdot \delta\mathbf{E} . \quad (5.35)$$

Or, by defining the dielectric permittivity tensor

$$\boldsymbol{\epsilon} = \epsilon_0\mathbf{1} + \frac{i}{\omega}\boldsymbol{\sigma} , \quad (5.36)$$

the dispersion relation can be written as

$$\left(\mathbf{k}\mathbf{k} - k^2\mathbf{1} + \frac{\omega^2}{c^2} \frac{\boldsymbol{\epsilon}}{\epsilon_0}\right) \cdot \delta\mathbf{E} = 0 . \quad (5.37)$$

This is the conventional way of writing the dispersion relation, see, e.g., equation 9.55 in Baumjohann and Treumann (1996). The dispersion relation correctly reduces to the non-relativistic dispersion relation, Equation 5.30, in the limit $c \rightarrow \infty$.

Chapter 6

Derivation of the conductivity tensor

In this chapter we derive an expression for the conductivity tensor, σ_s , for species s for a plasma described by a bi-Maxwellian distribution function (see Equation 6.8). The derivation is a generalization of the calculation in Ichimaru (1973) where a plasma with isotropic temperature, $T_{\parallel} = T_{\perp}$, is assumed. Similar derivations can be found in most books on plasma physics (see for instance Stix 1992; Baumjohann and Treumann 1996; Swanson 2003). The only novelty to the derivation presented here is that we use the plasma dispersion function of Ichimaru (1973), $W(\zeta)$, which differs from the standard plasma dispersion function in Fried and Conte (1961), $Z(\zeta)$. Modulo the different choice of notation, we have compared our results to Swanson (2003) and find agreement.

6.1 The conductivity tensor

An expression for σ_s for a magnetized plasma can be derived from the Vlasov equation (Equation 2.3), see, e.g., Ichimaru (1973), Stix (1992), and Swanson (2003). Here we briefly outline the procedure described in Chapter 10 and Appendix B in Baumjohann and Treumann (1996).

The main idea is that the linearized Vlasov equation can be solved for the perturbed distribution function, δf_s . The perturbed distribution function can in

6. Derivation of the conductivity tensor

turn be used to calculate the perturbed current by solving a velocity integral

$$\delta \mathbf{J}_s = e_s n_s \int dv^3 \mathbf{v} \delta f_s. \quad (6.1)$$

The form of δf_s will be such that the perturbed electric field, $\delta \mathbf{E}$, can be pulled outside the integral, i.e., one ends up with Equation 5.2 where σ_s is given by an integral over velocities that depends on the form of δf_s (but not on $\delta \mathbf{E}$).

In order to find σ_s the first step is thus to linearize the Vlasov equation (Equation 2.3). We find

$$\frac{d\delta f_s}{dt} = -\frac{e_s}{m_s} (\delta \mathbf{E} + \mathbf{v} \times \delta \mathbf{B}) \cdot \frac{\partial f_s}{\partial \mathbf{v}}, \quad (6.2)$$

where the time derivative is defined as

$$\frac{d}{dt} = \frac{\partial}{\partial t} + \mathbf{v} \cdot \nabla + \frac{e_s}{m_s} \mathbf{v} \times \mathbf{B} \cdot \frac{\partial}{\partial \mathbf{v}}, \quad (6.3)$$

the background magnetic field points in the z -direction, $\mathbf{B} = B \mathbf{e}_z$, and there is no background electric field. A formal solution for δf_s to this equation can be found by integrating over time

$$\delta f_s = -\frac{e_s}{m_s} \int_{-\infty}^t dt' [\delta \mathbf{E}(\mathbf{x}, t') + \mathbf{v} \times \delta \mathbf{B}(\mathbf{x}, t')] \cdot \frac{\partial f_s(\mathbf{v})}{\partial \mathbf{v}}, \quad (6.4)$$

where both \mathbf{x} and \mathbf{v} depend on time, t' . This equation is called an orbit integral because it depends on the orbits as given by \mathbf{x} and \mathbf{v} . In order to proceed, these are assumed to be given by the form they take in the equilibrium field, i.e., a constant velocity motion along the magnetic field superimposed with a gyration around the magnetic field (with gyration frequency Ω_s).

Furthermore, the dependence of Equation 6.4 on the perturbed magnetic field is removed by using Faraday's law (see Equation 5.8). We also assume a wavevector of the form $\mathbf{k} = k_\perp \mathbf{e}_x + k_\parallel \mathbf{e}_z$. Equation 6.4 is an integral over three velocity dimensions and time. Assuming gyrotropy of the distribution function (that f_s can be written as $f_s(v_\parallel, v_\perp)$), two of the integrals can be performed such that only the integrals over v_\parallel and v_\perp remain. This procedure is still somewhat involved and

we refer to Appendix B in Baumjohann and Treumann (1996) for the details.

In the end one finds that the conductivity tensor is given by (Ichimaru, 1973)

$$\boldsymbol{\sigma}_s = -\frac{1}{i\omega} \frac{e_s^2 n_s}{m_s} \boldsymbol{\Lambda}_s, \quad (6.5)$$

where the response tensor is given by¹

$$\boldsymbol{\Lambda}_s = \mathbf{1} + \sum_{n=-\infty}^{\infty} \int d^3v \left(\frac{n\Omega_s}{v_{\perp}} \frac{\partial f_s}{\partial v_{\perp}} + k_{\parallel} \frac{\partial f_s}{\partial v_{\parallel}} \right) \frac{\boldsymbol{\Pi}_n(v_{\parallel}, v_{\perp})}{n\Omega_s + k_{\parallel}v_{\parallel} - \omega}, \quad (6.6)$$

and $\boldsymbol{\Pi}_n(v_{\parallel}, v_{\perp})$ is defined in equation 3.72 in Ichimaru (1973) as

$$\boldsymbol{\Pi}_n(v_{\parallel}, v_{\perp}) = \begin{bmatrix} \frac{n^2\Omega_s^2}{k_{\perp}^2} J_n^2 & iv_{\perp} \frac{n\Omega_s}{k_{\perp}} J_n J'_n & v_{\parallel} \frac{n\Omega_s}{k_{\perp}} J_n^2 \\ -iv_{\perp} \frac{n\Omega_s}{k_{\perp}} J_n J'_n & v_{\perp}^2 J_n'^2 & -iv_{\parallel}v_{\perp} J_n J'_n \\ v_{\parallel} \frac{n\Omega_s}{k_{\perp}} J_n^2 & iv_{\parallel}v_{\perp} J_n J'_n & v_{\parallel}^2 J_n^2 \end{bmatrix}. \quad (6.7)$$

Here the argument of the Bessel function J_n and its derivative J'_n is $k_{\perp}v_{\perp}/\Omega_s$. The Bessel functions and the infinite sum over n appears due to a Jacobi-Anger expansion which was used to rewrite the orbit integral (Equation 6.4). So far the only assumption on the equilibrium distribution function is gyrotropy. The task of determining $\boldsymbol{\sigma}$ is equivalent to determining $\boldsymbol{\Lambda}_s$ for each plasma species, i.e., we need to perform the integrals over velocity space.

¹Equation 3.71 for the dielectric tensor in Ichimaru (1973) can be converted to the form given in Equations 6.5 and 6.6 by using equations 3.3 and 3.19 in Ichimaru (1973) which relate the dielectric tensor and the conductivity tensor. We have also used equation 1.19 for the plasma frequency of a multi-species plasma and equation 2.46 for the plasma frequency of species s . The $\boldsymbol{\Lambda}_s$ notation is also used in Heinemann and Quataert (2014).

6.2 Velocity space integrals

In the following we perform the velocity space integrals in Equation 6.6 for a reduced² gyrotropic distribution function given by

$$f_s = \frac{1}{(2\pi)^{3/2} v_{t,\parallel} v_{t,\perp}^2} \exp\left(-\frac{v_{\parallel}^2}{2v_{t,\parallel}^2} - \frac{v_{\perp}^2}{2v_{t,\perp}^2}\right), \quad (6.8)$$

where the velocity integral is defined by

$$\int d^3v = 2\pi \int_0^{\infty} dv_{\perp} v_{\perp} \int_{-\infty}^{\infty} dv_{\parallel}, \quad (6.9)$$

and $v_{t,\parallel}^2 = T_{\parallel}/m_s$ ($v_{t,\perp}^2 = T_{\perp}/m_s$) is the parallel (perpendicular) thermal velocity.

For this distribution function we have

$$\frac{n\Omega_s}{v_{\perp}} \frac{\partial f_s}{\partial v_{\perp}} + k_{\parallel} \frac{\partial f_s}{\partial v_{\parallel}} = -\left(\frac{n\Omega_s}{v_{t,\perp}^2} + \frac{k_{\parallel} v_{\parallel}}{v_{t,\parallel}^2}\right) f_s, \quad (6.10)$$

which does not depend on the perpendicular velocity, v_{\perp} . This means that the tensor $\mathbf{\Lambda}_s$ can be written as

$$\mathbf{\Lambda}_s = \mathbf{1} - \sum_{n=-\infty}^{\infty} \int_{-\infty}^{\infty} \left(\frac{n\Omega_s}{v_{t,\perp}^2} + \frac{k_{\parallel} v_{\parallel}}{v_{t,\parallel}^2}\right) \frac{\mathbf{S}}{n\Omega_s + k_{\parallel} v_{\parallel} - \omega} dv_{\parallel}, \quad (6.11)$$

where

$$\mathbf{S} = 2\pi \int_0^{\infty} v_{\perp} \mathbf{\Pi}_n(v_{\parallel}, v_{\perp}) f_s dv_{\perp}. \quad (6.12)$$

We proceed by calculating \mathbf{S} where only 6 elements are truly unique as it is Hermitian. Making use of the integrals listed in appendix A.1 we find after a few

²The distribution function is normalized such that $\int f_s d^3v = 1$.

simplifications that we can write \mathbf{S} as

$$\mathbf{S} = \begin{bmatrix} \frac{n^2\Omega_s^2}{k_\perp^2}\Gamma_n & i\frac{n\Omega_s^2}{k_\perp^2}\lambda\Gamma'_n & v_\parallel\frac{n\Omega_s}{k_\perp}\Gamma_n \\ -i\frac{n\Omega_s^2}{k_\perp^2}\lambda\Gamma'_n & v_{t,\perp}^2\left(\frac{n^2\Gamma_n}{\lambda} - 2\Gamma'_n\lambda\right) & -iv_\parallel\frac{\Gamma'_n}{k_\perp}\Omega_s\lambda \\ v_\parallel\frac{n\Omega_s}{k_\perp}\Gamma_n & iv_\parallel\frac{\Gamma'_n}{k_\perp}\Omega_s\lambda & v_\parallel^2\Gamma_n \end{bmatrix} \frac{\exp\left(-v_\parallel^2/2v_{t,\parallel}^2\right)}{\sqrt{2\pi}v_{t,\parallel}}. \quad (6.13)$$

where Γ_n is shorthand for

$$\Gamma_n(\lambda) = e^{-\lambda}I_n(\lambda), \quad (6.14)$$

where $I_n(\lambda)$ is the modified Bessel function of the first kind and Γ'_n is the derivative of Γ_n with respect to λ . Here, the argument λ has been defined as

$$\lambda \equiv \frac{k_\perp^2 v_{t,\perp}^2}{\Omega_s^2}. \quad (6.15)$$

Having found an expression for \mathbf{S} we are now ready to proceed with the integrals over parallel velocity in Equation 6.11. The details of this procedure can be found in Appendix A.2. In the end we find that

$$\Lambda_{xx} = \sum_{n=-\infty}^{\infty} n^2 \frac{\Gamma_n}{\lambda} A_n, \quad (6.16)$$

$$\Lambda_{xy} = \sum_{n=-\infty}^{\infty} in\Gamma'_n A_n, \quad (6.17)$$

$$\Lambda_{xz} = \sum_{n=-\infty}^{\infty} n \frac{\Gamma_n}{\sqrt{\lambda}} \zeta_n \frac{v_{t,\parallel}}{v_{t,\perp}} A_n, \quad (6.18)$$

$$\Lambda_{yy} = \sum_{n=-\infty}^{\infty} \left(\frac{n^2\Gamma_n}{\lambda} - 2\Gamma'_n\lambda \right) A_n, \quad (6.19)$$

$$\Lambda_{yz} = - \sum_{n=-\infty}^{\infty} i\sqrt{\lambda}\Gamma'_n \zeta_n \frac{v_{t,\parallel}}{v_{t,\perp}} A_n, \quad (6.20)$$

6. Derivation of the conductivity tensor

$$\Lambda_{zz} = \sum_{n=-\infty}^{\infty} \Gamma_n \zeta_n^2 \frac{v_{t,\parallel}^2}{v_{t,\perp}^2} A_n - \frac{v_{t,\parallel}^2}{v_{t,\perp}^2} \zeta_0^2, \quad (6.21)$$

where

$$A_n = \frac{\zeta_0}{\zeta_n} (1 - W(\zeta_n)) + \left(1 - \frac{v_{t,\perp}^2}{v_{t,\parallel}^2}\right) W(\zeta_n), \quad (6.22)$$

and the plasma dispersion function, $W(z)$, defined in Ichimaru (1973), is given by

$$W(z) = \frac{1}{\sqrt{2\pi}} \int_{-\infty}^{\infty} \frac{x e^{-x^2/2}}{x - z} dx. \quad (6.23)$$

The argument of the plasma dispersion function is ζ_n , given by

$$\zeta_n \equiv \frac{\omega - n\Omega_s}{k_{\parallel} v_{t,\parallel}}. \quad (6.24)$$

We list some properties of the plasma dispersion function in Appendix A.4 along with its relation to the standard plasma dispersion function defined in Fried and Conte (1961).

Our result for Λ_s can be more compactly written by introducing the temperature anisotropy, Δ , as well as a tensor, \mathbf{T}_n . The temperature anisotropy is defined as

$$\Delta \equiv \frac{v_{t,\perp}^2}{v_{t,\parallel}^2} - 1 = \frac{T_{\perp}}{T_{\parallel}} - 1, \quad (6.25)$$

and the tensor \mathbf{T}_n is defined as

$$\mathbf{T}_n = \begin{bmatrix} n^2 \frac{\Gamma_n}{\lambda} & in\Gamma'_n & \frac{n\Gamma_n \zeta_n}{\sqrt{\lambda}\sqrt{1+\Delta}} \\ -in\Gamma'_n & \frac{n^2 \Gamma_n}{\lambda} - 2\Gamma'_n \lambda & -\frac{i\sqrt{\lambda}\Gamma'_n \zeta_n}{\sqrt{1+\Delta}} \\ \frac{n\Gamma_n \zeta_n}{\sqrt{\lambda}\sqrt{1+\Delta}} & \frac{i\sqrt{\lambda}\Gamma'_n \zeta_n}{\sqrt{1+\Delta}} & \frac{\Gamma_n \zeta_n^2}{1+\Delta} \end{bmatrix}. \quad (6.26)$$

Using these definitions, Λ_s can be written as

$$\Lambda_s = \sum_{n=-\infty}^{\infty} \left[\frac{\zeta_0}{\zeta_n} (1 - W(\zeta_n)) - \Delta W(\zeta_n) \right] \mathbf{T}_n - \frac{1}{1 + \Delta} \zeta_0^2 \mathbf{e}_z \mathbf{e}_z. \quad (6.27)$$

We note that we have used the same notation as in Heinemann and Quataert (2014) and that our expressions for the response tensor Λ_s , and the tensor \mathbf{T}_n , reduce to equations 49 and 51 in their paper when $\Delta = 0$. Our expression for \mathbf{T}_n also agrees with equation 5.21 Ichimaru (1973) in this limit. We have also compared our expression for the conductivity tensor with the expression for the dielectric tensor for a hot magnetized plasma in Swanson (2003). We find agreement when the drift velocity, included in the derivation in Swanson (2003), is set to zero.

The expression for Λ_s given by Equation 6.27 can be used to compute the conductivity tensor by using Equation 6.5. Equation 6.27 forms the basis for Chapter 7 where we solve the Vlasov-fluid dispersion relation for a warm, magnetized plasma.

Chapter 7

Solutions to the Vlasov and Vlasov-fluid dispersion relations

In the two previous chapters we have spent significant effort in deriving the equations governing the linear dynamics of collisionless plasmas in both Vlasov-fluid framework and the Vlasov-Vlasov framework. In this chapter we are finally ready to look at some of the solutions to the dispersion relations given by Equations 5.29 and 5.30. The dispersion relations describe all the waves and instabilities that can be present in a uniform plasma with temperature anisotropies. For the sake of brevity we will have to limit the discussion. As the main purpose of developing this theory is for us to be able to compare with hybrid simulations, we choose to focus on the ion scale physics with special emphasis on the instabilities driven by temperature anisotropies. These are especially the firehose and mirror instabilities, interesting to us because of their potential influence on our studies of the intracluster medium (see Chapter 3).

This chapter is divided into two sections. In the first section we consider the simplifying limit of parallel propagation, $k = k_{\parallel}$, for the Vlasov-fluid dispersion relation given by Equation 5.24 in order to make some analytical progress. In the second section we describe our implementation of a dispersion solver which can solve the dispersion relations given by Equations 5.29 and 5.30 in the general case where $\mathbf{k} = k_{\perp} \mathbf{e}_x + k_{\parallel} \mathbf{e}_z$ and $\mathbf{B} = B \mathbf{e}_z$.

7.1 Transverse Vlasov-fluid dispersion relation

Let us consider Equation 5.24 for a plasma consisting of fluid electrons and a single ion species. For notational simplicity¹ we drop the subscript i on the ion mass, m , and cyclotron frequency, Ω . The dispersion relation, Equation 5.24, can in this case be written compactly by multiplying both sides with v_a^2/Ω^2 where v_a is the Alfvén speed and Ω is the ion cyclotron frequency. We also define the sound speed, c_s , as

$$c_s^2 = \frac{1}{m} \frac{dp_e}{dn_e}, \quad (7.1)$$

and find that the dispersion relation can be written as $\det \mathbf{D}_E = 0$ where

$$\mathbf{D}_E = \left(k^2 \mathbf{1} - \mathbf{k}\mathbf{k} \right) \frac{v_a^2}{\Omega^2} + \mathbf{\Lambda}_i + \mathbf{\Lambda}_e, \quad (7.2)$$

and

$$\mathbf{\Lambda}_e = \begin{bmatrix} 0 & i\omega/\Omega & 0 \\ -i\omega/\Omega & 0 & i\omega/\Omega k_\perp/k_\parallel \\ 0 & -i\omega/\Omega k_\perp/k_\parallel & -\omega^2/k_\parallel^2 c_s^2 \end{bmatrix}, \quad (7.3)$$

is the response tensor of the electron fluid and $\mathbf{\Lambda}_i$ is the response tensor of the warm ion species (see Equation 6.27).

We are interested in the limit of parallel propagation ($k_\perp = 0$) of the dispersion relation given by Equation 7.2. In this limit, λ , (Equation 6.15), also goes to zero, and the tensor \mathbf{T}_n (Equation 6.26), which enters in the definition of the ion response tensor (Equation 6.27), simplifies to

$$\lim_{\lambda \rightarrow 0} \mathbf{T}_n = \begin{bmatrix} (\delta_{n,1} + \delta_{n,-1})/2 & i(\delta_{n,1} - \delta_{n,-1})/2 & 0 \\ -i(\delta_{n,1} - \delta_{n,-1})/2 & (\delta_{n,1} + \delta_{n,-1})/2 & 0 \\ 0 & 0 & \frac{\zeta_n^2 \delta_{n,0}}{1 + \Delta} \end{bmatrix}, \quad (7.4)$$

¹This should not lead to confusion as these parameters do not enter for the electrons in the Vlasov-fluid framework.

see, e.g., equation 5.24 in Ichimaru (1973). In Equation 7.4, $\delta_{n,m}$ is the Kronecker delta with the property that $\delta_{n,m} = 1$ for $n = m$ and $\delta_{n,m} = 0$ for $n \neq m$. This greatly simplifies the dispersion relation as only three terms remain in the infinite sum over n in Equation 6.27.

The dispersion relation is currently written in the Cartesian basis, (e_x, e_y, e_z) , but we can further simplify the following analysis by realizing that the dispersion relation will be diagonal in the circular basis, (e_-, e_+, e_z) , where $e_- = (e_x - ie_y)/\sqrt{2}$ and $e_+ = (e_x + ie_y)/\sqrt{2}$. The change of basis proceeds in the same way as in Ichimaru (1973) but we consider here a Vlasov-fluid plasma with $\Delta \neq 0$. We introduce the unitary matrix (equation 5.26 in Ichimaru 1973)

$$\mathbf{U} = \frac{1}{\sqrt{2}} \begin{bmatrix} 1 & -i & 0 \\ -i & 1 & 0 \\ 0 & 0 & \sqrt{2} \end{bmatrix}, \quad (7.5)$$

which has the property that

$$\mathbf{U} \cdot \begin{pmatrix} E_x \\ E_y \\ E_z \end{pmatrix} = \begin{pmatrix} \frac{E_x - iE_y}{\sqrt{2}} \\ \frac{E_y - iE_x}{\sqrt{2}} \\ E_z \end{pmatrix}, \quad (7.6)$$

i.e., it transforms linearly polarized modes into circularly polarized modes. Note that \mathbf{U} is unitary such that $\mathbf{U}^\dagger \cdot \mathbf{U} = \mathbf{1}$ and $\mathbf{U} \cdot \mathbf{U}^\dagger = \mathbf{1}$ where \mathbf{U}^\dagger is the Hermitian conjugate of \mathbf{U} . Transformation of the unit vectors are given by $\mathbf{U} \cdot e_x = e_-$, $\mathbf{U} \cdot e_y = e_+$ and $\mathbf{U} \cdot e_z = e_z$. We can use \mathbf{U} to transform the dispersion relation as

$$\mathbf{U} \cdot \mathbf{D} \cdot \mathbf{U}^\dagger = \begin{bmatrix} D_- & 0 & 0 \\ 0 & D_+ & 0 \\ 0 & 0 & D_{\parallel} \end{bmatrix}, \quad (7.7)$$

and obtain a diagonal dispersion tensor which factorizes into three independent dispersion relations $D_- = 0$, $D_+ = 0$ and $D_{\parallel} = 0$.

We find that

$$\mathbf{U} \cdot (k^2 \mathbf{1} - \mathbf{k}\mathbf{k}) \cdot \mathbf{U}^\dagger \frac{v_a^2}{\Omega^2} = \frac{k_{\parallel}^2 v_a^2}{\Omega^2} \begin{bmatrix} 1 & 0 & 0 \\ 0 & 1 & 0 \\ 0 & 0 & 0 \end{bmatrix}, \quad (7.8)$$

such that the three dispersion relations are given by

$$D_- = \frac{k_{\parallel}^2 v_a^2}{\Omega^2} + \Lambda_{i,-} + \Lambda_{e,-} = 0, \quad (7.9)$$

$$D_+ = \frac{k_{\parallel}^2 v_a^2}{\Omega^2} + \Lambda_{i,+} + \Lambda_{e,+} = 0, \quad (7.10)$$

$$D_{\parallel} = \Lambda_{i,\parallel} + \Lambda_{e,\parallel} = 0, \quad (7.11)$$

where

$$\Lambda_{i,\pm} = \frac{\zeta_0}{\zeta_{\pm 1}} [1 - W(\zeta_{\pm 1})] - \Delta W(\zeta_{\pm 1}), \quad (7.12)$$

$$\Lambda_{i,\parallel} = -\zeta_0^2 (1 + \Delta) \left[W(\zeta_0) - \frac{\Delta}{(1 + \Delta)^2} \right], \quad (7.13)$$

$$\Lambda_{e,\pm} = \pm \frac{\omega}{\Omega}, \quad (7.14)$$

$$\Lambda_{e,\parallel} = -\frac{\omega^2}{k_{\parallel}^2 c_s^2}. \quad (7.15)$$

We can write down the dispersion relations by using the definition of ζ_n given in Equation 6.24. We obtain

$$D_{\mp} = \frac{k_{\parallel}^2 v_a^2}{\Omega^2} + \frac{\omega}{\omega \pm \Omega} \left[1 - W\left(\frac{\omega \pm \Omega}{k_{\parallel} v_{t,\parallel}}\right) \right] - \Delta W\left(\frac{\omega \pm \Omega}{k_{\parallel} v_{t,\parallel}}\right) \mp \frac{\omega}{\Omega} = 0, \quad (7.16)$$

$$D_{\parallel} = \left(\frac{\omega}{k_{\parallel} v_{t,\parallel}} \right)^2 (1 + \Delta) \left[W\left(\frac{\omega}{k_{\parallel} v_{t,\parallel}}\right) - \frac{\Delta}{(1 + \Delta)^2} \right] + \frac{\omega^2}{k_{\parallel}^2 c_s^2} = 0. \quad (7.17)$$

The solutions to Equation 7.16 are left (D_-) and right (D_+) hand polarized waves when $\omega > 0$ (and the other way around when $\omega < 0$).

If we set $\Delta = 0$, i.e., no temperature anisotropy, and subsequently consider the cold ion limit we obtain²

$$D_{\mp} = \frac{k_{\parallel}^2 v_a^2}{\Omega^2} + \frac{\omega}{\omega \pm \Omega} \mp \frac{\omega}{\Omega} = 0. \quad (7.18)$$

The solutions to Equation 7.18 are the whistler, $\omega_{\pm}^{(r)}$, and ion-cyclotron, $\omega_{\pm}^{(l)}$, solutions found for Hall MHD in Chapter 4 and given in Equations 4.14 and 4.15, respectively. Specifically, the solutions to the cold D_- dispersion relation are $\omega_-^{(l)}$ (ion-cyclotron) and $\omega_+^{(r)}$ (whistler) and the solutions to the cold D_+ dispersion relation are $\omega_-^{(r)}$ (whistler) and $\omega_+^{(l)}$ (ion-cyclotron). If we restrict ourselves to $\text{Re}(\omega) > 0$ then the D_- branch will correspond to whistler modes and the D_+ branch will correspond to ion-cyclotron modes.

The longitudinal dispersion relation given by Equation 7.17 describes ion-acoustic waves propagating parallel to the magnetic field. If we set $\Delta = 0$ it reduces to

$$D_{\parallel} = W\left(\frac{\omega}{k_{\parallel} v_{t,\parallel}}\right) + \frac{v_{t,\parallel}^2}{c_s^2} = 0. \quad (7.19)$$

The solution to this dispersion relation is ion-acoustic waves subject to ion Landau damping. The magnetic field does not modify the properties of this wave due to the parallel and longitudinal propagation. The derivation of Equation 7.19 can be done without using the full machinery developed here and we derive Equation 7.19 in a much simpler way in Chapter 11 where we discuss the physics of Landau damping and obtain the damping rates using PIC simulations.

In the following we will discuss some of the instabilities that can occur in plasmas where the temperature is anisotropic. Instability thresholds for these instabilities often depend on the ratio of thermal to magnetic pressure. For this reason, it is customary to introduce the parallel and perpendicular β s as

$$\beta_{\parallel} = 2 \frac{v_{t,\parallel}^2}{v_a^2}, \quad (7.20)$$

²i.e., we take the large argument expansion of the W function where $W \rightarrow 0$. See Appendix A.4.

$$\beta_{\perp} = 2 \frac{v_{t,\perp}^2}{v_a^2}. \quad (7.21)$$

We note that the temperature anisotropy is related to β_{\parallel} and β_{\perp} by $\Delta = \beta_{\perp}/\beta_{\parallel} - 1$ and that ζ_n , defined in Equation 6.24, can be written as

$$\zeta_n = \frac{\omega/\Omega - n}{k_{\parallel}v_a/\Omega} \sqrt{\frac{2}{\beta_{\parallel}}}, \quad (7.22)$$

in terms of β_{\parallel} .

7.1.1 Parallel firehose instability

The firehose instability (Rosenbluth, 1956; Chandrasekhar, Kaufman, and Watson, 1958; Parker, 1958; Vedenov and Sagdeev, 1958; Davidson and Völk, 1968) occurs in plasmas with anisotropic velocity distributions such that the parallel temperature is larger than the perpendicular temperature. The basic physical principle driving the instability is that a magnetic flux tube suffering a slight bend will go unstable if the parallel pressure, p_{\parallel} , exceeds the perpendicular pressure, p_{\perp} , and the restoring force from magnetic tension. Instability is predicted when (Treumann and Baumjohann, 1997)

$$\Delta < -\frac{2}{\beta_{\parallel}}. \quad (7.23)$$

The firehose instability is predicted by Braginskii MHD where it however suffers from a UV-catastrophe, i.e., its growth rate is proportional to the wavenumber, k_{\parallel} , and grows without bound (Schekochihin et al., 2005). When finite Larmor radii (FLR) effects are included in the dispersion relation, as in Equation 7.16, this problem is eliminated.

A numerical solution to Equation 7.16 for the parameters $\beta_{\parallel} = 4$, $\beta_{\perp} = 1$, i.e., $\Delta = -3/4$, is shown in Figure 7.1. The positive imaginary part (left panel) indicates that we are indeed dealing with an instability, the parallel firehose instability. The peak in growth rate occurs at $k_{\parallel}v_a/\Omega = 0.37$ and has a value of $\text{Im}(\omega)/\Omega = 0.189$. We use this information to initialize a simulation of the parallel firehose instability in Chapter 12, see Figure 12.5. The electron temperature

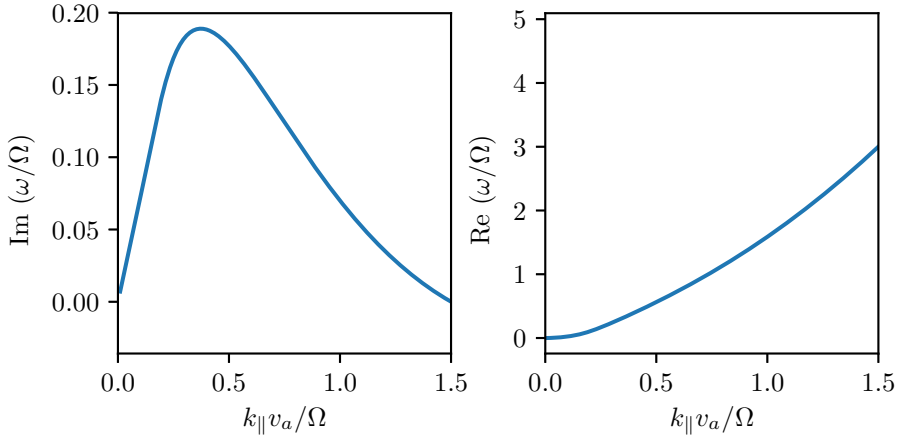


Figure 7.1: Growth rate and frequency of the parallel firehose instability for $\beta_{\parallel} = 4$ and $\beta_{\perp} = 1$ ($\Delta = -3/4$).

does not influence the linear theory for this instability. The parallel firehose instability is an overstability, as seen in Figure 7.1. We find excellent agreement with the publicly available Vlasov-fluid dispersion relation solver HYDROS (Told et al. 2016, see their figure 1).

7.1.2 Ion-cyclotron instability

The ion-cyclotron instability (Kennel and Petschek, 1966; Davidson and Ogden, 1975) occurs when the perpendicular temperature is greater than the parallel temperature. The instability happens when a left hand polarized wave propagating along the magnetic field has a frequency that coincides, i.e., is resonant, with the gyration frequency of the ions. Due to the difference in the sense of rotation for electrons and ions, this resonance happens between the left-hand polarized wave for the ion cyclotron instability while the electron cyclotron instability happens due to a resonance with a right hand polarized wave, see, e.g., Treumann and Baumjohann (1997).

Resonance is however not sufficient for instability as this can also lead to ion-cyclotron damping (coming up next). The ion-cyclotron instability also requires that the distribution function is such that there are more particles moving at a

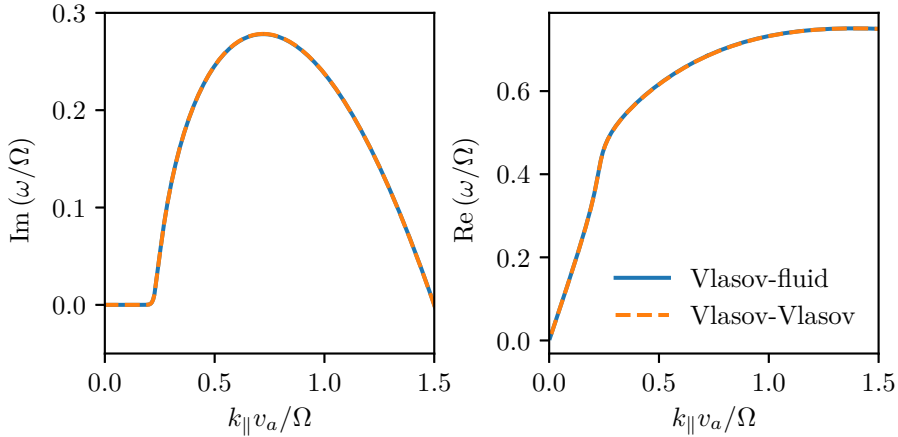


Figure 7.2: Growth rate of the ion-cyclotron instability with $\beta_{\parallel} = 1$ and $\beta_{\perp} = 4$ ($\Delta = 3$). Blue solid lines found using Vlasov-fluid theory and the dashed orange lines found using Vlasov ions and electrons.

higher speed than the phase velocity of the wave, leading to deceleration of the particles while feeding energy into the wave. A good illustration of this can be found on page 106 in Treumann and Baumjohann (1997).

We find that the D_- branch³ of Equation 7.16 is unstable to the ion-cyclotron instability when $T_{\perp} > T_{\parallel}$ ($\Delta > 0$). The numerical solution for $\beta_{\parallel} = 1$ and $\beta_{\perp} = 4$ ($\Delta = 3$) is shown in Figure 7.2. In this figure the blue solid lines are the solution to the D_- branch of Equation 7.2 and the orange dashed line is the solution to Equation 5.30. The latter solution assumes kinetic, isotropic electrons with the same temperature as the parallel ion temperature, i.e., $T_e = T_{\parallel}$, and a mass ratio between electrons and ions of $m_i/m_e = 1836$. The full Vlasov-Vlasov solution was found by using the general dispersion solver that we describe in Section 7.2. We find in both cases that the maximum growth rate is $\gamma/\Omega = 0.28$ and occurs at $k_{\parallel}v_a/\Omega = 0.72$. We also note that we again find excellent agreement with HYDROS (Told et al. 2016, see their figure 2). A simulation which shows the overstable nature of the ion-cyclotron instability, is presented in Figure 12.4 in Chapter 12.

³More specifically, we find that the D_- (D_+) branch is unstable for $\omega > 0$ ($\omega < 0$). Both correspond to left-handed ion-cyclotron waves, propagating in opposite directions.

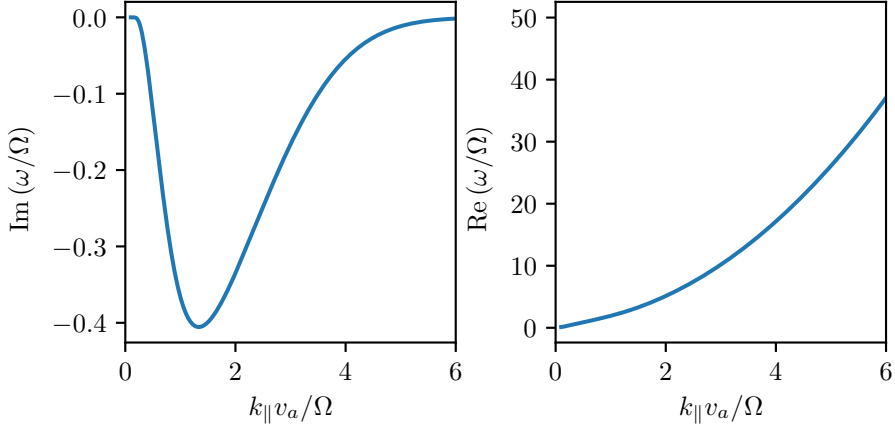


Figure 7.3: Ion-cyclotron damping for $\beta = 5$.

7.1.3 Ion-cyclotron damping

We consider a hot, but this time isotropic $\beta = \beta_{\parallel} = \beta_{\perp}$, plasma. When the distribution function is such that there are more particles moving at a slower speed than the phase velocity of the wave, the particles will be accelerated by the wave while removing energy from it. This leads to damping of the wave, called ion-cyclotron damping. We show a numerical solution for $\beta = 5$ in Figure 7.3. The maximal damping rate is $\gamma/\Omega = 0.41$ and occurs at $k_{\parallel}v_a/\Omega = 1.34$. We test the ability of our hybrid code to model ion-cyclotron damping in Chapter 12.

7.2 General Vlasov-fluid dispersion relation

In the previous section we looked at a specific limit, where $k = k_{\parallel}$, of the dispersion relation for a Vlasov-fluid plasma. The general dispersion relation given by Equation 5.29 has an infinite sum when $\mathbf{k} = k_{\perp}\mathbf{e}_x + k_{\parallel}\mathbf{e}_z$. While the dispersion relation is formidable in this case it is still possible to solve it numerically. We have implemented such a general dispersion solver which can be used to solve the dispersion relation for both a Vlasov-Vlasov (kinetic ions and electrons) as given by Equation 5.30 and a Vlasov-fluid plasma as given by Equation 5.29. There are already a number of plasma dispersion solvers available for the Vlasov-Vlasov

plasma, see, e.g., Roennmark (1982), Astfalk, Görler, and Jenko (2015), and Xie and Xiao (2016), but there is, to our knowledge, only one that solves the general⁴ Vlasov-fluid dispersion relation (Told et al., 2016). In their paper, entitled “A linear dispersion relation for the hybrid kinetic-ion/fluid-electron model of plasma physics,” the authors derive the Vlasov-fluid dispersion relation using the approach in Kazeminezhad et al. (1992). We have used a different approach where the dispersion relation is given in terms of the conductivity tensor (Chapters 5 and 6). Told et al. (2016) have made their dispersion relation solver publicly available and we have benefited from being able to compare with their solver.

The key ingredient in our dispersion solver is a Cython (Behnel et al., 2011) implementation of Equation 6.27 for the species dependent response tensor, Λ_s . This function can be called for each species for subsequent summation in order to obtain σ_i when solving the Vlasov-fluid dispersion relation or σ when solving the Vlasov-Vlasov dispersion relation. The main advantage of this approach is that we can reuse this function for both the Vlasov-fluid and the Vlasov-Vlasov dispersion relation solvers.

The solution to the dispersion relations is then found by passing the determinant of the dispersion tensor to the Scipy (Jones, Oliphant, and Peterson, 2001-2017) implementation of the Newton-Raphson method. Our solver has the limitation that it needs an initial guess for ω . This is a general problem for plasma dispersion solvers⁵. Initial guesses can be made using solutions to the cold plasma dispersion relations or known approximate solutions. Once a solution, ω_0 , is known, the solver uses this solution to find solutions close in parameter space, e.g., the solution ω_0 to $D(\omega_0, k_{\parallel}, k_{\perp}) = 0$ will often be a good guess when solving $D(\omega_1, k_{\parallel} + \delta k_{\parallel}, k_{\perp}) = 0$ for ω_1 , as long as δk_{\parallel} is small. This seems sufficiently efficient and we have not implemented quadratic polynomial extrapolation of the solutions as in DSHARK (Astfalk, Görler, and Jenko, 2015).

⁴Note however that Heinemann and Quataert (2014) solves the parallel ($k = k_{\parallel}$) Vlasov-fluid dispersion relation in the shearing sheet.

⁵One interesting exception is the dispersion solver of Xie and Xiao (2016) which uses a J -pole expansion of the plasma dispersion function in order to reduce the dispersion relation to a matrix eigenvalue problem. This method is not as accurate (especially for damped modes) but it is able to find all the solutions of the dispersion relation in one go without initial guesses. An especially promising idea, put forward in Xie and Xiao (2016), is to use their method to calculate solutions and then use a conventional solver to improve the accuracy.

We use the Scipy implementation of the Faddeeva function (see, e.g., Poppe and Wijers 1990), $w(z)$, to compute Ichimaru's plasma dispersion function as

$$W(z) = 1 + iz\sqrt{\pi/2} w(z/\sqrt{2}), \quad (7.24)$$

as well as the Scipy implementation of the exponentially scaled modified Bessel function of the first kind, i.e., $\Gamma_n(\lambda)$. The infinite sum over n is truncated to $\sum_{n=-N}^N$ where $N = 1000$ but the summation stops early if deemed converged, i.e., if the relative changes in the components of the tensor are all less than 10^{-16} . All the kinetic physics, and the computational bottleneck, is contained in this Cython level calculation of Λ_s and the rest of the solver is implemented using object-oriented Python.

In the following, we use the general dispersion relation solver to calculate growth rates of the oblique firehose instability and the mirror instability. Solutions from the solver are used to compare with simulations of the parallel and oblique firehose instabilities in Figure 12.6 in Chapter 12. We have also used the solver to calculate the frequencies of ion Bernstein modes in order to compare with the simulation presented in Figure 12.7 in Chapter 12.

7.2.1 Oblique firehose instability

A new kinetic instability was found by Hellinger and Matsumoto (2000) for oblique propagation. While the parallel firehose instability is a destabilization of whistler waves, this new oblique instability is a destabilization of the Alfvén wave. We adopt their convention of calling these two distinct instabilities, whistler firehose and Alfvén firehose. Using the plasma dispersion solver we can calculate the growth rate as a function of the wavenumber, k , and the inclination of the wavevector with respect to the background magnetic field, θ , i.e., $k_{\parallel} = k \cos \theta$ and $k_{\perp} = k \sin \theta$. We use $\beta_{\parallel} = 2.8$ and $\beta_{\perp} = 0.4\beta_{\parallel}$ in order to produce Figure 7.4 in which the parallel firehose instability is located at $\theta = 0$. This figure can be directly compared with figure 4 in Hellinger and Matsumoto (2000) who used almost the same parameters⁶. The maximum growth rate for the Alfvén fire-

⁶We have set $T_e = 0$ in the calculation while Hellinger and Matsumoto (2000) used $\beta_e = 2c_s^2/v_a^2 = 0.5$. Hellinger and Matsumoto (2000) found a maximum growth rate of $\gamma/\Omega = 0.59$

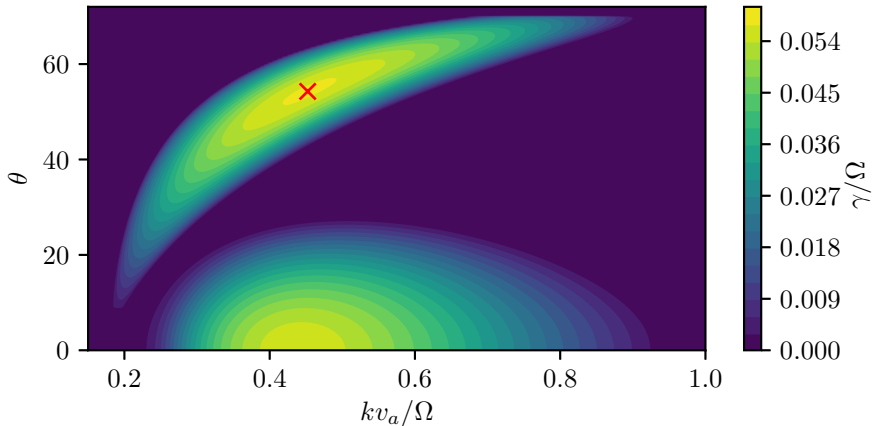


Figure 7.4: Contour plot of the growth rates for a plasma with $\beta_{\parallel} = 2.8$ and $\beta_{\perp} = 0.4\beta_{\parallel}$. The two instabilities are the whistler (parallel) firehose instability and the Alfvén (oblique) firehose instability. The maximum growth rate of the latter is indicated with a red cross.

hose instability is found at $kv_a/\Omega = 0.45$ and $\theta = 54$ deg and has a value of $\gamma/\Omega = 0.575$. It is indicated in the figure with a red cross.

One-dimensional simulations of the whistler and Alfvén firehose instabilities have been presented in Hellinger and Matsumoto (2000). Two-dimensional simulations where both the whistler and Alfvén firehose instabilities are present at the same time have also been presented by Hellinger and Matsumoto (2001) and Muñoz et al. (2016). The Alfvén firehose instability has been found to be even more efficient at isotropizing the temperature anisotropy than the whistler firehose instability. We present 1D simulations of the whistler and Alfvén firehose instabilities in Figure 12.6 and a 2D simulation in Figure 12.11 in Chapter 12.

7.2.2 Ion-cyclotron and mirror instabilities

The mirror instability (Chandrasekhar, Kaufman, and Watson, 1958; Barnes, 1966; Hasegawa, 1969; Hall, 1979) is, like the firehose instability, an instability that feeds

which is slightly higher than the value we find. This is consistent with the discussion in Hellinger and Matsumoto (2000) stating that the growth rate of the Alfvén firehose instability increases with electron temperature. Our general plasma dispersion solver is still work in progress and we have unfortunately not been able to find sensible solutions with $T_e \neq 0$.

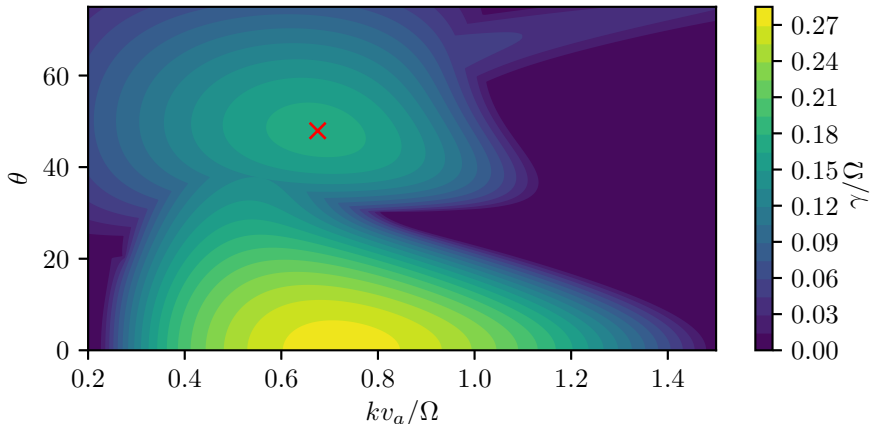


Figure 7.5: Contour plot of the growth rates for a plasma with $\beta_{\parallel} = 1$ and $\beta_{\perp} = 4$. The mode with maximal growth rate with $k = k_{\parallel}$ is recognized as the ion-cyclotron instability by comparing with Figure 7.2. The other mode is the mirror instability which has its maximum growth rate indicated with a red cross.

off anisotropy in the velocity distribution. We have already discussed this instability in the context of the intracluster medium in Chapter 3 where we used the instability criterion given by Equation 2.42 to limit the maximum viscous flux in the Braginskii MHD equations.

In this section we use the plasma dispersion solver we have developed to calculate the growth rate of the mirror instability. As mentioned previously, the mirror instability occurs when the perpendicular temperature exceeds the parallel temperature. The mirror instability is a destabilization of a slow-mode polarized wave which has anti-correlation between density and magnetic field strength perturbation (Hasegawa, 1969). We outline the physical mechanism for the instability as explained in Southwood and Kivelson (1993). In the fluid picture, the perpendicular pressure response to a magnetic field strength perturbation is given by (Hasegawa, 1969)

$$\frac{\delta p_{\perp}}{p_{\perp}} = \left(1 - \frac{T_{\perp}}{T_{\parallel}}\right) \frac{\delta B}{B} = -\Delta \frac{\delta B}{B}. \quad (7.25)$$

The perturbations in perpendicular pressure and magnetic field strength are seen

to have opposite signs if $T_{\perp} > T_{\parallel}$. An increase in magnetic field strength (caused by a compression of magnetic field lines) will then lead to a decrease in perpendicular thermal pressure. It will also lead to an increase in magnetic pressure given by $B\delta B/\mu_0$. If the loss in perpendicular thermal pressure outweighs the gain in perpendicular magnetic pressure, i.e., if

$$\delta p_{\perp} + \frac{B\delta B}{\mu_0} < 0, \quad (7.26)$$

then the result will be further compression of the magnetic field lines. This increases the magnetic field strength which lowers the perpendicular pressure and so on (Southwood and Kivelson, 1993). The need for compression of field lines to drive the instability shows why the mirror instability needs an oblique wavevector. One can see from Equation 7.25 that Equation 7.26 is most likely to be fulfilled if the initial thermal pressure of the plasma is higher than the magnetic pressure, i.e., in high β plasmas. A similar argument shows how regions with decreasing magnetic field strength will have increasing perpendicular pressure which leads the magnetic field to blow out in the perpendicular direction. The particles in the regions with increasing magnetic field strength will essentially be squeezed out of those regions by the mirror force⁷. We can combine Equations 7.25 and 7.26 to obtain the stability criterion for the mirror instability⁸

$$\Delta > \frac{1}{\beta_{\perp}}. \quad (7.28)$$

While the physical picture outlined above yields the correct criterion for instability it turns out that it is not entirely adequate. The problem is that the fluid picture does not correctly describe resonances of particles with low parallel velocity which Southwood and Kivelson (1993) found to play a crucial role. The growth rate of

⁷An explanation of the mirror force can be found in most books on plasma physics, see, e.g., Baumjohann and Treumann (1996) or Fitzpatrick (2014).

⁸This can also be written as

$$(1 + \Delta)\Delta > \frac{1}{\beta_{\parallel}}. \quad (7.27)$$

For $\beta_{\parallel} \gg 1$ the mirror instability is active when $|\Delta| \ll 1$ and the factor $(1 + \Delta)$ can be ignored, yielding Equation 2.41.

the mirror instability is found to be proportional to k_{\parallel} within the framework of Braginskii MHD (Schekochihin et al., 2005) and it thus also requires the inclusion of FLR effects in order to avoid an UV-catastrophe. It is thus necessary to treat and understand the mirror instability using kinetic theory (Southwood and Kivelson, 1993).

We calculate the growth rate of the mirror instability as a function of the wavenumber, k , and the inclination of the wavevector with respect to the background magnetic field, θ . We use the parameters $\beta_{\parallel} = 1$ and $\beta_{\perp} = 4$ and present the resulting growth rate map in Figure 7.5. For these parameters, the maximum growth rate occurs along $\theta = 0$. This region of instability is recognized to be the ion-cyclotron instability by comparing with Figure 7.2. The other distinct region in Figure 7.5 is the mirror instability. This instability is seen to have its maximum growth rate at $\theta = 48$ deg and $kv_a/\Omega = 0.68$ with a maximum growth rate of $\gamma/\Omega = 0.17$.

Chapter 8

Introduction to particle-in-cell simulations

In this chapter we introduce the basic principles of particle-in-cell (PIC) simulations of collisionless plasmas (Hockney and Eastwood, 1988; Birdsall and Langdon, 1991). We are interested in solving the Vlasov-fluid equations (Equations 2.3, 2.8 and 2.15, see Section 2.1) which describe the evolution of the phase-space distribution of the particles and the electromagnetic fields.

The Vlasov-fluid equations can be solved using Eulerian grid methods or the particle-in-cell method. A comparison of the two methods for plasma turbulence studies was presented in Cerri et al. (2017). Examples of codes that use grid based methods include the *HVM* code (Mangeney et al., 2002; Valentini et al., 2007) and the *Vlasiator* code (Alfthan et al., 2014). These codes face the challenge that the number of cells in a simulation scale with N^d where d is the dimension of the phase-space and N is the number of grid cells along each dimension¹. While different methods have been developed for bypassing this fundamental problem, e.g. the *Vlasiator* code limits the number of cells in velocity space in spatial regions of little interest, these simulations are still extremely expensive. The main advantage of the grid based method is that it does not suffer from the statistical noise that inevitably arises when using particle methods (due to a finite number of particles, see also Chapter 10).

¹Here considered to be the same for each dimension for illustrative purposes.

8. Introduction to particle-in-cell simulations

We have developed a code using particle methods. The advantage of the particle method compared to the grid based method is its simplicity and the lower computational cost. In this approach the evolution of the phase-space distribution function is studied by following the evolution of quasi-particles². These quasi-particles obey the same equations of motion as real, physical particles do, which is the reason for the terminology (see, e.g., Lapenta 2013). For brevity we will often simply refer to particles without explicitly stating that we are in fact dealing with quasi-particles which represent a phase-space volume.

In the general case, the particle phase-space is 6-dimensional (three spatial dimensions and three velocity dimensions). We have developed a code which only evolves five of these phase-space dimensions, namely x, y, v_x, v_y and v_z . The reduction of the phase-space is done by assuming that there is no spatial variation of variables along the z -direction. This means that field quantities can depend explicitly on the x and y coordinate but not on z . We do however retain all three components of the electromagnetic fields. A code that evolves two spatial dimensions but all three velocity components of the particles and all three components of the electromagnetic fields is referred to as a 2D-3V code.

We now proceed to explain why it is useful to include a grid even when using a particle method. Given a collection of N_p particles we could in principle calculate the force on each of them by adding up the forces from the electromagnetic fields produced by all the other particles. This many-body problem would not require a grid. It would however require $\sim N_p^2$ force calculations so that the computational effort quickly grows large. It turns out that uncorrelated systems can be modeled much more efficiently by introducing a grid upon which the field equations, i.e., Equations 2.8 and 2.15, are solved (Hockney and Eastwood, 1988). This combination of using particles and a grid is called the particle-in-cell (PIC) method. The computational cost then scales with $\sim N_p + N^2$ where N^2 is the number of grid cells for a code with two spatial dimensions. For weakly coupled systems $N_p \gg N$, and the computational cost will be dominated by the effort used on updating the particle positions and velocities. It is thus advantageous to use a grid because the computational cost then scales linearly with the number of

²In the literature, these are also sometimes referred to as super-particles, marker particles or macro-particles.

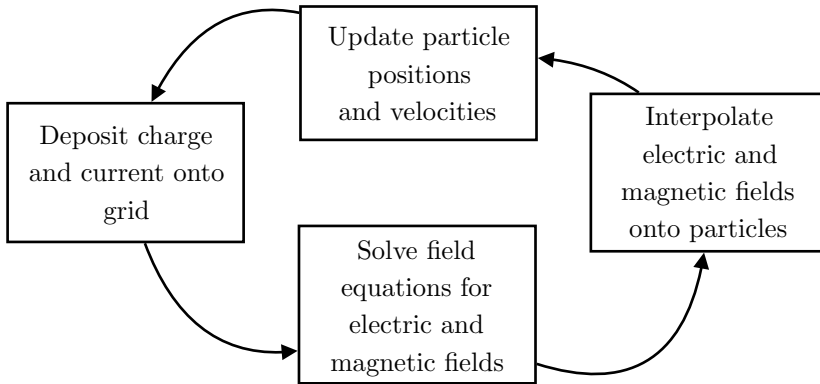


Figure 8.1: Flowchart for the PIC method.

particles instead of quadratically.

The PIC method consists of four distinct steps which are repeated in a cyclic manner, as illustrated in Figure 8.1. We briefly describe the four different steps in this chapter. These are *i*) the update of particle and positions and velocities (Section 8.1), *ii*) the deposition of charge and currents onto the grid (Section 8.2) *iii*) the solution of the field equations (Section 8.3) and *iv*) the interpolation of electric and magnetic fields to the particle positions (Section 8.2).

8.1 Particle mover

We use the Boris method (Boris, 1970) to update the positions and velocities of particles which are influenced by the Lorentz force due to an electric field, \mathbf{E} , and a magnetic field, \mathbf{B} . In order to do so, we need the electric and magnetic fields at the location of the particles. These quantities are however only known on the grid and interpolation is therefore required (see Section 8.2).

The equations of motion for the quasi-particles are³

$$m_s \frac{d\mathbf{v}}{dt} = e_s (\mathbf{E} + \mathbf{v} \times \mathbf{B}), \quad (8.1)$$

³That the quasi-particles obey the same equations of motion as real physical particles is shown in e.g. Lapenta (2013). The magnetic and electric fields are here understood to be interpolated values onto the location of the particle, see Section 8.2.

8. Introduction to particle-in-cell simulations

$$\frac{d\mathbf{x}}{dt} = \mathbf{v}, \quad (8.2)$$

for which the Lorentz force is approximated by (Birdsall and Langdon, 1991)

$$\frac{\mathbf{v}^{n+1/2} - \mathbf{v}^{n-1/2}}{\Delta t} = \frac{e_s}{m_s} \left(\mathbf{E}^n + \frac{\mathbf{v}^{n+1/2} + \mathbf{v}^{n-1/2}}{2} \times \mathbf{B}^n \right), \quad (8.3)$$

$$\frac{\mathbf{x}^{n+1} - \mathbf{x}^n}{\Delta t} = \mathbf{v}^{n+1/2}, \quad (8.4)$$

where n denotes the time step, corresponding to the time $t = n\Delta t$, where Δt is the increment in time per time step. Notice that the values of the particle positions are defined at integer time steps while the velocities are defined at half-integer time steps. This method, called leapfrog from its similarity to the children's game, is illustrated in Figure 8.2. Equation 8.3 is implicit as $\mathbf{v}^{n+1/2}$ appears on the RHS of the equation. The equation can in principle be solved by inverting a 3×3 matrix. A matrix inversion is however slow compared to the Boris method (Boris, 1970) that we outline below, following the description in Birdsall and Langdon (1991). First, calculate the vector, \mathbf{v}^- , given by

$$\mathbf{v}^- = \mathbf{v}^{n-1/2} + \frac{e_s \Delta t}{2m_s} \mathbf{E}^n, \quad (8.5)$$

and use it to obtain

$$\mathbf{v}' = \mathbf{v}^- + \mathbf{v}^- \times \mathbf{d}, \quad (8.6)$$

where

$$\mathbf{d} = \frac{e_s \Delta t}{2m_s} \mathbf{B}^n. \quad (8.7)$$

Then calculate

$$\mathbf{v}^+ = \mathbf{v}^- + \frac{2}{1 + d^2} \mathbf{v}' \times \mathbf{d}, \quad (8.8)$$

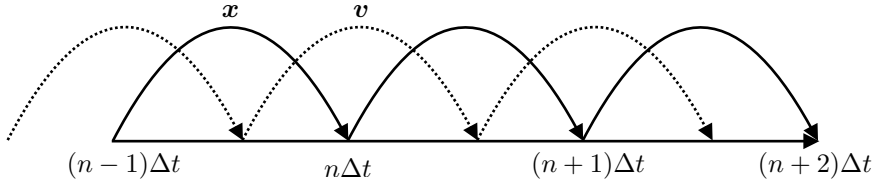


Figure 8.2: Illustration of the leapfrog method. The particle positions, \mathbf{x} , and velocities, \mathbf{v} , are defined at integer and half-integer time steps, respectively.

and use the value of \mathbf{v}^+ to finally obtain $\mathbf{v}^{n+1/2}$ as

$$\mathbf{v}^{n+1/2} = \mathbf{v}^+ + \frac{e_s \Delta t}{2m_s} \mathbf{E}^n. \quad (8.9)$$

The Boris push updates the particle velocity from time step $n - 1/2$ to time step $n + 1/2$ by using the values of the electric and magnetic fields at the location of the particle at time step n . This can be summarized as

$$\mathbf{v}^{n+1/2} = \mathbf{M}(\mathbf{E}^n, \mathbf{B}^n, \mathbf{x}^n) \cdot \mathbf{v}^{n-1/2}, \quad (8.10)$$

where \mathbf{M} represents the Boris update of the velocity outlined above. The update of the velocity is often referred to as a *kick*. The update of the position is much simpler

$$\mathbf{x}^{n+1} = \mathbf{x}^n + \Delta t \mathbf{v}^{n+1/2}, \quad (8.11)$$

and is referred to as a *drift*.

8.2 Interpolation

Interpolation is used both for depositing charge and current density of the ions onto the grid and for interpolating the values of the electric and magnetic fields onto the locations of the particles. In PIC literature the former is often referred to as the scatter step and the latter is referred to as the gather step.

We have implemented two different interpolation schemes called cloud-in-cell (CIC) and triangular-shaped-cloud (TSC), respectively. These names refer to the

8. Introduction to particle-in-cell simulations

interpretation of the quasi-particles as a charged cloud. The shape of these functions are given by the shape functions, $S(x)$, in Hockney and Eastwood (1988). The assignment functions, $W(x)$, are given by the integral of the shape functions and tell how much charge (or current) a particle contributes to each cell⁴. The one-dimensional versions of the CIC and TSC assignment functions are given by (Hockney and Eastwood, 1988)

$$W(x) = \begin{cases} 1 - |x| & |x| < 1 \\ 0 & \text{otherwise} \end{cases}, \quad (8.12)$$

and

$$W(x) = \begin{cases} \frac{3}{4} - x^2 & |x| < 1/2 \\ \frac{1}{2} \left(\frac{3}{2} - |x| \right)^2 & 1/2 < |x| < 3/2 \\ 0 & \text{otherwise} \end{cases}, \quad (8.13)$$

respectively. In two dimensions the charge is assigned according to the product of the one-dimensional assignment functions $W(\mathbf{x}) = W(x)W(y)$.

We can write the charge and current deposition as

$$\rho_g = \sum_s w_s e_s \sum_p^{N_p} W(\mathbf{x}_p - \mathbf{x}_g), \quad (8.14)$$

$$\mathbf{J}_g = \sum_s w_s e_s \sum_p^{N_p} \mathbf{v}_p W(\mathbf{x}_p - \mathbf{x}_g), \quad (8.15)$$

where the sums extend over all particles, N_p , and all ion particle species, s . Here w_s is a (per-species) weight factor given by $w_s = n_s N_g / N_p$ where n_s is the number density of physical particles of species s and N_g is the total number of grid cells. In Equations 8.14 and 8.15, the particle positions, \mathbf{x}_p , and the positions of the grid cells, \mathbf{x}_g , are measured in units of the grid cell length. The sources, ρ and \mathbf{J} , are needed for the field solver (Section 8.3) and are also useful diagnostics when

⁴The assignment function, $W(x)$, should not be confused with Ichimaru's plasma dispersion function, $W(z)$.

analyzing simulations.

Interpolation of magnetic and electric fields onto the location of a given particle is needed for the Boris push. The fields are here given by a sum over the grid cells

$$\mathbf{E}_p = \sum_g^{N_g} W(\mathbf{x}_p - \mathbf{x}_g) \mathbf{E}_g, \quad (8.16)$$

$$\mathbf{B}_p = \sum_g^{N_g} W(\mathbf{x}_p - \mathbf{x}_g) \mathbf{B}_g. \quad (8.17)$$

Not using the same interpolation scheme for the gather as for the scatter can lead to self-forces, i.e., the fields produced by the charge and current of a particle can end up exerting a force on itself (Hockney and Eastwood, 1988). This unphysical effect will lead to a change in the total momentum of the particles in the simulation. In order to avoid this problem we always use the same method (CIC or TSC) for source deposition and force interpolation. This is called the momentum-conserving method as it preserves the total momentum to machine precision (Hockney and Eastwood, 1988).

8.3 Field solver

Solving the field equations, Faraday's law and Ohm's law given by Equations 2.8 and 2.15, requires knowledge of the ion sources (density and current, found using Equations 8.14 and 8.15) and the magnetic field at the current time step.

The solution of the field equations depends on the time staggering (whether the fields are defined at integer or half-integer time steps) and the spatial staggering (fields can be defined at either cell corners or cell centers). These issues are discussed in detail in Chapter 9. For the time being we simply note that the update of the magnetic field depends on the electric field through Faraday's law (Equation 2.8) and that the electric field, in turn, depends on the electron pressure, density and current (Ohm's law, Equation 2.15). The former two can be found from the ion density (since we assume quasi-neutrality) and the latter can be found from a combination of Ampère's law for the total current (Equation 2.9, where the

magnetic field is needed) and the ion current.

8.4 A few implementation details

The code we have developed uses high-level language features of Python (Rossum, 1995) while maintaining high performance by using the low-level language C (Kernighan, 1988) for the most computationally intensive parts. The interfacing between Python and the high performance code is done using Cython (Behnel et al., 2011). We note that the most computationally intensive part will almost always be the operations related to the particles, unless very few particles per cell are used.

Development of the Python code has benefited greatly from experience gained while working on the *PhotonPlasma* code (Haugbølle, Frederiksen, and Nordlund, 2013). Similarly, access to an electrostatic, so-called skeleton code developed at the University of California Los Angeles (Decyk, 1995; Decyk, 2016) has enabled us to make rapid progress. The skeleton terminology is explained by Decyk (1995) in the following way:

These codes have been deliberately kept to a minimum, but they include all the essential pieces for which algorithms need to be developed. Thus the codes advance the particles, deposit their charge, and solve for the fields. Only one particle species is kept and the only diagnostic used is the particle and field energies. The codes use the electrostatic approximation and magnetic fields are neglected.

The skeleton code made available by Decyk (1995) thus contains the essential machinery for an electrostatic particle-in-cell code such as a particle mover, a charge deposition routine and a spectral solver for Poisson's equation. Most importantly, it contains an implementation for moving particles between different processors using message passing interface (MPI, Forum 1993). The hybrid code presented in this thesis uses this implementation of particle communication as well as a particle sorting routine. The code also uses MPI for the field equations⁵. Here we

⁵We have also experimented with OpenMP (Dagum and Menon, 1998) but at the time of writing this feature is turned off.

use guard layers on each side of each local grid and the Python package `mpi4py` (Dalcín et al., 2008) for communicating them across processors. This includes the charge and current densities for which a step where the charge is added (not just copied) is needed.

It is common knowledge that the benefits of using Python or other high-level languages comes at the cost of computational efficiency. This common knowledge is however being challenged by several projects which show that Python can be used for high performance computing (HPC). These projects include *REBOUND* (Rein and Liu, 2012), an N -body code for collisional dynamics; *FBPIC* (Lehe et al., 2016), a relativistic PIC code used to study plasma wake-field acceleration; *Dedalus* (Burns et al., In preparation), a framework for solving initial, boundary and eigenvalue problems and *spectralDNS* (Mortensen and Langtangen, 2016), a spectral hydrodynamics code used for direct numerical simulations of turbulence. The latter code, *spectralDNS*, has been found to match the performance of an equivalent code in C++ even when running on several thousand cores (Mortensen and Langtangen, 2016).

In contrast to these projects, the 2D code that we present in this thesis has not yet been thoroughly optimized and tested for efficiency. We have however made a simple comparison between the performance of the skeleton code by Decyk (1995) (written in C) and a Python version of the skeleton code. The Python code works by importing the functions in the C code using Cython (Behnel et al., 2011) in order to be able to call them within Python. We present a speed comparison in Figure 8.3. In the upper panel of this figure we show the execution time of the particle move (force interpolation, Boris push, deposition and MPI communication) for the two different versions of the code. The setup is a grid with resolution $n_x = 512$ and $n_y = 512N$ where N is the number of processors used. We keep the number of particles per cell fixed at 36. Since we increase the computational load in proportion to the number of processors the execution time should be constant⁶. However, we observe an increase in the execution time from roughly 20 seconds when using 1 processor to roughly 40 seconds when using 256 processors. We also observe an abrupt increase in the execution time when using

⁶This is a weak scaling test.

8. Introduction to particle-in-cell simulations

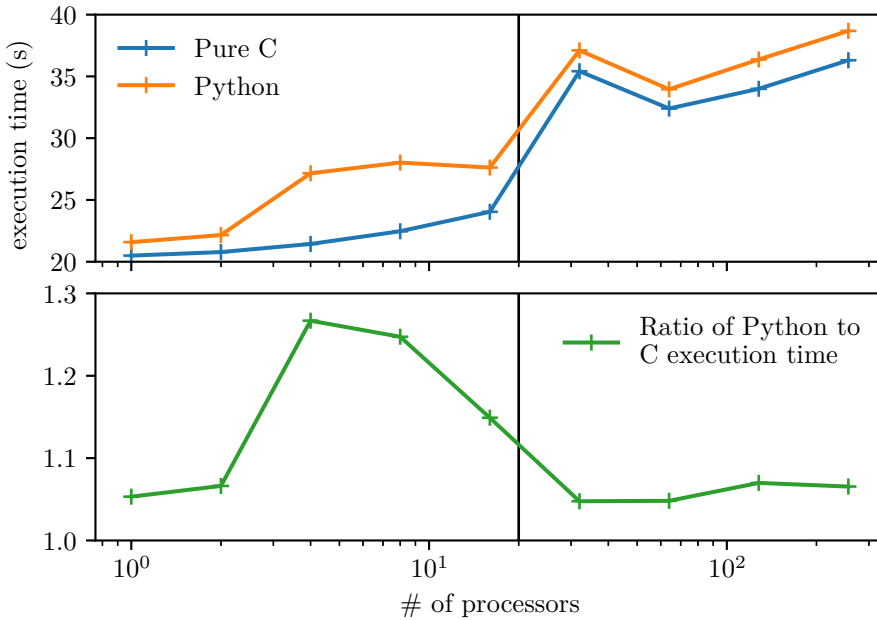


Figure 8.3: Comparison of performance between a C version and a Python version of the skeleton code made available by Decyk (1995). *Upper panel:* The execution time of the particle move. *Lower panel:* The ratio of the Python execution time to the C execution time.

32 processors and more. We attribute this to the architecture of the computer cluster which has 20 processors (with shared memory) per node. This indicates that the performance of the MPI communication between different nodes could be improved. We note that this trend is seen for both the Python and the C code. The loss in performance incurred by using Python instead of C can be estimated by calculating the ratio of the execution times. This is shown in the lower panel of Figure 8.3. The Python code is not more than 30% slower and many of the simulations are only 5% slower. This preliminary test encouraged us to continue developing a hybrid code in Python.

One of the key advantages of using Python is that it is possible to plot and animate different physical quantities while the code is running. This is especially useful for debugging and showcasing tests. Data storage is however still needed for analyzing computationally intensive simulations. We use the HDF5 format

(The HDF Group, 1997-2017) via the corresponding Python package `h5py` (Collette, 2013) to store both field and particle data with one file per MPI process at each requested time step. The inconvenience of having the data per processor is eliminated by a dedicated Python script which combines them. The resulting data can be read by visualization packages such as `Visit` (Childs et al., 2012) or `h5py` (Collette, 2013). Data analysis is performed with Python scripts with `Matplotlib` (Hunter, 2007) or with `IPython` (Perez and Granger, 2007) for interactively analyzing the data.

Another key advantage, or at least convenience, obtained by using a high-level language such as Python is that we have easy access to numerical libraries such as `Numpy` (Oliphant, 2007) and `SciPy` (Jones, Oliphant, and Peterson, 2001-2017). As an example, this has been useful for initializing a quiet Maxwellian (see Chapter 10) where the inverse error function is required or for initializing an eigenmode by calling the dispersion relation solvers discussed in Chapter 4 and 7.

Finally, we note that the development of the code has benefited greatly from using `Git` version control (Chacon, 2009) and continuous integration (CI), a development method where changes to the code results in the test suite running on a remote server.

Chapter 9

Numerical methods

Particle-in-cell codes generally have time staggering of particle positions and velocities as well as electromagnetic fields (\mathbf{B} and \mathbf{E}) and they also benefit from using a staggered grid in space for the field quantities (the electromagnetic fields and their sources). There are several options for both spatial staggering and time stepping procedures and different codes, such as *CAMELIA* (Matthews, 1994), *DHybrid* (Gargaté et al., 2007), *AIKEF* (Müller et al., 2011), *Pegasus* (Kunz, Stone, and Bai, 2014), *CHIEF* (Muñoz et al., 2016) and *AMITIS* (Fatemi et al., 2017), use different approaches. In this chapter we explain how we have chosen to stagger the grid quantities and the finite difference scheme that we employ. We also discuss two different methods for updating the equations in time. These are the predictor-corrector method and the Horowitz method, both of which are implemented in our code.

9.1 Staggering

The following discussion details how we have implemented spatial staggering: all components of \mathbf{E} are located at cell centers (i, j) and all components of \mathbf{B} are located at cell corners $(i + 1/2, j + 1/2)$. We also choose to deposit both the charge density and all components of the ion current density at cell centers.

This grid structure is outlined in Figure 9.1. In this figure cell centers, where \mathbf{E} , \mathbf{J}_s and ρ are stored, are indicated with an X and cell corners, where \mathbf{B} is

stored, are indicated with full circles. The thick solid line indicates the physical boundaries of the simulation domain. The X's and solid circles shown in blue are active cells, while the X's and solid circles shown in orange are ghost cells (also interchangeably called guard layers). The example shown in Figure 9.1 has a single guard layer on each side. This is sufficient for performing simulations with CIC interpolation and a second order finite difference scheme. We add one more guard layer on each side when TSC interpolation is used.

For a simulation with a single MPI process the physical boundaries for the grid in Figure 9.1 are identical to the physical boundaries of the entire simulation. These are defined to be located at $x = x_0$, $y = y_0$, $x = x_0 + L_x$ and $y = y_0 + L_y$ where x_0 , y_0 , L_x and L_y have user-defined values. This means that the first active cell in x has its cell center values (ρ and all components of \mathbf{J} and \mathbf{E}) located at $x = x_0 + \Delta x/2$ and its cell corner value (all components of \mathbf{B}) located at $x = x_0 + \Delta x$. The last active cell in x has its cell center values at $x = x_0 + L_x - \Delta x/2$ and its cell corner values at $x = x_0 + L_x$.

The same considerations apply for the y -direction with the caveat that the grid boundaries do not always coincide with the physical boundaries when more than one MPI process is used. In this case a grid as the one shown in Figure 9.1 is created on each processor. As the MPI domain decomposition is only along the y -direction the grid boundaries in the x -direction are still identical to the physical boundaries¹. The grid boundaries in the y -direction for the grid on each processor are however given by $y_0 + L_y R/N$ for the lower boundary and $y_0 + L_y (R+1)/N$ for the upper boundary. Here R is the rank of the process and N is the total number of MPI processes used.

We use MPI to communicate the values of guard layers from processor to processor. Each grid is a Python object with many of the grid properties stored as attributes. These are for instance `lby`, `lby`, `ubx`, and `uby`, corresponding to the indices of the first active cell at the lower edge of the domain (`lby`, `lby`) and the first guard layer at the upper edge of the domain (`ubx`, `uby`).

¹This is a limitation of the implementation of MPI domain decomposition in the skeleton code described in Chapter 8. Extending the MPI domain decomposition to be along both x and y is on the list of future improvements, see Chapter 13.

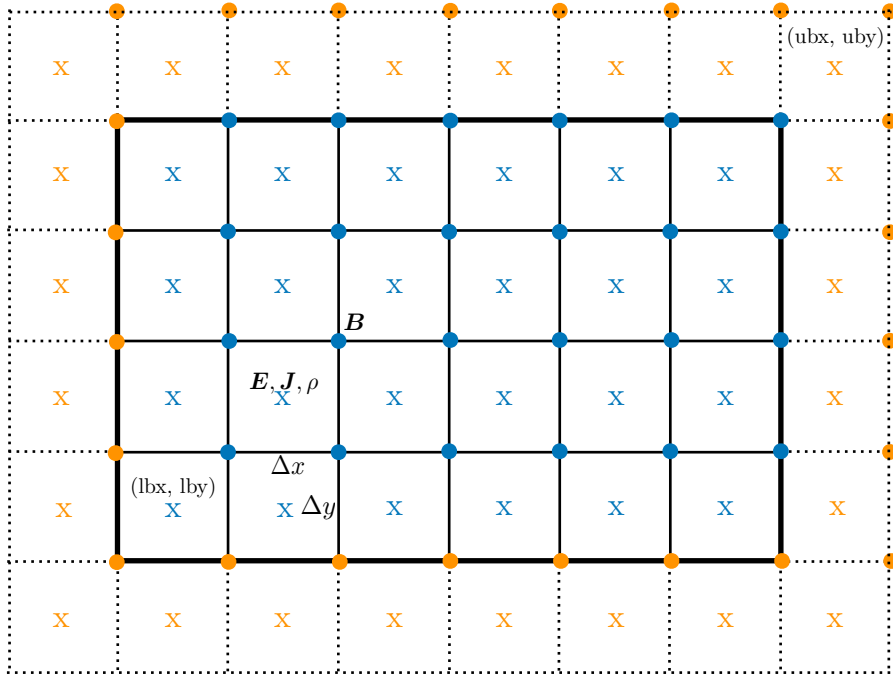


Figure 9.1: The grid layout with crosses (solid circles) indicating cell centers (corners). Blue symbols are active cells and orange symbols are guard layers. The thick black solid line indicates the grid boundaries. In the x -direction this is always equivalent to the physical boundaries while the boundaries in the y -direction are MPI boundaries.

9.1.1 Finite difference scheme

We use finite differences to approximate spatial derivatives. We can write the finite difference approximations to the first order derivatives along x and y in compact form by introducing finite difference operator notation (see for instance the appendix of Durran 2010)

$$\delta_{nx} f_{i,j} = \frac{f_{i+n/2,j} - f_{i-n/2,j}}{n\Delta x}, \quad (9.1)$$

$$\delta_{my} f_{i,j} = \frac{f_{i,j+m/2} - f_{i,j-m/2}}{m\Delta y}, \quad (9.2)$$

9. Numerical methods

Staggering	d/dx	d/dy
None	δ_{2x}	δ_{2y}
Along y	$\delta_{2x}\langle\cdot\rangle^y$	δ_y
Along x	δ_x	$\delta_{2y}\langle\cdot\rangle^x$
Along x and y	$\delta_x\langle\cdot\rangle^y$	$\delta_y\langle\cdot\rangle^x$

Table 9.1: Finite difference approximations to the derivative of a quantity depend on the staggering of the quantity. Here we show the 8 versions of the first order derivatives. Due to the interlaced grid only the upper and lower row are used in our hybrid code.

and an interpolation operator with the following properties

$$\langle f_{i,j} \rangle^x = \langle \cdot \rangle^x f_{i,j} = \frac{f_{i+1/2,j} + f_{i-1/2,j}}{2}, \quad (9.3)$$

$$\langle f_{i,j} \rangle^y = \langle \cdot \rangle^y f_{i,j} = \frac{f_{i,j+1/2} + f_{i,j-1/2}}{2}. \quad (9.4)$$

The resulting finite difference expressions for d/dx and d/dy are summarized in Table 9.1. We can then introduce a finite difference approximation to the curl, $\tilde{\nabla}$, defined by²

$$\tilde{\nabla} \times \mathbf{f}_{i,j} = \delta_y \langle f_{i,j}^z \rangle^x \mathbf{e}_x - \delta_x \langle f_{i,j}^z \rangle^y \mathbf{e}_y + \left(\delta_x \langle f_{i,j}^y \rangle^y - \delta_y \langle f_{i,j}^x \rangle^x \right) \mathbf{e}_z, \quad (9.5)$$

where \mathbf{f} is a vector field. Note that this procedure approximates the curl of \mathbf{f} at (i, j) by using values of \mathbf{f} at $(i \pm 1/2, j \pm 1/2)$. Using this notation for the curl of \mathbf{B} we find for Ampère's law (Equation 2.9)

$$\mathbf{J}_{i,j} = \mu_0^{-1} \tilde{\nabla} \times \mathbf{B}_{i,j}, \quad (9.6)$$

i.e., an approximation to \mathbf{J} at cell centers where the ion current is also deposited. A simple subtraction of the ion current from the total current, without further interpolation, is done to obtain the electron current, \mathbf{J}_e . In order to calculate $\mathbf{J}_e \times \mathbf{B}$ we do however need to interpolate \mathbf{B} from the cell corner to the cell

²Recall that we are considering a 2D-3V setting where the fields are constant along z .

center. Using a superscript e to indicate electron current we have

$$(\mathbf{J}^e \times \mathbf{B})_{i,j} = \mathbf{J}_{i,j}^e \times \langle \langle \mathbf{B}_{i,j} \rangle^x \rangle^y. \quad (9.7)$$

In order to have the gradient of the electron pressure approximated at cell centers, we use the following finite difference approximation to the gradient

$$\tilde{\nabla} f_{i,j} = \delta_{2x} f_{i,j} \mathbf{e}_x + \delta_{2y} f_{i,j} \mathbf{e}_y. \quad (9.8)$$

Our finite difference approximation to Ohm's law (Equation 2.14) can be summarized as

$$\mathbf{E}_{i,j} = \frac{\tilde{\nabla} p_{i,j}^e}{\rho_{i,j}^e} - \frac{(\mu_0^{-1} \tilde{\nabla} \times \mathbf{B}_{i,j} - \sum_s \mathbf{J}_{i,j}^s)}{\rho_{i,j}^e} \times \langle \langle \mathbf{B}_{i,j} \rangle^x \rangle^y. \quad (9.9)$$

Finally, we use the following spatial discretization

$$\frac{\partial \mathbf{B}_{i+1/2,j+1/2}}{\partial t} = -\tilde{\nabla} \times \mathbf{E}_{i+1/2,j+1/2}. \quad (9.10)$$

for Faraday's law (Equation 2.8).

9.1.2 Divergence of \mathbf{B}

Kunz, Stone, and Bai (2014) argue that the usage of an interlaced grid by e.g. Horowitz, Shumaker, and Anderson (1989) and Gargat e et al. (2007) leads to production of magnetic monopoles, i.e., that the $\nabla \cdot \mathbf{B} = 0$ constraint is not fulfilled by the finite difference discretization of Faraday's law when using Equation 9.10.

We believe that this criticism is unfounded, for the following reason. In order to assess whether the divergence of \mathbf{B} is zero to machine precision it is necessary to specify which finite difference approximation is used as several different options exist (T oth, 2000). We now prove that one finite discretization of $\nabla \cdot \mathbf{B}$ is identically zero on the Yee (Yee, 1966) mesh while a different finite discretization is identically zero on the interlaced grid. We limit the discussion to the 2D application we have in mind but provide the general 3D proof in Appendix A.7.

9. Numerical methods

For the Yee mesh³ Faraday's law can be written as

$$\frac{\partial B_{i+1/2,j}^x}{\partial t} = -\delta_y E_{i+1/2,j}^z, \quad (9.11)$$

$$\frac{\partial B_{i,j+1/2}^y}{\partial t} = \delta_x E_{i,j+1/2}^z. \quad (9.12)$$

If we use the finite difference approximation to $\nabla \cdot \mathbf{B} = 0$ given by

$$(\nabla \cdot \mathbf{B})_{i,j} = \delta_x B_{i,j}^x + \delta_y B_{i,j}^y, \quad (9.13)$$

to approximate the divergence of \mathbf{B} at cell centers, then we see that the time derivative of $\nabla \cdot \mathbf{B}$ is

$$\left(\nabla \cdot \frac{\partial \mathbf{B}}{\partial t} \right)_{i,j} = -\delta_x \delta_y E_{i,j}^z + \delta_y \delta_x E_{i,j}^z. \quad (9.14)$$

This is identically zero (to machine precision) as the δ_x and δ_y operators commute.

The approximation to $\nabla \cdot \mathbf{B}$ given by Equation 9.13 does not work on the interlaced grid. A natural finite difference approximation to $\nabla \cdot \mathbf{B} = 0$ at cell centers is in this case instead given by

$$\tilde{\nabla} \cdot \mathbf{B}_{i,j} = \delta_x \langle B_{i,j}^x \rangle^y + \delta_y \langle B_{i,j}^y \rangle^x. \quad (9.15)$$

This approximation to $\nabla \cdot \mathbf{B}$, combined with Equation 9.10, is zero to machine precision. We can show this using the notation introduced earlier. For the interlaced mesh Faraday's law can be written as

$$\frac{\partial B_{i+1/2,j+1/2}^x}{\partial t} = -\delta_y \langle E_{i+1/2,j+1/2}^z \rangle^x, \quad (9.16)$$

$$\frac{\partial B_{i+1/2,j+1/2}^y}{\partial t} = \delta_x \langle E_{i+1/2,j+1/2}^z \rangle^y, \quad (9.17)$$

³The Yee mesh is here defined to have B_x located at $(i + 1/2, j)$, B_y located at $(i, j + 1/2)$ and E_z located at $(i + 1/2, j + 1/2)$.

such that the time derivative of $\nabla \cdot \mathbf{B}$ at cell centers is given by

$$\begin{aligned} \tilde{\nabla} \cdot \frac{\partial \mathbf{B}_{i,j}}{\partial t} &= \delta_x \langle -\delta_y \langle E_{i,j}^z \rangle^x \rangle^y + \delta_y \langle \delta_x \langle E_{i,j}^z \rangle^y \rangle^x \\ &= \delta_x \delta_y \langle \cdot \rangle^x \langle \cdot \rangle^y (-1 + 1) E_{i,j}^z = 0 . \end{aligned} \quad (9.18)$$

Here, we have again used that all the operators commute. We can express this more generally, by stating that the finite difference approximations to the curl and divergence on the interlaced grid (Equations 9.5 and 9.15) have the property that⁴

$$\tilde{\nabla} \cdot (\tilde{\nabla} \times \mathbf{f}_{i,j}) = 0 . \quad (9.19)$$

We initialize non-trivial magnetic field configurations by taking the finite difference approximation to the curl of the magnetic vector potential, \mathbf{A} , i.e.

$$\mathbf{B}_{i+1/2,j+1/2} = \tilde{\nabla} \times \mathbf{A}_{i+1/2,j+1/2} , \quad (9.20)$$

where \mathbf{A} is defined at cell centers. This ensures that the initial $\tilde{\nabla} \cdot \mathbf{B}_{i,j}$ is zero. Combining this with Equation 9.18 ensures that it also remains zero at later times.

9.2 Time stepping procedures

In this section we outline two different procedures to update the quantities of interest in the simulation. The two procedures, a predictor-corrector method (Byers et al., 1978; Harned, 1982) and an iterative field solution method (Horowitz, Shumaker, and Anderson, 1989) both update the magnetic and electric fields using Faraday's and Ohm's laws and the particle positions and velocities using a Boris push.

For the sake of brevity, we introduce the notation for Ohm's law used in Winske et al. (2003), which is a simple shorthand for the fact that the electric field is a function of the magnetic field, charge density and ion current. The charge density and ion current are given by the particle positions, \mathbf{x} , and velocities, \mathbf{v} , so

⁴While our present concern is a 2D code we note that this also holds for the generalization to three dimensions for the finite difference representation of the curl and divergence such that $\tilde{\nabla} \cdot (\tilde{\nabla} \times \mathbf{f}_{i,j,k}) = 0$. See Appendix A.7.

the dependence of Ohm's law (defined in Equation 2.15) can be written as

$$\mathbf{E} = F(\mathbf{B}, \mathbf{x}, \mathbf{v}) . \quad (9.21)$$

All quantities in this equation should be given at the same point in time. We also use the shorthand for the Boris update of the velocity introduced in Equation 8.10.

The spatial discretization of the equations has been described in the previous section and so we do not include it explicitly in the discussion in this section.

We start out by summarizing the discussion in Byers et al. (1978) and Winske et al. (2003) regarding how it is not straightforward to compute the electric field at the next time step. Let us assume that we know initial values for the particle velocities and the magnetic field at time step $n - 1/2$ and the particle positions and the electric field at time step n , i.e., we know the set $\mathbf{v}^{n-1/2}$, $\mathbf{B}^{n-1/2}$, \mathbf{x}^n and \mathbf{E}^n . The goal is to calculate these values at the next time step, i.e., we need to find $\mathbf{v}^{n+1/2}$, $\mathbf{B}^{n+1/2}$, \mathbf{x}^{n+1} and \mathbf{E}^{n+1} . We can proceed by calculating \mathbf{B} at both n and $n + 1/2$ using Faraday's law

$$\mathbf{B}^{n+1/2} = \mathbf{B}^{n-1/2} - \Delta t \nabla \times \mathbf{E}^n , \quad (9.22)$$

$$\mathbf{B}^n = \frac{1}{2} (\mathbf{B}^{n-1/2} + \mathbf{B}^{n+1/2}) . \quad (9.23)$$

The knowledge of \mathbf{E}^n , \mathbf{B}^n and \mathbf{x}^n is sufficient information to calculate the velocity at $n + 1/2$ using the prescription by Boris (1970)

$$\mathbf{v}^{n+1/2} = \mathbf{M}(\mathbf{E}^n, \mathbf{B}^n, \mathbf{x}^n) \cdot \mathbf{v}^{n-1/2} . \quad (9.24)$$

Using this new velocity we can find the positions at $n + 1/2$ and $n + 1$ as

$$\mathbf{x}^{n+1} = \mathbf{x}^n + \Delta t \mathbf{v}^{n+1/2} , \quad (9.25)$$

$$\mathbf{x}^{n+1/2} = \frac{1}{2} (\mathbf{x}^{n-1/2} + \mathbf{x}^{n+1/2}) . \quad (9.26)$$

We now only need to calculate \mathbf{E}^{n+1} . Inspection of Ohm's law

$$\mathbf{E}^{n+1} = F(\mathbf{B}^{n+1}, \mathbf{x}^{n+1}, \mathbf{v}^{n+1}) , \quad (9.27)$$

reveals that the electric field at $n + 1$ depends on the magnetic field and particle positions and velocities at $n + 1$. We already know the particle positions \mathbf{x}^{n+1} and the magnetic field, \mathbf{B}^{n+1} , can be calculated using Faraday's law⁵

$$\mathbf{B}^{n+1} = \mathbf{B}^n - \Delta t \nabla \times \mathbf{E}^{n+1/2} . \quad (9.29)$$

The dependence of the electric field on the particle velocities at $n + 1$ evident in Equation 9.27 prevents us from proceeding in a simple manner. Several methods for circumventing this problem have been invented and a good overview can be found in Winske et al. (2003). Methods not discussed here include (but are not limited to) the current advance method (Matthews, 1994) and a predictor-corrector-corrector method (Kunz, Stone, and Bai, 2014). In the following two subsections we discuss the predictor-corrector and the Horowitz method.

9.2.1 Predictor-corrector method

The predictor-corrector method as applied to hybrid codes is well explained in Byers et al. (1978), Harned (1982) and Winske et al. (2003). Here we simply give a brief overview of our implementation of this method.

Let us start from the point where we realized that \mathbf{E}^{n+1} could not be calculated as we did not know \mathbf{v}^{n+1} . The predictor-corrector step solves this problem of not being able to calculate \mathbf{E}^{n+1} by instead predicting its value as

$$\hat{\mathbf{E}}^{n+1} = 2\mathbf{E}^{n+1/2} - \mathbf{E}^n , \quad (9.30)$$

where the hat denotes that it is a predicted value. From the values of $\mathbf{v}^{n+1/2}$, $\mathbf{B}^{n+1/2}$, \mathbf{x}^{n+1} and $\hat{\mathbf{E}}^{n+1}$ we can then proceed in the same way as outlined above⁶ to calculate predicted values $\hat{\mathbf{v}}^{n+3/2}$, $\hat{\mathbf{B}}^{n+3/2}$, $\hat{\mathbf{x}}^{n+3/2}$ at time step $n + 3/2$. From

⁵This requires knowledge of $\mathbf{E}^{n+1/2}$ which can however easily be computed as

$$\mathbf{E}^{n+1/2} = F(\mathbf{B}^{n+1/2}, \mathbf{x}^{n+1/2}, \mathbf{v}^{n+1/2}) , \quad (9.28)$$

and we already know $\mathbf{B}^{n+1/2}$, $\mathbf{x}^{n+1/2}$, and $\mathbf{v}^{n+1/2}$.

⁶The only difference is that time step indices are incremented with one and that hats are used to indicate that the error from not using the correct value of the electric field at $n + 1$ propagates.

these we can calculate the predicted electric field at $n + 3/2$ as

$$\hat{\mathbf{E}}^{n+3/2} = F(\hat{\mathbf{B}}^{n+3/2}, \hat{\mathbf{x}}^{n+3/2}, \hat{\mathbf{v}}^{n+3/2}), \quad (9.31)$$

which is then used to estimate the electric field at $n + 1$ as

$$\mathbf{E}^{n+1} = \frac{1}{2}(\mathbf{E}^{1/2} + \hat{\mathbf{E}}^{3/2}). \quad (9.32)$$

This latter step is called the corrector step. The predictor-corrector method is seen to require two particle pushes which makes it expensive.

9.2.2 Horowitz method

The second time stepping procedure that we have implemented in the code is an iterative solution for the field equations due to Horowitz, Shumaker, and Anderson (1989). Compared to the predictor-corrector method, the Horowitz method has the advantage that only a single update of the particles is needed. When a lot of particles are used per cell, the computational cost is essentially given by the cost to push the particles forward in time while the cost of solving the field equations is negligible. In this case it is possible to get a speedup by a factor approaching 2 by using the Horowitz method instead of the predictor-corrector method. The Horowitz method is also employed by Amano, Higashimori, and Shirakawa (2014).

The Horowitz method works as follows: given an initial condition with particle velocities at time step $n - 1/2$, and positions as well as electric and magnetic fields at time step n , we perform steps 1a to 2a as detailed below, and then repeat steps 2b to 2e until converged.

1. Update particle positions and velocities. Deposit sources.
 - (a) Kick the velocities to time step $n + 1/2$

$$\mathbf{v}^{n+1/2} = \mathbf{M}(\mathbf{E}^n, \mathbf{B}^n, \mathbf{x}^n) \cdot \mathbf{v}^{n-1/2}. \quad (9.33)$$

(b) Drift the positions by a half time step to $n + 1/2$

$$\mathbf{x}^{n+1/2} = \mathbf{x}^n + \frac{\Delta t}{2} \mathbf{v}^{n+1/2}. \quad (9.34)$$

(c) Deposit the charge density and ion current at $n + 1/2$

$$\mathbf{x}^{n+1/2}, \mathbf{v}^{n+1/2} \rightarrow \rho_e^{n+1/2}, \mathbf{J}_i^{n+1/2}. \quad (9.35)$$

(d) Drift the position by another half time step to $n + 1$

$$\mathbf{x}^{n+1} = \mathbf{x}^{n+1/2} + \frac{\Delta t}{2} \mathbf{v}^{n+1/2}. \quad (9.36)$$

2. Iteratively solve the field equations.

(a) Initialize the iteration by setting $k = 0$ and $\mathbf{E}_k^{n+1} = \mathbf{E}^n$.

(b) Estimate the electric field at $n + 1/2$ as

$$\mathbf{E}_k^{n+1/2} = \frac{1}{2} (\mathbf{E}_k^{n+1} + \mathbf{E}^n), \quad (9.37)$$

and use Faraday's law to calculate \mathbf{B}_{k+1}^{n+1}

$$\mathbf{B}_{k+1}^{n+1} = \mathbf{B}^n - \Delta t \nabla \times \mathbf{E}_k^{n+1/2}. \quad (9.38)$$

(c) Estimate the magnetic field at $n + 1/2$ as

$$\mathbf{B}_{k+1}^{n+1/2} = \frac{1}{2} (\mathbf{B}_{k+1}^{n+1} + \mathbf{B}^n), \quad (9.39)$$

and use Ohm's law to calculate \mathbf{E}_{k+1}^{n+1}

$$\mathbf{E}_{k+1}^{n+1} = -\mathbf{E}^n + 2F(\mathbf{B}_{k+1}^{n+1/2}, \mathbf{x}^{n+1/2}, \mathbf{v}^{n+1/2}). \quad (9.40)$$

(d) Set $k = k + 1$.

(e) Calculate the root-mean-squared (RMS) of the difference between \mathbf{E}_{k+1}^{n+1} and \mathbf{E}_k^{n+1} to check if converged.

9. Numerical methods

The tolerance on the RMS difference with respect to the previous iteration and the maximum number of iterations can be set by the user. If the tolerance is not reached within the maximum number of iterations the simulation is discontinued. This is normally an indication that the time step is too large or that the number of particles per cell should be increased. Horowitz, Shumaker, and Anderson (1989) use a tolerance of 10^{-3} and state that they reach convergence in 4-9 iterations. We set as the default a tolerance of 1.48×10^{-8} with a maximum of 20 iterations. For the cold tests presented in Chapter 12 convergence is reached within two iterations, despite the low number of particles per cell.

Chapter 10

Particle loading

Particle in cell simulations evolve the phase-space distribution function for each particle species. The phase-space distribution is a probability distribution and we therefore need to be able to generate random numbers from a variety of probability distributions in order to initialize the simulations.

A number of different algorithms for doing so exist and many of them, such as the uniform distribution or normal distribution, are easily accessible using Numpy (Oliphant, 2007). Particle simulations are however easily plagued by noise unless a significant amount of particles are used per computational cell. For instance, the noise in the density for a plasma with uniform density ρ is $\rho/\sqrt{N_p}$ if one initializes the positions of the particles by generating random numbers from the uniform distribution function. This is a fundamental problem with the PIC method which makes simulations computationally intensive. For testing purposes this is an issue because tests ideally should be inexpensive such that they can be run (often) on a personal computer. Code tests are often performed by comparing with the linear theory of waves and instabilities (see Chapter 11 and 12). In both cases, linear theory assumes that initial perturbations have small amplitudes. This makes linear tests especially expensive as the initial perturbation will be dominated by noise unless many particles are used. Furthermore, even with many particles per cell, the remaining particle noise is likely to make it difficult to notice subtle errors.

10. Particle loading

For testing purposes¹ we have thus found it useful to be able to initialize a so-called quiet start (Birdsall and Langdon, 1991). For a cold, uniform plasma, a quiet start is initialized simply by setting the particle positions on the grid with the same inter-particle distance. This makes the density field completely smooth even when using just a single particle per cell. For a non-uniform density profile and/or a warm plasma we can instead use inverse transform sampling (Devroye, 1986) of the probability distribution function to initialize the plasma with low noise. This procedure is explained in detail below.

10.1 Inverse transform sampling

The starting point for the inverse transform method is the probability integral transform, which states the following (Devroye, 1986): If x is a random variable with probability distribution function, $f(x)$, and cumulative distribution function, $F_x(x)$, given by

$$F_x(x) = \int_{-\infty}^x f(x') dx', \quad (10.1)$$

then the random variable

$$y = F_x(x), \quad (10.2)$$

has a uniform distribution on the interval $[0, 1]$ (Devroye, 1986).

The inverse transform sampling method works by inverting Equation 10.2, i.e.,

$$x = F_x^{-1}(y). \quad (10.3)$$

Equation 10.3 can be used to generate random numbers from $f(x)$ by generating random numbers from the uniform distribution. At first glance this is mostly useful for distribution functions where an analytical expression for the cumulative distribution function and its inverse exist. If the inverse does not exist it is however

¹Another technique to use few particles without having the simulation dominated by noise is the δf -method. This method is described and used in for instance Kunz, Stone, and Bai (2014).

still possible to solve Equation 10.2 directly using numerical root finding such as the Newton-Raphson method².

As described above, the inverse transform method is a convenient way of generating random numbers, x_j , from a probability distribution, $f(x)$, by generating random numbers, y_j from the uniform distribution on $[0, 1]$. If we instead let the numbers y_j be uniformly spaced on $[0, 1]$ then the resulting x_j represent the distribution function, $f(x)$, without noise. We illustrate this with two examples in the following sections.

10.2 Non-uniform density

Let us as an example consider a plasma with density profile

$$\rho(x) = \rho_0[1 + A \cos(k_x x)] , \quad (10.4)$$

on the interval $x = [0, L_x)$. Here A is the amplitude of the density perturbation and ρ_0 is the background density. The corresponding probability distribution is

$$f(x) = 1 + A \cos(k_x x) , \quad (10.5)$$

and has cumulative distribution function

$$F_x(x) = \int_0^x [1 + A \cos(k_x x')] dx' = x + A \frac{\sin(k_x x)}{k_x} . \quad (10.6)$$

This is a transcendental equation and the inverse of the cumulative distribution function does not have a simple form. We can however still find x_j by numerically solving³

$$y_j = x_j + A \frac{\sin(k_x x_j)}{k_x} , \quad (10.7)$$

²And even if neither $F(x)$ nor $F(x)^{-1}$ has an analytical form the method can still be used by approximating the probability distribution with polynomials (Olver and Townsend, 2013)

³Note that the cumulative distribution function is monotone increasing as the probability distribution function is always positive. This ensures that Equation 10.7 has a unique solution for each value of y_j .

10. Particle loading

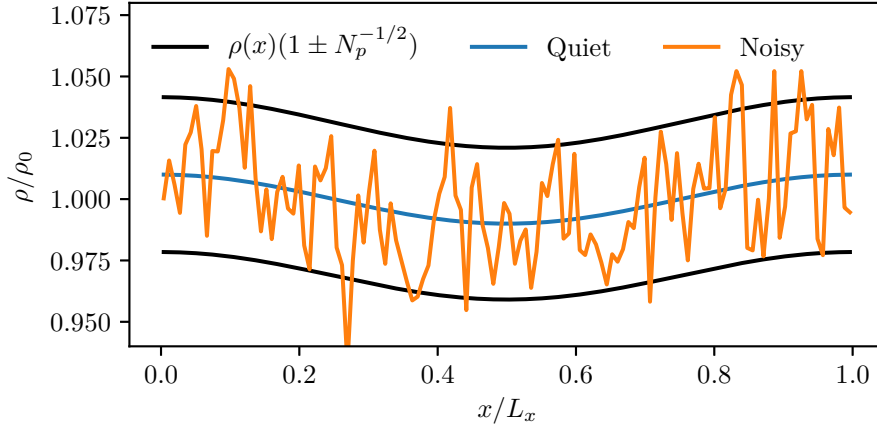


Figure 10.1: Density profile generated using 1024 particles per cell and 128 cells. The orange (blue) solid line was found by calculating the particle positions x_j by numerically solving equation 10.7 using random numbers (regularly spaced values) for y_j .

for each value of y_j . The values of x_j are then used as the particle positions. We present the density profile that results from such a calculation in Figure 10.1. This figure was produced by using $N_p = 1024$ particles per cell and $n_x = 128$ cells. The amplitude of the perturbation was set to $A = 1/100$ and the TSC assignment function was used to deposit the charge density. The blue line represents the density profile found when initializing the particles in a quiet manner (y_j is regularly spaced). This solution coincides with the density profile given by Equation 10.4 and the RMS difference is only $2 \cdot 10^{-6}$. The orange line represents the density found when initializing the particles in a noisy manner (y_j is found by generating random numbers from the uniform distribution). The RMS difference with respect to the analytic density profile is $2 \cdot 10^{-2}$, i.e., four orders of magnitude larger than when using the quiet initialization. The black solid lines in Figure 10.1 indicate the noise level expected when using 1024 particles per cell, given by $N_p^{-1/2}$ where N_p is the number of particles per cell.

10.3 Maxwellian with low noise

We have also found the inverse transform method useful for initializing the velocity distribution of the particles. This method is also described in Cartwright, Verboncoeur, and Birdsall (2000) and Birdsall and Langdon (1991). We consider a velocity distribution

$$f(v) = \frac{1}{\sqrt{2\pi}v_t} e^{-v^2/2v_t^2}, \quad (10.8)$$

which has the cumulative distribution function

$$F_v(v) = \frac{1}{2} \left[1 + \operatorname{erf} \left(\frac{v}{\sqrt{2}v_t} \right) \right], \quad (10.9)$$

where the error function is defined to be

$$\operatorname{erf}(z) = \frac{2}{\sqrt{\pi}} \int_0^z e^{-t^2} dt. \quad (10.10)$$

We can thus generate thermal velocities by solving

$$y_j = \frac{1}{2} \left[1 + \operatorname{erf} \left(\frac{v_j}{\sqrt{2}v_t} \right) \right], \quad (10.11)$$

for v_j . We find

$$v_j = \sqrt{2}v_t \operatorname{erf}^{-1}(2y_j - 1), \quad (10.12)$$

where $\operatorname{erf}^{-1}(z)$ is the inverse error function. The inverse error function is available from Scipy (Jones, Oliphant, and Peterson, 2001-2017) both at the Python and Cython level.

As for the example with the density profile, we can let the set of numbers y_j be randomly drawn numbers from the uniform distribution. In this case the set of numbers v_j will be randomly drawn numbers from $f(v)$ (Equation 10.8). As $f(v)$ is simply a normal distribution with zero mean and standard deviation v_t this could also easily be achieved with one line of code by using Numpy (Oliphant, 2007).

10. Particle loading

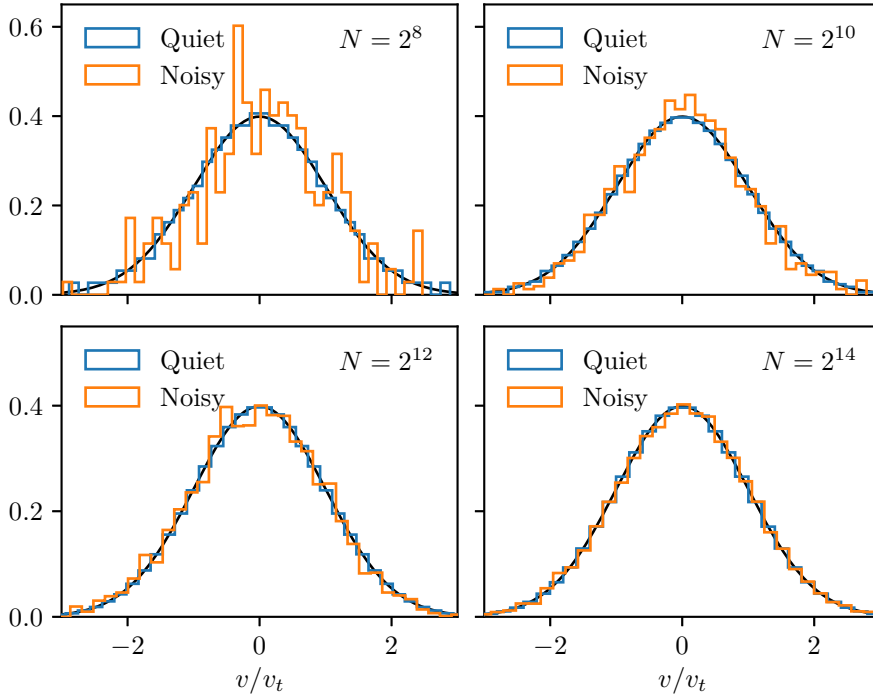


Figure 10.2: Histograms of velocities generated using equation 10.12 with a quiet method (blue) and a noisy method (orange) for $N = 2^8, 2^{10}, 2^{12}$ and 2^{14} numbers. The probability distribution function, $f(v)$, given by equation 10.8 is shown with a black solid line for reference.

The real benefit of the inverse transform sampling method is thus that we can let the set of numbers y_j be regularly spaced on $[0, 1)$. In this case we get what we will refer to as a quiet Maxwellian (as opposed to a noisy Maxwellian). As an illustration we show histograms for velocities generated using the two different methods (noisy and quiet) in Figure 10.2. The quiet Maxwellian is able to capture the correct mean and standard deviation of the distribution to a much better accuracy than the noisy Maxwellian. This has the advantage that it is possible to model the linear stages of kinetic phenomena using fewer particles per cell than when using the noisy Maxwellian. The utility of the quiet Maxwellian is seen in Figure 12.5 on page 135 in Chapter 12 where we use a quiet Maxwellian to follow the evolution of perturbations with a very low initial amplitude. We have also

used the quiet Maxwellian to study Landau damping of ion-acoustic waves. For this study we found similar results in a simulation with 2^{10} particles per cell using a quiet start as for a simulation with 2^{16} particles per cell using a noisy start. This means that a test of Landau damping can be performed roughly 64 times faster when using a quiet Maxwellian.

While these properties of quiet starts make them very convenient for testing purposes they should be used with care. The problem with quiet starts is that correlations are introduced into the simulation by the imposed artificial order. As detailed in Birdsall and Langdon (1991) this artificial order can lead to spurious results. For this reason quiet starts should only be used for testing purposes.

Chapter 11

Landau damping, aliasing and the finite grid instability

In this chapter we use linear theory to study Landau damping of ion-acoustic and electrostatic waves. We also investigate aliasing in PIC codes and one of the detrimental consequences it can have: the finite grid instability. The finite grid instability was originally discovered in full PIC codes (Langdon, 1970; Okuda, 1972) where it arises due to aliasing when the grid resolution is not sufficient to resolve the Debye length. This numerical instability is well-known and described in the two standard text books on PIC methods (Hockney and Eastwood, 1988; Birdsall and Langdon, 1991) but the corresponding instability in hybrid PIC codes was discovered more recently (Rambo, 1995).

While developing the hybrid code we experienced that a simple simulation of ion-acoustic waves with cold ions would go numerically unstable with a sawtooth profile in the charge density occurring at the grid scale. As we were initially unaware of the work by Rambo (1995) we thought that this was due to a bug in our code. Consequently, we spent significant effort on understanding and testing the numerical dispersion relation of ion-acoustic waves.

The chapter is organized as follows. In the first section we derive the dispersion relations for Landau damping of ion-acoustic waves and electrostatic modes. We also present results from simulations of Landau damping using the hybrid code. In the second section we present the numerical dispersion relations in Langdon

11. Landau damping, aliasing and the finite grid instability

(1970), Birdsall and Langdon (1991), Hockney and Eastwood (1988) and Rambo (1995). We then use the cold ion limit of the Vlasov-fluid version of the numerical dispersion relations to test our implementation of the second order finite difference scheme as well as CIC and TSC interpolation. In the third section we highlight how the finite grid instability for a hybrid code only depends on the temperature ratio T_i/T_e . This is in contrast to the electrostatic finite grid instability which can in principle be stabilized by increasing the numerical resolution.

11.1 Landau damping

We start out by deriving the dispersion relation for an unmagnetized plasma in both the electrostatic and the Vlasov-fluid limit. We then extend these dispersion relations to their numerical versions by applying the theory discussed on page 227-228 in Hockney and Eastwood (1988).

Starting from a 1D version of the Vlasov equation without a magnetic field (Equation 2.3)

$$\frac{\partial f_s}{\partial t} + v \frac{\partial f_s}{\partial x} + \frac{e_s}{m_s} E \frac{\partial f_s}{\partial v} = 0, \quad (11.1)$$

we assume perturbations of the form $\exp(-i\omega t + ikx)$, linearize, rearrange and integrate over velocity to obtain

$$\delta \hat{n}_s = -i \frac{e_s}{m_s} \delta \hat{E} \int_{-\infty}^{\infty} \frac{\partial f_s / \partial v}{\omega - kv} dv. \quad (11.2)$$

In Equation 11.2 the hats indicate that we are working with Fourier amplitudes. We assume a distribution function given by

$$f_s(v) = \frac{n_s}{\sqrt{2\pi}v_t} e^{-v^2/2v_t^2}, \quad (11.3)$$

where $v_t = \sqrt{T_s/m_s}$ is the thermal velocity and n_s is the mean number density, such that integration of Equation 11.2 over velocity yields

$$\delta \hat{n}_s = -i \frac{e_s n_s}{m_s} \frac{\delta \hat{E}}{kv_t^2} W\left(\frac{\omega}{kv_t}\right), \quad (11.4)$$

where $W(z)$ is Ichimaru's plasma dispersion function defined in Equation 6.23. Up until this point the derivations are identical for an electrostatic plasma and for the Vlasov-fluid plasma. The main difference arises in the way the electric field is calculated. We can in both cases define a potential, Φ , such that

$$E = -\frac{\partial\Phi}{\partial x}, \quad (11.5)$$

where Φ is found from Ohm's law for the Vlasov-fluid model (Equation 2.15 with $\mathbf{B} = 0$) and by the solution to Poisson's equation for the electrostatic model (Hockney and Eastwood, 1988). We have for the Vlasov-fluid model and the electrostatic model

$$\Phi = -\frac{T_e}{e} \log n_e, \quad \text{Vlasov-fluid} \quad (11.6)$$

$$\frac{\partial^2\Phi}{\partial x^2} = -\frac{e(n_i - n_e)}{\epsilon_0}, \quad \text{Electrostatic} \quad (11.7)$$

and assume charge neutrality $n_i = n_e = n_0$ for the Vlasov-fluid model and immobile ions for the electrostatic model. We find for the perturbed electric fields

$$\delta\hat{E} = -ik\frac{T_e}{en_0}\delta\hat{n}_i, \quad \text{Vlasov-fluid} \quad (11.8)$$

$$\delta\hat{E} = \frac{ie}{\epsilon_0 k}\delta\hat{n}_e, \quad \text{Electrostatic} \quad (11.9)$$

and the corresponding dispersion relations are then

$$1 + \frac{c_s^2}{v_t^2}W\left(\frac{\omega}{kv_t}\right) = 0, \quad \text{Vlasov-fluid} \quad (11.10)$$

$$1 + \frac{\omega_p^2}{k^2v_t^2}W\left(\frac{\omega}{kv_t}\right) = 0. \quad \text{Electrostatic} \quad (11.11)$$

Here we have used the sound speed $c_s^2 = T_e/m_i$ and the definition of the the plasma frequency in Equation 1.1.

For a cold plasma we can take the large argument expansion of the plasma

11. Landau damping, aliasing and the finite grid instability

dispersion function (Equation A.64), i.e.,

$$W\left(\frac{\omega}{kv_t}\right) \approx -\frac{k^2 v_t^2}{\omega^2}, \quad (11.12)$$

in order to find the dispersion relation for cold ion-acoustic waves, $\omega^2 = k^2 c_s^2$, and for cold electrostatic modes, $\omega^2 = \omega_p^2$. When the plasma is warm these waves are damped by Landau damping (Landau, 1946). The physical mechanism for Landau damping of the waves is energy transfer between the wave and particles (see, e.g., Fitzpatrick 2014). Particles which have approximately the same velocity as the phase velocity of the wave, $v_{\text{ph}} = \omega/k$, will gain (lose) energy if their speed is slightly smaller (larger) than v_{ph} . Landau damping of the wave occurs when there are more particles gaining energy from the wave than losing energy to it. This occurs when there are more particles with $v < v_{\text{ph}}$ than with $v > v_{\text{ph}}$, i.e., for $v > 0$ when

$$\left. \frac{\partial f}{\partial v} \right|_{v=v_{\text{ph}}} < 0. \quad (11.13)$$

The PIC code enables us to study Landau damping of electrostatic¹ waves and ion-acoustic waves. In order to illustrate Landau damping of ion-acoustic waves we perform simulations on a grid with resolution $n_x = 32$ with 2^{16} particles per cell. In the simulations presented here we initialize a uniform plasma using equidistant positions for the particles and a quiet Maxwellian distribution as described in Chapter 10. Additionally we add a perturbation to the velocity of the form

$$\delta v = A c_s \sin(kx), \quad (11.14)$$

where x is the position at $tkc_s = 0$ and the amplitude of the perturbation is $A = 0.01$. Here the wavenumber is $k = 2\pi/L$ where L is the length of the simulation domain. We use a simplified form of Ohm's law (Equation 2.15) where the magnetic field is zero. This means that the electric field does not depend on

¹We have implemented a solver for Poisson's equation that uses FFTs. The main focus of this thesis is the hybrid code so we will not go into detail on this here.

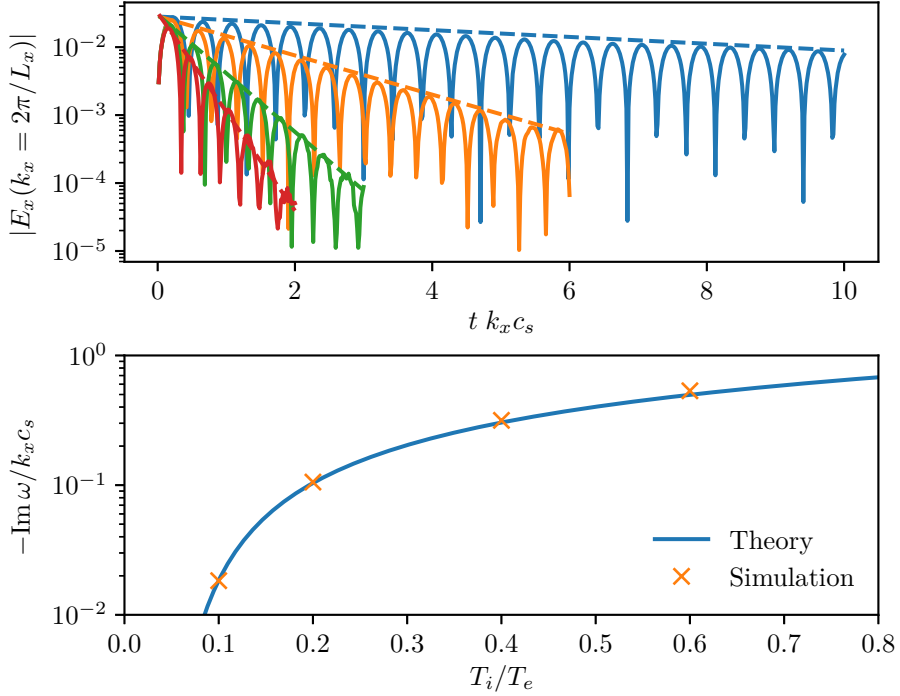


Figure 11.1: Landau damping of ion-acoustic waves.

the particle velocities and consequently that it is not necessary to use the methods described in Section 9.2. That is, instead of the predictor-corrector or Horowitz method we can simply leapfrog the equations.

The initial condition outlined above is only an exact eigenmode in the cold plasma limit. We nevertheless expect² the initialization to lead to ion-acoustic waves with

$$\rho(t) = \rho_0 [1 + A \cos(kx) \sin(\omega t)] e^{-\gamma t}, \quad (11.15)$$

$$v(t) = c_s A \sin(kx) \cos(\omega t) e^{-\gamma t}, \quad (11.16)$$

where ρ_0 is the mean charge density and γ is the Landau damping rate given by

²It is in principle possible to initialize the simulation with the exact perturbed distribution function, δf , but we have found satisfactory results by using the common approach of perturbing the velocity (or density) profile.

11. Landau damping, aliasing and the finite grid instability

$\gamma = -\text{Im}(\omega)$. As the electric field is given by Equations 11.5 and 11.6 it follows that the electric field will decay exponentially as well. We note that the decay in wave energy is associated with heating of the particles such that the total energy is conserved (disregarding the non-energy conservation of the explicit PIC method).

In order to study Landau damping, we follow the time evolution of the absolute value of the $k = 2\pi/L$ Fourier amplitude of the electric field. This quantity is shown with solid lines in the upper part of Figure 11.1 for simulations with $T_i/T_e = 0.1, 0.2, 0.4,$ and 0.6 (shown in blue, orange, green and red, respectively). The corresponding dashed lines are exponential fits to the peaks in the evolution of the absolute value of the Fourier amplitude of the electric field. We find a very good agreement with theory, as seen in the lower panel of Figure 11.1 where the growth rates from the simulations are plotted along with the theoretical curve (obtained by solving Equation 11.10). As expected from linear theory, we find that high temperature plasmas show stronger Landau damping.

11.2 Numerical dispersion relations

As outlined in Hockney and Eastwood (1988) (p. 227-228) the finite grid modifies the dispersion relations. For the hybrid plasma model one finds³

$$1 + \frac{c_s^2}{v_t^2} \sum_{n=-\infty}^{\infty} \frac{(-i\hat{D})}{k_n} \left(\frac{\widehat{W}(k_n)}{\Delta x} \right)^2 W\left(\frac{\omega}{k_n v_t}\right) = 0, \quad (11.17)$$

while the electrostatic plasma model has

$$1 + \frac{\omega_p^2}{v_t^2} \sum_{n=-\infty}^{\infty} \left(\epsilon_0 \hat{G} \right) \frac{(-i\hat{D})}{k_n} \left(\frac{\widehat{W}(k_n)}{\Delta x} \right)^2 W\left(\frac{\omega}{k_n v_t}\right) = 0. \quad (11.18)$$

Here, the ‘‘aliased’’ wave number is defined by

$$k_n = k - n \frac{2\pi}{\Delta x}, \quad (11.19)$$

³We have retained the notation in both Ichimaru (1973) and Hockney and Eastwood (1988) which unfortunately leads to a clash. Ichimaru’s dispersion function, $W(z)$, should however not be confused with the Fourier transform of the assignment function, $\widehat{W}(k)$.

and one factor of $\widehat{W}(k_n)/\Delta x$ arises because the electric field is interpolated onto the position of the particles and the other factor arises due to the deposition of charge onto the grid. The Fourier transform of the assignment functions depends on the order, p , of the interpolation scheme as

$$\frac{\widehat{W}(k)}{\Delta x} = \left(\frac{\sin(k\Delta x/2)}{k\Delta x/2} \right)^p, \quad (11.20)$$

where $p = 2$ for CIC and $p = 3$ for TSC. In equations 11.17 and 11.18 the spectral responses of the centered finite difference discretization of the first and second derivatives are given by (Hockney and Eastwood, 1988)

$$-i\widehat{D} = \frac{\sin(k\Delta x)}{\Delta x}, \quad (11.21)$$

$$\epsilon_0\widehat{G} = \frac{(\Delta x/2)^2}{\sin^2(\Delta x/2)}. \quad (11.22)$$

The numerical dispersion relations, Equations 11.17 and 11.18, will in general need to be solved numerically. The infinite sum can however be evaluated exactly for a cold plasma. Taking the large argument expansion of the plasma dispersion function and evaluating the sum by using the identity (equation 7-66 in Hockney and Eastwood 1988)

$$\frac{(-1)^s}{s!} \frac{d^s}{dx^s} \cot x = \sum_{n=-\infty}^{\infty} \frac{1}{(x - \pi n)^{s+1}}, \quad (11.23)$$

we find for the momentum conserving scheme in a hybrid code

$$\omega^2 = c_s^2 \frac{\sin^2(k\Delta x)}{(\Delta x)^2}, \quad \text{CIC} \quad (11.24)$$

$$\omega^2 = c_s^2 \frac{[5 + \cos(k\Delta x)] \sin^2(k\Delta x)}{6(\Delta x)^2}. \quad \text{TSC} \quad (11.25)$$

We observe that aliasing introduces an incorrect dependence of the frequency on the wavenumber. We obtain the correct dispersion relation, i.e., $\omega^2 = k^2 c_s^2$, in the limit $\Delta x \rightarrow 0$. The corresponding results for an electrostatic plasma are given in equation 7-67 in Hockney and Eastwood (1988).

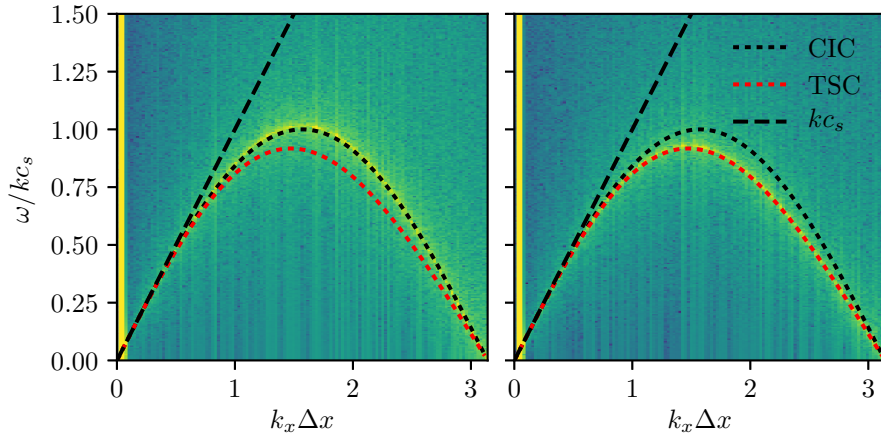


Figure 11.2: Aliasing of ion-acoustic waves in a cold plasma with CIC (left panel) and TSC (right panel) interpolation. We find agreement with the theoretical predictions given in Equations 11.24 and 11.25.

For testing purposes it is immensely useful to have the exact expressions for the aliased frequency given by Equations 11.24 and 11.25. The reason is that simulations should match very well at all wavelengths when comparing with exact expressions that include the errors due to the spatial discretization. Agreement with Equations 11.24 and 11.25 indicate that both interpolation, finite difference schemes and particle mover are working correctly⁴.

We test the theory for aliasing of ion-acoustic waves by exciting the fundamental mode in a cold plasma using a grid resolution of $n_x = 256$ and 256 particles per cell. The initialization of velocities and positions of particles is the same as used for Landau damping in the previous section but now with $v_t = 0$. In order to delay the onset of the resulting finite grid instability (to be discussed in the next section) we also change the amplitude of the perturbation to be very low, i.e., $A = 10^{-5}$. Even so, we have to limit the duration of the simulation to $tkc_s = 4$ in order to prevent the finite grid instability from affecting our results.

From the simulation we construct a discrete approximation to the function

⁴Here, correctly really means that the errors associated with the spatial discretization are as expected. This test would for instance be able to find a subtle error in the implementation of TSC interpolation which made it still work but at an effectively lower order.

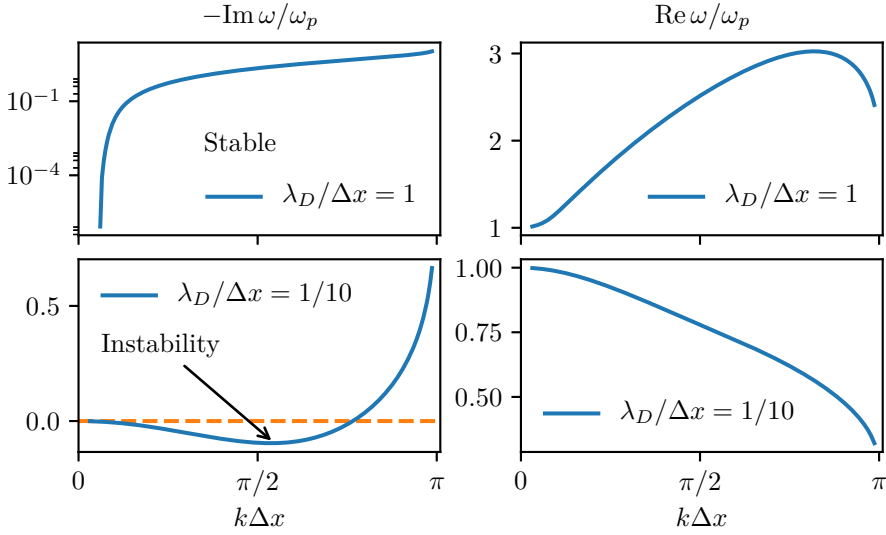


Figure 11.3: Warm plasma with $\lambda_D/\Delta x = 1$ which is numerically stable at all wavelengths (upper row) and warm plasma with $\lambda_D/\Delta x = 1/10$ which is numerically unstable (lower row).

$\rho(t, x)$. This function is then Fourier transformed in time and space by using FFTs to obtain $\hat{\rho}(\omega, k_x)$. The result is shown in Figure 11.2 where the left (right) panel shows a map of $\log(|\hat{\rho}|)$ for a simulation using CIC (TSC) interpolation. We observe in both cases that the power in the (k_x, ω) plane follows the theoretical curves given by Equation 11.24 and 11.25.

11.3 The finite grid instability

In the previous section we saw that a finite grid introduces an artificial wavenumber dependence on the frequencies of ion-acoustic waves and electrostatic modes. When the plasma is cold, the frequencies are real, and while these errors are not optimal, it is reassuring that the errors decrease as the spatial resolution is increased. When the plasma is warm, the frequency is no longer purely real and the imaginary part of the frequency is the Landau damping rate. Perhaps not surprisingly, aliasing also introduces errors into the imaginary part of the frequency. Langdon (1970) found that the aliasing errors can even change the sign of the imaginary

11. Landau damping, aliasing and the finite grid instability

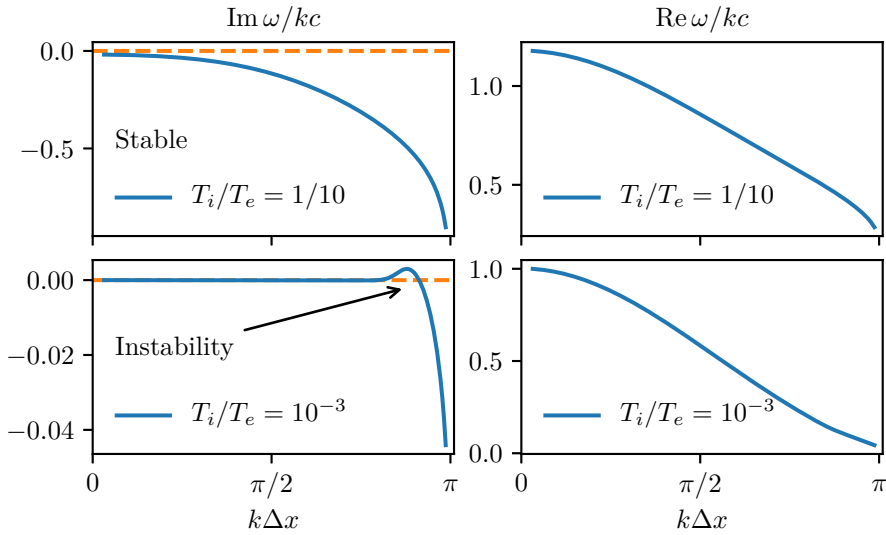


Figure 11.4: Warm Vlasov fluid with $T_i/T_e = 1/10$ which is numerically stable at all wavelengths (upper row) and very cold Vlasov fluid with $T_i/T_e = 10^{-3}$ which is numerically unstable at short wavelengths (lower row).

part. For a warm plasma, aliasing thus leads to Landau damping of the wrong sign, i.e., growth of a numerical instability. This is the finite grid instability.

We have solved Equation 11.18 in order to reproduce figures 7-2 and 7-3 in Hockney and Eastwood (1988), here shown in Figure 11.3. In this figure it is illustrated how numerical stability depends on the ratio of the Debye length, λ_D , to the length of a grid cell, Δx . Here the Debye length is given by $\lambda_D = v_t/\omega_p$. In the upper left panel of Figure 11.3 we see that marginally resolving the Debye length with $\lambda_D = \Delta x$ gives a stable simulation, i.e., the imaginary part is always negative and all modes will be damped. In the lower left panel of this figure we show how the simulation becomes numerically unstable if $\lambda_D < \Delta x$ (Langdon, 1970). In an electrostatic code one can in principle increase the numerical resolution in order to remove the instability for simulations of plasmas with low temperature⁵.

The solution to the numerical dispersion relation for a hybrid code, Equation 11.17, however only depends on the dimensionless parameter T_i/T_e . So while we

⁵Although it might not be computationally feasible to increase the resolution with a factor of 10 as in the example in Figure 11.3.

had the option of modifying the dimensionless parameter which governs the electrostatic case, in the Vlasov-fluid case the parameter is set solely by the physics of the simulation that we want to perform. In Figure 11.4 we show the solution to the numerical dispersion relation for $T_i/T_e = 1/10$ and $T_i/T_e = 10^{-3}$ for the momentum conserving scheme and TSC interpolation. We observe that the warm plasma is stable with damping at all wavelengths (with the $k\Delta x \rightarrow 0$ damping being due to physical Landau damping). The almost cold plasma is however numerically unstable as evident from the small peak with $\text{Im}(\omega) > 0$ in the lower left panel in Figure 11.4. The linear theory thus predicts an instability that grows close to the grid scale unless the ions are perfectly cold. A perfectly cold plasma is an idealization that we cannot hope to achieve in the code, as numerical heating will give the ions a temperature even though they are initialized with $T_i = 0$ (Rambo, 1997).

Chapter 12

Hybrid code experiments

We have presented the linear theory for Hall MHD and the Vlasov-fluid equations in Chapter 4-7 and the PIC method for solving the Vlasov-fluid equations in Chapters 8 and 9. In this chapter we use the former to test our implementation of the latter. We present 1D simulations of the whistler and ion-cyclotron waves, ion-cyclotron damping and instability, the parallel and the oblique firehose instability and the resonant ion beam instability. We also present a 2D simulation in which both the parallel and the oblique firehose instability can grow simultaneously.

For the sake of brevity, the examples presented are not exhaustive of the tests that are currently available in the code. Tests not presented in this thesis include 1D simulations of electron Landau damping, the electrostatic two-stream instability and the non-resonant ion beam instability as well as 2D simulations of ion-acoustic, electrostatic, whistler and magnetosonic waves with wavevectors inclined to the grid and single particle motion in constant fields (i.e., gyromotion and $\mathbf{E} \times \mathbf{B}$ -drift). The code also uses unit testing¹ of charge deposition, boundary conditions, MPI-communication and the finite difference scheme.

¹Unit testing is a popular software testing method whereby small units of the software are tested independently. Unit tests compliment the physics experiments presented in this chapter which simultaneously test all the features of the code. Contrary to these experiments, an error associated with a failed unit test is simpler to locate in the source code and often also easier to diagnose.

12.1 Whistler and ion-cyclotron waves

In this section we test the ability of our code to propagate whistler and ion-cyclotron waves and their low wavenumber counterpart, Alfvén waves. The dispersion relation for these circularly polarized waves is given by the Hall MHD dispersion relation when the ions are cold ($T_i = 0$). We derived this dispersion relation as well as the eigenfunctions for the cold whistler and ion-cyclotron waves in Chapter 4. We can use the analytic form of the eigenmodes and frequencies to excite specific wavemodes in the hybrid code. We perform a total of 14 such simulations in order to reproduce the dispersion relation numerically, see Figure 12.1. In this figure, results from simulations are shown with orange crosses and the theoretical dispersion relation of whistler and ion-cyclotron waves are shown with a blue solid line. The simulations are 1D with the magnetic field in the x -direction and have a numerical resolution of $n_x = 32$. The amplitude of the perturbation is $A = 5 \times 10^{-3}$ and the simulations are run for two wave periods. We use a quiet start and since the plasma is cold we only need to use a single particle per cell and CIC interpolation. The electron temperature is set to be $T_e = 0$ and the time step is calculated from the CFL condition on the grid scale, see Equation 4.17 in Chapter 4. In producing Figure 12.1 we have kept the resolution per wavelength fixed at 32 cells by varying the length of the box to be $L_x = 2\pi/k_x$ where k_x is the wavenumber under consideration. The numerical results presented in Figure 12.1 agree very well with the theory.

In order to quantify the numerical error in the simulations we can also calculate the RMS error with respect to the analytical solution. As our code is second order accurate in space (see Section 9.1) this error should decrease with grid resolution as n_x^{-2} . In order to test this, we perform a new set of simulations with $k_x v_a / \Omega = 1$ where the length of the simulation domain is fixed, $L_x \Omega / v_a = 2\pi$ and the grid resolution is varied as $n_x = 2^m$ with $m = 2, 3, \dots, 9$. Second order convergence is indeed observed, as evident in Figure 12.2 where we present the RMS error of the B_y component of the magnetic field as a function of the number of grid cells per wavelength.

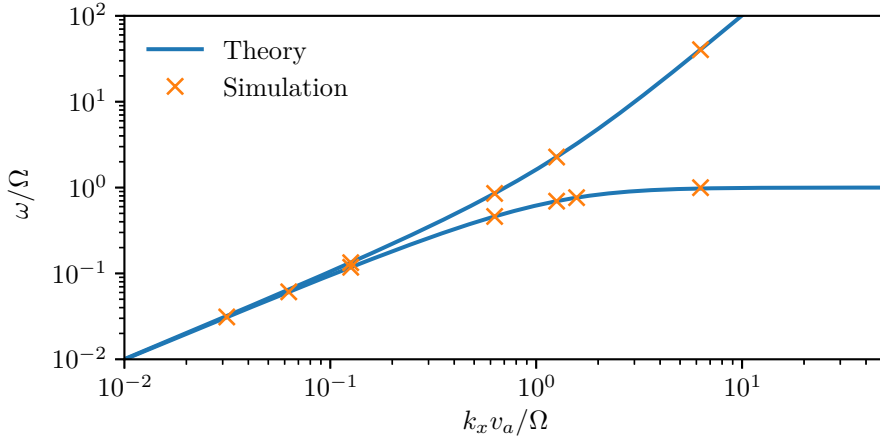


Figure 12.1: Dispersion relation for whistler and ion-cyclotron waves. The frequencies measured in simulations agree with the Hall MHD linear dispersion relation given by Equations 4.14 and 4.15.

12.2 Ion-cyclotron damping

From a theoretical point of view, we have seen that warm ions can lead to damping of waves, e.g. ion-cyclotron damping and Landau damping, which were introduced in Chapter 7 and 11, respectively. We have already studied Landau damping using the hybrid code in Chapter 11 and we now proceed with ion-cyclotron damping. We consider a plasma with equal parallel and perpendicular temperatures with $\beta = 5$ and $T_e = 0$. This physical setup was investigated in Figure 7.3 in Chapter 7 where it is evident that the maximal damping rate is $\gamma/\Omega = 0.41$ and occurs at $k_{\parallel}v_a/\Omega = 1.34$. Using this information, we perform a simulation where the length of the simulation domain L_x is set to be the wavelength of the most strongly damped mode. This simulation has $n_x = 32$ grid cells with 2^{18} particles per cell and is initialized using a quiet Maxwellian. The simulation uses CIC interpolation and the predictor-corrector method. Although the cold plasma eigenmode is not the correct eigenmode when the plasma is warm, we nevertheless use this eigenmode for initializing the simulation². We follow the evolution of

²It is in principle possible to obtain a better initial condition by utilizing the dispersion relations described in Chapter 7 but we have not yet pursued this.

12. Hybrid code experiments

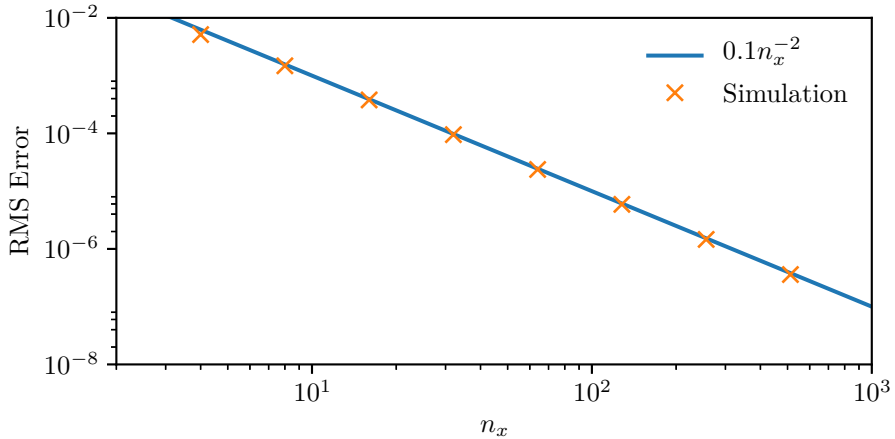


Figure 12.2: Second order convergence of whistler waves with $k_x v_a / \Omega = 1$.

the absolute value of the Fourier amplitude of the excited mode, see Figure 12.3. While the trend in the simulation data (solid orange line) follows the theoretical prediction (solid blue line) the match is not perfect. We attribute this discrepancy to the fact that we have not excited the eigenmode exactly.

12.3 Ion-cyclotron instability

For the ion cyclotron instability we consider $\beta_{\parallel} = 1$ and $\beta_{\perp} = 4$ in which case the wave can draw energy from the particles. We have previously calculated the maximum growth rate and the wave number at which it occurs, see Figure 7.2 in Chapter 7. We use this information to set up a simulation with $n_x = 32$, $L_x \Omega / v_a = 8.72$, and 2^{16} particles per cell. We use TSC interpolation and evolve the simulation until $\Omega t = 25$ using the Horowitz method. We plot the evolution of the Fourier amplitudes of the transverse magnetic field components in Figure 12.4. The amplitude starts out at a level of $\sim 10^{-3}$ corresponding to the noise level set by using a finite number of particles and not using a quiet Maxwellian. The high noise-level in this simulation highlights how well the quiet Maxwellian works for the parallel firehose instability to be discussed in the next section. The transverse components of the magnetic field (δB_y and δB_z) are seen to be out of phase as expected for circular polarization (see Chapter 4).

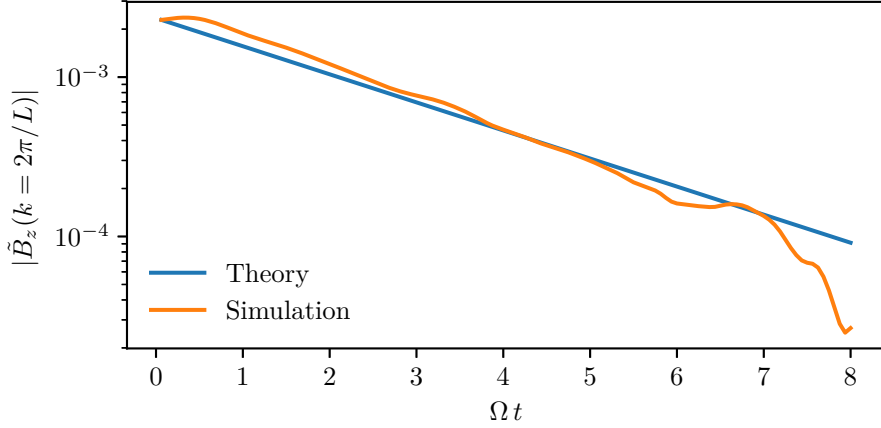


Figure 12.3: Ion-cyclotron damping for a plasma with $\beta = 5$.

12.4 Parallel firehose instability

The firehose instability is a microscale instability which feeds off anisotropy in velocity space, i.e., when the parallel temperature is greater than the perpendicular temperature. We consider the situation studied in Figure 7.1 in Chapter 7, i.e., $\beta_{\parallel} = 4$, $\beta_{\perp} = 1$, and $T_e = 0$. We initialize a uniform plasma with an anisotropic velocity distribution by using a quiet Maxwellian (introduced in Chapter 10). We seed the instability with Gaussian noise in the magnetic field components of amplitude $\delta B/B = 10^{-14}$. In order to have a clean growth of a single unstable mode we set the length of the box to be $L_x = 2\pi/k_{\max}$, where $k_{\max}v_a/\Omega = 0.37$ corresponds to the maximum growth rate of $\sigma_{\max}/\Omega = 0.189$. We use a modest grid resolution of $n_x = 32$ but employ 2^{14} particles per cell. The initial magnetic field is along the x -direction and we track the evolution of the Fourier amplitudes of δB_y and δB_z . This is shown in Figure 12.5 along with an exponential fit to the evolution of the amplitude of $\delta B = \sqrt{\delta B_x^2 + \delta B_y^2 + \delta B_z^2}$. The perpendicular magnetic field components are exponentially growing and oscillating with the y -component lagging behind the z -component with a phase shift of $\pi/2$. The quiet Maxwellian allows us to follow the exponential growth of the parallel firehose instability over 12 orders of magnitude and the error in the growth rate is less than 1%. In comparison, we were only able to follow the evolution of the ion-cyclotron

12. Hybrid code experiments

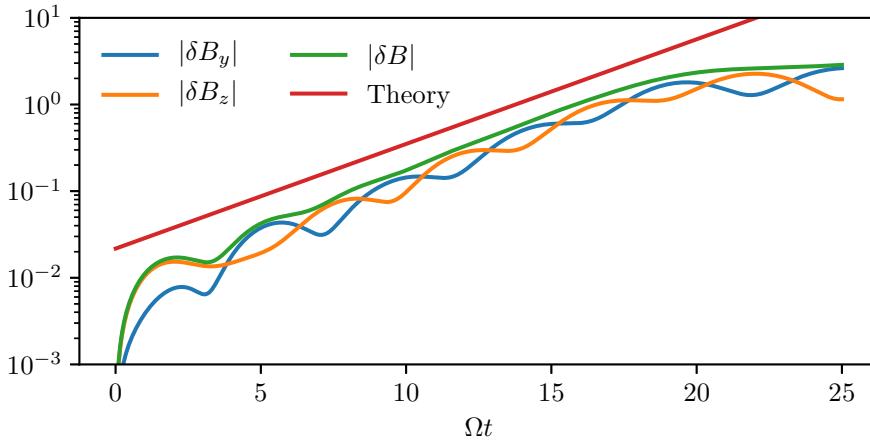


Figure 12.4: Evolution of the transverse magnetic field for the ion-cyclotron instability.

instability over 2 orders of magnitude, despite using four times as many particles per cell.

12.5 Oblique firehose instability

The oblique firehose instability was discussed in Chapter 7, see especially Figure 7.4. This instability occurs when the wave vector, \mathbf{k} , is inclined with respect to the magnetic field, \mathbf{B} . In this section we consider a plasma with $\beta_{\parallel} = 4$ and $\beta_{\perp} = 1$ which is unstable to both the whistler and the Alfvén firehose instability (depending on the inclination angle, θ). Note that these are the parameters used in Section 12.4 which however differ from the parameters used to produce Figure 7.4 in Chapter 7.

We can use the hybrid code to perform 1D simulations of the oblique firehose instability where the background magnetic field is in the xy -plane, oriented with an inclination $-\theta$ with respect to the x -axis (Hellinger and Matsumoto, 2000; Kunz, Stone, and Bai, 2014). For a 1D simulation along x , the wave vector of the mode under study will then be forced to lie along the x -axis.

We consider a series of simulations, varying θ from parallel propagation to highly oblique propagation. The maximum growth rate as a function of θ is found

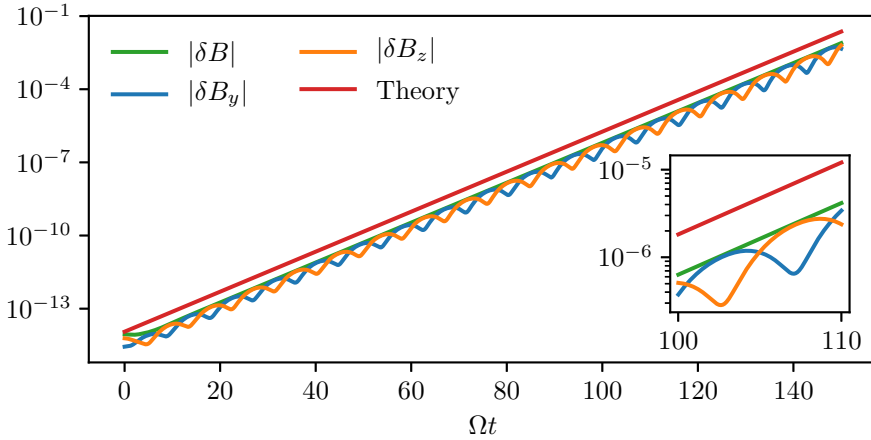


Figure 12.5: Evolution of the transverse magnetic field for the parallel firehose instability with $\beta_{\parallel} = 4$ and $\beta_{\perp} = 1$.

by producing a map of growth rates in the (k, θ) -plane and finding the maximum values along the k -direction. The resulting theoretical growth rates are presented in Figure 12.6 and the results from simulations are shown with crosses. These simulations were initialized by setting the length of the simulation domain to be equal to the maximally unstable wavelength. The simulations did not use a quiet Maxwellian and the resulting growth is less accurate than for the parallel firehose instability presented in Section 12.4. In order to produce Figure 12.6 we have thus had to adjust the fitting range for the exponential evolution in the simulations.

12.6 Ion Bernstein modes

Ion Bernstein modes have their wavevector perpendicular to the magnetic field. These modes have purely real frequencies which at high $k_{\perp} v_a / \Omega$ are very close to resonance with multiples of the ion cyclotron frequency, i.e., the frequencies are given by $\omega \pm n\Omega$ where $n \in \mathbb{N}$. We perform a simulation of these modes with a setup which is very similar to the one presented in the code paper for *CHIEF* (Muñoz et al., 2016). We take the magnetic field to be along the z -direction and initialize a 1D simulation of length $L_x \Omega / v_a = 63.6$ with a resolution of $n_x = 512$. The time step is set to be $\Omega \Delta t = 0.0318$ and the ions have an isotropic velocity

12. Hybrid code experiments

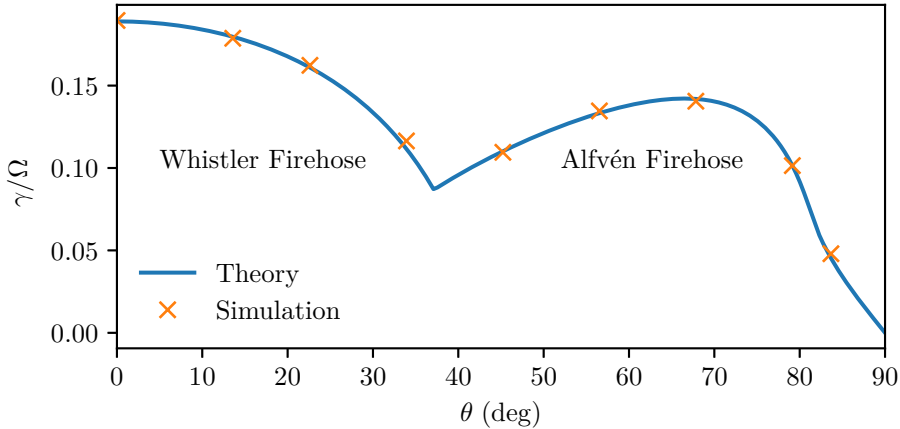


Figure 12.6: Growth rates for the whistler and Alfvén firehose instabilities as a function of the inclination, θ , between \mathbf{k} and \mathbf{B} for $\beta_{\parallel} = 4$ and $\beta_{\perp} = 1$.

distribution with $\beta = 1/10$. The electron temperature is set to be the same as the temperature of the ions, i.e., $T_e/T_i = 1$. The number of particles per cell is 256 using TSC interpolation. As in Muñoz et al. (2016) we let the ion Bernstein modes grow from the thermal noise and evolve the simulation until $\Omega t = 600$.

The data analysis is very similar to the one used to study aliasing of ion-acoustic waves in Chapter 11. We construct a 2D array which is a discrete representation of the function $E_x(x, t)$. We then perform a 2D discrete Fourier transform (DFT) using Numpy’s fast Fourier transform (FFT) in order to find $\hat{E}_x(k_x, \omega)$. We present a map of $\log |\hat{E}_x(k_x, \omega)|^2$ in Figure 12.7 along with theoretical predictions for the frequencies.

These theoretical predictions were found using the general Vlasov-fluid dispersion relation solver presented in Chapter 7. We initialize our dispersion solver with an initial guess of $n\Omega$ with $n = 1$ to 8 at $k_{\perp}v_a/\Omega = 20$ and then iterate towards lower k_{\perp} . For each mode there is some minimum value of k_{\perp} at which the solver fails to converge. This cutoff occurs at higher k_{\perp} for the higher frequency modes resulting in a region of (k_{\perp}, ω) -space in which modes are not present. The boundary between this region and the region with ion Bernstein modes is roughly delineated by the fast magnetosonic mode with dispersion relation $\omega = k_{\perp} \sqrt{v_a^2 + c_s^2}$. The power spectrum obtained from the simulation shows

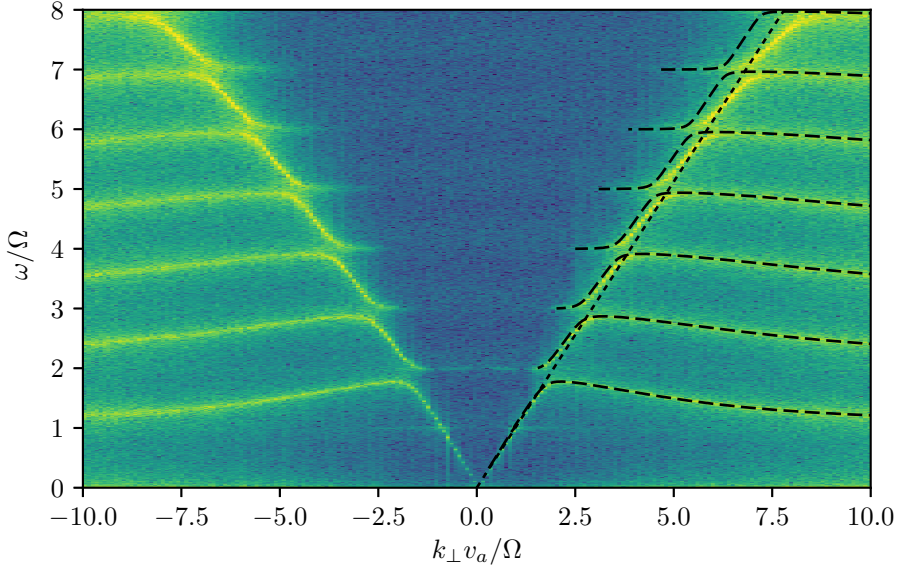


Figure 12.7: Power spectrum of \hat{E}_x . Theoretical curves for ion Bernstein modes shown with long-dashed solid lines and for the magnetosonic wave with a short-dashed solid line for the $k_\perp > 0$ modes. The power spectrum is symmetric around $k_\perp = 0$.

the same behavior and agrees well with the theory.

Some discrepancy between theory and simulation is however seen at high frequency in Figure 12.7. Similar discrepancies were seen at even lower frequencies in preliminary simulations with lower spatial resolution ($n_x = 128$ and $n_x = 256$). This indicates that the discrepancy observed in Figure 12.7 decreases with grid resolution. This could be due to spatial aliasing (as for the ion-acoustic waves) not included in the linear theory for the ion Bernstein modes. Another potential issue could be the resolution in time. The highest frequency mode ($\omega = 8\Omega$) has $1/\omega\Delta t \approx 4$, i.e., the frequency is only resolved with four time steps. A future improvement to this test could thus probably be obtained by decreasing the time step and/or increasing the grid resolution.

The overall trend of the dispersion curves of the ion Bernstein modes in Figure 12.7 differs from the one observed in Muñoz et al. (2016). In figure 5 in Muñoz et al. (2016) the ion Bernstein modes have frequencies $n\Omega$ at high k_\perp which increase

12. Hybrid code experiments

to $(n + 1)\Omega$ at low k_{\perp} . This is in contrast to our simulations where ion Bernstein modes have frequencies $n\Omega$ at high k_{\perp} which increase at intermediate k_{\perp} before returning to a value of $n\Omega$ at low k_{\perp} . The underlying reason for this difference is the difference in the way electron physics is included in the simulations. While our code assumes massless electrons the *CHIEF* code includes electron inertia. This difference is also present in the theoretical predictions. In Muñoz et al. (2016) the theoretical dispersion curves are calculated by solving a longitudinal dispersion relation where electron physics is included by taking the cold electron limit (their equation 28). In contrast, our theoretical curves are found by using the Vlasov-fluid dispersion relation solver introduced in Chapter 7 and setting $k_{\parallel}v_a/\Omega$ to have a very small value (10^{-8}). This solver assumes massless electrons but, unlike the dispersion relation in Muñoz et al. (2016), the results depend on the electron temperature, T_e . Our results agree qualitatively with the theoretical dispersion of ion Bernstein modes presented in figure 6 in Told et al. (2016), in which the hybrid dispersion relation is also solved.

12.7 Ion beam instability

In this section we study the ion beam instability which arises when a tenuous beam of ions traverses a stationary background plasma with a velocity that exceeds the Alfvén velocity, v_a . We consider a beam of ions with density n_b propagating through a stationary plasma with density n_0 . The total density is thus $n_b + n_0$. The plasma has a magnetic field in the direction of beam propagation. We can transform this system into a coordinate frame in which the total ion current is zero, that is

$$n_b v_b + n_0 v_0 = 0, \tag{12.1}$$

where v_b is the beam velocity and v_0 is the velocity of the stationary plasma in this frame. Plasma species with a drifting velocity were not included in the derivation of the conductivity tensor in Chapter 6. As a result the plasma dispersion solver presented in Chapter 7 is not capable of finding the frequencies in this case and we instead refer to the literature. Assuming cold ions, the dispersion relation is

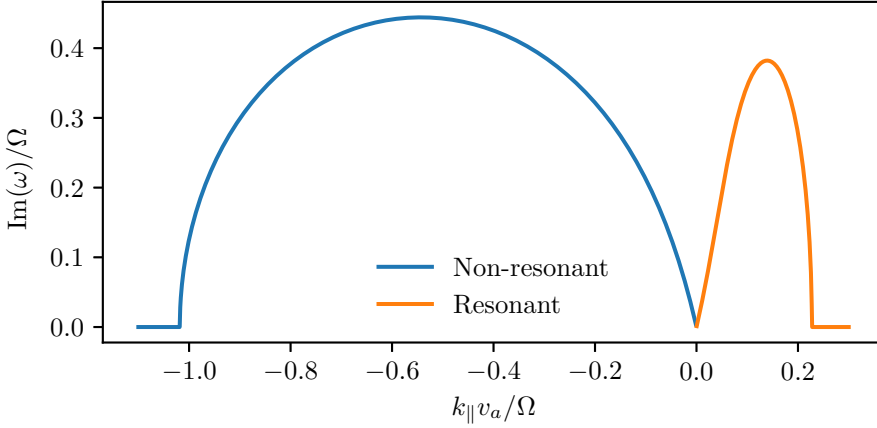


Figure 12.8: Resonant ($k > 0$) and non-resonant ($k < 0$) ion beam instability.

(Scharer and Trivelpiece, 1967; Winske and Leroy, 1984)

$$\frac{k_{\parallel}^2 v_a^2}{\Omega^2} + \alpha \frac{\omega - k_{\parallel} v_b}{\omega - k_{\parallel} v_b + \Omega} + (1 - \alpha) \frac{\omega - k_{\parallel} v_0}{\omega - k_{\parallel} v_0 + \Omega} - \frac{\omega}{\Omega} = 0, \quad (12.2)$$

where

$$\alpha = \frac{n_b}{n_0 + n_b}, \quad (12.3)$$

is the ratio of the beam and electron number densities.

A numerical solution of Equation 12.2 is shown for $v_b/v_a = 10$, $\alpha = 1/10$ and $v_0 = -n_b v_b/n_0$ in Figure 12.8. In this figure the resonant instability with $k_{\parallel} > 0$ arises due to a resonance of the beam velocity with the ion-cyclotron frequency such that the maximum growth rate occurs when (Winske and Leroy, 1984)

$$\text{Re}(\omega) - k_{\parallel} v_b + \Omega \approx 0. \quad (12.4)$$

The non-resonant instability with $k_{\parallel} < 0$ is due to the bulk motion of the beam through the plasma. With the parameters used here, the growth rate of the non-resonant instability is seen to slightly dominate the growth rate of the resonant instability. The growth rate of the non-resonant instability however decreases

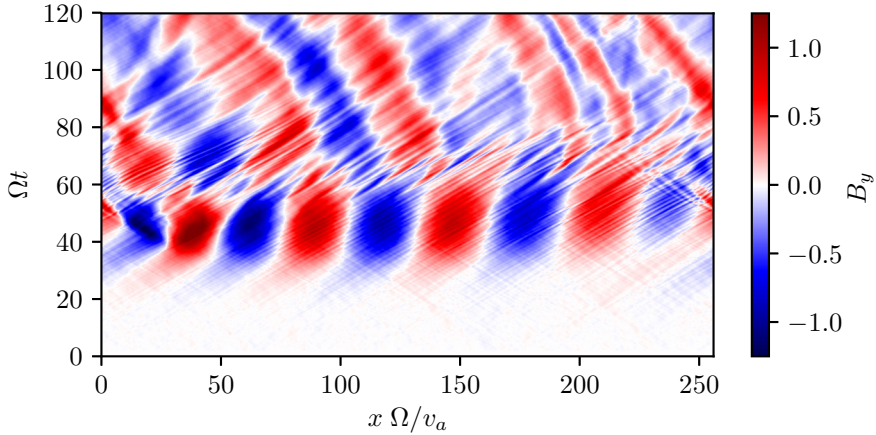


Figure 12.9: Evolution of B_y as a function of time for the resonant ion beam instability.

rapidly as the α parameter is decreased such that the resonant instability is dominant for $\alpha \lesssim 0.08$ for this beam velocity ($v_b = 10$). We have performed simulations showing that we can recover the maximal growth rate for the resonant and non-resonant instabilities by setting up simulations with L_x equal to the wavelength of the dominant modes. For the sake of brevity, we do not present a discussion of these simulations of the linear regime.

We instead proceed to set up a simulation of the nonlinear evolution of the resonant ion beam instability. The parameters are almost identical to the ones used in Muñoz et al. (2016). We consider a very tenuous beam with $\alpha = 0.02$ traversing at $v_b/v_a = 10$ through a background plasma with $\beta = 1$. We initialize the two different populations of ions each with 1024 particles per cell but with their particle weights adjusted such that one particle species has density n_b and the other has density n_0 . Adjusting the particle weights makes it possible to follow the evolution of a very tenuous beam with good statistics on the distribution in phase-space³. We use TSC interpolation with the predictor-corrector method and set the electron temperature to be such that $T_e/T_i = 1/10$. We furthermore align

³The way this works in our code is that two particle arrays are created with the particle weight stored as an attribute to the array. That is, we do not have the option of modifying the particle weight per particle, a method that is used in, for instance, the PhotonPlasma code (Haugbølle, Frederiksen, and Nordlund, 2013).

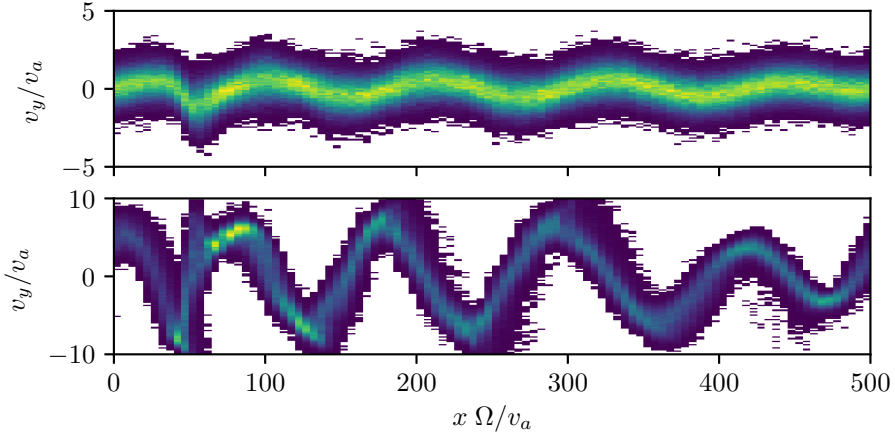


Figure 12.10: The particle phase-space at $\Omega t = 40$. The core (beam) ions are shown in the upper (lower) panel. Notice the difference in axis limits.

the magnetic field with the x -direction on a $n_x = 512$ grid with $L_x \Omega / v_a = 256$ and evolve the simulation until $\Omega t = 120$.

The evolution of B_y is shown in Figure 12.9 as a function of time. In the linear stage of the instability waves are propagating to the right while they propagate to the left in the nonlinear stage. Comparing Figure 12.9 with figure 8.a in Muñoz et al. (2016) we see that their figure has much smoother features than ours. This might simply be due to their use of $n_x = 1024$, i.e., twice the numerical resolution, but it is also possible that the smoothness observed in their figure 8 is due to binomial filtering of the sources which they include as an option in their code.

We also consider the evolution of the phase-space distribution of the core ions and the beam ions. This is shown at $\Omega t = 40$ in Figure 12.10 with the core (beam) ions in the upper (lower) panel. We observe that the beam ions have acquired a significant velocity in the perpendicular direction (v_y) with velocities that approach the initial beam velocity. The perturbation is sinusoidal (as seen for the B_y component as well). In contrast, the core ions are only slightly perturbed.

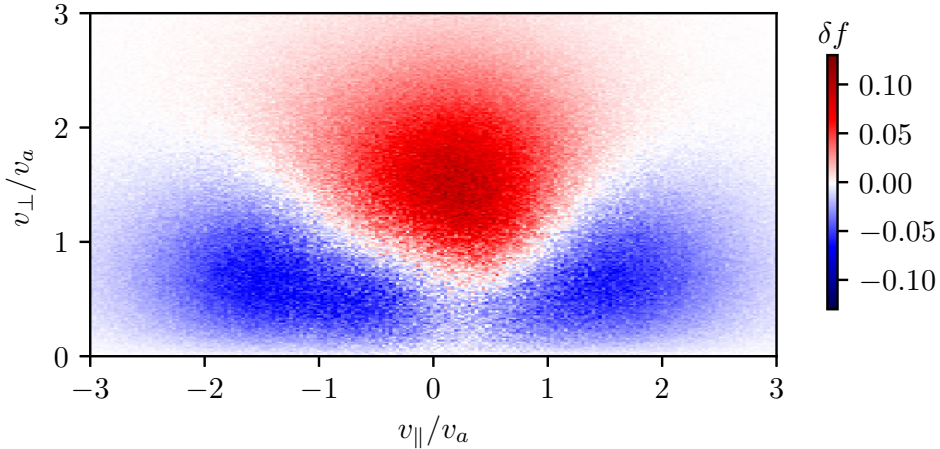


Figure 12.11: The change in velocity space distribution between the initial ($\Omega t = 0$) and the one at $\Omega t = 400$, produced by subtracting the normalized histograms.

12.8 Firehose instability in 2D

In this section we present a 2D simulation of the firehose instability. The setup is the same as in Hellinger and Matsumoto (2001) and Muñoz et al. (2016), i.e., $n_x = L_x \Omega / v_a = 256$, $n_y = L_y \Omega / v_a = 128$, with 256 particles per cell⁴. We use TSC interpolation and the Horowitz method. The initial ion temperatures are $\beta_{||} = 2.8$ and $\beta_{\perp} = 0.4\beta_{||}$, these parameters were also used in the paper on the oblique firehose instability by Hellinger and Matsumoto (2000) and for producing Figure 7.4 in Chapter 7. We use $\Omega \Delta t = 8 \times 10^{-3}$ for the time step and evolve the system until $\Omega t = 400$.

The firehose instability feeds off the energy stored in the velocity space anisotropy. In a simulation where the instability is initialized with a velocity space anisotropy, like the one performed here, the velocity space anisotropy will thus decrease as a function of time due to the action of the firehose instability. The Alfvén firehose instability has been shown to be even more effective than the whistler firehose instability at decreasing the pressure anisotropy (Hellinger and Matsumoto, 2000;

⁴A more detailed analysis of this physical system can be found in Hellinger and Matsumoto (2001) and Muñoz et al. (2016).

Hellinger and Matsumoto, 2001; Muñoz et al., 2016). Both kinds of firehose instabilities can be present simultaneously in our 2D simulation. The resulting change in the velocity space distribution can be seen by subtracting the velocity space distribution at $\Omega t = 0$ from the velocity space distribution at $\Omega t = 400$. Defining the parallel and perpendicular velocities with respect to the initial magnetic field, $v_{\parallel} = v_x$ and $v_{\perp}^2 = v_y^2 + v_z^2$, we show the resulting change in the velocity space distribution in Figure 12.11. This figure clearly shows that the firehose instability changes the velocity space distribution by increasing the perpendicular velocity component (shown in red) at the cost of a decrease in parallel velocities (shown in blue).

We can quantify this change by calculating the pressure anisotropy of all the particles (neglecting any eventual spatial dependency). We use as an estimate of the parallel and perpendicular temperatures the standard deviations of the corresponding particle velocities. We find $T_{\perp}/T_{\parallel} = 0.41$ at $\Omega t = 0$ and $T_{\perp}/T_{\parallel} = 0.7$ at $\Omega t = 400$, showing that the temperature anisotropy has been significantly reduced⁵.

⁵The fact that we do not get $T_{\perp}/T_{\parallel} = 0.40$ at $\Omega t = 0$ is probably due to the rather low number of particles, $\sim 8 \times 10^6$, in the simulation.

Chapter 13

Conclusion and future prospects

In this PhD thesis we have studied weakly collisional and collisionless astrophysical plasmas by using two different frameworks, i.e., Braginskii MHD and Vlasov-fluid theory. We used Braginskii MHD in Chapter 3 and Papers I-III in order to investigate the effect of composition gradients on the stability properties of the ICM. Using the results of Peng and Nagai (2009), we explicitly showed in Paper I that their model for the radial temperature and composition profiles can be unstable at all radii. In the inner regions of the cluster model, the instability under consideration is the heat- and particle-flux-driven buoyancy instability (HPBI) while the instability in the outer regions is the magneto-thermo-compositional instability (MTCI). These instabilities, originally found and analyzed by Pessah and Chakraborty (2013), are generalizations of the heat-flux-driven buoyancy instability (HBI) and the magneto-thermal instability (MTI) (Balbus, 2000, 2001; Quataert, 2008) to a setting with both thermal and compositional gradients.

In order to study the instabilities numerically, and thereby be able to investigate their nonlinear evolution and saturation, we modified the MHD code Athena (Stone et al., 2008). This modification was presented in Paper II where we thoroughly tested the changes to the code and performed the first idealized simulations of the MTCI and the HPBI. These simulations studied constant temperature atmospheres with a composition that increases with height, a situation that is stable according to both the Schwarzschild (Schwarzschild, 1958) and Ledoux criteria (Ledoux, 1947) but is unstable according to the stability criteria put forward in

13. Conclusion and future prospects

Pessah and Chakraborty (2013). This investigation showed that both the MTCI and the HPBI act to mix the composition and reorient the magnetic field to be inclined on average by about 45 deg with respect to gravity.

In Paper III, we lifted the assumption of locality by extending the vertical domain of the simulations to be several scale heights. We also relaxed the assumption of a constant temperature background atmosphere. This required extending the capabilities of Athena to allow for non-constant transport coefficients for the anisotropic heat conductivity and viscosity (χ_{\parallel} and ν_{\parallel}). In order to compare with linear theory in this quasi-global setting, we also extended previous analytical treatments by Pessah and Chakraborty (2013) and Paper I. The simulations of the HBPI showed that the instability is able to drive mixing of composition on time scales that are shorter than the time scale upon which composition gradients form in sedimentation models. If this turns out to be a general consequence, this would seem to indicate that helium sedimentation is not an issue for X-ray observations. This conclusion may however not be too robust since the growth rate of the HPBI depends on the initial composition gradient. A final conclusion can thus only be reached by considering a model which can adequately describe the effect of helium sedimentation while simultaneously taking the weakly collisional stability properties of the plasma into account. The development of such a theory is still work in progress.

Besides the neglect of helium sedimentation, another serious defect is the treatment of microscale physics. In particular, Braginskii MHD is known to be inadequate at modeling microscale instabilities (Schekochihin et al., 2005) and we use an ad-hoc model for limiting the pressure anisotropy when including Braginskii viscosity. While helium mixing was found in all simulations, regardless of whether Braginskii viscosity was included or not, this is still a shortcoming of the current approach, and a proper treatment of the microphysics might lead to qualitatively different results.

In a collisionless plasma, the diffusive transport of heat and momentum is mediated via electromagnetic forces. The nonlinear evolution and saturation of microscale instabilities is consequently believed to play a role in setting the transport properties of collisionless plasmas. Computer simulations using PIC simulations are a useful tool for calculating the effective collisionality of collisionless

plasmas subject to microscale instabilities. Some of these studies have shown that the effective heat conductivity can be reduced by the ion mirror instability and the electron whistler instability (Komarov et al., 2016; Riquelme, Quataert, and Verscharen, 2016). This effect is caused by pitch-angle scattering and electron trapping in regions of low magnetic field. The suppression of heat conductivity could potentially influence the evolution and saturation of the MTI and the HBI (and their generalizations presented in Chapter 3) which have growth rates that depend on the magnitude of the anisotropic heat conductivity, χ_{\parallel} . While PIC simulations can be used to study small scale instabilities in the ICM they are prohibitively expensive for it to be feasible to use them to study the large scale dynamics. We are instead currently investigating the consequences of reduced heat conductivity by performing Braginskii MHD simulations of the MTI using a subgrid model for the heat conductivity (Berlok, Pessah, and Quataert, 2017, in preparation).

We have presented a new Vlasov-fluid code in Chapters 8-12. This 2D-3V code is written in Python and is MPI enabled along one of the spatial dimensions. Python was chosen for its usability and, as discussed in Chapter 8, several other projects have already successfully demonstrated that Python is a viable option for HPC applications. The Vlasov-fluid code presented in Chapters 8-12 currently contains several options for interpolation (CIC and TSC, see Chapter 8) and several methods for evolving the equations in time (the predictor-corrector and the Horowitz method, see Chapter 9). The code has been tested and is able to convincingly reproduce results from linear theory (see Chapter 12). Future modifications to the code could include *i)* extending the code to allow for all three spatial dimensions, *ii)* implementing the expanding/compressing box used by, e.g., Matteini et al. (2006, 2012), Hellinger et al. (2015), and Sironi and Narayan (2015), and *iii)* implementing the shearing box in order to study the collisionless magneto-rotational instability (MRI) as in Kunz, Stone, and Bai (2014) and Kunz, Stone, and Quataert (2016) and the shear-driven firehose and mirror instabilities as in Kunz, Schekochihin, and Stone (2014).

The general dispersion relation solver presented in Chapter 7 could also be improved and made publicly available in the future. Firstly, an easy-to-use Python dispersion solver which includes many of the textbook examples of plasma waves and instabilities would have merit for teaching purposes. Secondly, interesting re-

13. Conclusion and future prospects

search avenues could be *i)* the inclusion of finite electron inertia and resistivity in the Vlasov-fluid dispersion relation solver, *ii)* a generalization of the expression for the conductivity tensor to allow for drifting species (Equation 6.27 in Chapter 6), *iii)* the ability of the solver to return the eigenmodes as well as the eigenvalue for a given solution and *iv)* the possibility of using the Hall dispersion relation solver presented in Chapter 4 to generate initial guesses for the Vlasov-fluid dispersion relation solver. These, very feasible, ideas for modifications would make the dispersion relation solver a powerful tool for comparing with Vlasov-fluid simulations. As it stands, the dispersion relation solver presented in Chapter 7 already contains a feature not included in the *HYDROS* dispersion relation solver (Told et al., 2016), i.e., it has the ability to include several ion species in the calculation. While this feature of the solver has not yet been properly tested, and is consequently not presented in Chapter 7, it could prove very useful for investigating the role of helium in the ICM. The motivation for such an investigation is that studies of the solar wind have shown that the helium component can be important (Hellinger and Trávníček, 2013; Verscharen, Bourouaine, and Chandran, 2013; Verscharen et al., 2013; Yoon et al., 2015). An interesting prospect would therefore be to use the solver to calculate the properties of an ICM with different helium compositions in order to understand how helium sedimentation could change the microphysics of the ICM. Subsequent simulations of a hydrogen-helium plasma could then be performed by employing the Vlasov-fluid code that we have developed.

Other interesting avenues that the Vlasov-fluid code could be used for in the future include studies of collisionless turbulence (e.g. Franci et al. 2015) and collisionless shocks and cosmic rays (e.g. Gargaté et al. 2010 and Caprioli and Spitkovsky 2013). There is thus no shortage of interesting problems that can be targeted with a Vlasov-fluid code. As the major hurdle of development is done, the code now shows promise for deepening our knowledge of collisionless astrophysical plasmas.

Bibliography

- Landau, L. D. (1946). "On the vibrations of the electronic plasma." In: *J. Phys.(USSR)* 10. [Zh. Eksp. Teor. Fiz.16,574(1946)], pp. 25–34.
- Ledoux, P. (1947). "Stellar Models with Convection and with Discontinuity of the Mean Molecular Weight." In: *The Astrophysical Journal* 105, p. 305.
- Biermann, Ludwig (1951). "Kometenschweife und solare Korpuskularstrahlung." In: *Zeitschrift fur Astrophysik* 29, p. 274.
- Chew, G. F., M. L. Goldberger, and F. E. Low (1956). "The Boltzmann Equation and the One-Fluid Hydromagnetic Equations in the Absence of Particle Collisions." In: *Royal Society of London Proceedings Series A* 236, pp. 112–118.
- Rosenbluth, M (1956). *Stability of the pinch*. Tech. rep. Los Alamos Scientific Lab., N. Mex.
- Biermann, L (1957). "Solar corpuscular radiation and the interplanetary gas." In: *The Observatory* 77, pp. 109–110.
- Chandrasekhar, S., A. N. Kaufman, and K. M. Watson (1958). "The Stability of the Pinch." In: *Proceedings of the Royal Society of London Series A* 245, pp. 435–455.
- Parker, E. N. (1958). "Dynamical Instability in an Anisotropic Ionized Gas of Low Density." In: *Physical Review* 109, pp. 1874–1876.
- Schwarzschild, M. (1958). *Structure and Evolution of the Stars*.
- Vedenov, AA and RZ Sagdeev (1958). "Some properties of the plasma with anisotropic distribution of the velocities of ions in the magnetic field." In: *Sov Phys Dokl.* Vol. 3, p. 278.
- Velikhov, EP (1959). "Stability of an ideally conducting liquid flowing between cylinders rotating in a magnetic field." In: *Sov. Phys. JETP* 36.9, pp. 995–998.

Bibliography

- Chandrasekhar, S (1960). "The Stability Of Non-dissipative Couette Flow In Hydromagnetics." In: *Proc. Natl. Acad. Sci.* 46.2, pp. 253–257. DOI: 10 . 1073 / pnas . 46 . 2 . 253.
- Fried, B. D. and S. D. Conte (1961). *The Plasma Dispersion Function*.
- Spitzer, L. (1962). *Physics of Fully Ionized Gases*.
- Braginskii, S.I (1965). "Transport processes in plasma." In: *Review of Plasma Physics*.
- Barnes, A. (1966). "Collisionless Damping of Hydromagnetic Waves." In: *Physics of Fluids* 9, pp. 1483–1495.
- Kennel, C. F. and H. E. Petschek (1966). "Limit on stably trapped particle fluxes." In: *Journal of Geophysical Research* 71.1, pp. 1–28.
- Yee, K. S. (1966). "Numerical solution of initial boundary value problems involving maxwell's equations in isotropic media." In: *IEEE Trans. Antennas Propag.* 14.3, pp. 302–307.
- Courant, R., K. Friedrichs, and H. Lewy (1967). "On the Partial Difference Equations of Mathematical Physics." In: *IBM Journal of Research and Development* 11, pp. 215–234.
- Scharer, J. E. and A. W. Trivelpiece (1967). "Cyclotron Wave Instabilities in a Plasma." In: *Physics of Fluids* 10, pp. 591–595.
- Davidson, Ronald C and Heinrich J Völk (1968). "Macroscopic quasilinear theory of the garden-hose instability." In: *The Physics of Fluids* 11.10, pp. 2259–2264.
- Hasegawa, A. (1969). "Drift mirror instability of the magnetosphere." In: *Physics of Fluids* 12, pp. 2642–2650.
- Boris, J. P. (1970). In: *Proceeding of Fourth Conference on Numerical Simulations of Plasmas*.
- Langdon, A. B. (1970). "Effects of the Spatial Grid in Simulation Plasmas." In: *Journal of Computational Physics* 6, pp. 247–267.
- Freidberg, J. P. (1972). "Vlasov-Fluid Model for Studying Gross Stability of High- β Plasmas." In: *Physics of Fluids* 15.6, p. 1102.
- Okuda, Hideo (1972). "Nonphysical noises and instabilities in plasma simulation due to a spatial grid." In: *Journal of Computational Physics* 10.3, pp. 475 –486.
- Ichimaru, S. (1973). *Basic principles of plasma physics: a statistical approach*. Benjamin/Cummings Publishing Company.

- Davidson, R. C. and J. M. Ogden (1975). "Electromagnetic ion cyclotron instability driven by ion energy anisotropy in high-beta plasmas." In: *Physics of Fluids* 18, pp. 1045–1050.
- Fabian, A. C. and J. E. Pringle (1977). "On the spatial distribution of heavy elements in X-ray emitting clusters of galaxies." In: *Monthly Notices of the Royal Astronomical Society* 181, 5P–7P.
- Byers, J. A., B. I. Cohen, W. C. Condit, and J. D. Hanson (1978). "Hybrid simulations of quasineutral phenomena in magnetized plasma." In: *J. Comput. Phys.* 27.3, pp. 363–396.
- Hall, A. N. (1979). "Finite ion Larmor radius modifications to the firehose and mirror instabilities." In: *Journal of Plasma Physics* 21.3, pp. 431–443.
- Harned, D. S. (1982). "Quasineutral hybrid simulation of macroscopic plasma phenomena." In: *J. Comput. Phys.* 47.3, pp. 452–462.
- Roennmark, K. (1982). *Waves in homogeneous, anisotropic multicomponent plasmas (WHAMP)*. Tech. rep.
- Gilfanov, M. R. and R. A. Syunyaev (1984). "Intracluster Gravitational Separation of Deuterium and Helium in Rich Galaxy Clusters." In: *Soviet Astronomy Letters* 10, pp. 137–140.
- Winske, D. and M. M. Leroy (1984). "Sentman." In: *Journal of Geophysical Research* 89, pp. 2673–2688.
- Devroye, Luc (1986). *Non-Uniform Random Variate Generation (originally published with)*. New York: Springer-Verlag.
- Sarazin, Craig L. (1986). "X-ray emission from clusters of galaxies." In: *Reviews of Modern Physics* 58.1, pp. 1–115.
- Hockney, R. W. and J. W. Eastwood (1988). *Computer Simulation Using Particles*. New York, NY: Taylor & Francis Group, p. 540.
- Kernighan, Brian W. (1988). *The C Programming Language*. Ed. by Dennis M. Ritchie. 2nd. Prentice Hall Professional Technical Reference.
- Horowitz, E. J., D. E. Shumaker, and D. V. Anderson (1989). "QN3D: A three-dimensional quasi-neutral hybrid particle-in-cell code with applications to the tilt mode instability in field reversed configurations." In: *J. Comput. Phys.* 84.2, pp. 279–310.

Bibliography

- Poppe, G. P. M. and C. M. J. Wijers (1990). “More Efficient Computation of the Complex Error Function.” In: *ACM Trans. Math. Softw.* 16.1, pp. 38–46. DOI: 10.1145/77626.77629.
- Balbus, Steven A. and John F. Hawley (1991). “A powerful local shear instability in weakly magnetized disks. I - Linear analysis.” In: *The Astrophysical Journal* 376.9, p. 214.
- Birdsall, C. K. and A. B. Langdon (1991). *Plasma Physics via Computer Simulation*.
- Kazeminezhad, F., J. M. Dawson, J. N. Leboeuf, R. Sydora, and D. Holland (1992). “A vlasov particle ion zero mass electron model for plasma simulations.” In: *J. Comput. Phys.* 102.2, pp. 277–296.
- Stix, T. H. (1992). *Waves in Plasmas*. New York: American Institute of Physics.
- Forum, The MPI (1993). *MPI: A Message Passing Interface*.
- Gary, S. P. (1993). *Theory of Space Plasma Microinstabilities*.
- Southwood, David J and Margaret G Kivelson (1993). “Mirror instability: 1. Physical mechanism of linear instability.” In: *Journal of Geophysical Research: Space Physics* 98.A6, pp. 9181–9187.
- Matthews, A. (1994). “Current Advance Method and Cyclic Leapfrog for 2D Multispecies Hybrid Plasma Simulations.” In: *J. Comput. Phys.* 112.1, pp. 102–116.
- Decyk, Viktor K. (1995). “Skeleton PIC codes for parallel computers.” In: *Computer Physics Communications* 87.1. Particle Simulation Methods, pp. 87–94.
- Rambo, P. W. (1995). “Finite-Grid Instability in Quasineutral Hybrid Simulations.” In: *Journal of Computational Physics* 118, pp. 152–158.
- Rossum, Guido (1995). *Python Reference Manual*. Tech. rep. Amsterdam, The Netherlands, The Netherlands.
- Baumjohann, W. and R. A. Treumann (1996). *Basic space plasma physics*.
- Rambo, P. W. (1997). “Numerical Heating in Hybrid Plasma Simulations.” In: *Journal of Computational Physics* 133, pp. 173–180.
- The HDF Group (1997-2017). *Hierarchical Data Format*.
- Treumann, R. A. and W. Baumjohann (1997). *Advanced space plasma physics*.
- Balbus, Steven A and John F Hawley (1998). “Instability, turbulence, and enhanced transport in accretion disks.” In: *Reviews of Modern Physics* 70.1, pp. 1–53.

- Dagum, Leonardo and Ramesh Menon (1998). "OpenMP: An Industry-Standard API for Shared-Memory Programming." In: *IEEE Comput. Sci. Eng.* 5.1, pp. 46–55.
- Balbus, S. A. (2000). "Stability, Instability, and "Backward" Transport in Stratified Fluids." In: *The Astrophysical Journal* 534, pp. 420–427.
- Boyd, John P. (2000). *Chebyshev and Fourier Spectral Methods*. DOVER.
- Cartwright, K. L., J. P. Verboncoeur, and C. K. Birdsall (2000). "Loading and Injection of Maxwellian Distributions in Particle Simulations." In: *Journal of Computational Physics* 162, pp. 483–513.
- Hellinger, P. and H. Matsumoto (2000). "New kinetic instability: Oblique Alfvén fire hose." In: *Journal of Geophysical Research* 105, pp. 10519–10526.
- Tóth, G. (2000). "The $\nabla \cdot \mathbf{B} = 0$ Constraint in Shock-Capturing Magnetohydrodynamics Codes." In: *J. Comput. Phys.* 161.2, pp. 605–652.
- Balbus, S. A. (2001). "Convective and Rotational Stability of a Dilute Plasma." In: *The Astrophysical Journal* 562, pp. 909–917.
- Birn, J. et al. (2001). "Geospace Environmental Modeling (GEM) Magnetic Reconnection Challenge." In: *Journal of Geophysical Research: Space Physics* 106.A3, pp. 3715–3719.
- Hellinger, P. and H. Matsumoto (2001). "Nonlinear competition between the whistler and Alfvén fire hoses." In: *J. Geophys. Res. Sp. Phys.* 106.A7, pp. 13215–13218.
- Jones, Eric, Travis Oliphant, Pearu Peterson, et al. (2001-2017). *SciPy: Open source scientific tools for Python*. [Online; accessed 6/7 2017].
- Schwenn, Rainer (2001). "Solar Wind: Global Properties." In: *The Encyclopedia of Astronomy and Astrophysics* 2301, pp. 1–9.
- Carilli, C. L. and G. B. Taylor (2002). "Cluster Magnetic Fields." In: *Annual Review of Astronomy and Astrophysics* 40, pp. 319–348.
- Mangeney, A., F. Califano, C. Cavazzoni, and P. Travnicek (2002). "A Numerical Scheme for the Integration of the Vlasov–Maxwell System of Equations." In: *J. Comput. Phys.* 179.2, pp. 495–538.
- Quataert, Eliot, William Dorland, and Gregory W Hammett (2002). "The Magnetorotational Instability in a Collisionless Plasma." In: *The Astrophysical Journal* 577.1, pp. 524–533.

Bibliography

- Chuzhoy, L. and A. Nusser (2003). “Gravitational diffusion in the intracluster medium.” In: *Monthly Notices of the Royal Astronomical Society* 342, pp. L5–L8.
- Gammie, Charles F., Jonathan C. McKinney, and Gabor Toth (2003). “HARM: A Numerical Scheme for General Relativistic Magnetohydrodynamics.” In: *The Astrophysical Journal* 589.1, pp. 444–457.
- Quataert, Eliot (2003). “Radiatively Inefficient Accretion Flow Models of Sgr A*.” In: *Astronomische Nachrichten* 324.SUPPL.1, pp. 435–443.
- Sharma, Prateek, Gregory W Hammett, and Eliot Quataert (2003). “Transition from Collisionless to Collisional Magnetorotational Instability.” In: *The Astrophysical Journal* 596.2, pp. 1121–1130.
- Swanson, Donald G. (2003). *Plasma Waves, 2nd Edition (Series in Plasma Physics)*. 2nd ed. Taylor & Francis.
- Winske, D., L. Yin, N. Omidi, H. Karimabadi, and K. Quest (2003). “Hybrid Simulation Codes: Past, Present and Future – A Tutorial.” In: *Lect. Notes Phys. Sp. Plasma Simul.* Ed. by J. Büchner, M. Scholer, and C. Dum. Springer Berlin/Heidelberg, pp. 136–165.
- Balbus, Steven A (2004). “Viscous Shear Instability in Weakly Magnetized, Dilute Plasmas.” In: *The Astrophysical Journal* 616.2, pp. 857–864.
- Chuzhoy, L. and A. Loeb (2004). “Element segregation in giant galaxies and X-ray clusters.” In: *Monthly Notices of the Royal Astronomical Society* 349, pp. L13–L17.
- Hazeltine, Richard D and François L Waelbroeck (2004). *The framework of plasma physics*. Westview.
- Parrish, Ian J. and James M. Stone (2005). “Nonlinear Evolution of the Magnetothermal Instability in Two Dimensions.” In: *The Astrophysical Journal* 633.1, pp. 334–348.
- Schekochihin, A. A., S. C. Cowley, R. M. Kulsrud, G. W. Hammett, and P. Sharma (2005). “Plasma Instabilities and Magnetic Field Growth in Clusters of Galaxies.” In: *The Astrophysical Journal* 629, pp. 139–142.
- Spitkovsky, A. (2005). “Simulations of relativistic collisionless shocks: shock structure and particle acceleration.” In: *Astrophysical Sources of High Energy Particles and Radiation*. Ed. by T. Bulik, B. Rudak, and G. Madejski. Vol. 801. Amer-

- ican Institute of Physics Conference Series, pp. 345–350. DOI: 10.1063/1.2141897.
- Voit, G Mark (2005). “Tracing cosmic evolution with clusters of galaxies.” In: *Reviews of Modern Physics* 77, January, pp. 207–258.
- Howes, Gregory G, Steven C Cowley, William Dorland, Gregory W Hammett, Eliot Quataert, and Alexander A Schekochihin (2006). “Astrophysical Gyrokinetics: Basic Equations and Linear Theory.” In: *The Astrophysical Journal* 651.1, pp. 590–614.
- Marsch, E, L Zhao, and C.-Y Tu (2006). “Limits on the core temperature anisotropy of solar wind protons.” In: *Ann. Geophys. Eur. Geosci. Union* 24.7, pp. 2057–2063.
- Matteini, Lorenzo, Simone Landi, Petr Hellinger, and Marco Velli (2006). “Parallel proton fire hose instability in the expanding solar wind: Hybrid simulations.” In: *Journal of Geophysical Research* 111.A10, A10101.
- Sharma, Prateek, Gregory W Hammett, Eliot Quataert, and James M Stone (2006). “Shearing box simulations of the MRI in a collisionless plasma.” In: *The Astrophysical Journal* 637.2, pp. 952–967.
- Somov, B. V. (2006). *Plasma Astrophysics, Part I: Fundamentals and Practice*.
- Vikhlinin, A., A. Kravtsov, W. Forman, C. Jones, M. Markevitch, S. S. Murray, and L. Van Speybroeck (2006). “Chandra Sample of Nearby Relaxed Galaxy Clusters: Mass, Gas Fraction, and Mass-Temperature Relation.” In: *The Astrophysical Journal* 640, pp. 691–709.
- Brecht, Stephen H. and Stephen A. Ledvina (2007). “The Solar Wind Interaction With the Martian Ionosphere/Atmosphere.” In: *Space Science Reviews* 126.1-4, pp. 15–38.
- Ferraro (2007). “Finite Larmor Radius Effects on the Magnetorotational Instability.” In: *The Astrophysical Journal* 662, pp. 512–516.
- Gargaté, L., R. Bingham, R. A. Fonseca, and L. O. Silva (2007). “dHybrid: A massively parallel code for hybrid simulations of space plasmas.” In: *Comput. Phys. Commun.* 176.6, pp. 419–425.
- Hunter, John D. (2007). “Matplotlib: A 2D Graphics Environment.” In: *Computing in Science and Engg.* 9.3, pp. 90–95.

- Markevitch, M. (2007). “Helium abundance in galaxy clusters and Sunyaev-Zeldovich effect.” In: *ArXiv e-prints*.
- Markevitch, Maxim and Alexey Vikhlinin (2007). “Shocks and cold fronts in galaxy clusters.” In: *Physics Reports* 443.443, pp. 1–53.
- McNamara, B.R. and P.E.J. Nulsen (2007). “Heating Hot Atmospheres with Active Galactic Nuclei.” In: *Annual Review of Astronomy and Astrophysics* 45.1, pp. 117–175.
- Mignone, A., G. Bodo, S. Massaglia, T. Matsakos, O. Tesileanu, C. Zanni, and A. Ferrari (2007). “PLUTO: A Numerical Code for Computational Astrophysics.” In: *The Astrophysical Journal Supplement* 170, pp. 228–242.
- Oliphant, Travis E. (2007). “Python for Scientific Computing.” In: *Computing in Science and Engg.* 9.3, pp. 10–20.
- Parker, Eugene Newman (2007). *Conversations on electric and magnetic fields in the cosmos*. Vol. 11. Princeton University Press.
- Perez, Fernando and Brian E. Granger (2007). “IPython: A System for Interactive Scientific Computing.” In: *Computing in Science and Engg.* 9.3, pp. 21–29.
- Pringle, James E and Andrew King (2007). *Astrophysical flows*. Cambridge University Press.
- Sharma, Prateek, Eliot Quataert, Gregory W. Hammett, and James M. Stone (2007). “Electron Heating in Hot Accretion Flows.” In: *The Astrophysical Journal* 667.2, pp. 714–723.
- Valentini, F., P. Trávníček, F. Califano, P. Hellinger, and A. Mangeney (2007). “A hybrid-Vlasov model based on the current advance method for the simulation of collisionless magnetized plasma.” In: *J. Comput. Phys.* 225.1, pp. 753–770.
- Zurbuchen, Thomas H (2007). “A New View of the Coupling of the Sun and the Heliosphere.” In: *Annu. Rev. Astron. Astrophys* 45, pp. 297–338.
- Dalcín, Lisandro, Rodrigo Paz, Mario Storti, and Jorge D’Elía (2008). “MPI for Python: Performance improvements and MPI-2 extensions.” In: *Journal of Parallel and Distributed Computing* 68.5, pp. 655–662.
- Pandey, B. P. and M. Wardle (2008). “Hall magnetohydrodynamics of partially ionized plasmas.” In: *Monthly Notices of the Royal Astronomical Society* 385, pp. 2269–2278.

- Parrish, I. J., J. M. Stone, and N. Lemaster (2008). “The Magnetothermal Instability in the Intracluster Medium.” In: *The Astrophysical Journal* 688, pp. 905–917.
- Quataert, Eliot (2008). “Buoyancy Instabilities in Weakly Magnetized Low-Collisionality Plasmas.” In: *The Astrophysical Journal* 673, pp. 758–762.
- Stone, James M., Thomas A. Gardiner, Peter Teuben, John F. Hawley, and Jacob B. Simon (2008). “Athena: A New Code for Astrophysical MHD.” In: *The Astrophysical Journal Supplement Series* 178, pp. 137–177.
- Bale, S D, J C Kasper, G G Howes, E Quataert, C Salem, and D Sundkvist (2009). “Magnetic Fluctuation Power Near Proton Temperature Anisotropy Instability Thresholds in the Solar Wind.” In: *Phys. Rev. Lett.* 103.21.
- Chacon, Scott (2009). *Pro Git*. 1st. Berkely, CA, USA: Apress.
- Parrish, I. J., E. Quataert, and P. Sharma (2009). “Anisotropic Thermal Conduction and the Cooling Flow Problem in Galaxy Clusters.” In: *The Astrophysical Journal* 703, pp. 96–108.
- Peng, Fang and Daisuke Nagai (2009). “Effect of Helium Sedimentation on X-Ray Measurements of Galaxy Clusters.” In: *The Astrophysical Journal* 693, pp. 839–846.
- Andreon, S. (2010). “The stellar mass fraction and baryon content of galaxy clusters and groups.” In: *Monthly Notices of the Royal Astronomical Society* 407, pp. 263–276.
- Bonafede, A., L. Feretti, M. Murgia, F. Govoni, G. Giovannini, D. Dallacasa, K. Dolag, and G. B. Taylor (2010). “The Coma cluster magnetic field from Faraday rotation measures.” In: *Astronomy and Astrophysics* 513, A30, A30.
- Durrant, D. R. (2010). *Numerical Methods for Fluid Dynamics*.
- Gargaté, L., R. A. Fonseca, J. Niemiec, M. Pohl, R. Bingham, and L. O. Silva (2010). “the Nonlinear Saturation of the Non-Resonant Kinetically Driven Streaming Instability.” In: *Astrophys. J.* 711.2, pp. L127–L132. DOI: 10.1088/2041-8205/711/2/L127.
- Holmström, Mats (2010). “Hybrid modeling of plasmas.” In:
- Piel, Alexander (2010). *Plasma physics: an introduction to laboratory, space, and fusion plasmas*. Springer Science & Business Media.

- Shtykovski, P. and M. Gilfanov (2010). “Thermal diffusion in the intergalactic medium of clusters of galaxies.” In: *Monthly Notices of the Royal Astronomical Society* 401, pp. 1360–1368.
- Yamada, Masaaki, Russell Kulsrud, and Hantao Ji (2010). “Magnetic reconnection.” In: *Reviews of Modern Physics* 82.1, pp. 603–664.
- Behnel, S., R. Bradshaw, C. Citro, L. Dalcin, D.S. Seljebotn, and K. Smith (2011). “Cython: The Best of Both Worlds.” In: *Computing in Science Engineering* 13.2, pp. 31–39.
- Borovsky, Joseph E. and S. Peter Gary (2011). “Electron-ion Coulomb scattering and the electron Landau damping of Alfvén waves in the solar wind.” In: *Journal of Geophysical Research: Space Physics* 116.A7, n/a–n/a.
- Cerfon, A. J. and J. P. Freidberg (2011). “Magnetohydrodynamic stability comparison theorems revisited.” In: *Physics of Plasmas* 18.1, 012505, p. 012505.
- Kunz, Matthew W. (2011). “Dynamical stability of a thermally stratified intracluster medium with anisotropic momentum and heat transport.” In: *Monthly Notices of the Royal Astronomical Society* 417, pp. 602–616.
- Müller, Joachim, Sven Simon, Uwe Motschmann, Josef Schüle, Karl-Heinz Glassmeier, and Gavin J Pringle (2011). “AIKEF: Adaptive hybrid model for space plasma simulations.” In: *Computer Physics Communications* 182.4, pp. 946–966.
- Chen, Francis F (2012). *Introduction to plasma physics*. Springer Science & Business Media.
- Childs, Hank et al. (2012). “VisIt: An End-User Tool For Visualizing and Analyzing Very Large Data.” In: *High Performance Visualization—Enabling Extreme-Scale Scientific Insight*, pp. 357–372.
- Kunz, Matthew W., Tamara Bogdanović, Christopher S. Reynolds, and James M. Stone (2012). “Buoyancy Instabilities in a Weakly Collisional Intracluster Medium.” In: *The Astrophysical Journal* 754, p. 122.
- Latter, H. N. and M. W. Kunz (2012). “The HBI in a quasi-global model of the intracluster medium.” In: *Monthly Notices of the Royal Astronomical Society* 423, pp. 1964–1972.

- Matteini, Lorenzo, Petr Hellinger, Simone Landi, Pavel M. Trávníček, and Marco Velli (2012). “Ion kinetics in the solar wind: Coupling global expansion to local microphysics.” In: *Space Science Reviews*. Vol. 172. 1-4, pp. 373–396.
- Parrish, I. J., M. McCourt, E. Quataert, and P. Sharma (2012a). “The effects of anisotropic viscosity on turbulence and heat transport in the intracluster medium.” In: *Monthly Notices of the Royal Astronomical Society* 422, pp. 704–718.
- (2012b). “Turbulent pressure support in the outer parts of galaxy clusters.” In: *Monthly Notices of the Royal Astronomical Society* 419, pp. L29–L33.
- Rein, H. and S.-F. Liu (2012). “REBOUND: an open-source multi-purpose N-body code for collisional dynamics.” In: *Astron. Astrophys.* 537, A128. DOI: 10.1051/0004-6361/201118085.
- Riquelme, Mario A, Eliot Quataert, Prateek Sharma, and Anatoly Spitkovsky (2012). “Local Two-Dimensional Particle-in-Cell Simulations of the Collisionless Magnetorotational Instability.” In: *The Astrophysical Journal* 755.1, p. 50.
- Bartelmann, Matthias (2013). *Theoretical Astrophysics - An Introduction*. WILEY-VCH.
- Caprioli, D and A Spitkovsky (2013). “Cosmic-Ray-Induced Filamentation Instability In Collisionless Shocks.” In: *Astrophys. J. Lett.* 765.8pp. DOI: 10.1088/2041-8205/765/1/L20.
- Collette, Andrew (2013). *Python and HDF5*. O’Reilly.
- Haugbølle, T., J. T. Frederiksen, and Å. Nordlund (2013). “photon-plasma: A modern high-order particle-in-cell code.” In: *Phys. Plasmas* 20.6, p. 062904.
- Hellinger, Petr and Pavel M. Trávníček (2013). “Protons and alpha particles in the expanding solar wind: Hybrid simulations.” In: *J. Geophys. Res. Sp. Phys.* 118.9, pp. 5421–5430. DOI: 10.1002/jgra.50540.
- Hoshino, Masahiro (2013). “Particle Acceleration During Magnetorotational Instability in a Collisionless Accretion Disk.” In: *The Astrophysical Journal* 773.2, p. 118.
- Lapenta, Giovanni (2013). *Particle In Cell Methods. With Application to Simulations in Space. Weather*.
- Olver, S. and A. Townsend (2013). “Fast inverse transform sampling in one and two dimensions.” In: *ArXiv e-prints*.

- Pessah, M. E. and S. Chakraborty (2013). “The Stability of Weakly Collisional Plasmas with Thermal and Composition Gradients.” In: *The Astrophysical Journal* 764, 13, p. 13.
- Verscharen, Daniel, Sofiane Bourouaine, and Benjamin D G Chandran (2013). “Instabilities Driven By The Drift And Temperature Anisotropy Of Alpha Particles In The Solar Wind.” In: *Astrophys. J.* 773.13pp. DOI: 10.1088/0004-637X/773/2/163.
- Verscharen, Daniel, Sofiane Bourouaine, Benjamin D G Chandran, and Bennett A Maruca (2013). “A Parallel-propagating Alf Enic Ion-beam Instability In The High-beta Solar Wind.” In: *The Astrophysical Journal* 773.8pp.
- Alfthan, S. von, D. Pokhotelov, Y. Kempf, S. Hoilijoki, I. Honkonen, A. Sandroos, and M. Palmroth (2014). “Vlasiator: First global hybrid-Vlasov simulations of Earth’s foreshock and magnetosheath.” In: *J. Atmos. Solar-Terrestrial Phys.* 120, pp. 24–35.
- Amano, Takanobu, Katsuaki Higashimori, and Keisuke Shirakawa (2014). “A robust method for handling low density regions in hybrid simulations for collisionless plasmas.” In: *J. Comput. Phys.* 275, pp. 197–212.
- Berlok, T. (2014). “Instabilities in weakly magnetized, hot, heterogenous plasmas.” Master’s thesis. Blegdamsvej 17, 2100 Copenhagen, DK: University of Copenhagen.
- Fitzpatrick, Richard (2014). *Plasma physics: an introduction*. Crc Press.
- Freidberg, Jeffrey P (2014). *Ideal MHD*. Cambridge University Press.
- Heinemann, Tobias and Eliot Quataert (2014). “Linear Vlasov Theory in the Shearing Sheet Approximation With Application To the Magneto-Rotational Instability.” In: *The Astrophysical Journal* 792.1, p. 70.
- Kunz, M. W., A. A. Schekochihin, and J. M. Stone (2014). “Firehose and Mirror Instabilities in a Collisionless Shearing Plasma.” In: *Physical Review Letters* 112.20, 205003, p. 205003.
- Kunz, M. W., J. M. Stone, and X.-N. Bai (2014). “Pegasus: A new hybrid-kinetic particle-in-cell code for astrophysical plasma dynamics.” In: *J. Comput. Phys.* 259, pp. 154–174.
- Mantz, A. B., S. W. Allen, R. G. Morris, D. A. Rapetti, D. E. Applegate, P. L. Kelly, A. von der Linden, and R. W. Schmidt (2014). “Cosmology and as-

- trophysics from relaxed galaxy clusters - II. Cosmological constraints.” In: *Monthly Notices of the Royal Astronomical Society* 440, pp. 2077–2098.
- Yuan, Feng and Ramesh Narayan (2014). “Hot Accretion Flows Around Black Holes.” In: *Annu. Rev. Astron. Astrophys* 52, pp. 529–88.
- Astfalk, P., T. Görler, and F. Jenko (2015). “DSHARK: A dispersion relation solver for obliquely propagating waves in bi-kappa-distributed plasmas.” In: *Journal of Geophysical Research (Space Physics)* 120, pp. 7107–7120.
- Berlok, T. and M. E. Pessah (2015). “Plasma Instabilities in the Context of Current Helium Sedimentation Models: Dynamical Implications for the ICM in Galaxy Clusters.” In: *The Astrophysical Journal* 813, 22, p. 22.
- Franci, Luca, Simone Landi, Lorenzo Matteini, Andrea Verdini, and Petr Hellinger (2015). “High-resolution Hybrid Simulations Of Kinetic Plasma Turbulence At Proton Scales.” In: *Astrophys. J.* 812.1, p. 21. DOI: 10.1088/0004-637X/812/1/21.
- Hellinger, P., L. Matteini, S. Landi, A. Verdini, L. Franci, and P. M. Trávníček (2015). “Plasma Turbulence and Kinetic Instabilities At Ion Scales in the Expanding Solar Wind.” In: *Astrophys. J.* 811.2, p. L32. DOI: 10.1088/2041-8205/811/2/L32.
- Hoshino, Masahiro (2015). “Angular momentum transport and particle acceleration during magnetorotational instability in a kinetic accretion disk.” In: *Physical Review Letters* 114.6.
- Quataert, E, 1< T Heinemann, and A Spitkovsky (2015). “Linear instabilities driven by differential rotation in very weakly magnetized plasmas.” In: *MNRAS* 447, pp. 3328–3341.
- Ressler, S M, 1< A Tchekhovskoy, E Quataert, M Chandra, and C F Gammie (2015). “Electron thermodynamics in GRMHD simulations of low-luminosity black hole accretion.” In: *MNRAS* 454, pp. 1848–1870.
- Sironi, Lorenzo and Ramesh Narayan (2015). “Electron Heating By the Ion Cyclotron Instability in Collisionless Accretion Flows. I. Compression-Driven Instabilities and the Electron Heating Mechanism.” In: *The Astrophysical Journal* 800.2, p. 88.
- Yoon, Peter H., Jungjoon Seough, Junga Hwang, and Yasuhiro Nariyuki (2015). “Macroscopic quasi-linear theory and particle-in-cell simulation of helium ion

Bibliography

- anisotropy instabilities.” In: *J. Geophys. Res. Sp. Phys.* 120.8, pp. 6071–6084.
DOI: 10.1002/2015JA021495.
- Balbus, S. A. and W. J. Potter (2016). “Surprises in astrophysical gasdynamics.” In: *Reports on Progress in Physics* 79.6, 066901, p. 066901.
- Berlok, T. and M. E. Pessah (2016a). “Local Simulations of Instabilities Driven by Composition Gradients in the ICM.” In: *The Astrophysical Journal* 824, 32, p. 32.
- (2016b). “On Helium Mixing in Quasi-global Simulations of the Intracluster Medium.” In: *The Astrophysical Journal* 833, 164, p. 164.
- Decyk, V. (2016). “A portable approach for PIC on emerging architectures.” In: *APS April Meeting Abstracts*.
- Foucart, Francois, Mani Chandra, Charles F Gammie, and Eliot Quataert (2016). “Evolution of accretion discs around a kerr black hole using extended magnetohydrodynamics.” In: *MNRAS* 456, pp. 1332–1345.
- Komarov, S. V., E. M. Churazov, M. W. Kunz, and A. A. Schekochihin (2016). “Thermal conduction in a mirror-unstable plasma.” In: *Monthly Notices of the Royal Astronomical Society* 460, pp. 467–477.
- Kunz, Matthew W, James M Stone, and Eliot Quataert (2016). “Magnetorotational Turbulence and Dynamo in a Collisionless Plasma.” In: *Physical Review Letters* 117.23.
- Lehe, Rémi, Manuel Kirchen, Igor A Andriyash, Brendan B Godfrey, and Jean-Luc Vay (2016). “A spectral, quasi-cylindrical and dispersion-free Particle-In-Cell algorithm.” In: *Comput. Phys. Commun.* 203, pp. 66–82.
- Mortensen, Mikael and Hans Petter Langtangen (2016). “High performance Python for direct numerical simulations of turbulent flows.” In: *Computer Physics Communications* 203, pp. 53–65.
- Muñoz, P. A., N. Jain, P. Kilian, and J. Büchner (2016). “A new hybrid code (CHIEF) implementing the inertial electron fluid equation without approximation.” In: *arXiv Prepr.* Pp. 1–42.
- Ressler, Sean M, Alexander Tchekhovskoy, Eliot Quataert, and Charles F Gammie (2016). “The Disc-Jet Symbiosis Emerges: Modeling the Emission of Sagittarius A* with Electron Thermodynamics.” In: *MNRAS* 15.November, pp. 1–15.
DOI: 10.1093/mnras/stx364.

- Riquelme, M. A., E. Quataert, and D. Verscharen (2016). “PIC Simulations of the Effect of Velocity Space Instabilities on Electron Viscosity and Thermal Conduction.” In: *The Astrophysical Journal* 824, 123, p. 123.
- Told, D., J. Cookmeyer, P. Astfalk, and F. Jenko (2016). “A linear dispersion relation for the hybrid kinetic-ion/fluid-electron model of plasma physics.” In: *New Journal of Physics* 18.7, 075001, p. 075001.
- Xie, H. and Y. Xiao (2016). “PDRK: A General Kinetic Dispersion Relation Solver for Magnetized Plasma.” In: *Plasma Science and Technology* 18, 97, p. 97.
- Berlok, T., M. E. Pessah, and E. Quataert (2017). “Heat conduction models in simulations of the magneto-thermal instability.” In: *Manuscript in preparation*.
- Cerri, S. S., L. Franci, F. Califano, S. Landi, and P. Hellinger (2017). “Plasma turbulence at ion scales: a comparison between particle in cell and Eulerian hybrid-kinetic approaches.” In: *Journal of Plasma Physics* 83.2.
- Chandra, Mani, Francois Foucart, and Charles F. Gammie (2017). “grim: A Flexible, Conservative Scheme for Relativistic Fluid Theories.” In: *The Astrophysical Journal* 837.1, p. 92.
- Fatemi, Shahab, Andrew R. Poppe, Gregory T. Delory, and William M. Farrell (2017). “AMITIS: A 3D GPU-Based Hybrid-PIC Model for Space and Plasma Physics.” In: *Journal of Physics: Conference Series* 837.1, p. 012017.
- Hirabayashi, Kota and Masahiro Hoshino (2017). “Stratified Simulations of Collisionless Accretion Disks.” In: *The Astrophysical Journal* 842.1, p. 36.
- Sadhukhan, S., H. Gupta, and S. Chakraborty (2017). “On the helium fingers in the intracluster medium.” In: *Monthly Notices of the Royal Astronomical Society* 469, pp. 2595–2601.
- Burns, K. J., G. M. Vasil, J. S. Oishi, D. Lecoanet, B. P. Brown, and E. Quataert (In preparation). “Dedalus: A Flexible Framework for Spectrally Solving Differential Equations.” In: *In preparation*.

Appendix A

Various derivations

A.1 Integrals in perpendicular velocity

Inspection of the Λ tensor shows that we need integrals of the following types¹.

$$\int_0^\infty x J_n(px)^2 e^{-ax^2} dx = \frac{\Gamma_n(\lambda)}{2a}, \quad (\text{A.1})$$

$$\int_0^\infty x^2 J_n(px) J'_n(px) e^{-ax^2} dx = \frac{\Gamma'_n(\lambda)}{2ap} \lambda, \quad (\text{A.2})$$

$$\int_0^\infty x^3 J'_n(px)^2 e^{-ax^2} dx = \frac{1}{4a^2} \left(\frac{n^2 \Gamma_n}{\lambda} - 2\Gamma'_n \lambda \right), \quad (\text{A.3})$$

where

$$\Gamma_n(\lambda) = e^{-\lambda} I_n(\lambda), \quad (\text{A.4})$$

and

$$\lambda = \frac{p^2}{2a}. \quad (\text{A.5})$$

¹See also equation 4.67 and page 106 in Ichimaru, 1973

A. Various derivations

These integrals (Equations A.1-A.3) are derived below. Our starting point is the Weber integral (see, e.g., Appendix B in Baumjohann and Treumann 1996)

$$\int_0^\infty x J_n(px) J_n(rx) e^{-ax^2} dx = (2a)^{-1} \exp\left(-\frac{p^2 + r^2}{4a}\right) I_n\left(\frac{pr}{2a}\right), \quad (\text{A.6})$$

which we can use to derive expressions for all three integrals. An expression for the first integral is immediately found by setting $r = p$

$$\int_0^\infty x J_n(px)^2 e^{-ax^2} dx = (2a)^{-1} \exp\left(-\frac{p^2}{2a}\right) I_n\left(\frac{p^2}{2a}\right) = \frac{\Gamma_n(\lambda)}{2a}, \quad (\text{A.7})$$

We note that the relations between I_n and Γ_n and their derivatives are given by

$$I_n = \Gamma_n e^\lambda, \quad (\text{A.8})$$

$$I'_n = (\Gamma'_n + \Gamma_n) e^\lambda, \quad (\text{A.9})$$

$$I''_n = (\Gamma''_n + 2\Gamma'_n + \Gamma_n) e^\lambda, \quad (\text{A.10})$$

which is useful for rewriting expression in terms of Γ_n and its derivatives.

An expression for the second integral (Equation A.2) is found by differentiating the expression on both sides with respect to p and then subsequently setting $r = p$. By the chain rule $d/dp J_n(px) = x J'_n(px)$ so

$$\int_0^\infty x^2 J_n(px) J'_n(px) e^{-ax^2} dx = \frac{1}{2a} e^{-\lambda} \frac{p}{2a} (I'_n - I_n) = \frac{\Gamma'_n(\lambda)}{2ap} \lambda. \quad (\text{A.11})$$

For the last integral (Equation A.3), we differentiate with respect to both p and r on both sides and find

$$\begin{aligned} \int_0^\infty x^3 J'_n(px)^2 e^{-ax^2} dx &= \frac{1}{4a^2} e^{-\lambda} (\lambda I_n - 2\lambda I'_n + I'_n + \lambda I''_n) \\ &= \frac{1}{4a^2} (\lambda \Gamma''_n + \Gamma'_n + \Gamma_n). \end{aligned} \quad (\text{A.12})$$

In the last step we have again used Equations A.9-A.10. This expression can be

further simplified by using Bessel's modified equation

$$\lambda^2 I_n'' + \lambda I_n' - (\lambda^2 + n^2) I_n = 0. \quad (\text{A.13})$$

We find that

$$\lambda \Gamma_n'' + \Gamma_n' + \Gamma_n = \frac{n^2 \Gamma_n}{\lambda} - 2\Gamma_n' \lambda, \quad (\text{A.14})$$

which simplifies the integral to the form given in Equation A.3.

A.2 Integrals in parallel velocity

We consider integrals of the form

$$\frac{1}{\sqrt{2\pi}} \int_{-\infty}^{\infty} \frac{x^n e^{-x^2/2}}{x-z} dx, \quad (\text{A.15})$$

with $n = 0, 1, 2$ and 3 . These integrals can be written in terms of the $W(z)$ function introduced in Ichimaru (1973)

$$W(z) = \frac{1}{\sqrt{2\pi}} \int_{-\infty}^{\infty} \frac{x e^{-x^2/2}}{x-z} dx, \quad (\text{A.16})$$

where the $W(z)$ function corresponds to the $n = 1$ integral. Using the partial fractions

$$\frac{x}{x-z} = 1 + z \frac{1}{x-z}, \quad (\text{A.17})$$

$$\frac{x^2}{x-z} = x + z \frac{x}{x-z}, \quad (\text{A.18})$$

$$\frac{x^3}{x-z} = x^2 + z \frac{x^2}{x-z} = x^2 + xz + z^2 \frac{x}{x-z}, \quad (\text{A.19})$$

we can show that the relation between $W(z)$ and the $n = 0$ integral is given by

$$W(z) = \frac{1}{\sqrt{2\pi}} \left[\int_{-\infty}^{\infty} e^{-x^2/2} dx + z \int_{-\infty}^{\infty} \frac{e^{-x^2/2}}{x-z} dx \right]$$

A. Various derivations

$$= 1 + \frac{z}{\sqrt{2\pi}} \int_{-\infty}^{\infty} \frac{e^{-x^2/2}}{x-z} dx, \quad (\text{A.20})$$

or

$$\frac{1}{\sqrt{2\pi}} \int_{-\infty}^{\infty} \frac{e^{-x^2/2}}{x-z} dx = \frac{W(z) - 1}{z}. \quad (\text{A.21})$$

The two remaining integrals, that we need to calculate the conductivity tensor in Chapter 6, are then given by

$$\frac{1}{\sqrt{2\pi}} \int_{-\infty}^{\infty} \frac{x^2 e^{-x^2/2}}{x-z} dx = zW(z), \quad (\text{A.22})$$

$$\frac{1}{\sqrt{2\pi}} \int_{-\infty}^{\infty} \frac{x^3 e^{-x^2/2}}{x-z} dx = 1 + z^2 W(z). \quad (\text{A.23})$$

Using these integrals we observe that

$$\sqrt{2\pi} v_{t,\parallel} A_l = \int_{-\infty}^{\infty} \frac{v_{\parallel}^l e^{-v_{\parallel}^2/2v_{t,\parallel}^2}}{n\Omega_s + k_{\parallel}v_{\parallel} - \omega} dv_{\parallel} = \frac{v_{t,\parallel}^l}{k_{\parallel}} \int_{-\infty}^{\infty} \frac{x^l e^{-x^2/2}}{x-z} dx, \quad (\text{A.24})$$

where we have set $x = v_{\parallel}/v_{t,\parallel}$ such that $dv_{\parallel} = v_{t,\parallel} dx$. The four relevant integrals are

$$A_0 = \frac{1}{k_{\parallel} v_{t,\parallel}} \frac{W(\zeta_n) - 1}{\zeta_n}, \quad (\text{A.25})$$

$$A_1 = \frac{1}{k_{\parallel}} W(\zeta_n), \quad (\text{A.26})$$

$$A_2 = \frac{v_{t,\parallel}}{k_{\parallel}} \zeta_n W(\zeta_n), \quad (\text{A.27})$$

$$A_3 = \frac{v_{t,\parallel}^2}{k_{\parallel}} \left[1 + \zeta_n^2 W(\zeta_n) \right], \quad (\text{A.28})$$

where

$$\zeta_n = \frac{\omega - n\Omega_s}{k_{\parallel} v_{t,\parallel}}. \quad (\text{A.29})$$

We find that the six independent components of Λ are given by

$$\Lambda_{xx} = 1 - \frac{n^2 \Omega_s^2}{k_\perp^2} \Gamma_n \left(\frac{n \Omega_s}{v_{t,\perp}^2} A_0 + \frac{k_\parallel}{v_{t,\parallel}^2} A_1 \right), \quad (\text{A.30})$$

$$\Lambda_{xy} = -i \frac{n \Omega_s^2}{k_\perp^2} \lambda \Gamma'_n \left(\frac{n \Omega_s}{v_{t,\perp}^2} A_0 + \frac{k_\parallel}{v_{t,\parallel}^2} A_1 \right), \quad (\text{A.31})$$

$$\Lambda_{xz} = -\frac{n \Omega_s}{k_\perp} \Gamma_n \left(\frac{n \Omega_s}{v_{t,\perp}^2} A_1 + \frac{k_\parallel}{v_{t,\parallel}^2} A_2 \right), \quad (\text{A.32})$$

$$\Lambda_{yy} = 1 - v_{t,\perp}^2 \left(\frac{n^2 \Gamma_n}{\lambda} - 2 \Gamma'_n \lambda \right) \left(\frac{n \Omega_s}{v_{t,\perp}^2} A_0 + \frac{k_\parallel}{v_{t,\parallel}^2} A_1 \right), \quad (\text{A.33})$$

$$\Lambda_{yz} = i \frac{\Gamma'_n}{k_\perp} \Omega_s \lambda \left(\frac{n \Omega_s}{v_{t,\perp}^2} A_1 + \frac{k_\parallel}{v_{t,\parallel}^2} A_2 \right), \quad (\text{A.34})$$

$$\Lambda_{zz} = 1 - \Gamma_n \left(\frac{n \Omega_s}{v_{t,\perp}^2} A_2 + \frac{k_\parallel}{v_{t,\parallel}^2} A_3 \right). \quad (\text{A.35})$$

Noting that

$$\frac{\zeta_0}{\zeta_n} = \frac{\omega}{\omega - n \Omega_s}, \quad (\text{A.36})$$

such that

$$\frac{n \Omega_s}{\omega - n \Omega_s} = \frac{\omega}{\omega - n \Omega_s} - 1 = \frac{\zeta_0}{\zeta_n} - 1, \quad (\text{A.37})$$

as well as

$$\frac{n \Omega_s}{k_\parallel v_{t,\parallel}} = \zeta_0 - \zeta_n, \quad (\text{A.38})$$

we find

$$\left(\frac{n \Omega_s}{v_{t,\perp}^2} A_0 + \frac{k_\parallel}{v_{t,\parallel}^2} A_1 \right) = \frac{1}{v_{t,\perp}^2} \left[\left(\frac{\zeta_0}{\zeta_n} - 1 \right) (W - 1) + \frac{v_{t,\perp}^2}{v_{t,\parallel}^2} W \right], \quad (\text{A.39})$$

A. Various derivations

$$\left(\frac{n\Omega_s}{v_{t,\perp}^2} A_1 + \frac{k_{\parallel}}{v_{t,\parallel}^2} A_2 \right) = \frac{1}{v_{t,\perp}^2 k_{\parallel}} \left(n\Omega_s W(\zeta_n) + \frac{v_{t,\perp}^2}{v_{t,\parallel}^2} (\omega - n\Omega_s) W(\zeta_n) \right), \quad (\text{A.40})$$

$$\left(\frac{n\Omega_s}{v_{t,\perp}^2} A_2 + \frac{k_{\parallel}}{v_{t,\parallel}^2} A_3 \right) = \frac{v_{t,\parallel}^2}{v_{t,\perp}^2} (\zeta_0 - \zeta_n) \zeta_n W(\zeta_n) + 1 + \zeta_n^2 W(\zeta_n). \quad (\text{A.41})$$

Plugging this into our expression for Λ we then see that

$$\Lambda_{xx} = 1 - \sum_{n=-\infty}^{\infty} n^2 \frac{\Gamma_n}{\lambda} \left[\left(\frac{\zeta_0}{\zeta_n} - 1 \right) (W - 1) + \frac{v_{t,\perp}^2}{v_{t,\parallel}^2} W \right], \quad (\text{A.42})$$

$$\Lambda_{xy} = - \sum_{n=-\infty}^{\infty} in \Gamma'_n \left[\left(\frac{\zeta_0}{\zeta_n} - 1 \right) (W - 1) + \frac{v_{t,\perp}^2}{v_{t,\parallel}^2} W \right], \quad (\text{A.43})$$

$$\Lambda_{xz} = - \sum_{n=-\infty}^{\infty} n \frac{\Gamma_n}{\sqrt{\lambda}} \frac{v_{t,\parallel}}{v_{t,\perp}} \left[(\zeta_0 - \zeta_n) W + \frac{v_{t,\perp}^2}{v_{t,\parallel}^2} \zeta_n W \right], \quad (\text{A.44})$$

$$\Lambda_{yy} = 1 - \sum_{n=-\infty}^{\infty} \left(\frac{n^2 \Gamma_n}{\lambda} - 2\Gamma'_n \lambda \right) \left[\left(\frac{\zeta_0}{\zeta_n} - 1 \right) (W - 1) + \frac{v_{t,\perp}^2}{v_{t,\parallel}^2} W \right] \quad (\text{A.45})$$

$$\Lambda_{yz} = \sum_{n=-\infty}^{\infty} i\sqrt{\lambda} \Gamma'_n \frac{v_{t,\parallel}}{v_{t,\perp}} \left[(\zeta_0 - \zeta_n) W + \frac{v_{t,\perp}^2}{v_{t,\parallel}^2} \zeta_n W \right], \quad (\text{A.46})$$

$$\Lambda_{zz} = 1 - \sum_{n=-\infty}^{\infty} \Gamma_n \left[\frac{v_{t,\parallel}^2}{v_{t,\perp}^2} (\zeta_0 - \zeta_n) \zeta_n W(\zeta_n) + 1 + \zeta_n^2 W(\zeta_n) \right], \quad (\text{A.47})$$

along with $\Lambda_{yx} = \Lambda_{yx}^*$, $\Lambda_{zx} = \Lambda_{zx}^*$ and so on.

We can simplify further by using the following sums (see Appendix A.3)

$$\sum_{n=-\infty}^{\infty} n^2 \frac{\Gamma_n(\lambda)}{\lambda} = 1, \quad (\text{A.48})$$

$$\sum_{n=-\infty}^{\infty} n \Gamma'_n = 0, \quad (\text{A.49})$$

$$\sum_{n=-\infty}^{\infty} \Gamma'_n = 0. \quad (\text{A.50})$$

This means that we can add a term linear in $\Gamma_n n$ in the expression for Λ_{xz} . This will not contribute anything as the corresponding sum is zero. In the same way

we can also add a term linear in Γ'_n in Λ_{yz} . In Λ_{zz} we can add and subtract $\sum_n \Gamma_n \frac{v_{t,\parallel}^2}{v_{t,\perp}^2} \zeta_n \zeta_0$ and perform the sum. These manipulations are done such that all elements of the tensor \mathbf{T}_n have a common factor.

A.3 Bessel function sums

The following sums are easy to find in the literature (see, e.g., Ichimaru 1973).

$$\sum_{n=-\infty}^{\infty} J_n(\lambda)^2 = 1, \quad (\text{A.51})$$

$$\sum_{n=-\infty}^{\infty} n^2 J_n(\lambda)^2 = \frac{\lambda^2}{2}, \quad (\text{A.52})$$

$$e^{-\lambda} \sum_{n=-\infty}^{\infty} I_n(\lambda) = \sum_{n=-\infty}^{\infty} \Gamma_n(\lambda) = 1. \quad (\text{A.53})$$

There is however a particular sum that arises in the conductivity tensor which we have been unable to find. The sum is

$$\sum_{n=-\infty}^{\infty} n^2 I_n(\lambda), \quad (\text{A.54})$$

and we can find its value by using the Weber integral²

$$\int_0^{\infty} x J_n(px)^2 e^{-ax^2} dx = \frac{e^{-\lambda}}{2a} I_n(\lambda), \quad (\text{A.55})$$

to show that

$$\sum_{n=-\infty}^{\infty} \int_0^{\infty} x n^2 J_n(px)^2 e^{-ax^2} dx = \frac{e^{-\lambda}}{2a} \sum_{n=-\infty}^{\infty} n^2 I_n(\lambda), \quad (\text{A.56})$$

²The sum of the modified Bessel functions can be similarly derived using the Weber integral and the sum over J_n^2 .

A. Various derivations

which upon evaluating the sum on the LHS becomes

$$\frac{p^2}{2} \int_0^\infty x^3 e^{-ax^2} dx = \frac{e^{-\lambda}}{2a} \sum_{n=-\infty}^{\infty} n^2 I_n(\lambda). \quad (\text{A.57})$$

This integral can easily be solved and we find

$$\sum_{n=-\infty}^{\infty} n^2 I_n(\lambda) = \lambda e^\lambda, \quad (\text{A.58})$$

or, as it appears in the conductivity tensor

$$\sum_{n=-\infty}^{\infty} n^2 \frac{\Gamma(\lambda)}{\lambda} = 1. \quad (\text{A.59})$$

A.4 Ichimaru's plasma dispersion function

The standard plasma dispersion function is defined as

$$Z(\zeta) = \frac{1}{\sqrt{\pi}} \int_{-\infty}^{\infty} \frac{e^{-x^2}}{x - \zeta} dx, \quad (\text{A.60})$$

by Fried and Conte (1961). The $W(z)$ function introduced in Ichimaru (1973) is defined as

$$W(z) = \frac{1}{\sqrt{2\pi}} \int_{-\infty}^{\infty} \frac{x e^{-x^2/2}}{x - z} dx. \quad (\text{A.61})$$

Using Equation A.20 they can be seen to be related by

$$W(z) = 1 + \frac{z}{\sqrt{2}} Z(z/\sqrt{2}). \quad (\text{A.62})$$

The small argument expansion of $W(z)$ is given by (Ichimaru 1973 equation 4.4)

$$W(z) \approx i\sqrt{\frac{\pi}{2}} z \exp(-z^2/2) + 1 - z^2 + \frac{z^4}{3} - \dots, \quad (\text{A.63})$$

and the large argument expansion is given by (Ichimaru 1973 equation 4.6)

$$W(z) \approx i\sqrt{\frac{\pi}{2}}z \exp(-z^2/2) - \frac{1}{z^2} - \frac{3}{z^4} - \dots \quad (\text{A.64})$$

A.5 Linearized Hall MHD equations

The linearized Hall MHD equations can be written as

$$\delta \mathbf{E} = -\delta \mathbf{u} \times \mathbf{B} + \eta \delta \mathbf{J} + \eta_H \delta \mathbf{J} \times \mathbf{b}, \quad (\text{A.65})$$

$$\delta \mathbf{J} = \mu_0^{-1} B i \mathbf{k} \times \delta \mathbf{b}, \quad (\text{A.66})$$

$$-i\omega B \delta \mathbf{b} + i \mathbf{k} \times \delta \mathbf{E} = 0, \quad (\text{A.67})$$

$$-i\omega \frac{\delta \rho}{\rho} + i \mathbf{k} \cdot \delta \mathbf{u} = 0, \quad (\text{A.68})$$

$$-i\omega \delta \mathbf{u} + i \mathbf{k} \frac{\delta \rho}{\rho} c_s^2 - B \frac{\delta \mathbf{J} \times \mathbf{b}}{\rho} = 0, \quad (\text{A.69})$$

where the equations above are the linearized versions of Ohm's law, Ampère's law, Faraday's law, the continuity equation and the momentum equation, respectively. In these equations $\mathbf{b} = \mathbf{B}/B$ and $\delta \mathbf{b} = \delta \mathbf{B}/B$.

By substituting the expression for $\delta \mathbf{J}$ into the momentum equation we find

$$-\omega \delta \mathbf{u} + \mathbf{k} \frac{\delta \rho}{\rho} c_s^2 - v_a^2 (\mathbf{k} \times \delta \mathbf{b}) \times \mathbf{b} = 0, \quad (\text{A.70})$$

where the Alfvén velocity is defined as

$$v_a^2 = \frac{B^2}{\mu_0 \rho}. \quad (\text{A.71})$$

We also substitute $\delta \mathbf{J}$ into Ohm's law and find

$$\delta \mathbf{E} = -\delta \mathbf{u} \times \mathbf{B} + \eta \mu_0^{-1} B i \mathbf{k} \times \delta \mathbf{b} + \eta_H \mu_0^{-1} B i (\mathbf{k} \times \delta \mathbf{b}) \times \mathbf{b}. \quad (\text{A.72})$$

This expression for $\delta \mathbf{E}$ is then used in Faraday's law

$$-\omega \delta \mathbf{b} + \mathbf{k} \times \left(-\delta \mathbf{u} \times \mathbf{b} + \frac{\eta}{\mu_0} i \mathbf{k} \times \delta \mathbf{b} + \frac{\eta_H}{\mu_0} i (\mathbf{k} \times \delta \mathbf{b}) \times \mathbf{b} \right) = 0. \quad (\text{A.73})$$

Equations A.68, A.70 and A.73 can be written as an eigenvalue problem, see Equation 4.5 on page 46.

A.6 Hall conductivity tensor

We can also construct a conductivity tensor from the linearized Hall MHD equations. We start out by noting that the continuity equation can be written as

$$\mathbf{k} \frac{\delta \rho}{\rho} = \frac{1}{\omega} \mathbf{k} \mathbf{k} \cdot \delta \mathbf{u} . \quad (\text{A.74})$$

We use this to write the momentum equation as

$$-\omega \delta \mathbf{u} + \frac{c_s^2}{\omega} \mathbf{k} \mathbf{k} \cdot \delta \mathbf{u} + iB \frac{\delta \mathbf{J} \times \mathbf{b}}{\rho} = 0 , \quad (\text{A.75})$$

which can be manipulated to yield

$$\left[c_s^2 \mathbf{k} \mathbf{k} - \omega^2 \mathbf{1} \right] \cdot \delta \mathbf{u} = \frac{iB\omega}{\rho} \mathbf{b} \times \delta \mathbf{J} , \quad (\text{A.76})$$

or

$$\delta \mathbf{u} = \frac{iB\omega}{\rho} \left[c_s^2 \mathbf{k} \mathbf{k} - \omega^2 \mathbf{1} \right]^{-1} \cdot (\mathbf{b} \times \mathbf{1}) \cdot \delta \mathbf{J} , \quad (\text{A.77})$$

where

$$\mathbf{b} \times \mathbf{1} = \begin{bmatrix} 0 & -b_z & b_y \\ b_z & 0 & -b_x \\ -b_y & b_x & 0 \end{bmatrix} . \quad (\text{A.78})$$

Ohm's law can be written as

$$\delta \mathbf{E} = \mathbf{B} \times \delta \mathbf{u} + \eta \delta \mathbf{J} - \eta_H \mathbf{b} \times \delta \mathbf{J} , \quad (\text{A.79})$$

or, upon substitution of $\delta\mathbf{u}$ from the momentum equation

$$\delta\mathbf{E} = \eta\delta\mathbf{J} + (\mathbf{b} \times \mathbf{1}) \left(\frac{iB^2\omega}{\varrho} [c_s^2\mathbf{k}\mathbf{k} - \omega^2\mathbf{1}]^{-1} \cdot (\mathbf{b} \times \mathbf{1}) - \eta_H\mathbf{1} \right) \cdot \delta\mathbf{J}. \quad (\text{A.80})$$

Now, the conductivity tensor is defined as

$$\delta\mathbf{J} = \boldsymbol{\sigma} \cdot \delta\mathbf{E}, \quad (\text{A.81})$$

so that we can read off $\boldsymbol{\sigma}^{-1}$ directly as

$$\boldsymbol{\sigma}^{-1} = \eta\mathbf{1} + \mu_0 v_a^2 (\mathbf{b} \times \mathbf{1}) \left(i\omega [c_s^2\mathbf{k}\mathbf{k} - \omega^2\mathbf{1}]^{-1} \cdot (\mathbf{b} \times \mathbf{1}) - \Omega^{-1}\mathbf{1} \right). \quad (\text{A.82})$$

Here we have used the Alfvén velocity, $v_a^2 = B^2/\mu_0\varrho$, and $\eta_H = \mu_0 v_a^2/\Omega$ to rewrite the expression slightly. The plasma dispersion relation is given by $\det \mathbf{D} = 0$ where $\mathbf{D} \cdot \delta\mathbf{E} = 0$ and

$$\mathbf{D} = k^2\mathbf{1} - \mathbf{k}\mathbf{k} - i\omega\mu_0\boldsymbol{\sigma}. \quad (\text{A.83})$$

It turns out that inverting $\boldsymbol{\sigma}^{-1}$ in order to obtain $\boldsymbol{\sigma}$ is tricky when $\eta = 0$ as the determinant of $\boldsymbol{\sigma}^{-1}$ is zero. This happens because the relation between δE_z and δJ_z is undetermined when $\eta = 0$. A 2×2 submatrix which describes the relation between $\delta\mathbf{J}$ and $\delta\mathbf{E}$ in the xy -plane is however invertible.

Instead of dealing with this problem we will instead simply rewrite the dispersion relation as

$$\mathbf{D} = \boldsymbol{\sigma}^{-1} \cdot (k^2\mathbf{1} - \mathbf{k}\mathbf{k}) - i\omega\mu_0\mathbf{1}. \quad (\text{A.84})$$

We note that the conductivity tensor is sometimes defined as

$$\delta\mathbf{J} = \boldsymbol{\sigma} \cdot (\delta\mathbf{E} + \mathbf{u} \times \mathbf{B}), \quad (\text{A.85})$$

such that the current is proportional to the electric field in the frame of the plasma, i.e., $\delta\mathbf{J} = \boldsymbol{\sigma} \cdot \delta\mathbf{E}'$ where $\delta\mathbf{E}' = \delta\mathbf{E} + \mathbf{u} \times \mathbf{B}$ is the electric field in the frame of the plasma, see, e.g., Somov (2006). We have opted to define the conductivity tensor

as $\delta \mathbf{J} = \boldsymbol{\sigma} \cdot \delta \mathbf{E}$ such that the dispersion relation can be written as in Equation A.83, i.e., in the same way as in Chapter 5.

A.7 Divergence of B

For a three-dimensional code with i, j and k being indices in the x, y and z direction the curl is approximated as

$$\tilde{\nabla} \times \mathbf{f}_{i,j,k} = \left(\delta_y \langle \cdot \rangle^x \langle \cdot \rangle^z f_{i,j,k}^z - \delta_z \langle \cdot \rangle^x \langle \cdot \rangle^y f_{i,j,k}^y \right) \mathbf{e}_x \quad (\text{A.86})$$

$$+ \left(\delta_z \langle \cdot \rangle^x \langle \cdot \rangle^y f_{i,j,k}^x - \delta_x \langle \cdot \rangle^y \langle \cdot \rangle^z f_{i,j,k}^z \right) \mathbf{e}_y \quad (\text{A.87})$$

$$+ \left(\delta_x \langle \cdot \rangle^y \langle \cdot \rangle^z f_{i,j,k}^y - \delta_y \langle \cdot \rangle^x \langle \cdot \rangle^z f_{i,j,k}^x \right) \mathbf{e}_z, \quad (\text{A.88})$$

and the divergence is approximated as

$$\tilde{\nabla} \cdot \mathbf{f}_{i,j,k} = \delta_x \langle \cdot \rangle^y \langle \cdot \rangle^z f_{i,j,k}^x + \delta_y \langle \cdot \rangle^x \langle \cdot \rangle^z f_{i,j,k}^y + \delta_z \langle \cdot \rangle^x \langle \cdot \rangle^y f_{i,j,k}^z, \quad (\text{A.89})$$

for an interlaced grid. Here we have introduced finite difference operator notation (see for instance the appendix of Durran 2010)

$$\delta_{nx} f_{i,j,k} = \frac{f_{i+n/2,j,k} - f_{i-n/2,j,k}}{n\Delta x}, \quad (\text{A.90})$$

$$\delta_{ny} f_{i,j,k} = \frac{f_{i,j+n/2,k} - f_{i,j-n/2,k}}{n\Delta y}, \quad (\text{A.91})$$

$$\delta_{nz} f_{i,j,k} = \frac{f_{i,j,k+n/2} - f_{i,j,k-n/2}}{n\Delta z}, \quad (\text{A.92})$$

and an interpolation operator with the following properties

$$\langle f_{i,j,k} \rangle^x = \langle \cdot \rangle^x f_{i,j,k} = \frac{f_{i+1/2,j,k} + f_{i-1/2,j,k}}{2}, \quad (\text{A.93})$$

$$\langle f_{i,j,k} \rangle^y = \langle \cdot \rangle^y f_{i,j,k} = \frac{f_{i,j+1/2,k} + f_{i,j-1/2,k}}{2}, \quad (\text{A.94})$$

$$\langle f_{i,j,k} \rangle^z = \langle \cdot \rangle^z f_{i,j,k} = \frac{f_{i,j,k+1/2} + f_{i,j,k-1/2}}{2}, \quad (\text{A.95})$$

to write the finite difference approximations to the first order derivatives along x , y and z .

Now

$$\begin{aligned} \tilde{\nabla} \cdot (\tilde{\nabla} \times \mathbf{f}_{i,j,k}) &= \delta_x \langle \cdot \rangle^y \langle \cdot \rangle^z \left(\delta_y \langle \cdot \rangle^x \langle \cdot \rangle^z f_{i,j,k}^z - \delta_z \langle \cdot \rangle^x \langle \cdot \rangle^y f_{i,j,k}^y \right) + \\ &\quad \delta_y \langle \cdot \rangle^x \langle \cdot \rangle^z \left(\delta_z \langle \cdot \rangle^x \langle \cdot \rangle^y f_{i,j,k}^x - \delta_x \langle \cdot \rangle^y \langle \cdot \rangle^z f_{i,j,k}^z \right) + \\ &\quad \delta_z \langle \cdot \rangle^x \langle \cdot \rangle^y \left(\delta_x \langle \cdot \rangle^y \langle \cdot \rangle^z f_{i,j,k}^y - \delta_y \langle \cdot \rangle^x \langle \cdot \rangle^z f_{i,j,k}^x \right), \end{aligned} \tag{A.96}$$

can also be written as

$$\begin{aligned} \delta_y \langle \cdot \rangle^x \langle \cdot \rangle^z \delta_z \langle \cdot \rangle^x \langle \cdot \rangle^y f_{i,j,k}^x &- \delta_z \langle \cdot \rangle^x \langle \cdot \rangle^y \delta_y \langle \cdot \rangle^x \langle \cdot \rangle^z f_{i,j,k}^x + \\ \delta_z \langle \cdot \rangle^x \langle \cdot \rangle^y \delta_x \langle \cdot \rangle^y \langle \cdot \rangle^z f_{i,j,k}^y &- \delta_x \langle \cdot \rangle^y \langle \cdot \rangle^z \delta_z \langle \cdot \rangle^x \langle \cdot \rangle^y f_{i,j,k}^y + \\ \delta_x \langle \cdot \rangle^y \langle \cdot \rangle^z \delta_y \langle \cdot \rangle^x \langle \cdot \rangle^z f_{i,j,k}^z &- \delta_y \langle \cdot \rangle^x \langle \cdot \rangle^z \delta_x \langle \cdot \rangle^y \langle \cdot \rangle^z f_{i,j,k}^z = 0, \end{aligned} \tag{A.97}$$

as the operators commute. For the finite difference and interpolation operators introduced above it is an exact cancellation of 384 terms. The proof outlined above however works for any interpolation or finite difference approximation, as long as the operations commute.

Paper I

Plasma Instabilities in the Context of Current Helium Sedimentation Models: Dynamical Implications for the ICM in Galaxy Clusters.

Reprinted from

The Astrophysical Journal, Volume 813, November 2015

doi:10.1088/0004-637X/813/1/22

with the permission of IOP Publishing.

PLASMA INSTABILITIES IN THE CONTEXT OF CURRENT HELIUM SEDIMENTATION MODELS: DYNAMICAL IMPLICATIONS FOR THE ICM IN GALAXY CLUSTERS

THOMAS BERLOK AND MARTIN E. PESSAH

Niels Bohr International Academy, Niels Bohr Institute, Blegdamsvej 17, DK-2100 Copenhagen Ø, Denmark; berlok@nbi.dk, mpessah@nbi.dk

Received 2015 May 21; accepted 2015 September 21; published 2015 October 22

ABSTRACT

Understanding whether Helium can sediment to the core of galaxy clusters is important for a number of problems in cosmology and astrophysics. All current models addressing this question are one-dimensional and do not account for the fact that magnetic fields can effectively channel ions and electrons, leading to anisotropic transport of momentum, heat, and particle diffusion in the weakly collisional intracluster medium (ICM). This anisotropy can lead to a wide variety of instabilities, which could be relevant for understanding the dynamics of heterogeneous media. In this paper, we consider the radial temperature and composition profiles as obtained from a state-of-the-art Helium sedimentation model and analyze its stability properties. We find that the associated radial profiles are unstable to different kinds of instabilities depending on the magnetic field orientation at all radii. The fastest growing modes are usually related to generalizations of the magnetothermal instability (MTI) and the heat-flux-driven buoyancy instability which operate in heterogeneous media. We find that the effect of sedimentation is to increase (decrease) the predicted growth rates in the inner (outer) cluster region. The unstable modes grow quickly compared to the sedimentation timescale. This suggests that the composition gradients as inferred from sedimentation models, which do not fully account for the anisotropic character of the weakly collisional environment, might not be very robust. Our results emphasize the subtleties involved in understanding the gas dynamics of the ICM and argue for the need of a comprehensive approach to address the issue of Helium sedimentation beyond current models.

Key words: diffusion – galaxies: clusters: intracluster medium – instabilities – magnetohydrodynamics (MHD)

1. INTRODUCTION

Galaxy clusters are important astrophysical probes since their masses can be used to constrain cosmological parameters (Mantz et al. 2014 and references therein). The distribution of mass as a function of radius can be inferred by modeling the observed X-ray emission produced by Bremsstrahlung in the hot intracluster medium (ICM). The intensity of the emission depends on the radial distribution of temperature and density, as well as the composition of the gas. While the temperature of the ICM is reasonably well determined (Vikhlinin et al. 2006), the composition of the plasma is not. The reason for this is that many of the elements are completely ionized at the characteristic temperatures of the ICM, and thus their abundances cannot be directly inferred. Therefore, the interpretation of the X-ray data normally relies on assuming a model for the composition of the gas. A widely adopted approximation consists of assuming the composition of the plasma to be uniform (see Bulbul et al. 2011 for an analysis where this assumption is relaxed). Elements heavier than hydrogen are expected to sediment over cosmological timescales (Fabian & Pringle 1977), therefore the assumption of a homogeneous ICM relies on this process being inefficient. Turbulence and tangled magnetic fields, or a combination of both, have been invoked as potential agents (Markevitch 2007).

Even though the mass ratio between Helium (He) and Hydrogen (H) is small, because He is the most abundant of the heavy elements, it has the potential to induce significant variations in the mean molecular weight. If He sedimentation does take place and this is not accounted for when modeling galaxy clusters, this could induce biases in the cosmological parameters derived (Qin & Wu 2000; Markevitch 2007; Peng & Nagai 2009). This could prove to be a problem for precision

cosmology and highlights the importance of understanding the distribution of heavy elements in the ICM (Fabian & Pringle 1977; Gilfanov & Syunyaev 1984; Chuzhoy & Nusser 2003; Chuzhoy & Loeb 2004; Peng & Nagai 2009; Shtykovskiy & Gilfanov 2010). Most of the previous work on this subject is based on solving Burgers' equations for a multicomponent plasma (Burgers 1969; Thoul et al. 1994) and all of these assume spherical symmetry in order to predict the composition of the ICM as a function of radius. Studies addressing the long term evolution of the composition of the ICM have considered the dynamical effects of magnetic fields in a rather crude way, usually encapsulating their effects in a parameter that regulates the slow down of the sedimentation process (Peng & Nagai 2009).

A more recent, and somewhat parallel, line of developments has helped us realize that the dynamical properties of magnetized, weakly collisional, stratified plasmas can be rather subtle. Balbus (2000, 2001) and Quataert (2008) showed that stratified plasmas that are stable according to the Schwarzschild criterion could turn unstable due to the presence of a magnetic field, even if its strength is too weak to be mechanically important. The plasma can become unstable because even a very weak magnetic field can effectively alter transport processes by channeling electrons and ions, leading to anisotropic heat conduction and Braginskii viscosity (Braginskii 1965; Kunz 2011).

Previous studies have considered plane-parallel, fully ionized *homogeneous* atmospheres with a temperature gradient in the direction of gravity. In this setting there are two instabilities that feed on the gradient in temperature. The Magnetothermal Instability (MTI) has the fastest growth rate when the magnetic field is perpendicular to gravity and the temperature decreases with height (Balbus 2000, 2001). The

Heat-flux-driven Buoyancy Instability (HBI) has the fastest growth rate when the magnetic field is parallel to gravity and the temperature increases with height (Quataert 2008). Because of the temperature profiles observed in typical cool-core galaxy clusters (Vikhlinin et al. 2006), the MTI is believed to be active in the outer parts of the ICM while the HBI is believed to be relevant in the inner parts of the ICM. These instabilities have been studied extensively in the literature both analytically (Balbus 2000, 2001; Quataert 2008; Kunz 2011; Latter & Kunz 2012) and numerically with initially local simulations with anisotropic heat conduction (Parrish & Stone 2005, 2007; Parrish & Quataert 2008) and since then with elaborate physical models (Parrish et al. 2008, 2009; Bogdanović et al. 2009; Parrish et al. 2010; Ruszkowski & Oh 2010; McCourt et al. 2011, 2012; Kunz et al. 2012; Parrish et al. 2012a, 2012b).

The aforementioned works that deal with the weakly collisional character of the magnetized plasma have usually adopted a homogeneous atmosphere as a model for the ICM. On the other hand, the sedimentation models are usually one-dimensional and do not fully account for dynamical properties of the magnetic field. In an effort to better understand the interplay between the Helium distribution in the ICM and its weakly collisional and weakly magnetized nature, Pessah & Chakraborty (2013) considered the presence of a gradient in the Helium composition and extended previous stability criteria. Their work shows that a gradient in composition can modify the stability properties of a stratified atmosphere. This could have consequences for the Helium sedimentation models which could be unstable to plasma instabilities.

The equations used to model the plasma in Pessah & Chakraborty (2013) describe the stability properties of a weakly collisional plasma subject to a background composition gradient, but they do not account for the process of Helium sedimentation which is estimated to occur on longer time-scales.¹ Because of this, the equations are thus unable to predict how a gradient in composition arises from an initial homogeneous plasma. A framework that simultaneously considers the physics responsible for Helium sedimentation together with the anisotropic transport properties governing dilute, magnetized plasmas has yet to be developed. A key goal for the future is therefore to develop such a model in order to determine from first principles the rate at which Helium can sediment in a weakly collisional, magnetized medium. In lieu of such a fully consistent theory, this paper has a more modest goal. Our aim is to understand the kind of instabilities, and their associated timescales and length scales, that can feed off the temperature and composition profiles that emerge from state-of-the-art models for Helium sedimentation in the ICM (Peng & Nagai 2009; Shtykovskiy & Gilfanov 2010).

The rest of the paper is organized as follows. In Section 2, we introduce the equations that we use to model the weakly collisional three-component plasma. In Section 3, we derive an extended version of the dispersion relation presented by Pessah & Chakraborty (2013) to account for the effects of magnetic tension, which can be important in cluster cores. In Section 4, we discuss the stability criteria for atmospheres with temperature and composition gradients. In Section 5, we solve the dispersion relation for isothermal atmospheres in order to gain insight into the type of instabilities that can be excited solely by

composition gradients. In Section 6, we consider the temperature and composition gradients derived from the Helium sedimentation model of Peng & Nagai (2009). By allowing the background magnetic field to have an arbitrary inclination with respect to gravity we identify the most relevant instabilities in different regions of the ICM. Finally, we conclude by discussing future prospects for addressing the problem of Helium sedimentation in galaxy clusters on more fundamental grounds in Section 7.

2. THE EQUATIONS OF KINETIC MHD FOR A BINARY MIXTURE

The kinetic MHD equations for a fully ionized binary mixture of Hydrogen and Helium can be written as (Pessah & Chakraborty 2013)

$$\frac{\partial \rho}{\partial t} + \nabla \cdot (\rho \mathbf{v}) = 0, \quad (1)$$

$$\frac{\partial(\rho \mathbf{v})}{\partial t} + \nabla \cdot \left(\rho \mathbf{v} \mathbf{v} + P_T \mathbf{I} - \frac{B^2}{4\pi} \hat{\mathbf{b}} \hat{\mathbf{b}} \right) = -\nabla \cdot \Pi + \rho \mathbf{g}, \quad (2)$$

$$\frac{\partial \mathbf{B}}{\partial t} = \nabla \times (\mathbf{v} \times \mathbf{B}), \quad (3)$$

$$\frac{\rho T}{\mu} \frac{ds}{dt} = -\nabla \cdot \mathbf{Q}_s - \Pi : \nabla \mathbf{v}, \quad (4)$$

$$\frac{dc}{dt} = -\nabla \cdot \mathbf{Q}_c. \quad (5)$$

Here, the Lagrangian and Eulerian derivatives are related via $d/dt = \partial/\partial t + \mathbf{v} \cdot \nabla$, ρ is the mass density, \mathbf{v} is the fluid velocity, $\mathbf{g} = (0, 0, -g)$ is the gravitational acceleration, and \mathbf{I} stands for the 3×3 identity matrix. The symbols \perp and \parallel refer, respectively, to the directions perpendicular and parallel to the magnetic field \mathbf{B} whose direction is given by the unit vector $\hat{\mathbf{b}} = \mathbf{B}/B = (b_x, 0, b_z)$. The total pressure is $P_T = P + B^2/8\pi$, where P is the thermal pressure and the entropy per unit mass is defined by

$$s = \frac{3k_B}{2m_H} \ln(P\rho^{-5/3}), \quad (6)$$

where k_B is Boltzmann's constant and m_H is the proton mass. The adiabatic index, γ , has been set to $5/3$ in the preceding equations and throughout the remainder of the paper.

The composition of the plasma, c , is defined to be the ratio of the Helium density to the total gas density

$$c = \frac{\rho_{\text{He}}}{\rho_{\text{H}} + \rho_{\text{He}}}. \quad (7)$$

The associated mean molecular weight, μ , influences the dynamics of the plasma through the equation of state

$$P = \frac{\rho k_B T}{\mu m_H}, \quad (8)$$

where T is the temperature. We assume a completely ionized plasma consisting of Helium and Hydrogen and the mass concentration of Helium, c , is therefore related to the mean

¹ We discuss the limitations of this work in this regard in Appendix A.1.

molecular weight, μ , by

$$\mu = \frac{4}{8 - 5c}. \quad (9)$$

The evolution of the binary mixture is influenced by three different non-ideal effects, namely Braginskii viscosity, which is described through the viscosity tensor (Braginskii 1965)

$$\Pi = -3\rho\nu_{\parallel}\left(\hat{\mathbf{b}}\hat{\mathbf{b}} - \frac{1}{3}\mathbf{I}\right)\left(\hat{\mathbf{b}}\hat{\mathbf{b}} - \frac{1}{3}\mathbf{I}\right) : \nabla\mathbf{v}, \quad (10)$$

anisotropic heat conduction described by the heat flux (Spitzer 1962; Braginskii 1965)

$$\mathbf{Q}_s = -\chi_{\parallel}\hat{\mathbf{b}}\hat{\mathbf{b}} \cdot \nabla T, \quad (11)$$

and anisotropic diffusion of Helium described by the composition flux

$$\mathbf{Q}_c = -D\hat{\mathbf{b}}\hat{\mathbf{b}} \cdot \nabla c. \quad (12)$$

The transport coefficients (χ_{\parallel} , ν_{\parallel} , and D) all depend on the temperature, as well as the composition of the plasma. The dependences are given in Appendix B by Equations (64)–(66), respectively. For more details on the kinetic MHD approximation and its limitations see the relevant discussions in Kunz et al. (2012), Schekochihin et al. (2005), Pessah & Chakraborty (2013) and references therein.

3. THE DISPERSION RELATION

We consider an initially motionless, plane-parallel atmosphere with gradients in both temperature and the mean molecular weight. A local linear mode analysis of this atmosphere, using Equations (1)–(5) and following the procedure in Pessah & Chakraborty (2013), leads to the dispersion relation

$$\sum_{i=0}^4 A_i + \omega_v \sum_{i=1}^5 B_i = 0, \quad (13)$$

where the coefficients are given by

$$A_0 = \sigma^2 \tilde{\sigma}^4 k^2, \quad (14)$$

$$A_1 = \sigma \tilde{\sigma}^4 (\omega_D + \omega_c) k^2, \quad (15)$$

$$A_2 = \sigma^2 \tilde{\sigma}^2 N^2 (k_x^2 + k_y^2) + \tilde{\sigma}^4 \omega_c \omega_D k^2, \quad (16)$$

$$A_3 = \sigma \tilde{\sigma}^2 g \omega_c \left\{ \frac{d \ln T}{dz} \mathcal{K} - \frac{d \ln \mu}{dz} (k_x^2 + k_y^2) \right\} + \sigma \tilde{\sigma}^2 \omega_D N^2 (k_x^2 + k_y^2), \quad (17)$$

$$A_4 = \tilde{\sigma}^2 \omega_c \omega_D N_{T/\mu}^2 \mathcal{K}, \quad (18)$$

$$B_1 = \sigma^3 \tilde{\sigma}^2 k_{\perp}^2, \quad (19)$$

$$B_2 = \sigma^2 \tilde{\sigma}^2 (\omega_D + \omega_c) k_{\perp}^2, \quad (20)$$

$$B_3 = \sigma^3 b_x^2 k_y^2 N^2 + \sigma \tilde{\sigma}^2 \omega_c \omega_D k_{\perp}^2, \quad (21)$$

$$B_4 = \sigma^2 b_x^2 k_y^2 (N_{T/\mu}^2 \omega_c + N^2 \omega_D), \quad (22)$$

$$B_5 = \sigma b_x^2 k_y^2 N_{T/\mu}^2 \omega_c \omega_D. \quad (23)$$

Here, $k_{\parallel} = \hat{\mathbf{b}} \cdot \mathbf{k}$ and $k_{\perp}^2 = k^2 - k_{\parallel}^2$ and we have defined

$$\begin{aligned} \omega_c &= \frac{2}{5} \frac{\chi_{\parallel} T}{P} k_{\parallel}^2, \\ \omega_v &= 3\nu_{\parallel} k_{\parallel}^2, \\ \omega_D &= D k_{\parallel}^2, \end{aligned} \quad (24)$$

which are the inverse timescales associated with anisotropic heat conduction, viscosity, and particle diffusion. Furthermore, we have introduced the quantity

$$\mathcal{K} = (1 - 2b_z^2)(k_x^2 + k_y^2) + 2b_x b_z k_x k_z, \quad (25)$$

as well as the Brunt–Väisälä frequency, N , such that

$$N^2 = \frac{2}{5} \frac{m_{\text{H}}}{k_{\text{B}}} g \frac{ds}{dz}, \quad (26)$$

and the quantity

$$N_{T/\mu}^2 = g \frac{d}{dz} \ln \left(\frac{T}{\mu} \right). \quad (27)$$

The effects of magnetic tension, which are neglected in Pessah & Chakraborty (2013) and could be important in the inner parts of the ICM (Carilli & Taylor 2002), are contained in

$$\tilde{\sigma}^2 = \sigma^2 + \omega_{\Lambda}^2, \quad (28)$$

where

$$\omega_{\Lambda} = k_{\parallel} v_{\Lambda}, \quad (29)$$

is the Alfvén frequency and $v_{\Lambda} = B/\sqrt{4\pi\rho}$ is the Alfvén velocity.

3.1. Characteristic Scales and Dimensionless Variables

There are a number of characteristic scales that are useful to introduce. The dynamical frequency, ω_{dyn} , is given by

$$\omega_{\text{dyn}} = \sqrt{\frac{g}{H}}, \quad (30)$$

where H is the thermal pressure scale height and g is the gravitational acceleration. We will use that hydrostatic equilibrium requires

$$g \frac{d \ln P}{dz} = -\omega_{\text{dyn}}^2. \quad (31)$$

The plasma- β , given by the ratio of the thermal velocity and the Alfvén speed squared $\beta = v_{\text{th}}^2/v_{\Lambda}^2$, where $v_{\text{th}}^2 = P/\rho$, provides a measure of the strength of the magnetic field.

We also define the Knudsen number

$$\text{Kn} = \frac{\lambda_{\text{mfp}}}{H}, \quad (32)$$

which is a measure of the collisionality of the plasma. Here, λ_{mfp} is the mean-free-path of ion collisions. Intuitively, $\text{Kn}^{-1} = H/\lambda_{\text{mfp}}$ is the average number of collisions an ion experiences as it traverses a distance of one scale height. So $\text{Kn}^{-1} \gg 1$ ($\text{Kn}^{-1} \ll 1$) corresponds to high (low) collisionality. As in Pessah & Chakraborty (2013), we define an effective ion-

ion collision frequency

$$\nu_{ii}^{\text{eff}} = \frac{v_{\text{th}}^2}{2\nu_{\parallel}}, \quad (33)$$

which can be used to express the inverse Knudsen number as

$$\text{Kn}^{-1} = \frac{\nu_{ii}^{\text{eff}}}{\omega_{\text{dyn}}}, \quad (34)$$

by using that $\lambda_{\text{mfip}} = v_{\text{th}}/\nu_{ii}^{\text{eff}}$.

In Section 5, it will prove useful to use a dimensionless form of the theory and present the results in terms of variables that have been scaled using the characteristic time provided by ω_{dyn}^{-1} and the characteristic length given by $(\lambda_{\text{mfip}}H)^{1/2}$. In order to accomplish this, we assume that the inverse timescales for heat conduction and Braginskii viscosity are related to the dynamical frequency via (Kunz 2011)

$$\omega_c \simeq 10k_{\parallel}^2 \lambda_{\text{mfip}} H \omega_{\text{dyn}}, \quad (35)$$

$$\omega_v \simeq \frac{3}{2}k_{\parallel}^2 \lambda_{\text{mfip}} H \omega_{\text{dyn}}. \quad (36)$$

When diffusion of Helium is included in the analysis we furthermore assume that

$$\omega_D \simeq \frac{1}{4}k_{\parallel}^2 \lambda_{\text{mfip}} H \omega_{\text{dyn}}. \quad (37)$$

The approximations given by Equations (35)–(37) are justified in Appendix A.2.

Note that the local linear analysis leading to the dispersion relation in Pessah & Chakraborty (2013) is only valid when the wavenumbers involved satisfy the inequalities

$$\sqrt{\text{Kn}} \ll k_{\parallel}(\lambda_{\text{mfip}}H)^{1/2} \ll \sqrt{\text{Kn}^{-1}}, \quad (38)$$

$$\frac{1}{10\sqrt{\beta\text{Kn}}} \ll k_{\parallel}(\lambda_{\text{mfip}}H)^{1/2} \ll \sqrt{\beta\text{Kn}}. \quad (39)$$

The dispersion relation in Equation (13) is also valid even when the inequality given by Equation (39) is not fulfilled because the effects of magnetic tension, which are proportional to the product βKn in dimensionless variables, are included in its derivation. The dispersion relation is, however, still only adequate for describing scales that are both much longer than the mean-free-path of ion collisions (the fluid limit) and much shorter than the scale height of the atmosphere considered (the local limit). The modes of interest therefore need to fulfill Equation (38).

In the resulting dimensionless variables the gradients in the temperature and the mean molecular weight enter as $d \ln T/d \ln P$ and $d \ln \mu/d \ln P$, making it easier to compare the results of this paper with previous work (Pessah & Chakraborty 2013).

4. STABILITY PROPERTIES

The stability criterion for a stratified *collisional* atmosphere is known as the Schwarzschild criterion (Schwarzschild 1958). According to this criterion, the plasma is stable if the entropy increases with height, z , i.e., if

$$\frac{ds}{dz} > 0. \quad (40)$$

If the atmosphere is stratified in temperature and composition, the criterion determining the stability of the atmosphere becomes

$$\frac{d \ln T/\mu}{d \ln P} < \frac{2}{5}. \quad (41)$$

This is the Ledoux criterion known from stellar convection theory (Ledoux 1947). Isothermal atmospheres with

$$\frac{d \ln \mu}{d \ln P} > -\frac{2}{5}, \quad (42)$$

are therefore stable according to the Ledoux criterion. On the other hand, atmospheres with a uniform composition need to fulfill

$$\frac{d \ln T}{d \ln P} < \frac{2}{5}. \quad (43)$$

If Equation (41) is not fulfilled a fluid element that is perturbed upwards (downwards) will expand (contract) and continue to rise (sink). We will refer to this type of instability as gravity modes.

Atmospheres that satisfy the Ledoux criterion for stability (which assumes that the plasma is collisional) are seen to be unstable when transport processes are anisotropic in a weakly collisional plasma. When anisotropic heat conduction is taken into account, isothermal atmospheres with $-2/5 < d \ln \mu/d \ln P < 0$ are unstable regardless of the magnetic field inclination with respect to gravity. When anisotropic particle diffusion is considered even atmospheres with $d \ln \mu/d \ln P > 0$ can become unstable.

The analysis carried out in Pessah & Chakraborty (2013) shows that there are a host of instabilities that can feed off temperature and composition gradients (see their Figures 2 and 4 for an overview of their results). Here, we focus our attention on the instabilities that have the dominant growth rates for the cluster model of Peng & Nagai (2009) in the regime in which heat conduction is fast with respect to the dynamical timescale, i.e., $\omega_c \gg \omega_{\text{dyn}}$. For convenience, we summarize here some of the most relevant features of these instabilities.

1. The Magneto-thermo-compositional Instability (MTCI) has its fastest growth rate when the magnetic field is perpendicular to the direction of gravity. In the limit of a weak magnetic field the MTCI stability criterion is

$$\frac{d \ln \mu/T}{d \ln P} > 0 \quad \text{if } b_x \neq 0. \quad (44)$$

As pointed out in Pessah & Chakraborty (2013), this criterion for stability is not affected by anisotropic particle diffusion. This feature of the MTCI is explained in further detail in Section 5.2.1.

2. The Heat- and Particle-flux-driven Buoyancy Instability (HPBI) has its fastest growth rate when the magnetic field is parallel to the direction of gravity. If we ignore particle diffusion and magnetic field tension, the HPBI stability criterion is

$$\frac{d \ln \mu T}{d \ln P} > 0 \quad \text{if } b_z \neq 0, \omega_D \ll \omega_{\text{dyn}}. \quad (45)$$

Note that even if this criterion is fulfilled, overstable modes might be present, see Equation (57) in Pessah & Chakraborty (2013).

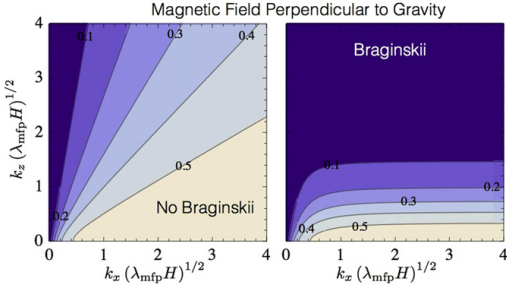


Figure 1. Contour plots of $\sigma/\omega_{\text{dyn}}$ for the MTCI with $d \ln \mu/d \ln P = -1/3$ without (left) and with Braginskii viscosity (right). Because of the similarity between the MTI and the MTCI these figures are similar to Figure 5 in Kunz (2011).

3. The diffusive HPBI, which depends on anisotropic diffusion of particles, has its fastest growth rate when the magnetic field is parallel to the direction of gravity. The diffusive HPBI ($\omega_D \neq 0$) has a stability criterion which is qualitatively different from the non-diffusive HPBI ($\omega_D = 0$). The criterion for stability for the diffusive HPBI is

$$\frac{d \ln T/\mu}{d \ln P} > 0 \quad \text{if } b_z \neq 0, \omega_D \gg \omega_{\text{dyn}}. \quad (46)$$

4. A type of instability driven by anisotropic diffusion of Helium, which we refer to as diffusion modes, also depend on $\omega_D \neq 0$. Diffusion modes have their fastest growth rate when the magnetic field is parallel to the direction of gravity. The stability criterion for diffusion modes is²

$$\left| \frac{d \ln T}{d \ln P} \right| > \left| \frac{d \ln \mu}{d \ln P} \right| \quad \text{if } b_z \neq 0, \omega_D \neq 0. \quad (47)$$

When the mean molecular weight is constant, Equation (44) reduces to the stability criterion for the MTI and Equations (45) and (46) both reduce to the stability criterion for the HBI. These instabilities, driven by thermal gradients in weakly collisional, homogeneous plasmas, have been studied in great detail (Balbus 2000, 2001; Parrish & Stone 2005, 2007; Parrish & Quataert 2008; Parrish et al. 2008; Quataert 2008; Kunz 2011; Kunz et al. 2012; Latter & Kunz 2012; Parrish et al. 2012a).

Before considering the instabilities that are present when the temperature and composition gradients are those obtained from current sedimentation models, we consider a series of simpler cases in order to build our intuition.

5. APPLICATION TO ISOTHERMAL ATMOSPHERES

In order to shed light on the instabilities that are driven by composition gradients we focus our attention on the case of isothermal atmospheres in which the mean molecular weight increases with height. For these atmospheres, the stability

² There is a typo in the text below Equation (63) in Pessah & Chakraborty (2013) where the stability criterion is missing an absolute value sign acting on the left hand side of the inequality. This typo does not affect any conclusions or figures in their paper.

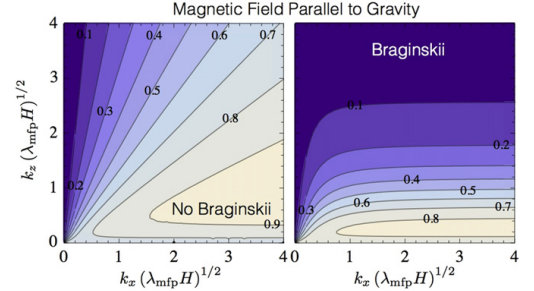


Figure 2. Contour plots of $\sigma/\omega_{\text{dyn}}$ for the HPBI with $d \ln \mu/d \ln P = -1$ without (left) and with Braginskii viscosity (right). The qualitative behavior is similar to the HBI but the maximum growth rates are located at smaller $k_z (\lambda_{\text{mfp}} H)^{1/2}$. Gravity modes are seen at low $k_z (\lambda_{\text{mfp}} H)^{1/2}$.

criteria for the HPBI and the MTCI, Equations (45) and (44), both reduce to $d \ln \mu/d \ln P > 0$. In the following we analyze simple magnetic field geometries and assume, for simplicity, that the magnetic field strength is negligible and thus $\omega_A = 0$. In this section, we calculate the growth rates associated with axisymmetric modes as a function of the wavenumbers k_x and k_z . Here, k_x is the wavenumber perpendicular to gravity and k_z is the wavenumber parallel to gravity. The latter corresponds to the radial direction in the ICM. We relate our results to the findings of Kunz (2011), who analyzed the MTI and the HBI in detail.

5.1. Isothermal Atmospheres with No Particle Diffusion

We solve the dispersion relation, Equation (13), for an isothermal atmosphere with a gradient in composition in the limit where diffusion of particles is neglected ($\omega_D = 0$).

5.1.1. Magnetic Field Perpendicular to Gravity

We start out by considering the configuration where the MTCI is maximally unstable, namely, a horizontal magnetic field, i.e., $b_x = 1$. We consider an atmosphere with $d \ln \mu/d \ln P = -1/3$. This atmosphere is stable according to the Ledoux criterion, Equation (42), which means that it would be stable if the plasma were collisional. However, it is unstable according to the MTCI criterion that applies in the weakly collisional regime.

There is an interesting correspondence between the MTI and MTCI, which is useful in order to make connections with previous results. In order to illustrate this, let us ignore particle diffusion of He ($\omega_D = 0$). In this case, the dispersion relation given by Equation (13) only depends on the gradients in temperature and mean molecular weight through the combination $d \ln(T/\mu)/d \ln P$. This means that the dispersion relation for the MTCI at constant temperature with $d \ln \mu/d \ln P = -1/3$, is identical to the dispersion relation for the MTI with $d \ln T/d \ln P = 1/3$. The crucial difference is of course that in the former case the instabilities are driven by the temperature gradient, whereas in the latter case they are driven by the composition gradient.

The correspondence between MTI and MTCI is illustrated in Figure 1, where we show the growth rate of unstable modes when $d \ln \mu/d \ln P = -1/3$ and obtain a similar result as Kunz (2011) did for the MTI with $d \ln T/d \ln P = 1/3$. In the

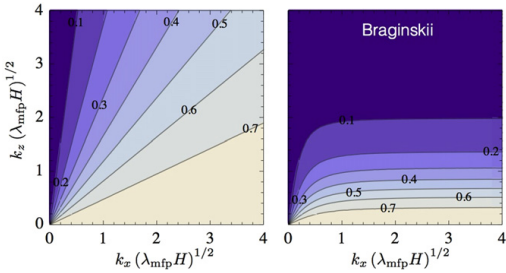


Figure 3. Contour plots of $\sigma/\omega_{\text{dyn}}$ for gravity modes with $d \ln \mu/d \ln P = -1$ which appear even without anisotropic transport. Left: Without Braginskii viscosity and the growth rate of gravity modes is independent of the magnetic field inclination. Right: With Braginskii viscosity and the gravity modes with $k_z(\lambda_{\text{mfp}}H)^{1/2} \gtrsim 2$ have negligible growth rate due to damping by Braginskii viscosity. The damping depends on the magnetic field inclination which is taken to be $\theta = 90^\circ$.

left panel of Figure 1, Braginskii viscosity is not included and the maximum growth rate has $k_z = 0$. The maximum growth rate of $\sigma/\omega_{\text{dyn}} = 0.5$ is confined to a wedge in wavenumber space with $k_z \lesssim 0.5k_x$. In the right panel of Figure 1, Braginskii viscosity is included and the growth rate of $\sigma/\omega_{\text{dyn}} = 0.5$ is now confined to a thin band with $k_z(\lambda_{\text{mfp}}H)^{1/2} \lesssim 0.3$. We observe that the growth rates are only significant when $k_z(\lambda_{\text{mfp}}H)^{1/2} \ll k_x(\lambda_{\text{mfp}}H)^{1/2}$. This preference for parallel wavenumbers ($k_{\text{max}} \approx k_{\parallel}$, where k_{max} is the wavenumber for σ_{max}) is thoroughly investigated by Kunz (2011). Due to the identical dispersion relations for the MTI and the MTCI at constant temperature, we therefore refer to Equations (62) (without Braginskii viscosity) and (64) (with Braginskii viscosity) in Kunz (2011) for approximate limits on the magnitude of k_{\perp} above which the growth rates become negligible.

5.1.2. Magnetic Field Parallel to Gravity

Next, we consider the case of $b_z = 1$, i.e., a vertical magnetic field, where the HPBI is maximally unstable. The growth rate for the HPBI as a function of wavenumber is shown in Figure 2 for the case of $d \ln \mu/d \ln P = -1$.

In the left panel of Figure 2, Braginskii viscosity is not included and the large growth rates are confined to $k_z \lesssim k_x$. In the right panel of Figure 2, Braginskii viscosity is included and the preference for $k_{\perp} \gg k_{\parallel}$ is increased. The growth rate of $\sigma/\omega_{\text{dyn}} = 0.8$ is now confined to $0.05 \lesssim k_z(\lambda_{\text{mfp}}H)^{1/2} \lesssim 0.3$. We conclude that the HPBI favors wavenumbers that have a large perpendicular component and that the available wavenumber space is a narrow band with $k_{\perp} \gg k_{\parallel}$ when Braginskii viscosity is included in the analysis.

Figure 2 looks remarkably similar to the corresponding figure for the HBI (with $d \ln T/d \ln P = -1$) presented in Kunz (2011) but they are not identical at low $k_z(\lambda_{\text{mfp}}H)^{1/2}$. Even though the HBI and HPBI both have the property that $\sigma = 0$ for $k_{\parallel} = 0$ we observe that $\sigma/\omega_{\text{dyn}} \approx 0.7$ along the line of $k_{\parallel} = 0$ in both the left and right panels of Figure 2. The explanation is that gravity modes are unstable for different signs of the logarithmic derivatives of T and μ , as seen in Equations (42) and (43). The growth rate of gravity modes for $d \ln \mu/d \ln P = -1$ at these wavenumbers has the value $\sigma/\omega_{\text{dyn}} \approx 0.7$. The reason for gravity modes at low

$k_z(\lambda_{\text{mfp}}H)^{1/2}$ is that heat conduction is too slow to drive the HPBI when k_{\parallel} is small. The gravity modes do not depend on heat conduction and they are therefore dominant in this slow conduction limit.

The gravity modes are not seen at high $k_z(\lambda_{\text{mfp}}H)^{1/2}$ because they are damped by Braginskii viscosity. Even though the HPBI is also damped by Braginskii viscosity, the HPBI turns out to have a higher growth rate than the gravity modes at high $k_z(\lambda_{\text{mfp}}H)^{1/2}$. Gravity modes are present even in the absence of anisotropic transport, as illustrated in the left panel of Figure 3. The damping of gravity modes by Braginskii viscosity is demonstrated in the right panel of Figure 3.

An important conclusion in Kunz (2011) is that the local mode analysis for the HBI is not strictly valid when Braginskii viscosity is taken into account because the largest growth rates are obtained for $k_{\parallel} < H^{-1}$, implying that Equation (38) is not satisfied. The HPBI has its maximum growth rate at even longer wavelengths than for the HBI and we therefore reach a similar conclusion for the HPBI at constant temperature as Kunz (2011) did for the HBI. A quasi-global model has been developed for the HBI by Latter & Kunz (2012). This kind of approach can also be generalized to develop quasi-global models including composition gradients.

5.1.3. More General Magnetic Field Geometries

In this section, we explore the consequences of the presence of a magnetic field which is inclined at an angle θ with respect to the horizontal. The components of \hat{b} are thus given by $b_x = \cos \theta$ and $b_z = \sin \theta$. In the previous two sections, and in agreement with Kunz (2011), we showed that Braginskii viscosity can play a significant role in the growth of modes driven by composition gradients. Therefore, we include both anisotropic heat conduction and Braginskii viscosity in our analysis.

We consider an atmosphere with $d \ln \mu/d \ln P = -1$ which is maximally unstable to the MTCI when $\theta = 0^\circ$ and to the HPBI when $\theta = 90^\circ$. Figure 4 shows the unstable modes that emerge as the inclination of the magnetic field is varied, increasing from $\theta = 0^\circ$ in the leftmost panel to $\theta = 90^\circ$ in the rightmost panel. The directions of $\mathbf{k} = k_{\parallel}$ and $\mathbf{k} = k_{\perp}$ are indicated with a red solid line and a red dashed line, respectively. In the previous sections we argued that the MTCI has its maximum growth rate for wavenumbers with $k_{\parallel} \gg k_{\perp}$ while the HPBI has its maximum growth rate for $k_{\perp} \gg k_{\parallel}$. This provides an intuitive way to interpret Figure 4 which illustrates that the isothermal atmosphere is unstable regardless of the magnetic field inclination, θ .

The results displayed in Figure 4 can be analyzed further with the insights gained earlier in this section. Only the MTCI is unstable in the first panel ($\theta = 0^\circ$) and the most unstable wavenumbers lie in a band along $k_z = k_{\perp} = 0$. In the second panel, this unstable band is rotated to lie along $\theta = 30^\circ$, which is the angle of k_{\parallel} with respect to the horizontal. At the same time, a new unstable band has appeared in the direction $\mathbf{k} = \mathbf{k}_{\perp}$. This is the HPBI which prefers $k_{\perp} \gg k_{\parallel}$. We note again that both the MTCI and the HPBI have zero growth rate along $k_{\parallel} = 0$ (the dashed line) and so the growth rates seen along this line must be due to gravity modes.

In the third panel ($\theta = 45^\circ$), both unstable bands have rotated by another 15° . The maximum growth rate of the HPBI (MTCI) unstable band has increased (decreased) to $\sigma/\omega_{\text{dyn}} = 0.6$ ($\sigma/\omega_{\text{dyn}} = 0.7$). The maximum growth rate is

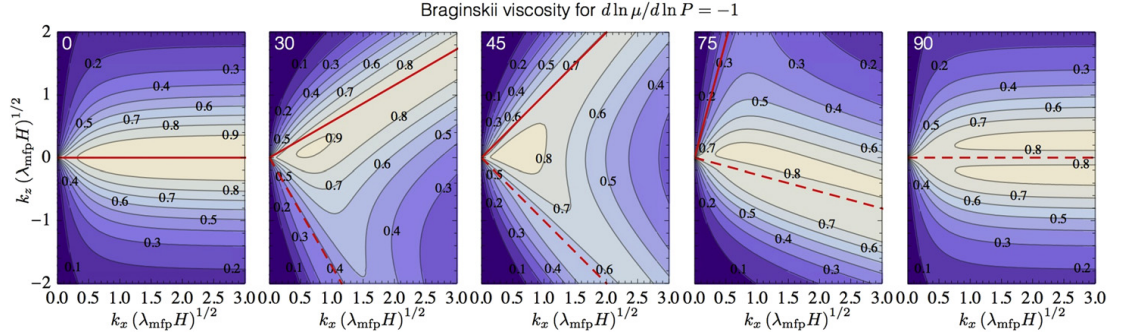


Figure 4. Contour plots of $\sigma/\omega_{\text{dyn}}$ for an isothermal atmosphere with $d \ln \mu / d \ln P = -1$, with Braginskii viscosity. The red solid line indicates $k = k_{\parallel}$ and the red dashed line indicates $k_{\perp} = 0$. The MTCI has its maximum growth rate for $k = k_{\parallel}$ and the HPBI has its maximum growth rate with a small parallel component ($k \gg k_{\parallel}$). The inclination of the magnetic field is written in degrees at the top, left corner in each panel.

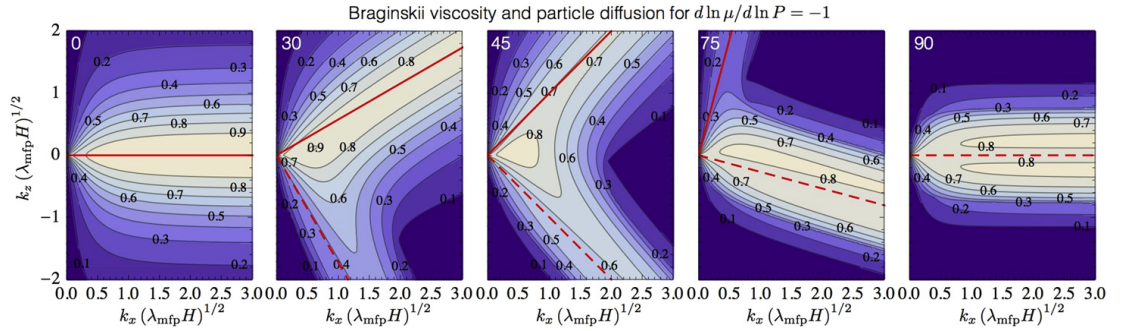


Figure 5. Contour plots of $\sigma/\omega_{\text{dyn}}$ for an isothermal atmosphere with $d \ln \mu / d \ln P = -1$, with Braginskii viscosity and particle diffusion. The red solid line indicates $k = k_{\parallel}$ and the red dashed line indicates $k_{\perp} = 0$. The inclination of the magnetic field is written in degrees at the top, left corner in each panel. From left to right: The MTCI at constant temperature is weakened as the magnetic field becomes more vertical. It has its fastest growing modes along $k = k_{\parallel}$. The slow diffusion modes and the diffusive HPBI are maximally unstable when the magnetic field is vertical. They are visible from the second figure and onwards. In the last figure the field is entirely vertical and the MTCI is stabilized. The instabilities that remain are the slow diffusion modes, the diffusive HPBI and the gravity modes.

found in a region around $k_z = 0$ and it difficult to associate this wavenumber with a specific instability. In the fourth panel ($\theta = 75^\circ$), the maximum growth rate of the HPBI unstable band has increased even further and it is now larger than the maximum growth rate of the MTCI whose growth rate has decreased down to $\sigma/\omega_{\text{dyn}} = 0.3$. In the final panel ($\theta = 90^\circ$), the MTCI is completely stabilized and only the modes associated with the HPBI remain.

5.2. Diffusion of Helium

In this section, we consider the stability properties of a weakly collisional, weakly magnetized, binary plasma with Braginskii viscosity and anisotropic diffusion of particles. We focus our attention on isothermal atmospheres that are stratified in composition.

5.2.1. An Atmosphere with $d \ln \mu / d \ln P = -1$

We start out by considering an atmosphere with $d \ln \mu / d \ln P = -1$ which is unstable to gravity modes. When the effect of anisotropic diffusion of He is ignored, this atmosphere is generally unstable to both the MTCI and the

HPBI, as shown in the previous section. In this section diffusion of particles is included in the analysis.

The anisotropic diffusion of He enables a number of new processes (Pessah & Chakraborty 2013). First and foremost, a new type of instabilities, termed diffusion modes, appear. These modes only exist due to anisotropic diffusion of Helium and their growth rate increase with the value of the diffusion coefficient, D . Second, a new type of instability, termed the diffusive HPBI (Pessah & Chakraborty 2013) appears in place of the HPBI when $\omega_D \gg \omega_{\text{dyn}}$.

The stability criterion for the MTCI is unaffected by the presence of particle diffusion, as seen in Equations (60) and (68) in Pessah & Chakraborty (2013). The fact that the stability criterion of the MTCI is unaffected can be understood intuitively by considering a fluid parcel moving upwards in a gravitational potential while being connected to its previous surroundings by a magnetic field line. The vertical displacement of the parcel gives rise to an expansion of the parcel. In the absence of heat transfer to the parcel this expansion would lead to a decrease in the temperature. Due to anisotropic heat conduction, however, the magnetic field line is effectively an isotherm. The parcel is therefore heated from below,

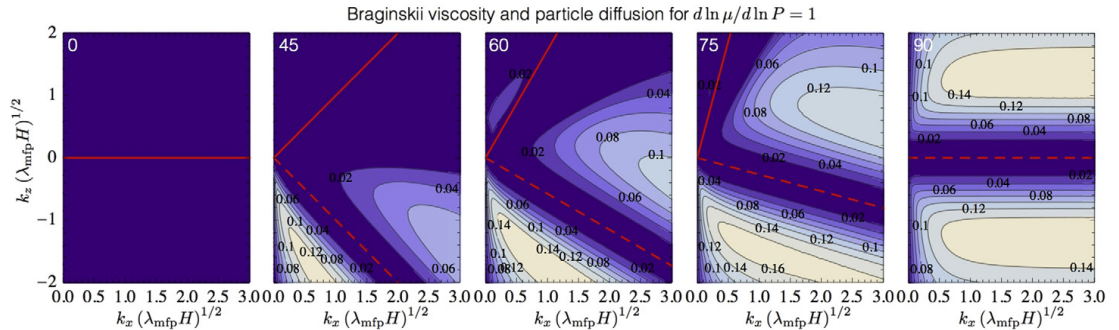


Figure 6. Diffusion modes for $d \ln \mu/d \ln P = 1$. This instability is driven by diffusion of He and is only unstable when $D = 0$ and $b_z \neq 0$. The diffusion mode with $d \ln \mu/d \ln P = 1$ operates on a smaller length scale than the diffusion mode with $d \ln \mu/d \ln P = -1$.

rendering it unstable. This mechanism for instability is the same as for the MTI but with the mean molecular weight playing the role of the temperature in the background atmosphere. The mean molecular weight is initially constant along the field line and it is unaffected by expansions or contractions of the fluid parcel. The vertical displacement does therefore not give rise to any anisotropic particle diffusion along the field line and we conclude that the MTCI should be largely unaffected by $D \neq 0$.

The new features enabled by particle diffusion are illustrated in Figure 5, which only differs from Figure 4 in that particles are able to diffuse along magnetic field lines, i.e., $\omega_D = k_{\parallel}^2 \lambda_{\text{mfp}} H \omega_{\text{dyn}}/4$. The first and leftmost panels of Figures 4 and 5 are identical because the MTCI is mostly unaffected by particle diffusion, as explained above. The second panel shows the MTCI unstable band along k_{\parallel} and the diffusion modes along k_{\perp} . In the third panel, where the magnetic field is inclined at 45° , there is a region of stability between the two bands of unstable modes. This is in stark contrast with the third panel of Figure 4 where the corresponding region has significant growth rates. The fifth and rightmost panel of Figure 5 can be roughly divided into two unstable bands: an inner band with a growth rate of $\sigma/\omega_{\text{dyn}} = 0.7$ and an outer band with a maximum growth rate of $\sigma/\omega_{\text{dyn}} = 0.2$. The inner band has the same growth rate as the gravity modes seen in the fifth panel of Figure 4 and the second panel of Figure 2. The maximum growth rate of $\sigma/\omega_{\text{dyn}} = 0.8$ is confined to a small area of wavenumber space. Furthermore, we see that a large region of wavenumber space is stable when particle diffusion is included. We conclude that the instabilities have an even stronger tendency to prefer $k_{\perp} \gg k_{\parallel}$ when particle diffusion is included.

5.2.2. An Atmosphere with $d \ln \mu/d \ln P = 1$

Next, we consider an atmosphere with $d \ln \mu/d \ln P = 1$. This atmosphere is only unstable when anisotropic diffusion of particles is taken into account. Furthermore, the unstable modes require that the magnetic field has a vertical component, i.e., $b_z \neq 0$. The growth rates of the diffusion modes are shown in Figure 6. These diffusion modes have a preference for $k_{\perp} \gg k_{\parallel}$ but they have zero growth rate if $k_{\parallel} = 0$. Interestingly, they grow on a smaller length scale than the diffusion modes found for $d \ln \mu/d \ln P < 0$. This type of atmosphere (isothermal with the mean molecular weight decreasing with height) is

relevant in the context of the boundary between the intermediate and the outer ICM in the model of Peng & Nagai (2009) that we discuss next.

6. APPLICATIONS TO SEDIMENTATION MODELS

Having gained some insight into the various instabilities that can be triggered by the presence of a composition gradient in an isothermal environment, we now address the stability properties of more realistic scenarios, relevant to the conditions expected in the ICM. In order to accomplish this, we consider one of the models for Helium sedimentation introduced in Peng & Nagai (2009). Before we present the analysis of the stability of a cluster model in which Helium has sedimented efficiently, we provide a brief summary of the assumptions and procedure involved in deriving these models.

6.1. Spherically Symmetric Helium Sedimentation Models

In the He sedimentation model of Peng & Nagai (2009) the plasma is assumed to be in hydrostatic equilibrium in the gravitational potential that is mainly due to dark matter. The composition is initially uniform with $c = 0.25$ ($\mu = 0.59$) at all radii as given by the primordial abundance of Helium. The temperature of the cluster has a radial dependence that is motivated by observations and it is fixed in time. This amounts to assuming that heating and cooling are balanced at all radii. This assumption is also made, for instance, in Shtykovskiy & Gilfanov (2010). Furthermore, because the stellar mass content of a cluster is smaller than the total Helium mass, enrichment from galaxies can be ignored (Markevitch 2007).

Given this initial setup, the Burgers' equations (Burgers 1969; Thoul et al. 1994) are solved for each ion species of the plasma assumed to consist of Hydrogen and Helium ions, as well as electrons. The diffusion velocity of the Helium ions is found by assuming that the gravitational force on the Helium ions is balanced by the force due to electric fields, the gradient in partial pressure and resistance due to collisions with Hydrogen ions. The result is a slow gravitational settling of Helium ions toward the core and the development of a non-uniform composition profile. This change in the composition of the gas takes the cluster out of hydrostatic equilibrium. This is caused by the change in the pressure which depends on the mean molecular weight, μ , see Equation (8). Burgers' equations only describe the relative motion of the species and so a momentum equation for the bulk flow of the gas needs to

be solved in order to describe the restoration of hydrostatic equilibrium. The radial distribution of Hydrogen and Helium is evolved by repeating these steps over cosmological timescales.

6.2. Evolving the Composition in Sedimentation Models

A brief summary of the calculations involved in the models described in detail in Peng & Nagai (2009) can be outlined as follows.

The total density distribution (gas + dark matter) of the cluster is given by the Navarro–Frenk–White profile (Navarro et al. 1997)

$$\rho_{\text{tot}}(r) = \frac{\rho_s}{r/r_s(1+r/r_s)^2}, \quad (48)$$

where ρ_s is a normalization constant and r_s is a characteristic scale. The total mass, $M(r)$, enclosed within the radius, r , can be found by integrating the density distribution. This yields

$$M(r) = 4\pi\rho_s r_s^3 \left[\ln(1+r/r_s) - \frac{r/r_s}{1+r/r_s} \right], \quad (49)$$

from which one can find the gravitational acceleration at a distance r

$$g(r) = \frac{GM(r)}{r^2}, \quad (50)$$

where G is the gravitational constant.

As per convention, r_{500} (r_{2500}) is defined to be the radius inside of which the mean density is 500 (2500) times the critical density of the universe. The value of r_s is chosen such that $r_s = 0.25r_{500}$. The model presented here has $r_{500} = 1.63$ Mpc, $r_{2500} = 0.75$ Mpc and a total cluster mass, $M(r_{500}) = 1.24 \times 10^{15} M_\odot$ where M_\odot is the solar mass. The ratio of the mass of the ICM to the total mass of the cluster is assumed to be 0.15 at r_{500} . The temperature profile is given by

$$\frac{T(r)}{T_0} = \frac{(r/0.045r_s)^{1.9} + 0.45}{(r/0.045r_s)^{1.9} + 1} \frac{1.216}{[1 + (r/0.6r_s)^2]^{0.45}}, \quad (51)$$

where $T_0 = 10$ keV. The parameters used in the model and the functional dependence of $T(r)$ are motivated by a *Chandra* sample of 13 nearby, relaxed galaxy clusters (Vikhlinin et al. 2006). The density, ρ , and pressure, P , of the gas is found by solving the equation of hydrostatic equilibrium

$$\frac{dP}{dr} = -\rho g(r), \quad (52)$$

where the gravitational potential is given by Equation (50) and the pressure is related to the density by Equation (8).

Burgers' equations, namely, the continuity and momentum equations for each species, s , are given by (Burgers 1969; Thoul et al. 1994)

$$\frac{\partial n_s}{\partial t} + \frac{1}{r^2} \frac{\partial(r^2 n_s u_s)}{\partial r} = 0, \quad (53)$$

$$\frac{\partial P_s}{\partial r} + n_s A_s m_{\text{H}} g - n_s Z_s e E = \sum_t K_{st} (w_t - w_s), \quad (54)$$

where n_s is the number density, u_s is the velocity, and w_s is the velocity of species s relative to the bulk velocity of the fluid, u . The mass and charge numbers of ion species s are given by A_s

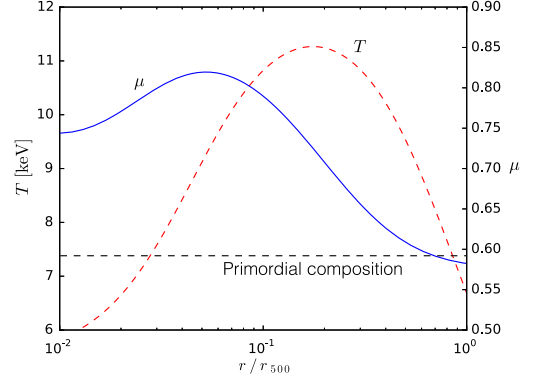


Figure 7. Mean molecular weight profile (blue line) in a 11 Gyr-old galaxy cluster and the temperature profile (red dashed line) used in the model of Peng & Nagai (2009). The dashed black line indicates the primordial composition at $t = 0$ Gyr which is $\mu = 0.59$.

and Z_s . The electric field is given by E and the resistance coefficients are given by

$$K_{st} = f_B^{-1} \frac{4\sqrt{2\pi}}{3} \frac{e^4 Z_s^2 Z_t^2 m_{st}^{1/2}}{(k_B T)^{3/2}} n_s n_t \ln \Lambda_{st}, \quad (55)$$

where m_{st} is the reduced mass and $\ln \Lambda_{st}$ is the Coulomb logarithm of species s and t , which we set to 40 (see more details in Appendix B). The parameter f_B^{-1} is the magnetic suppression factor that regulates the slow down of the sedimentation process envisioned to arise as a result of tangled magnetic fields. The profiles shown in Figure 7 have been obtained by setting $f_B = 1$ and thus ignore this effect.

Burgers' equations are solved along with the momentum equation for the bulk motion of the gas

$$\rho \frac{du}{dt} = -\frac{\partial P}{\partial r} - \rho g(r), \quad (56)$$

and the distribution of elements is found as a function of time.

We show the results from a calculation using this method in Figure 7 which was produced by rerunning the code³ developed by Peng & Nagai (2009). In this figure, the mean molecular weight profile for a 11 Gyr-old cluster is shown along with the temperature profile used for the calculation. A simple explanation of the peak in the mean molecular weight is that the resistance coefficient depends strongly on temperature. This means that He sedimentation will tend to be most effective where the temperature is high. The dashed black line shows the initial (primordial) composition of the plasma.

Efficient sedimentation in the ICM can lead to biases in the estimates of key parameters of clusters if the sedimentation is not taken into account in the data analysis. The specific model described here would lead to biases of 6% in the total mass and gas mass at $r = r_{2500}$ if a homogeneous plasma is assumed. This would create a bias of 12% in the gas mass fraction of the cluster and a bias of around 20% in the estimate for the Hubble constant (see Figure 4 in Peng & Nagai 2009). In the next

³ The authors of Peng & Nagai (2009) kindly provided us with a copy of the original Fortran code used for their paper.

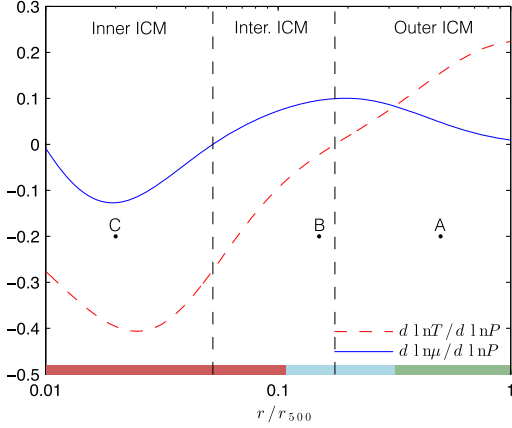


Figure 8. Gradients $d \ln T / d \ln P$ (red dashed line) and $d \ln \mu / d \ln P$ (blue line) as a function of radius in the model of Peng & Nagai (2009) at $t = 11$ Gyr. The ICM is divided into inner ICM, intermediate ICM and outer ICM. The color bar illustrates which instabilities could be triggered, see Figure 9 for the color coding. The labels A, B, and C indicate the radii used to produce Figures 11–13.

section we discuss how the composition profile inferred from the model could be unstable at all radii due to plasma instabilities.

6.3. Stability Analysis of Helium Sedimentation Models

The model presented in Peng & Nagai (2009) provides estimates for the derivatives $d \ln T / d \ln P$ and $d \ln \mu / d \ln P$ as a function of radius. This is illustrated in Figure 8, where we have divided the ICM into three regions. The inner ICM which extends from $r/r_{500} = 0.01$ to the radius where $d \ln \mu / d \ln P = 0$ ($r/r_{500} = 0.05$) and the outer ICM which extends from the radius where $d \ln T / d \ln P = 0$ ($r/r_{500} = 0.18$) to the radius $r/r_{500} = 1$. The intermediate ICM is defined to be the region in between the previous two.

Before delving into details, we can provide a qualitative idea about which parts of the ICM are prone to the different types of instabilities. In order to do this, we consider the numerical values of the gradients in temperature and composition in the context of the stability diagrams introduced in Pessah & Chakraborty (2013; see Figures 2 and 3 in their paper). The comparison is facilitated by using a parametric plot in the $(d \ln \mu / d \ln P, d \ln T / d \ln P)$ plane, see Figure 9. The colored sections in this figure indicate the regions of parameter space which are subject to the different types of instabilities discussed in Section 4. The extent of these regions is also indicated with color bars at the bottom of Figure 8. The red color bar indicates the region where the diffusive HPBI could be active and the blue bar indicates the region where the diffusive HPBI and the diffusion modes could be active. Finally, the region highlighted by the green bar is unstable to the MTCI and the conduction modes.⁴ These conclusions require, of course, that the magnetic field geometry allows for the various instabilities to be triggered.

⁴ The conduction modes are important in the slow conduction limit, $\omega_c \ll \omega_{\text{dyn}}$, see Pessah & Chakraborty (2013).

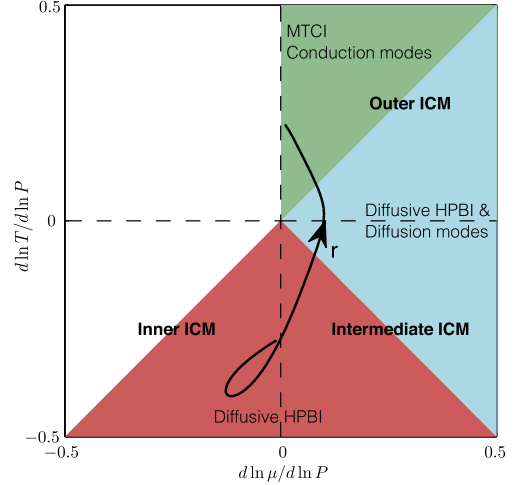


Figure 9. Parametric plot in the $(d \ln \mu / d \ln P, d \ln T / d \ln P)$ plane as a function of r/r_{500} (black line with arrow indicating the direction of increasing radial distance). Red is unstable to the diffusive HPBI. Blue is unstable to the diffusive HPBI and the diffusion modes. Green is unstable to the MTCI and the conduction modes. Comparing this figure with the stability diagrams of Pessah & Chakraborty (2013) leads to the color bars identifying the different regions in Figure 8.

The stability criteria derived in Pessah & Chakraborty (2013) assume that magnetic tension is negligible. In order to assess whether this effect could be important, we need a model for the magnetic field strength in the ICM. We can estimate the plasma β as a function of cluster radius, $\beta(r)$, for the model of Peng & Nagai (2009), by using

$$B(r) = B_0 \left(\frac{n_e(r)}{n_e(0)} \right)^\eta, \quad (57)$$

where n_e is the electron number density, $B_0 = 4.7 \mu\text{G}$, and $\eta = 0.5$, as found for the Coma cluster in Bonafede et al. (2010). The quantitative results therefore depend on this choice while the qualitative results should not. Using this model, we illustrate in Figure 10 the potential role that magnetic tension could play, especially in the inner parts of the ICM. The assumptions made in Pessah & Chakraborty (2013) are valid within region 4 in Figure 10. The dispersion relation derived in this paper extends the validity of the analysis to also include regions 2 and 5 where magnetic tension is important. For the sake of completeness, we recall that the fluid approximation breaks down in region 1 and 3 and that the local approximation in the linear analysis breaks down in region 6 and 7.

In what follows, we discuss the growth rates and the characteristic distances on which the various instabilities could operate in the cluster model of Peng & Nagai (2009) at $t = 11$ Gyr. Using the radial profiles provided by the model, we can calculate the values of the needed parameters ($d \ln T / d \ln P$, $d \ln \mu / d \ln P$, ω_{dyn} , H , λ_{mfP} , Kn , χ_{\parallel} , ν_{\parallel} , D) as a function of radius. In addition to the model of Peng & Nagai (2009) we consider a magnetic field given by Equation (57) to estimate β .

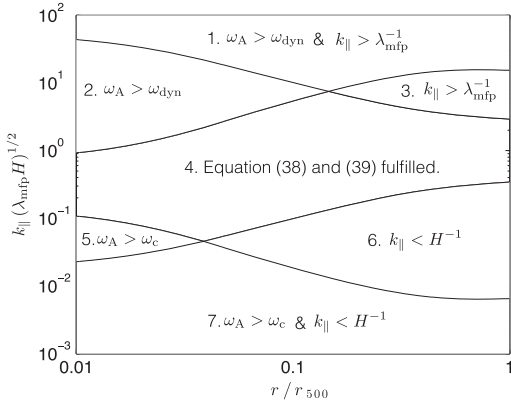


Figure 10. Validity of the local linear analysis as a function of radius. The results of Pessah & Chakraborty (2013) are valid within region 4. The effects of magnetic tension should be accounted for in regions 2 and 5. The fluid approximation breaks down in region 1 and 3 and the local approximation breaks down in region 6 and 7.

In order to assess the influence of the sedimentation of Helium on the stability properties of the ICM we solve the dispersion relation for the sedimentation model of Peng & Nagai (2009) at both $t = 0$ Gyr and $t = 11$ Gyr. We include anisotropic heat conduction, Helium diffusion, Braginskii viscosity and a finite β in the calculations in Sections 6.4–6.6. The effect of Braginskii viscosity is to damp perturbations with short perpendicular wavenumbers. The effect of the magnetic tension is to stabilize modes with short parallel wavenumbers and, in general, to inhibit the growth rates. The role of magnetic tension in decreasing the maximum growth rate is investigated in Section 7. In the following we consider each of the three regions of the ICM defined in Figure 8 separately.

6.4. Outer ICM

In the model of Peng & Nagai (2009) at $t = 11$ Gyr, both the temperature and the mean molecular weight decrease with radial distance in the outer ICM, as illustrated in Figure 7. In the inner part of the outer ICM we have $d \ln \mu / d \ln P > d \ln T / d \ln P$, see Figure 8, and this makes this region unstable to diffusion driven modes and the diffusive HPBI at short parallel wavenumbers and to the diffusion modes at long parallel wavenumbers. In the outer part of the outer ICM we have $d \ln \mu / d \ln P < d \ln T / d \ln P$ which makes this region unstable to the MTCI and to conduction modes at long parallel wavenumbers. The model at $t = 0$ Gyr, before Helium has had time to sediment, is unstable to the MTI. We note that these conclusions depend on the magnetic field geometry.

As an illustration, we consider a magnetic field inclined at $\theta = 45^\circ$ at a specific radial distance, $r/r_{500} = 0.5$, indicated with a letter A on Figure 8. Using values evaluated at this location ($d \ln T / d \ln P = 0.16$ and $d \ln \mu / d \ln P = 0.05$ at $t = 11$ Gyr and $d \ln T / d \ln P = 0.16$ and $d \ln \mu / d \ln P = 0$ at $t = 0$ Gyr) we calculate the growth rates, as shown in Figure 11. In the panel on the left (right) we show the growth rate as a function of wavenumber for the model at $t = 0$ Gyr ($t = 11$ Gyr). We observe that the maximum growth rate is

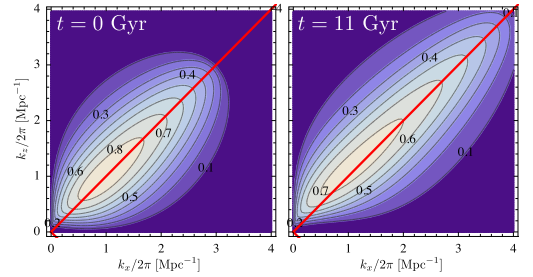


Figure 11. Contour plots of the growth rate in Gyr^{-1} for the outer ICM (location C). This region is unstable to the MTI at $t = 0$ Gyr (left panel) or the MTCI and the conduction modes at $t = 11$ Gyr (right panel). The most unstable modes are found at intermediate parallel wavenumbers because magnetic tension stabilizes modes with a high parallel wavenumber. The maximum growth rate is decreased by 15% with respect to the homogeneous case.

$\sigma \approx 0.87 \text{ Gyr}^{-1}$ without Helium sedimentation ($t = 0$ Gyr) and $\sigma \approx 0.75 \text{ Gyr}^{-1}$ with Helium sedimentation ($t = 11$ Gyr) such that the instabilities grow unstable on a timescale of either 1.15 Gyr or 1.3 Gyr, respectively. The presence of Helium sedimentation is concluded to lead to a decrease in the growth rate by approximately 15%, in agreement with the rough estimate in Pessah & Chakraborty (2013). Considering a characteristic scale $L = 2\pi/k$, the fastest growing mode corresponds to $(L_x, L_z) = (1.0, 1.0)$ Mpc at $t = 0$ Gyr. This scale is slightly decreased to $(L_x, L_z) = (0.9, 0.8)$ Mpc at $t = 11$ Gyr. The unstable modes found are describable by a fluid approach (at this radial distance $\lambda_{\text{mfp}} = 30$ kpc) but they are not strictly describable by a local linear analysis (at this radial distance $H = 0.35$ Mpc). The value of ω_{dyn}^{-1} at this distance is roughly 0.3 Gyr so the instability grows on a timescale a factor of a few larger than the dynamical timescale.

6.5. Intermediate ICM

According to the model at $t = 11$ Gyr, the temperature increases while the mean molecular weight decreases with radial distance in the intermediate ICM. The stability diagrams of Pessah & Chakraborty (2013) then reveal that the intermediate ICM is unstable to the diffusive HPBI in the entire region. Furthermore, the outer part of the intermediate ICM is unstable to the diffusion modes.

For illustrative purposes, we consider the radial distance indicated with a letter B on Figure 8 which is located at $r/r_{500} = 0.15$. At this location, $d \ln T / d \ln P = -0.02$ and $d \ln \mu / d \ln P = 0.1$ at $t = 11$ Gyr and so the diffusion modes and the diffusive HPBI are expected to be active. In the absence of sedimentation this radial distance is unstable to the HBI ($d \ln T / d \ln P = -0.03$ and $d \ln \mu / d \ln P = 0$ at $t = 0$ Gyr). We consider the growth rates for the $t = 0$ Gyr cluster in the left panel and the $t = 11$ Gyr in the right panel of Figure 12. In this figure we have assumed $\theta = 75^\circ$. The intermediate region is stabilized by the gradient in composition at $t = 11$ Gyr if anisotropic particle diffusion is neglected ($D = 0$) but when anisotropic particle diffusion is taken into account ($D \neq 0$) the diffusive HPBI and diffusion modes could be active. This can be understood from the criteria for stability for the HPBI, the diffusive HPBI and the diffusion modes, given by Equations (45)–(47), respectively. While Equation (45) is satisfied Equations (46) and (47) are not. We conclude that even though

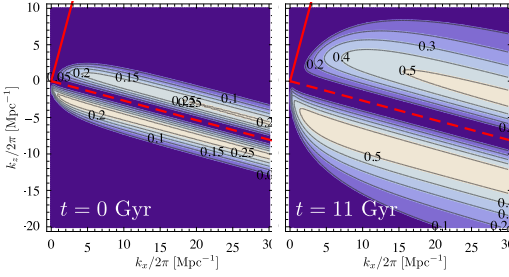


Figure 12. Contour plots of the growth rate in Gyr^{-1} for the intermediate ICM (location B). This region is unstable to the HBI at $t = 0$ Gyr (left panel) or the diffusion modes and the diffusive HPBI at $t = 11$ Gyr (right panel). This region is only unstable at $t = 11$ Gyr if $D \neq 0$. The maximum growth rate is increased with 110% with respect to the homogeneous case.

diffusion modes only grow on a diffusive timescale, ω_D^{-1} , they can be dominant if the instabilities that grow on a conduction timescale, ω_c^{-1} , are not active. The diffusive HPBI, however, requires that $\omega_D \gg \omega_{\text{dyn}}$, a requirement that is not fulfilled in the unstable region in Figure 12. The diffusion modes are active regardless of whether $\omega_D \gg \omega_{\text{dyn}}$ or $\omega_D \ll \omega_{\text{dyn}}$, and so the growth rates present in Figure 12 are interpreted to be due to the diffusion modes. The maximum growth rates are $\sigma \approx 0.28 \text{ Gyr}^{-1}$ at $t = 0$ Gyr and $\sigma \approx 0.59 \text{ Gyr}^{-1}$ at $t = 11$ Gyr corresponding to timescales of 3.6 Gyr and 1.7 Gyr, respectively. The maximum growth rate is increased by 110% with respect to the homogeneous case. The most unstable scales are $(L_x, L_z) = (0.32, 0.35) \text{ Mpc}$ at $t = 0$ Gyr and $(L_x, L_z) = (0.15, 0.15) \text{ Mpc}$ at $t = 11$ Gyr.

6.6. Inner ICM

In the inner ICM both the temperature and the mean molecular weight increase with radial distance at $t = 11$ Gyr. This implies that this region is only unstable with respect to the diffusive HPBI at $t = 11$ Gyr. At $t = 0$ Gyr, it is unstable to the HBI. The magnetic field strength increases toward the center of the ICM and so we expect the magnetic tension to dampen the growth rates more severely in the inner ICM.

We consider the radial distance indicated with a letter C on Figure 8, which is located at $r/r_{500} = 0.02$. At this radius, $d \ln T/d \ln P = -0.4$, $d \ln \mu/d \ln P = -0.13$ at $t = 11$ Gyr and $d \ln T/d \ln P = -0.51$, $d \ln \mu/d \ln P = 0$ at $t = 0$ Gyr. Due to the low value of $\beta K_n \approx 2$, we expect magnetic tension to influence the dynamics as highlighted in Figure 13. We assume that $\theta = 90^\circ$ which is the maximally unstable configuration. In Figure 13, the left panel shows the growth rates at $t = 0$ Gyr and the right panel shows the growth rates at $t = 11$ Gyr. Braginskii viscosity makes the HPBI have a preference for $k_\perp \gg k_\parallel$, as explained in Section 5. Magnetic tension also acts to inhibit the growth of modes with a high parallel wavenumber. Braginskii viscosity and magnetic tension are therefore the reasons for the zero growth rates at high vertical wavenumbers, k_z . The wavenumbers are not restricted in the x -direction (perpendicular to gravity) and so the fastest growth rates are attained for short distances in the x -direction because heat conduction is effective on short distance scales. The maximum growth rate is therefore found for $L_z \approx 25 \text{ kpc}$ and an even shorter length scale in the x -direction. The fluid limit is, however, only valid as long as $L_x \gg \lambda_{\text{mfp}} \approx 40 \text{ pc}$ at

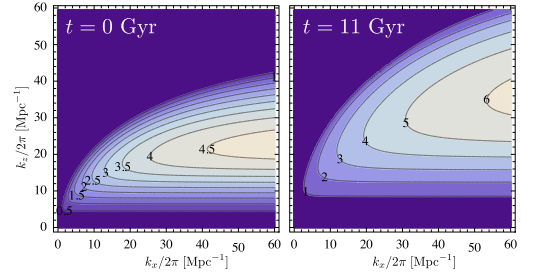


Figure 13. Contour plots of the growth rate in Gyr^{-1} for the inner ICM (location A). This region is unstable to the HBI at $t = 0$ Gyr (left panel) and to the diffusive HPBI at $t = 11$ Gyr (right panel). In both cases, the maximum growth rate is significantly decreased and the most unstable modes are found at longer parallel wavelengths because of magnetic tension. The maximum growth rate is increased by 40% with respect to the homogeneous case.

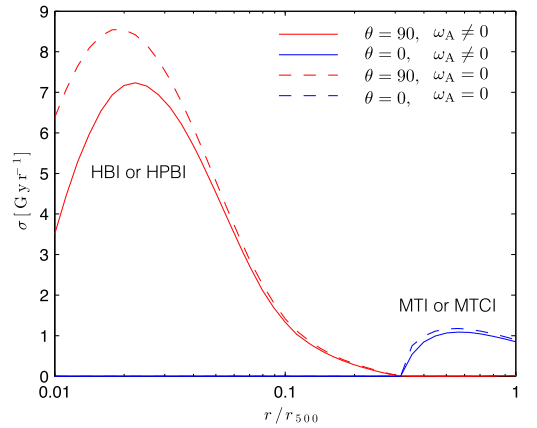


Figure 14. Maximum growth rates as a function of radius in the cluster model of Peng & Nagai (2009) at $t = 11$ Gyr in the limit where magnetic tension is neglected (dashed lines) and when it is taken into account (solid lines).

this distance. The vertical length scale of the fastest growing mode should be much smaller than $H \approx 50 \text{ kpc}$ but this is not the case. The maximum growth rates are $\sigma \approx 5 \text{ Gyr}^{-1}$ without sedimentation and $\sigma \approx 7.2 \text{ Gyr}^{-1}$ with sedimentation corresponding to timescales for growth of 0.20 Gyr and 0.14 Gyr, respectively. When sedimentation is present, we find that the maximum growth rate is increased by 40% with respect to the homogeneous case.

6.7. Magnetic Tension Decreases the Growth Rates

In order to assess how the effect of magnetic tension modifies the growth rates we compare the solutions we obtain when we set $\omega_A = 0$ with those found when we set ω_A equal to the value found by combining the model of Peng & Nagai (2009) at $t = 11$ Gyr with Equation (57). The maximum growth rates as a function of radius for a field with $\theta = 90^\circ$ and $\theta = 0^\circ$ inclination with respect to the direction of gravity are shown in Figure 14. The solid lines include $\omega_A \neq 0$ while the dashed lines are found by solving the $\omega_A = 0$ limit of the dispersion relation. We conclude that magnetic tension decreases the

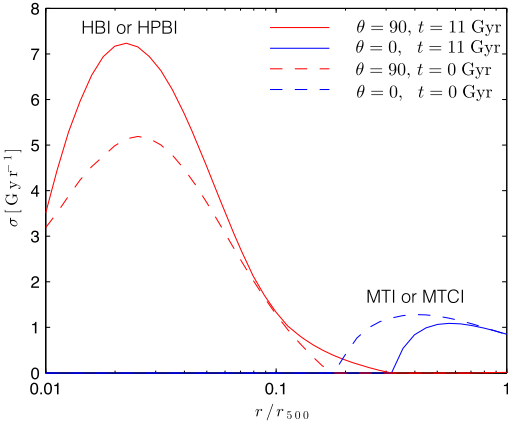


Figure 15. Maximum growth rate as a function of radius in the cluster model of Peng & Nagai (2009) at $t = 0$ (dashed) and $t = 11$ Gyr (solid) for a field with $\theta = 90^\circ$ (red) and $\theta = 0^\circ$ (blue) inclination with respect to the direction of gravity. The effects of a finite β are included. The sedimentation increases (decreases) the theoretically predicted growth rates in the inner (outer) cluster.

maximum growth rate at all radii but the effect is seen to be most significant in the inner cluster region (Carilli & Taylor 2002; Kunz 2011; Pessah & Chakraborty 2013).

7. DISCUSSION AND PROSPECTS

Understanding whether He sedimentation in galaxy clusters is efficient or whether it can be hindered by tangled magnetic fields, turbulence, or mergers remains an open question in astrophysics. Addressing this problem from first principles demands a better understanding of the processes involved in the weakly collisional, magnetized plasma constituting the ICM. As a first step in this endeavor, we have taken a simple approach to gauge the importance of various dynamical instabilities, related to the MTI and HBI, that can feed off temperature and composition gradients (Pessah & Chakraborty 2013) as expected from state-of-the-art sedimentation models (Peng & Nagai 2009).

We have shown that if a gradient in the composition of the ICM arises due to Helium sedimentation, as modeled for example in Peng & Nagai (2009), this might not be a stable equilibrium. We illustrated this by showing that, depending on the magnetic field orientation, the radial profile of the sedimentation model is unstable, to different kinds of instabilities, at all radii. The instabilities are shown to grow on timescales that are short compared to the life-time of a typical cluster. Our findings are summarized in Figure 15 where we show the maximum growth rate as a function of radius for both the homogeneous cluster model ($t = 0$ Gyr) and the cluster model with a gradient in composition ($t = 11$ Gyr) for a magnetic field that is either parallel or perpendicular to the direction of gravity. In this figure we find that, in accordance with Pessah & Chakraborty (2013), Helium sedimentation can lead to an increase in the maximum growth rate in the inner cluster region but a decrease in the maximum growth rate in the outer cluster region. The figure illustrates that the composition gradients, as inferred from sedimentation models which do not fully account for the weakly collisional character of the

environment, are not necessarily robust even though the entropy increases with radius. This contrasts the arguments regarding the stability of composition gradients put forth in Markevitch (2007), which predates the discovery of the HBI (Quataert 2008).

The instabilities discussed in this paper could provide an efficient mechanism for diminishing the mean molecular weight gradient in the ICM by turbulently mixing the Helium content. Whether this is the case depends on how the instabilities saturate as well as the large scale dynamical processes that contribute to determining the global gradient in the mean molecular weight. There are several processes that could play a role in this regard at both small and large scales. Understanding their influence will lead to a more realistic picture of the ICM dynamics. We mention a few examples below.

The equations of kinetic MHD used in this paper do not incorporate the physics responsible for the composition gradients found in sedimentation models based on Burger's equations. They are therefore not able to self-consistently describe the coupling of magnetic fields to the sedimentation process. One possible route forward would be to extend the equations of kinetic MHD and take the sedimentation process into account by following Bahcall & Loeb (1990). This would allow us to describe the dynamical influence of the magnetic field at the cost of using a one-fluid model instead of the commonly used multifluid models. Even though an extension of the kinetic MHD framework would describe unmagnetized sedimentation less precisely than Burgers' equations (Thoul et al. 1994), this would be a step forward in our understanding of sedimentation processes in the ICM.

Our idealized model of the ICM consisted of a weakly collisional, plane-parallel atmosphere in hydrostatic equilibrium. Real clusters are most likely not in perfect hydrostatic equilibrium as the ICM can be stirred by mergers and accretion. The ensuing turbulence can contribute with a significant fraction of the pressure support needed to counteract gravity (Lau et al. 2009; Nelson et al. 2014). The instabilities we have described could be influenced by such turbulence, as well as by the cosmological expansion over timescales comparable to the age of the universe (Ruszkowski et al. 2011).

Another issue raised in this paper is that some of the fastest growing modes grow on scales that are not strictly local in height. This means that there is a need for a quasi-global theory as developed in Latter & Kunz (2012) in order to correctly describe the linear dynamics of the weakly collisional medium. Other issues may affect the plasma dynamics at small scales. Very fast microscale instabilities, such as the firehose and mirror instabilities, could play a key role in the ICM (Schekochihin & Cowley 2006; Schekochihin et al. 2010; Kunz et al. 2011). These instabilities are not correctly described in the framework of kinetic MHD (Schekochihin et al. 2005). This might not be a problem if the microinstabilities saturate in such a way that they drive the pressure anisotropy to marginal stability (Schekochihin et al. 2008; Rosin et al. 2011). This is still an outstanding issue in the study of homogeneous plasmas. The microinstabilities are not a concern for the linear evolution of the MTI and the HBI but they are important for simulations of their nonlinear evolution (Kunz et al. 2012). We anticipate the need to deal with similar issues for simulations of the nonlinear evolution of the instabilities that are driven by gradients in composition.

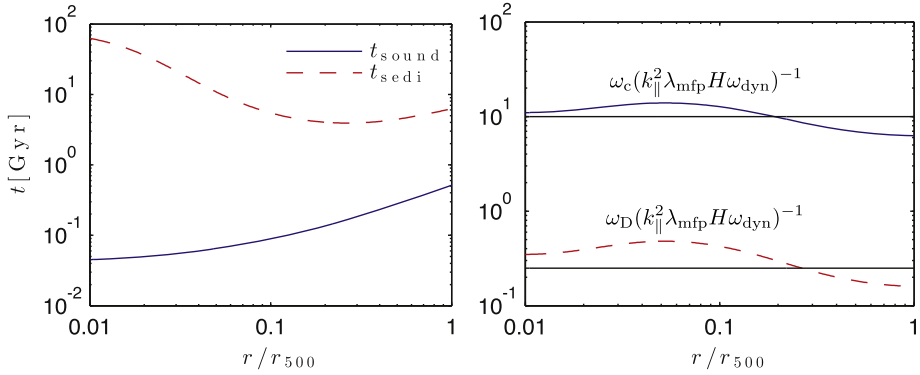


Figure 16. Left: The timescale for sedimentation across a scale height (red dashed) and the timescale for sound to cross a scale height (blue) as a function of radius in the model of Peng & Nagai (2009). Right: The dimensionless values of ω_c (blue) and ω_D (red dashed) are shown as a function of radius. The approximations given in Equations (35) and (37) are indicated with solid horizontal lines.

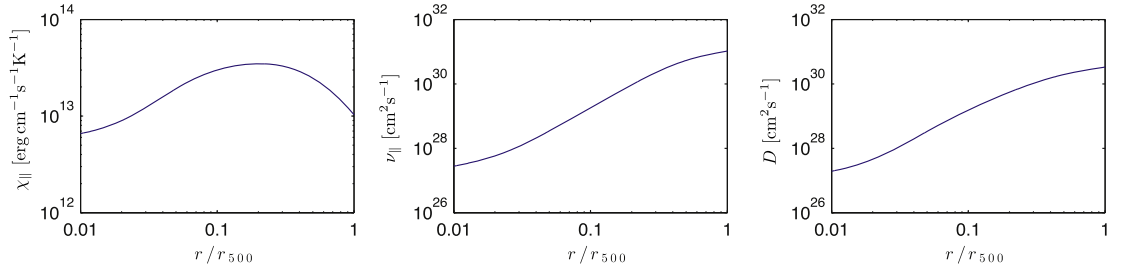


Figure 17. The values of χ_{\parallel} (left), ν_{\parallel} (middle), and D (right) as function of radius in the cluster model of Peng & Nagai (2009) at $t = 11$ Gyr.

We are grateful to Daisuke Nagai and Fang Peng for giving us a copy of their Fortran code that we used to reproduce the data in their sedimentation model. We are grateful to the anonymous referee for a thoughtful and detailed report. The suggestion to make a more comprehensive comparison between a homogeneous and a heterogeneous ICM inspired us to produce several new figures and helped us to significantly improve the final version of this manuscript. We acknowledge useful discussions with Daisuke Nagai, Matthew Kunz, Prateek Sharma, Ellen Zweibel, and Ian Parrish during the 3rd ICM Theory and Computation Workshop held at the Niels Bohr Institute in 2014. We also thank Sagar Chakraborty and Henrik Latter for valuable comments. The research leading to these results has received funding from the European Research Council under the European Union's Seventh Framework Programme (FP/2007-2013) under ERC grant agreement 306614. T.B. also acknowledges support provided by a Lørup Scholar Stipend and M.E.P. also acknowledges support from the Young Investigator Programme of the Villum Foundation.

APPENDIX A CHARACTERISTIC TIMESCALES FOR SEDIMENTATION AND ANISOTROPIC TRANSPORT

A.1. Helium Sedimentation

In this paper we have built on the stability analysis of Pessah & Chakraborty (2013) and applied these tools to the Helium profile provided by the sedimentation model of Peng & Nagai

(2009) in order to calculate the growth rates of instabilities that could be present in this model of the ICM. In our calculations we have assumed that the composition profiles evolve on timescales that are longer than the characteristic timescales in which the instabilities operate. Within this framework, we found that the relevant instabilities grow on timescales comparable to the dynamical timescale. We show here that our approach is justified because the timescales involved in the sedimentation process are much longer than the dynamical timescale. In order to estimate the timescale for sedimentation, we use an approximation for the sedimentation velocity, w_{He} , given by

$$w_{\text{He}} \simeq 80 \text{ km s}^{-1} \left(\frac{T}{10 \text{ keV}} \right)^{3/2} \left(\frac{g}{10^{-7.5} \text{ cm s}^{-2}} \right) \times \left(\frac{n_{\text{H}}}{10^{-3} \text{ cm}^{-3}} \right)^{-1}, \quad (58)$$

in Peng & Nagai (2009) for a single Helium ion immersed in a Hydrogen background. Here, n_{H} is the Hydrogen number density. The separation of timescales is illustrated in Figure 16 where we show the time for a He ion to sediment a distance of one scale height ($t_{\text{sed}} = H/w_{\text{He}}$) along with the dynamical timescale ($t_{\text{sound}} = H/v_{\text{th}} = \omega_{\text{dyn}}^{-1}$) as a function of radius in the cluster. We observe that the timescales differ by more than an order of magnitude, providing support to our assumption.

A.2. Heat Conduction, Braginskii Viscosity, and Particle Diffusion

In order to estimate the timescale for particle diffusion we use Equations (64)–(66) to estimate the coefficients χ_{\parallel} , ν_{\parallel} and D . We calculate the dimensionless values of ω_c , ω_v , and ω_D by scaling them with $k_{\parallel}^2 \lambda_{\text{mfp}} H \omega_{\text{dyn}}$ where the frequencies ω_c , ω_v , and ω_D are defined in Equation (24). The dimensionless values of ω_c and ω_D are shown as a function of radius (using the model of Peng & Nagai 2009) in the right panel of Figure 16. From this figure we estimate that the diffusion timescale is roughly 40 times longer than the timescale for heat conduction, enabling us to estimate ω_D as in Equation (37). The dimensionless value of ω_v does not depend on any physical parameters and is therefore 3/2 at all radii.

APPENDIX B TRANSPORT PROPERTIES OF A HYDROGEN-HELIUM PLASMA

The procedure used to derive the kinetic MHD equations for a binary mixture is similar to the procedure used for a pure Hydrogen plasma (Braginskii 1965; Kulsrud 1983).

The non-ideal transport coefficients for a plasma consisting of Hydrogen and Helium ions as well as electrons are found by using the Krook operator in the Vlasov–Landau–Maxwell equations

$$\frac{\partial f_s}{\partial t} + \mathbf{v} \cdot \nabla f_s + \left[\frac{q_s}{m_s} \left(\mathbf{E} + \frac{\mathbf{v} \times \mathbf{B}}{c} \right) + \mathbf{g} \right] \frac{\partial f_s}{\partial \mathbf{v}} = C[f_s]. \quad (59)$$

Here, f_s is the one-particle phase-space distribution of species s and q_s (m_s) is the particle charge (mass). The Krook operator is given by (Snyder et al. 1997)

$$C[f_s] = -\sum_t \nu_{st} (f_s - F_{Mst}), \quad (60)$$

where the sum extends over all species and the equilibrium function, F_{Mst} , is given by

$$F_{Mst} = \frac{n_s}{(2\pi T_s/m_s)^{3/2}} \exp \left[-\frac{m_s}{2T_s} (v_{\parallel} - u_{\parallel,t})^2 - \frac{m_s}{2T_s} v_{\perp}^2 \right]. \quad (61)$$

Here, the collision frequency between species s and t is given by

$$\nu_{st} = \frac{4\sqrt{2\pi}}{3} \frac{n_t m_{st}^{1/2} e^4 (Z_s Z_t)^2}{m_s (k_B T)^{3/2}} \ln \Lambda_{st}, \quad (62)$$

where $\ln \Lambda_{st}$ is the Coulomb logarithm and

$$m_{st} = \frac{m_s m_t}{m_s + m_t}, \quad (63)$$

is the reduced mass. Furthermore, the mean velocity in the parallel direction of species s is $u_{\parallel,s}$ and we assume that all species have the same temperature, $T_s = T$.

Following Peng & Nagai (2009) and Shtykovskiy & Gilfanov (2010), we use $\ln \Lambda_{st} = 40$ which is a characteristic value for the ICM. One can derive the kinetic MHD equations, given by Equations (1)–(4), by assuming that the distribution function is gyrotropic and calculating moments in velocity space of the Landau–Vlasov equation (Kulsrud 1983). If it is

assumed that the distribution function is Gaussian when calculating the moments v_{\parallel}^4 , v_{\perp}^4 , and $v_{\parallel}^2 v_{\perp}^2$, the equations are closed and one can show that (see, for instance, A. A. Schekochihin & M. W. Kunz, in preparation)

$$\chi_{\parallel} = \frac{5}{2} \frac{k_B}{\nu_{e-e} + \nu_{e-H} + \nu_{e-He}} \frac{P_e}{m_e} \quad (64)$$

for the heat conductivity, and

$$\nu_{\parallel} = \frac{1}{\rho} \left(\frac{n_{\text{He}}}{\nu_{\text{He-H}} + \nu_{\text{He-He}}} + \frac{n_{\text{H}}}{\nu_{\text{H-H}} + \nu_{\text{H-He}}} \right) k_B T \quad (65)$$

for the Braginskii viscosity. In these expressions the heat conduction due to ions and the viscosity due to electrons is neglected. This approximation is good because $m_{\text{H}}, m_{\text{He}} \gg m_e$.

The anisotropic diffusion coefficient due to a gradient in the composition was approximated by Bahcall & Loeb (1990). In terms of the ratio of the Helium density to the total gas density, c , it can be expressed as Pessah & Chakraborty (2013)

$$D = \frac{3}{16} \sqrt{\frac{5m_{\text{H}}}{2\pi}} \frac{(k_B T)^{5/2}}{e^2 \rho \ln \Lambda_{\text{H-He}}} \left[\frac{4-c}{(2-c)(8-5c)} \right]. \quad (66)$$

Using the model of Peng & Nagai (2009), we show the transport coefficients as a function of radius in Figure 17.

REFERENCES

- Bahcall, J. N., & Loeb, A. 1990, *AJ*, **360**, 267
 Balbus, S. A. 2000, *AJ*, **534**, 420
 Balbus, S. A. 2001, *AJ*, **562**, 909
 Bogdanović, T., Reynolds, C. S., Balbus, S. A., & Parrish, I. J. 2009, *AJ*, **704**, 211
 Bonafede, A., Feretti, L., Murgia, M., et al. 2010, *A&A*, **513**, A30
 Braginskii, S. 1965, in *Review of Plasma Physics*, Vol. 1, ed. M. A. Leontovich (New York: Consultants Bureau)
 Bulbul, G. E., Hasler, N., Bonamente, M., et al. 2011, *A&A*, **533**, 6
 Burgers, J. M. 1969, *Flow Equations for Composite Gases* (New York: Academic Press)
 Carilli, C. L., & Taylor, G. B. 2002, *ARA&A*, **40**, 319
 Chuzhoy, L., & Loeb, A. 2004, *MNRAS*, **349**, L13
 Chuzhoy, L., & Nusser, A. 2003, *MNRAS*, **342**, L5
 Fabian, A. C., & Pringle, J. E. 1977, *MNRAS*, **181**, 5P
 Gilfanov, M. R., & Syunyaev, R. A. 1984, *SvAL*, **10**, 137
 Kulsrud, R. M. 1983, in *Basic Plasma Physics: Selected Chapters*, *Handbook of Plasma Physics*, Vol. 1, ed. A. A. Galeev & R. N. Sudan (Amsterdam: North Holland Publishing), 1
 Kunz, M. W. 2011, *MNRAS*, **417**, 602
 Kunz, M. W., Bogdanović, T., Reynolds, C. S., & Stone, J. M. 2012, *AJ*, **754**, 122
 Kunz, M. W., Schekochihin, A. A., Cowley, S. C., Binney, J. J., & Sanders, J. S. 2011, *MNRAS*, **410**, 2446
 Latter, H. N., & Kunz, M. W. 2012, *MNRAS*, **423**, 1964
 Lau, E. T., Kravtsov, A. V., & Nagai, D. 2009, *AJ*, **705**, 1129
 Ledoux, P. 1947, *AJ*, **105**, 305
 Mantz, A. B., Allen, S. W., Morris, R. G., et al. 2014, *MNRAS*, **440**, 2077
 Markevitch, M. 2007, arXiv:0705.3289
 McCourt, M., Parrish, I. J., Sharma, P., & Quataert, E. 2011, *MNRAS*, **413**, 1295
 McCourt, M., Sharma, P., Quataert, E., & Parrish, I. J. 2012, *MNRAS*, **419**, 3319
 Navarro, J. F., Frenk, C. S., & White, S. D. M. 1997, *AJ*, **490**, 493
 Nelson, K., Lau, E. T., & Nagai, D. 2014, *AJ*, **792**, 25
 Parrish, I. J., McCourt, M., Quataert, E., & Sharma, P. 2012a, *MNRAS*, **422**, 704
 Parrish, I. J., McCourt, M., Quataert, E., & Sharma, P. 2012b, *MNRAS*, **419**, L29
 Parrish, I. J., & Quataert, E. 2008, *AJL*, **677**, L9
 Parrish, I. J., Quataert, E., & Sharma, P. 2009, *AJ*, **703**, 96

- Parrish, I. J., Quataert, E., & Sharma, P. 2010, *ApJL*, 712, L194
Parrish, I. J., & Stone, J. M. 2005, *ApJ*, 633, 334
Parrish, I. J., & Stone, J. M. 2007, *ApJ*, 664, 135
Parrish, I. J., Stone, J. M., & Lemaster, N. 2008, *ApJ*, 688, 905
Peng, F., & Nagai, D. 2009, *ApJ*, 693, 839
Pessah, M. E., & Chakraborty, S. 2013, *ApJ*, 764, 13
Qin, B., & Wu, X.-P. 2000, *ApJL*, 529, L1
Quataert, E. 2008, *ApJ*, 673, 758
Rosin, M. S., Schekochihin, A. A., Rincon, F., & Cowley, S. C. 2011, *MNRAS*, 413, 7
Ruszkowski, M., Lee, D., Brüggen, M., Parrish, I., & Oh, S. P. 2011, *ApJ*, 740, 81
Ruszkowski, M., & Oh, S. P. 2010, *ApJ*, 713, 1332
Schekochihin, A. A., & Cowley, S. C. 2006, *AN*, 327, 599
Schekochihin, A. A., Cowley, S. C., Kulsrud, R. M., Hammett, G. W., & Sharma, P. 2005, *ApJ*, 629, 139
Schekochihin, A. A., Cowley, S. C., Kulsrud, R. M., Rosin, M. S., & Heinemann, T. 2008, *PhRvL*, 100, 081301
Schekochihin, A. A., Cowley, S. C., Rincon, F., & Rosin, M. S. 2010, *MNRAS*, 405, 291
Schwarzschild, M. 1958, *Structure and Evolution of the Stars* (Princeton, NJ: Princeton Univ. Press)
Shtykovskiy, P., & Gilfanov, M. 2010, *MNRAS*, 401, 1360
Snyder, P. B., Hammett, G. W., & Dorland, W. 1997, *PhPl*, 4, 3974
Spitzer, L. 1962, *Physics of Fully Ionized Gases* (2nd ed.; New York: Interscience)
Thoul, A. A., Bahcall, J. N., & Loeb, A. 1994, *ApJ*, 421, 828
Vikhlinin, A., Kravtsov, A., Forman, W., et al. 2006, *ApJ*, 640, 691

Paper II

Local Simulations of Instabilities Driven by Composition Gradients in the ICM.

Reprinted from
The Astrophysical Journal, Volume 824, June 2016
doi:10.3847/0004-637X/824/1/32
with the permission of IOP Publishing.



LOCAL SIMULATIONS OF INSTABILITIES DRIVEN BY COMPOSITION GRADIENTS IN THE ICM

THOMAS BERLOK AND MARTIN E. PESSAH

Niels Bohr International Academy, Niels Bohr Institute, Blegdamsvej 17, DK-2100 Copenhagen Ø, Denmark; berlok@nbi.dk, mpessah@nbi.dk

Received 2016 March 7; accepted 2016 April 13; published 2016 June 8

ABSTRACT

The distribution of helium in the intracluster medium (ICM) permeating galaxy clusters is not well constrained due to the very high plasma temperature. Therefore, the plasma is often assumed to be homogeneous. A nonuniform helium distribution can, however, lead to biases when measuring key cluster parameters. This has motivated one-dimensional models that evolve the ICM composition assuming that the effects of magnetic fields can be parameterized or ignored. Such models for nonisothermal clusters show that helium can sediment in the cluster core, leading to a peak in concentration offset from the cluster center. The resulting profiles have recently been shown to be linearly unstable when the weakly collisional character of the magnetized plasma is considered. In this paper, we present a modified version of the MHD code Athena, which makes it possible to evolve a weakly collisional plasma subject to a gravitational field and stratified in both temperature and composition. We thoroughly test our implementation and confirm excellent agreement against several analytical results. In order to isolate the effects of composition, in this initial study we focus our attention on isothermal plasmas. We show that plasma instabilities, feeding off gradients in composition, can induce turbulent mixing and saturate by rearranging magnetic field lines and alleviating the composition gradient. Composition profiles that increase with radius lead to instabilities that saturate by driving the average magnetic field inclination to roughly 45° . We speculate that this effect may alleviate the core insulation observed in homogeneous settings, with potential consequences for the associated cooling flow problem.

Key words: diffusion – galaxies: clusters: intracluster medium – instabilities – magnetohydrodynamics (MHD)

Supporting material: animations

1. INTRODUCTION

Atmospheres composed of a plasma that is weakly collisional and weakly magnetized have stability properties that differ qualitatively from collisional atmospheres. Instabilities such as the magnetothermal instability (MTI; Balbus 2000, 2001) and the heat-flux-driven buoyancy instability (HBI; Quataert 2008) can arise when there is a gradient in the temperature either parallel or anti-parallel to the gravitational field. These instabilities, which feed off a gradient in temperature, have been extensively studied (Balbus 2000, 2001; Parrish & Stone 2005, 2007; Parrish & Quataert 2008; Parrish et al. 2008, 2009, 2010, 2012a, 2012b; Quataert 2008; Bogdanović et al. 2009; Ruszkowski & Oh 2010; Kunz 2011; McCourt et al. 2011, 2012; Kunz et al. 2012; Latter & Kunz 2012), and they are believed to be important for the understanding of the dynamical evolution of the intracluster medium (ICM) of galaxy clusters.

These studies assumed that the composition of the plasma is uniform, an assumption that might not be appropriate if heavier elements are able to sediment toward the core of the cluster (Fabian & Pringle 1977). In parallel and complementary studies, the long-term evolution of the radial distribution of elements has been studied using one-dimensional models (Fabian & Pringle 1977; Gilfanov & Syunyaev 1984; Chuzhoy & Nusser 2003; Chuzhoy & Loeb 2004; Peng & Nagai 2009; Shtykovskiy & Gilfanov 2010). The ensuing nonuniform composition has been argued to introduce biases in cluster properties as inferred from observations (Markevitch 2007; Peng & Nagai 2009).

While the studies of the MTI and HBI assumed a uniform plasma, the sedimentation models have yet to include magnetic fields. In an attempt to bridge the gap between the different

approaches, and with the goal of understanding the long-term evolution of the composition of the ICM, Pessah & Chakraborty (2013) studied the stability properties of weakly collisional atmospheres with gradients in both temperature and composition. They found that gradients in composition, either parallel or anti-parallel to the gravitational field, can trigger instabilities. In a subsequent study, Berlok & Pessah (2015) carried out a comprehensive study using linear mode analysis and showed that these instabilities are expected to render the composition profiles obtained with current sedimentation models unstable, as it was illustrated using the model of Peng & Nagai (2009).

In this paper, we present the first nonlinear, two-dimensional (2D), numerical simulations of the instabilities that feed off a gradient in composition using a modified version of the MHD code Athena (Stone et al. 2008). The instabilities considered are (i) the magneto-thermo-compositional instability (MTCI), which is maximally unstable when the magnetic field is perpendicular to gravity; (ii) the heat- and particle-flux-driven buoyancy instability (HPBI), which is maximally unstable when the magnetic field is parallel to gravity; and (iii) the diffusion modes, which are maximally unstable when the magnetic field is parallel to gravity. These instabilities arise due to the weakly collisional nature of the ICM, which fundamentally changes the transport properties of a plasma. In this regime, where the gyro-radii of the particles are much smaller than the mean free path for particle collisions, the transport of heat, momentum, and particles will be primarily along the magnetic field lines.

The MTCI and HPBI will be present in isothermal atmospheres in which the composition increases with height, while diffusion modes can be present regardless of the direction of the gradient in composition (Pessah & Chakraborty 2013).

The linear dispersion relation presented in Berlok & Pessah (2015) is used to compare with the linear evolution of the simulations. We find good agreement, thereby confirming both the linear theory and our numerical method. For the nonlinear evolution of the instabilities we find that the magnetic field inclination goes to roughly 45° independently of whether the magnetic field is initially horizontal (MTCI) or vertical (HPBI). This is contrary to the instabilities driven by temperature gradients, where the average magnetic field becomes almost vertical (horizontal) for an initially horizontal (vertical) magnetic field (Parrish & Stone 2005; Parrish & Quataert 2008). The simple explanation is that the MTCI and HPBI, both of which grow when the composition increases with height, can operate simultaneously. They are therefore driving the average angle in opposite directions, compromising at roughly 45° . The MTI and HBI, being dependent on temperature gradients in opposite directions, cannot grow at the same time, and so they grow unabated by their counterpart. We also find that both types of instabilities cause turbulent mixing of the helium concentration. We conclude that, in the idealized numerical settings that we employ, instabilities driven by the free energy supplied by a gradient in composition saturate by alleviating the gradient and thereby removing the source of free energy.

The rest of the paper is organized as follows: we start out by introducing the equations of kinetic MHD in Section 2 and how they can be solved numerically in Section 3. In Section 4 we demonstrate that the simulations agree with the linear theory for isothermal atmospheres, and we illustrate how the growth rates depend on some of the key parameters of the problem. We also use atmospheres with gradients in both temperature and composition, motivated by the model of Peng & Nagai (2009) and discussed in Berlok & Pessah (2015), to show that the theory and simulations also agree with both gradients present. In Section 5, we consider the nonlinear evolution of the MTCI and HPBI in isothermal atmospheres in order to determine how they saturate. We summarize and outline future work in Section 6.

2. KINETIC MHD FOR A BINARY MIXTURE

We consider a fully ionized, weakly magnetized, and weakly collisional plasma consisting of a mixture of hydrogen and helium. We model such a plasma using the set of equations introduced in Pessah & Chakraborty (2013),¹

$$\frac{\partial \rho}{\partial t} + \nabla \cdot (\rho \mathbf{v}) = 0, \quad (1)$$

$$\frac{\partial (\rho \mathbf{v})}{\partial t} + \nabla \cdot \left(\rho \mathbf{v} \mathbf{v} + P_T \mathbf{I} - \frac{B^2}{4\pi} \hat{\mathbf{b}} \hat{\mathbf{b}} \right) = -\nabla \cdot \Pi + \rho \mathbf{g}, \quad (2)$$

$$\begin{aligned} \frac{\partial E}{\partial t} + \nabla \cdot \left[(E + P_T) \mathbf{v} - \frac{\mathbf{B}(\mathbf{B} \cdot \mathbf{v})}{4\pi} \right] \\ = -\nabla \cdot \mathbf{Q}_s - \nabla \cdot (\Pi \cdot \mathbf{v}) + \rho \mathbf{g} \cdot \mathbf{v}, \end{aligned} \quad (3)$$

$$\frac{\partial \mathbf{B}}{\partial t} = \nabla \times (\mathbf{v} \times \mathbf{B}), \quad (4)$$

$$\frac{\partial (c\rho)}{\partial t} + \nabla \cdot (c\rho \mathbf{v}) = -\nabla \cdot \mathbf{Q}_c. \quad (5)$$

In these equations ρ is the mass density, \mathbf{v} is the fluid velocity, \mathbf{B} is the magnetic field with direction $\hat{\mathbf{b}} = (b_x, 0, b_z)$, $\mathbf{g} = (0, 0, -g)$ is the gravitational acceleration, and \mathbf{I} is the identity matrix. The total pressure is $P_T = P + B^2/8\pi$, where P is the thermal pressure and the total energy density, E , is

$$E = \frac{1}{2} \rho v^2 + \frac{B^2}{8\pi} + \frac{P}{\gamma - 1}, \quad (6)$$

where $\gamma = 5/3$ is the adiabatic index.

The composition of the plasma, c , is defined to be the ratio of the helium density to the total gas density

$$c \equiv \frac{\rho_{\text{He}}}{\rho_{\text{H}} + \rho_{\text{He}}} = \frac{\rho_{\text{He}}}{\rho}, \quad (7)$$

and the associated mean molecular weight, μ , is given by

$$\mu = \frac{4}{8 - 5c}, \quad (8)$$

for a completely ionized plasma consisting of helium and hydrogen. The mean molecular weight can modify the dynamics of the plasma through the equation of state

$$P = \frac{\rho k_B T}{\mu m_H}, \quad (9)$$

where k_B is Boltzmann's constant, T is the temperature, and m_H is the proton mass.

We consider the plasma to be influenced by three different nonideal effects: Braginskii viscosity, which arises due to differences in pressure parallel (p_{\parallel}) and perpendicular (p_{\perp}) to the magnetic field, described by the viscosity tensor (Braginskii 1965)

$$\Pi = -3\rho\nu_{\parallel} \left(\hat{\mathbf{b}} \hat{\mathbf{b}} - \frac{1}{3} \mathbf{I} \right) \left(\hat{\mathbf{b}} \hat{\mathbf{b}} - \frac{1}{3} \mathbf{I} \right) : \nabla \mathbf{v}, \quad (10)$$

anisotropic heat conduction described by the heat flux (Spitzer 1962; Braginskii 1965),

$$\mathbf{Q}_s = -\chi_{\parallel} \hat{\mathbf{b}} \hat{\mathbf{b}} \cdot \nabla T, \quad (11)$$

and anisotropic diffusion of composition described by the composition flux (Bahcall & Loeb 1990),

$$\mathbf{Q}_c = -D \hat{\mathbf{b}} \hat{\mathbf{b}} \cdot \nabla c. \quad (12)$$

The transport coefficients for Braginskii viscosity (ν_{\parallel}), heat conductivity (χ_{\parallel}), and diffusion of composition (D) depend on the temperature, density, and composition of the plasma. The dependences are given by Equations (64)–(66) in Berlok & Pessah (2015). Finally, we define the thermal velocity, $v_{\text{th}} = \sqrt{P/\rho}$, and the plasma- β given by $\beta = 8\pi P/B^2 = 2v_{\text{th}}^2/v_A^2$, where $v_A = B/\sqrt{4\pi\rho}$ is the Alfvén velocity.²

3. NUMERICAL METHOD AND INITIAL CONDITIONS

The equations of kinetic MHD, Equations (1)–(5), are solved using a modified version of the conservative MHD code Athena (Stone et al. 2008). The algorithms used in Athena are

¹ For further details on the kinetic MHD approximation and its limitations see the relevant discussions in Kunz et al. (2012), Schekochihin et al. (2005), Pessah & Chakraborty (2013), and references therein.

² Note that this definition of β differs from the one in Berlok & Pessah (2015) by a factor of 2.

described in Gardiner & Stone (2005) and Stone & Gardiner (2009), and a description of the implementation of anisotropic thermal conduction and Braginskii viscosity can be found in Parrish & Stone (2005) and Parrish et al. (2012b), respectively.

In order to carry out the numerical simulations of interest, we have modified Athena to include a spatially varying mean molecular weight, μ . This is done by using the inbuilt method for adding a passive scalar, defined by a spatially varying concentration, c , and then making it active by using the value of c when calculating the temperature used in the heat conduction module. Furthermore, we implemented a module that takes account of diffusion of helium by using operator splitting. This module has been built by following the same approach employed in the heat conduction module that is already present in the current publicly available version of Athena (Parrish & Stone 2005; Sharma & Hammett 2007). Our implementation allows for nonconstant values of the parameters ν_{\parallel} , χ_{\parallel} , and D through user-defined functions. This feature is, however, not used in this work, as we employ a local approximation and thus treat these parameters as constants. The diffusion terms are solved explicitly, which can make the time-step constraint on viscosity, thermal conduction, and diffusion of helium very restrictive. In order to circumvent this, we use subcycling, which we limit to a maximum of 10 steps per MHD step (Kunz et al. 2012).

3.1. Plane-parallel Atmosphere with Gradients in Temperature and Composition

In this section, we introduce the two different atmospheres used as initial conditions in the simulations. The atmospheres considered are plane-parallel, i.e., all quantities are constant along a horizontal slice, perpendicular to gravity. The atmosphere is assumed to be composed of an ideal gas, characterized by the equation of state given by Equation (9), and is assumed to be in hydrostatic equilibrium, i.e.,³

$$\frac{\partial P}{\partial z} = -g\rho. \quad (13)$$

3.1.1. Isothermal Atmosphere with a Composition Gradient in the Absence of Particle Diffusion

The simplest atmosphere we use is inspired by the original numerical work on the MTI (Parrish & Stone 2005). We consider an isothermal atmosphere with $T = T_0$ and

$$P = P_0 \left(1 - \frac{z}{3H_0}\right)^3, \quad (14)$$

$$\mu = \mu_0 \left(1 - \frac{z}{3H_0}\right)^{-1}. \quad (15)$$

where P_0 , T_0 , and μ_0 are the values of the pressure, temperature, and mean molecular weight at $z = 0$, respectively, and H_0 is the scale height

$$H_0 = \frac{k_B T_0}{\mu_0 m_{\text{H}} g}. \quad (16)$$

The density can be determined using Equation (9).

³ We consider high- β plasmas and do not include the magnetic pressure in the derivations of the equilibria.

This isothermal atmosphere is used for simulations of the linear regime of the MTCI in Section 4.1 and the linear regime of the HPBI in Section 4.2. It is also used for simulations of the nonlinear regime of the MTCI and HPBI in Section 5. The magnetic field can have any orientation as long as $D = 0$. The structure of this atmosphere is, however, not in equilibrium if $D \neq 0$ and $b_z \neq 0$. In that case, we will have to use a more sophisticated atmosphere, which we introduce next.

3.1.2. Atmosphere with Thermal and Composition Gradients

Steady state requires that the divergence of the heat and particle fluxes vanish, i.e.,

$$\nabla \cdot \mathbf{Q}_s = 0, \quad (17)$$

$$\nabla \cdot \mathbf{Q}_c = 0. \quad (18)$$

Both conditions are trivially satisfied if $b_z = 0$ and $D = 0$. If, however, $b_z \neq 0$ and $D \neq 0$, these requirements can still be met by simple atmospheric models if χ_{\parallel} and D do not depend on z . Such an assumption is reasonable for the local simulations that we will consider, where the height of the box, L_z , satisfies the criterion $L_z \ll H_0$. When there is both a gradient in temperature T and mean molecular weight μ , the requirements that $\nabla \cdot \mathbf{Q}_s = 0$ and $\nabla \cdot \mathbf{Q}_c = 0$ can be integrated to yield

$$T(z) = T_0 + s_T z, \quad (19)$$

$$c(z) = c_0 + s_c z, \quad (20)$$

where $s_T = (T_z - T_0)/L_z$ and $s_c = (c_z - c_0)/L_z$ are the constant slopes in temperature and composition. Here T_0 (T_z) is the temperature at the bottom (top) of the box and c_0 (c_z) is the helium mass concentration at the bottom (top) of the box.

The pressure is found by solving Equation (13), leading to

$$P(z) = P_0 \left(\frac{T(z)\mu(z)}{T_0\mu_0} \right)^{\alpha}, \quad (21)$$

where $\mu(z)$ is related to $c(z)$ by Equation (8) and the constant α is given by

$$\alpha = -\frac{T_0}{H_0} \frac{4}{4s_T + 5\mu_0 T_0 s_c}. \quad (22)$$

This solution for the pressure profile of the atmosphere is replaced with a simple exponential atmosphere, $P(z) = P_0 \exp(-z/H_0)$, with scale height H_0 if $s_T = s_c = 0$.

We use this model atmosphere to perform simulations of modes driven by diffusion in Section 4.3. These modes are unstable when there is a vertical gradient in composition, a nonzero vertical component of the magnetic field, $b_z \neq 0$, and anisotropic diffusion of helium, $D \neq 0$. We also use this atmosphere in Section 4.4 for simulations of the linear regime of the MTCI and the HBPI with gradients in both temperature and composition.

3.2. Boundary Conditions

Periodic boundary conditions are used in the horizontal direction in all simulations. In the vertical direction we have implemented two different sets of boundary conditions: (i) the conventional reflective boundary conditions and (ii) a set of boundary conditions that we will call quasi-periodic boundary conditions. Both sets of boundary conditions are explained in detail in Appendix B. Here we give a brief account of the

Table 1
Simulations of the Linear Regime Using Quasi-periodic Boundary Conditions

Simulation	(n_x, n_z)	θ	β_0	χ_{\parallel}	ν_{\parallel}	D	Resolution	Figure
MTCL_chi	(1, 0)	0°	2×10^8	...	0	0	64×64	3(a)
MTCL_B	(1, 0)	0°	...	3×10^{-4}	0	0	64×64	3(b)
HPBL_nu	(1, 1)	90°	2×10^8	10^{-4}	...	0	64×64	4(a)
HPBL_n	(..., ...)	90°	2×10^6	10^{-4}	0	0	256×256	4(b)
D-mode_D	(1, 1)	90°	2×10^8	10^{-3}	0	...	256×256	5(a)
D-mode_nu	(1, 1)	90°	2×10^8	10^{-3}	...	10^{-3}	64×64	5(b)
MTCL_ICM ^a	(..., 0)	0°	2×10^6	1.4×10^{-2}	4.0×10^{-4}	0	256×32	6(a)
HPBL_ICM ^a	(..., ...)	90°	2×10^6	2.7×10^{-4}	4.5×10^{-6}	0	256×256	6(b)

Note. Each row represents a series of simulations, where the ellipses denote that the associated parameter is being varied.

^a Using gradients in both temperature and composition.

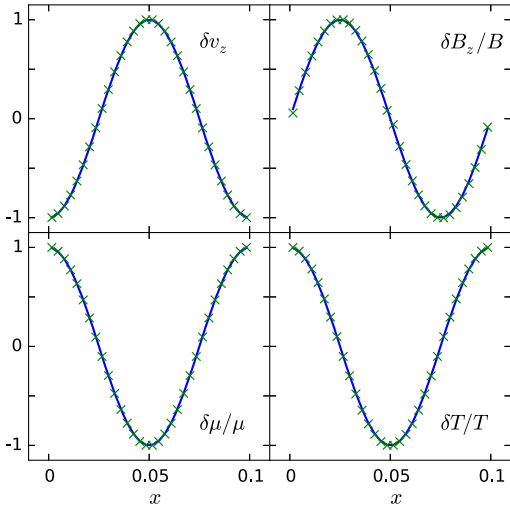


Figure 1. Four of the components of the perturbation at $z = L_z/2$ for a mode with $k_x = 2\pi/L_x$ at time $t = 5$ in a simulation with resolution 32×32 . The simulation (green crosses) matches the theory (blue lines). The magnetic field is $\pi/2$ out of phase with the velocity perturbation, as expected for a purely growing mode.

motivation for using these two sets of boundary conditions and their key differences.

The *quasi-periodic boundary conditions* are periodic in the relative changes in the physical quantities. We have found that these boundary conditions are a necessity in order for the simulations to reproduce the growth rates predicted by the local linear mode analysis. We believe that this is due to the assumption of periodicity in the perturbed quantities that is made when the dispersion relation is derived. This problem has also been encountered in previous studies of the MTI (Rasera & Chandran 2008). These boundary conditions are used in all simulations presented in Section 4.

The *reflective boundary conditions* maintain hydrostatic equilibrium by extrapolating pressure and density into the ghost zones at the top and bottom of the computational domain. The values of temperature and composition are held fixed at their initial values in the ghost zones. The velocity z -component is reflected symmetrically around the boundaries. If the magnetic

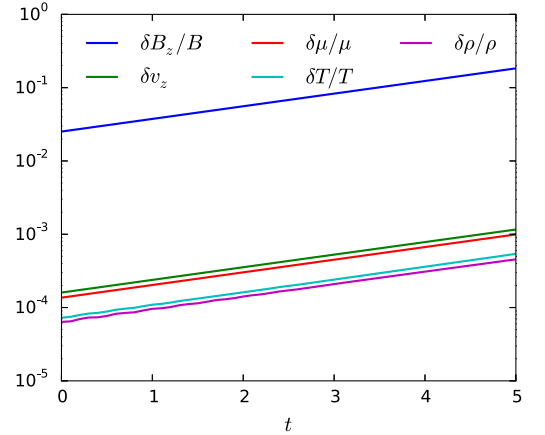


Figure 2. Evolution of box-averaged quantities. The perturbed quantities grow exponentially with a growth rate $\sigma = 0.40$.

field is initially vertical (horizontal), it is forced to remain vertical (horizontal) at the boundaries. These boundary conditions are used in the simulations presented in Section 5.

4. SIMULATIONS OF THE LINEAR REGIME

The equations are made dimensionless by scaling the density with ρ_0 , distances with H_0 , and velocities with the thermal velocity $v_{\text{th},0}$. The magnetic field strength B_0 is found from the dimensionless parameter β_0 . Here the subscript “0” denotes the value at the bottom of the computational domain, $z = 0$. With this convention, the unit of time is $H_0/v_{\text{th},0}$, temperature is scaled with T_0 , μ is scaled with μ_0 , pressure, as well as energy density, is scaled with $P_0 = \rho_0 v_{\text{th},0}^2$, and the value of g is unity. As a consequence, the coefficient for anisotropic heat conduction, χ_{\parallel} , is scaled with $\rho_0^3 v_{\text{th},0}^3 H_0/T_0$, and the coefficients for Braginskii viscosity, ν_{\parallel} , and anisotropic diffusion of composition, D , are both scaled with $v_{\text{th},0} H_0$.

We begin by comparing the simulations with the linear theory. In order to do so, we use the quasi-periodic boundary conditions described in the previous section and in Appendix B. A Cartesian box of size $[0, L_x] \times [0, L_z]$ with $L_x = L_z = 0.1$ and a resolution of 64×64 is used in all

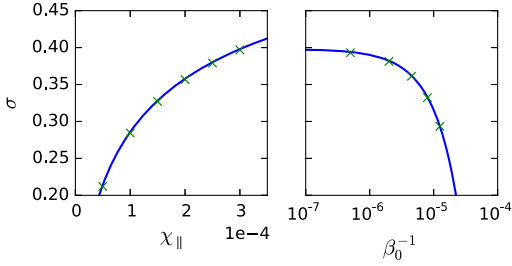


Figure 3. Growth rates for the MTCI. Left: the growth rate increases with the value of χ_{\parallel} . Right: the growth rate decreases with increasing initial magnetic field strength. The solid blue lines represent the theoretical values evaluated at $z = L_z/2$. The green crosses are growth rates obtained from the simulations.

simulations unless otherwise noted. An overview of the simulations of the linear regime can be found in Table 1.

The instabilities are excited by seeding a given mode, with components $(\delta v_x, \delta v_z, \delta B_x, \delta B_z, \delta \rho/\rho, \delta T/T, \delta \mu/\mu)$, as derived by solving the eigenvalue system associated with the dispersion relation introduced in Pessah & Chakraborty (2013) and Berlok & Pessah (2015). We set the overall mode amplitude by enforcing $\delta \rho/\rho = 10^{-4}$, so that the velocity perturbation is subsonic (Parrish & Stone 2005). The amplitudes of the other components are fixed by the solution to the linear eigenvalue problem, which predicts that unstable modes grow exponentially as $\exp(\sigma t)$ while the ratio of their components remains constant in time.

We begin by considering $D = 0$ and the hydrostatic atmosphere given in Section 3.1.1, which has $d \ln \mu / d \ln P = -1/3$ and $d \ln T / d \ln P = 0$. This atmosphere is unstable regardless of whether the magnetic field is oriented horizontally (MTCI) or vertically (HPBI), as described in Berlok & Pessah (2015).

4.1. The Magneto-thermo-compositional Instability

When the magnetic field is perpendicular to gravity, the general dispersion relation, Equation (13) in Berlok & Pessah (2015), reduces to

$$\sigma^2 \approx -g \frac{d \ln(T/\mu)}{dz} \frac{k_x^2 + k_y^2}{k^2}, \quad (23)$$

in the limit of fast heat conduction and weak magnetic field. When μ increases with height and the atmosphere is isothermal, we have $\sigma > 0$. This is the instability known as the MTCI (Pessah & Chakraborty 2013). In order to excite a single MTCI mode, we use a perturbation of the form⁴ $k_z = 0$ and $k_x = 2\pi/L_x$. We are interested in a direct visual comparison of the spatial dependence of the perturbations in the simulations and the one expected from the linear theory. In order to illustrate this, we consider a setting with $\chi_{\parallel} = 3 \times 10^{-4}$ and $\beta_0 = 2 \times 10^8$. In Figure 1, we show the values of the perturbations (green crosses) δv_z , $\delta B_z/B$, $\delta \mu/\mu$, and $\delta T/T$ as a function of the x -coordinate. The data slices are drawn at a fixed height, $z = L_z/2$ at the time $t = 5$ in

⁴ We note that $k_y = 0$ in all the simulations presented in this paper.

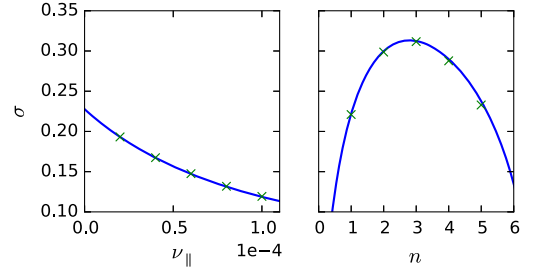


Figure 4. Growth rates for the local HPBI. Left: the growth rate decreases with the value of ν_{\parallel} . Right: the growth rate as a function of the mode number, $n = n_x = n_z$. The solid blue lines represent the theoretical values evaluated at $z = L_z/2$. The green crosses are growth rates obtained from the simulations.

dimensionless units. The numerical results show good agreement with the analytical results shown with blue solid lines.

In order to calculate the growth rate of the mode, we perform an exponential fit to the time evolution of the box average of the absolute value of any of the perturbed quantities, which are shown in Figure 2. As expected from the local linear mode analysis, the amplitudes of the various components of the perturbation grow exponentially at the same rate.

The growth rate of the MTCI depends on, among other things, the value of the heat conductivity, χ_{\parallel} , and the initial magnetic field strength, B_0 . In order to illustrate this dependence, and at the same time test our modification to the code, we perform a parameter study. In the left panel of Figure 3, we show how the growth rate increases with the value of the heat conductivity, χ_{\parallel} . This is to be expected because the MTCI is driven by heat transfer along magnetic field lines. In the right panel of Figure 3, we show how the growth rate decreases with the value of β_0^{-1} . The explanation for this behavior is that magnetic tension tends to stabilize the MTCI (Berlok & Pessah 2015). Magnetic tension has stabilizing effects in the limit $\omega_A \gg \omega_{\text{dyn}}$, where $\omega_A = k_{\parallel} v_A$ and $\omega_{\text{dyn}} = \sqrt{g/H_0}$. In dimensionless units, this requirement can be written as $2k_{\parallel}^2 \gg \beta$. From this estimate, the growth rates shown in the right panel of Figure 3 should be negligible when $\beta_0^{-1} \gg 10^{-4}$. The simulations and the solution to the dispersion relation show that the growth rates are already inhibited by magnetic tension at lower values of β_0^{-1} . These examples were generated by running 10 simulations at a modest resolution (64×64). At this resolution the growth rates match to within a percent of the values expected from linear theory.

4.2. The Heat- and Particle-flux-driven Buoyancy Instability

When the magnetic field is parallel to gravity, the general dispersion relation reduces to

$$\sigma^2 \approx g \frac{d \ln(T\mu)}{dz} \frac{k_x^2 + k_y^2}{k^2}, \quad (24)$$

in the limit of fast heat conduction and weak magnetic field. The isothermal atmosphere where μ increases with height, which we considered in the previous section, is therefore also unstable when the magnetic field is vertical. In this case, the instability has been termed the HPBI (Pessah & Chakraborty 2013).

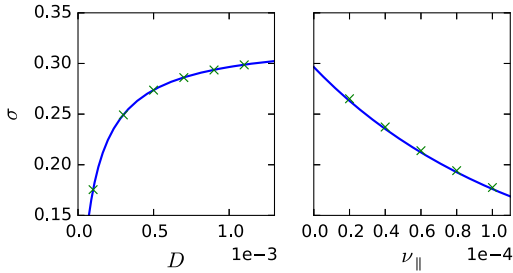


Figure 5. Growth rate as a function of D (left) and ν_{\parallel} for fixed values of $\chi_{\parallel} = D = 10^{-3}$ (right). The solid blue line represents the theoretical values evaluated at $z = L_z/2$, and the green crosses are growth rates obtained from the simulations.

In this example, we include Braginskii viscosity, which inhibits the growth rate by damping perturbations perpendicular to the magnetic field. Braginskii viscosity can be important for the HPBI (Berlok & Pessah 2015). The mechanism is similar to the mechanism described by Kunz (2011) for the HBI. In order to excite a single mode of the HPBI, we use a perturbation with wavenumbers $k_x = 2\pi n_x/L_x$ and $k_z = 2\pi n_z/L_z$, where $n = n_x = n_z$ is the mode number. We show the growth rate as a function of the Braginskii viscosity coefficient, ν_{\parallel} in the left panel of Figure 4. These simulations used a fixed value of $\chi_{\parallel} = 10^{-4}$, $n = 1$, and a numerical resolution of 64×64 . As expected, the growth rate indeed decreases with increasing value of viscosity ν_{\parallel} .

The second dependence we study for the HPBI is the one on the mode number, n . High wavenumbers require higher numerical resolution in order to be resolved, and we use a resolution of 256×256 for these simulations. For the sake of simplicity, Braginskii viscosity is not included in these simulations. The result is shown in the right panel of Figure 4. The growth rate increases for increasing wavenumber because small wavelength perturbations have a shorter timescale for heat conduction. When the wavelength is too short, magnetic field tension renders the modes stable. A naive estimate, using $2k_{\parallel}^2 \gg \beta$, suggests that this should happen when $n \gg 16$, but the exact solution to the dispersion relation shows that the instability is quenched already when $n = 7$. Using such simulations, we can directly see the cutoff in unstable wavenumbers resulting from magnetic field tension (as in this case) or viscosity (not shown here).

4.3. Modes Driven by Diffusion

One of the interesting findings of Pessah & Chakraborty (2013) is that there are instabilities that are driven by particle diffusion. This means that even though the equilibrium is stable according to Equation (24), the fact that $D \neq 0$ makes the equilibrium unstable. In order to study these unstable modes, we assume, for simplicity, an isothermal atmosphere with an initially vertical magnetic field.

In this case, as explained in Section 3.1, an equilibrium configuration needs to fulfill $\nabla \cdot \mathbf{Q}_c = 0$, and so we consider the atmosphere given in Section 3.1.2 as an initial condition. According to Equation (24), this configuration is unstable to the HPBI for an isothermal atmosphere when the helium concentration increases vertically. If instead the helium

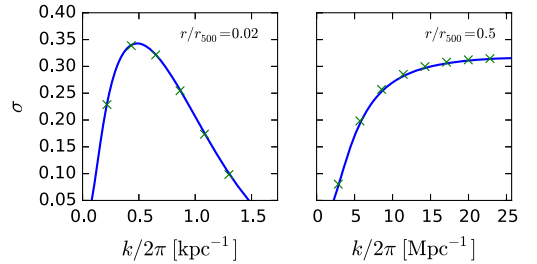


Figure 6. Left: growth rates in the inner region as a function of $k = k_x = k_z$. Right: growth rates in the outer region as a function of k_x for $k_z = 0$. The solid blue line represents the theoretical values evaluated at $z = L_z/2$, and the green crosses are growth rates obtained from the simulations.

concentration decreases with height, the atmosphere is stable in the absence of anisotropic particle diffusion. Choosing the slope in composition to be $s_c = -0.01$, we do not observe any instabilities in the simulation when $D = 0$. The situation changes dramatically, turning unstable when $D \neq 0$. The growth rates found in such simulations are compared with the predictions from the linear theory in Figure 5. Since the modes are driven by diffusion of helium, we expect the growth rate to increase with the value of D (left panel). The modes have a damped growth rate when Braginskii viscosity is included. We observe a decrease in the growth rate with increasing ν_{\parallel} , in agreement with the solution to the dispersion relation (right panel).

4.4. Gradients in Temperature and Composition

Having tested the case of isothermal atmospheres, we now consider a more general situation where both $dT/dz \neq 0$ and $d\mu/dz \neq 0$. In order to work with sensible values for these gradients, we consider the models in Peng & Nagai (2009), who analyzed the long-term evolution of the concentration of helium in a one-dimensional setting by solving a coupled set of Burgers' equations for a multicomponent plasma in the absence of a magnetic field. Berlok & Pessah (2015) analyzed the stability of the Peng & Nagai (2009) model by focusing on local regions, characterized by fixed temperature and composition gradients, and modeling these as a plane-parallel atmosphere.

In this section, we present local simulations with gradients in temperature and composition estimated at $r/r_{500} = 0.02$ and $r/r_{500} = 0.5$ with $r_{500} = 1.63$ Mpc in the Peng & Nagai (2009) model. These are the locations that were analyzed in Sections 6.6 and 6.4 in Berlok & Pessah (2015), indicated with a C and an A in Figure 8 in that paper. These two locations correspond to the inner region where the temperature and composition increase with radius and the outer region where the temperature and composition decrease with radius. At these radii, the values for the logarithmic gradients are $d \ln T / d \ln P = -0.4$ and $d \ln \mu / d \ln P = -0.13$ at $r/r_{500} = 0.02$ and $d \ln T / d \ln P = 0.16$ and $d \ln \mu / d \ln P = 0.05$ at $r/r_{500} = 0.5$.

We use the equilibrium derived in Section 3.1.2 with values taken from the model of Peng & Nagai (2009), $T_0 = 6.6$ keV ($T_0 = 9.5$ keV) and $c_0 = 0.56$ ($c_0 = 0.29$) for the inner (outer) region. The computational domain is $L_x = L_z = H_0/10$ where $H_0 = 50$ kpc for the inner region and $L_x = 10L_z = H_0$ where $H_0 = 0.35$ Mpc for the outer region. The gradients in

Table 2
Overview of the Simulations of the Nonlinear Regime Using the Reflective Boundary Conditions

Simulation	θ	β_0	χ_{\parallel}	ν_{\parallel}	D	Resolution	Figure
MTCI256	0°	2×10^8	5×10^{-4}	0	0	256×256	7(a), 8, 10
HPBI128	90°	2×10^8	5×10^{-4}	0	0	128×128	9
HPBI256	90°	2×10^8	5×10^{-4}	0	0	256×256	9
HPBI512	90°	2×10^8	5×10^{-4}	0	0	512×512	7(b), 9, 10

composition and temperature are set such that the dimensionless values of $d \ln T / d \ln P$ and $d \ln \mu / d \ln P$ in the plane-parallel atmosphere agree with the values in the model of Peng & Nagai (2009). They are given by $s_c = 2.9 \text{ Mpc}^{-1}$ ($s_c = -0.19 \text{ Mpc}^{-1}$) and $s_T = 0.058 \text{ keV kpc}^{-1}$ ($s_T = -4.3 \text{ keV Mpc}^{-1}$) for the inner (outer) region.

The values for ν_{\parallel} , χ_{\parallel} , and D are calculated from the model of Peng & Nagai (2009) as explained in the appendix of Berlok & Pessah (2015). The dimensionless values are so large that high-resolution numerical simulations become very computationally expensive. As this is a test, we have arbitrarily reduced the values by a factor of 100 in the simulations. We use a value of $\beta = 2 \times 10^6$ for both sets of simulations and adopt a resolution of 32×256 (MTCI) and 256×256 (HPBI). Some of the details of the simulations are listed in Table 1 with the names HPBI_ICM and MTCI_ICM. The growth rates also depend on the wavenumbers, k_x and k_z . For the HPBI (in the inner region) we take $k = k_x = k_z$ and investigate growth rate as a function of k . For the MTCI (in the outer region) we take $k_z = 0$ and investigate the growth rate as a function of k_x . The results are shown in Figure 6, with the growth rates of the HPBI in the left panel and the growth rates of the MTCI in the right panel. An estimate shows that the HPBI should be suppressed by magnetic tension for $k/2\pi \gg 3.4 \text{ kpc}^{-1}$ and the MTCI should be suppressed for $k/2\pi \gg 450 \text{ Mpc}^{-1}$. The growth rates are in units of 50 and 280 Myr, respectively. Therefore, in physical units, the maximum growth rates in these simulations are $\sigma_{\max} = 6.4 \text{ Gyr}^{-1}$ for the HPBI and $\sigma_{\max} = 1.2 \text{ Gyr}^{-1}$ for the MTCI.

5. SIMULATIONS OF THE NONLINEAR REGIME

In order to study the nonlinear evolution of the MTCI and the HPBI, we use the reflective boundaries described in Appendix B. We use the isothermal atmospheres presented in Section 3.1.1 and seed both velocity components with Gaussian noise with a standard deviation of 10^{-4} . The simulations are run without Braginskii viscosity or anisotropic diffusion of helium, but anisotropic heat conduction is accounted for with a value of $\chi_{\parallel} = 5 \times 10^{-4}$. We use a value of 2×10^8 for the plasma- β . An overview of the simulations of the nonlinear regime can be found in Table 2.

We start out by studying the evolution of the MTCI, i.e., we consider an atmosphere threaded by a horizontal magnetic field. The subsequent evolution of the magnetic field and the plasma composition is illustrated in the upper panel of Figure 7. In this figure, it is evident that the MTCI is able to mix the helium content and to completely rearrange the initially ordered magnetic field. The resulting growths in kinetic and magnetic energy densities are shown, respectively, in the left and right panels of Figure 8. The kinetic energies associated with the two velocity components are roughly in equipartition throughout the simulation, i.e., $\langle \rho v_x^2 \rangle \approx \langle \rho v_z^2 \rangle$ with $\langle \rho v_z^2 \rangle$ always larger but

never exceeding $\langle \rho v_x^2 \rangle$ by more than an order of magnitude. The exponential phase of the instability ends at $t \approx 30$. After this point in time, both the kinetic and magnetic energies saturate, with the former exceeding the latter by two orders of magnitude. In spite of the fact that $\langle B_z^2 \rangle$ vanishes initially, by the end of the simulation the energies associated with the two magnetic field components are roughly in equipartition with $\langle B_z^2 \rangle$ larger than $\langle B_x^2 \rangle$ by a factor of ≈ 2 , with $\langle B_z^2 \rangle$ having grown by a factor of ≈ 8 with respect to its initial value.

We now consider the evolution of the HPBI. The setup is essentially the same, but the initial magnetic field is now vertical.⁵ The evolution of the HPBI is illustrated in the lower panel of Figure 7 with a resolution of 512×512 . The initial vertical magnetic field is rearranged by the HPBI, and, as for the MTCI, the helium content is mixed by the action of the instability. The HPBI leads to growth in the magnetic and kinetic energy densities. In order to assess whether this growth is numerically converged, we have also run simulations at resolutions of 128×128 and 256×256 . We show the evolution of $\langle B_x^2 \rangle / 8\pi$ and $\langle B_z^2 \rangle / 8\pi$ for the three different numerical resolutions in Figure 9. We observe that the instability leads to exponential growth followed by saturation in both $\langle B_x^2 \rangle / 8\pi$ and $\langle B_z^2 \rangle / 8\pi$. While the growth rate increases with increasing resolution, the values in the saturated state agree quite well.

It is also of interest to understand how the magnetic field changes from being initially vertical to having a large horizontal component because the magnetic field inclination has consequences for heat transport along the vertical direction of the box. Such studies have been done for both the MTI (Parrish & Stone 2005, 2007) and the HBI (Parrish & Quataert 2008). These studies were motivated by a need to understand the cooling flow problem of galaxy clusters (Fabian 1994), and whether magnetic fields could alleviate this problem. While the MTI could potentially increase heat transport toward the core by making the magnetic field be preferentially in the radial direction (Parrish et al. 2008), the HBI has been shown to lead to core insulation by driving the magnetic field to be perpendicular to the radial direction (Parrish & Quataert 2008; Bogdanović et al. 2009; Parrish et al. 2009), which would exacerbate the cooling flow problem.

In Figure 10, we show the average magnetic field inclination as a function of time for the simulations of the MTCI and the HPBI. The average inclination saturates to a value of approximately $\theta \approx 45^\circ$ for both the simulations. This behavior is qualitatively different from the behavior of the magnetic field inclination for the MTI and the HBI. The difference can be explained in the following way. The MTI, which is maximally unstable when the magnetic field is horizontal, has been found to drive the saturated magnetic field to be roughly vertical

⁵ The boundary conditions on the magnetic field are also slightly different; see Appendix B.

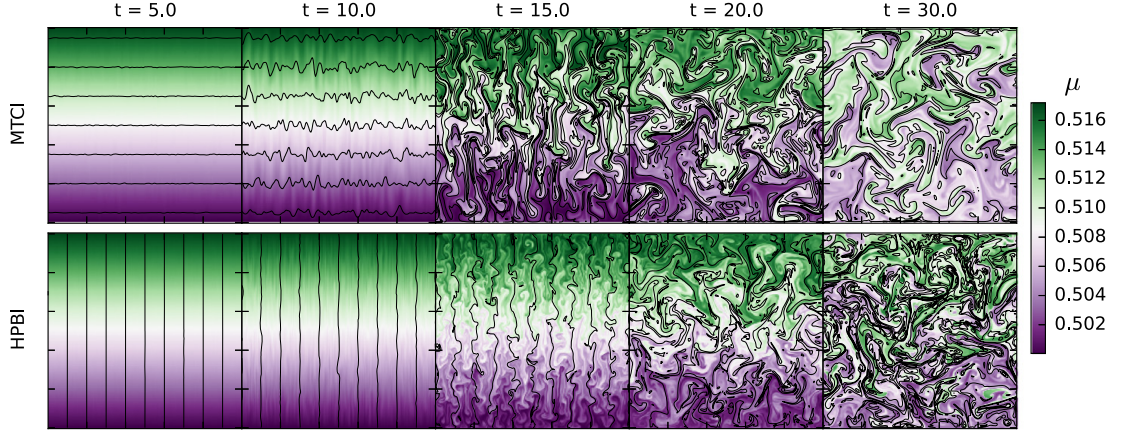


Figure 7. Evolution of instabilities in an isothermal atmosphere with $d \ln \mu / d \ln P = -1/3$. The magnetic field lines are shown as solid black lines. The composition of the plasma is shown with green representing a high concentration and purple representing a low concentration. The MTCI (upper panel) and the HPBI (lower panel) both give rise to mixing of the helium content. The size of the computational domain is $H_0/10 \times H_0/10$. The motions generated by the instabilities can be hinted at by comparing neighboring snapshots but are best understood from the animated version of this figure (see the online version).

(Animations (a and b) of this figure are available.)

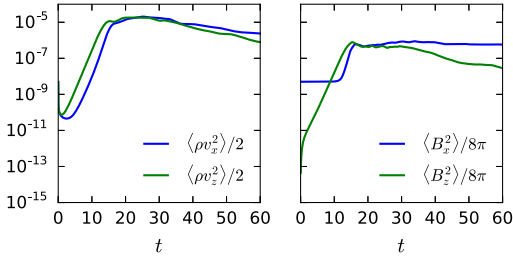


Figure 8. Evolution of kinetic (left panel) and magnetic (right panel) energies for the MTCI. After the initial phase of exponential growth, the instability saturates with energies that are roughly in equipartition.

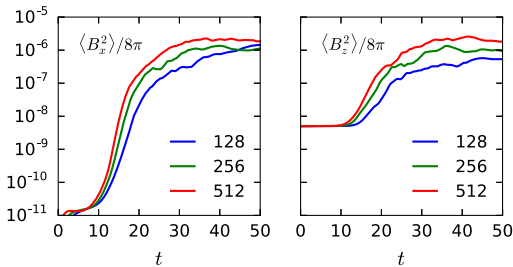


Figure 9. Convergence of $\langle B_x^2 \rangle / 8\pi$ and $\langle B_z^2 \rangle / 8\pi$ as a function of resolution. The highest resolution is much more expensive to run because of the prohibitive time step constraint due to heat conduction; see Appendix A.

(Parrish & Stone 2007). The HBI, which is maximally unstable when the magnetic field is vertical, drives the magnetic field to be roughly horizontal (Parrish & Quataert 2008). These instabilities depend on gradients in temperature that have

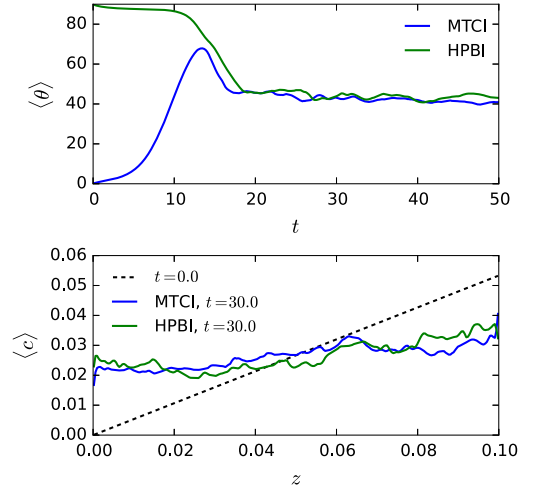


Figure 10. Upper panel: evolution of the average inclination of the magnetic field for the MTCI and the HPBI. Both instabilities seem to drive the average inclination toward 45° . Lower panel: the average along x of c for the MTCI (blue) and the HPBI (green) at the end of the exponential phase of the simulations ($t = 30$). The initial gradient in c (dashed black line) is diminished by the instabilities.

opposite directions, and so they cannot be present at the same time. On the other hand, both the MTCI and the HPBI require a mean molecular weight that increases with height, and so they can both be present at the same time. This feature of the MTCI and the HPBI was discussed in Berlok & Pessah (2015); see especially Figure 4 in that paper. The interpretation of the left panel of Figure 10 is therefore that the MTCI aims at driving

the magnetic field angle toward 90° while the HPBI aims at driving the magnetic field angle toward 0° . In the end, they reach a compromise at roughly 45° .

The helium mass concentration, c , dramatically changes, and the initial gradient is diminished by the instability as time progresses. This is illustrated in the lower panel of Figure 10 for both the MTCI and the HPBI. As explained in the introduction, gradients in composition can introduce biases in key cluster parameters. We are therefore interested in understanding whether such gradients, if initially present, will be robust. The simulations presented here are heavily idealized, among many reasons because the gas is assumed to be initially isothermal and the simulations are local. Nevertheless, these simulations serve as a proof of principle that gradients in composition can indeed be altered by turbulent mixing induced by plasma instabilities. Future work, using realistic gradients for temperature and composition as well as transport coefficients, should allow us to understand whether such mixing can occur on timescales relevant for galaxy clusters.

6. SUMMARY AND DISCUSSION

In this paper we have introduced a modified version of Athena (Stone et al. 2008) for performing kinetic MHD simulations of weakly collisional plasmas with nonuniform composition. We have employed this modified code to perform the first simulations of the MTCI, the HPBI, and the diffusion modes introduced in Pessah & Chakraborty (2013). The set of simulations, aimed at investigating the linear evolution of these instabilities, served as a test for both the modification to Athena and the local linear mode analysis in Pessah & Chakraborty (2013) and Berlok & Pessah (2015).

The simulations of weakly collisional, isothermal atmospheres with a gradient in helium presented in Section 5 showed that the plasma instabilities, feeding off gradients in composition, can induce turbulent mixing of the helium content. This conclusion is valid for compositions that increase in the direction anti-parallel to gravity, regardless of whether the initial magnetic field is parallel or perpendicular to the direction of gravity. In the saturated state, the magnetic field components in the x and z directions have roughly the same average energy, but the energies are a factor of 10 higher for the HPBI than for the MTCI. The kinetic energy components are also roughly in equipartition. In both cases, the instabilities saturate by driving the average magnetic field inclination to roughly 45° . This effect seems to open the possibility of alleviating the core insulation observed in previous homogeneous simulations of the HBI, provided that the global cluster dynamics were to allow for an increase in the mean molecular weight with radius in the inner region, as envisioned by current (one-dimensional, unmagnetized) helium sedimentation models (Peng & Nagai 2009).

The simulations of the nonlinear regime of the MTCI and the HPBI presented in this paper considered an isothermal atmosphere as the equilibrium background. It would be an improvement to use the model of Peng & Nagai (2009) to determine the gradients in both temperature and composition. This would provide insight into the saturation of instabilities in potentially more realistic scenarios where the dynamical evolution is determined by the simultaneous effects of both gradients. Before proceeding with this endeavor, there are, however, a few issues that would be desirable to address, as we detail below.

It was found in Berlok & Pessah (2015) that the HPBI, if present in the inner regions of the ICM model of Peng & Nagai (2009), will have its fastest growth rates at wavelengths that are longer than the scale height of the atmosphere. This conclusion is similar to what was found for the HBI in Kunz (2011). Neither local linear theory nor local simulations will therefore capture the physics of the HPBI in the inner region of the ICM. This implies that both a quasi-global theory and simulations are needed in order to study the influence of the possible gradient in composition on the dynamics of the inner region of the ICM.

Local simulations of the MTI have been shown to underestimate the turbulence (McCourt et al. 2011), and boundary effects can also modify the conclusions from local simulations. The solution to this problem for the MTI has been to sandwich the unstable region between stable layers, thereby isolating it from the boundaries (Parrish & Stone 2005, 2007; Kunz et al. 2012). A similar approach seems reasonable for the MTCI.

Other complications stem from the fact that pressure anisotropies, shown to be important for the evolution of the MTI and HBI (Kunz 2011; Kunz et al. 2012), can give rise to microscale instabilities such as the firehose and mirror instability (Schekochihin & Cowley 2006; Schekochihin et al. 2010). These small-scale instabilities are only excited once the pressure anisotropy grows beyond $|p_{\parallel} - p_{\perp}|/P \gtrsim \beta^{-1}$. They do not appear in the tests of the linear regime of the MTCI, HPBI, and the diffusion modes presented in Section 4 because we terminate the simulations before the stability criterion is violated. They are not present in the simulations of the nonlinear regime in Section 5 because we take the pressure to be isotropic in these simulations (no Braginskii viscosity). The problem with microscale instabilities is that they are not correctly described by the framework of kinetic MHD (Schekochihin et al. 2005), an issue that will need to be addressed for simulations of the nonlinear evolution of the MTCI and the HPBI when Braginskii viscosity is included (see Kunz et al. 2012 for a discussion of these issues in the context of the MTI and the HBI).

All this being said, our study suggests that, at least in the idealized settings that we considered here, gradients in composition are able to drive turbulent mixing of the composition in weakly collisional, magnetized plasmas. This motivates future work on the generation and sustainment of both temperature and composition gradients in galaxy clusters and their potential influence on the global dynamics of the ICM. We envision that the modified version of Athena that we developed will be a useful asset in this context. In order to model more realistically the physics of the ICM, future improvements could include extending the simulations to three dimensions and adding optically thin cooling in order to study the cooling flow problem. Furthermore, the equations of kinetic MHD, as embodied in Equations (1)–(5), cannot account for the slow sedimentation of helium that is the core feature in the model of Peng & Nagai (2009). An extension of the framework of kinetic MHD to include this effect would allow us to self-consistently include sedimentation in the simulations (Bahcall & Loeb 1990; Berlok & Pessah 2015) and study the effects of the instabilities described in this paper in a dynamic, slowly varying background.

We acknowledge useful discussions with Daisuke Nagai, Matthew Kunz, Prateek Sharma, Ellen Zweibel, and Ian Parrish during the 3rd ICM Theory and Computation Workshop held at

the Niels Bohr Institute in 2014. We thank Sagar Chakraborty, Colin McNally, Gareth C. Murphy, and Henrik Latter for valuable discussions and comments. We are grateful to Oliver Gressel for suggesting using the quasi-periodic boundary conditions for testing the linear theory and to Tobias Heinemann for aid in rendering magnetic field lines. We also thank the anonymous referee for a number of useful suggestions that helped improve the manuscript. The research leading to these results has received funding from the European Research Council under the European Union's Seventh Framework Programme (FP/2007–2013) under ERC grant agreement 306614. T.B. also acknowledges support provided by a L rup Scholar Stipend, and M.E.P. also acknowledges support from the Young Investigator Programme of the Villum Foundation.

APPENDIX

In this appendix, we describe the numerical methods used in this paper. We use the publicly available MHD code Athena, which solves the conservative form of the MHD equations. The algorithms used are described in Gardiner & Stone (2005) and Stone & Gardiner (2009), and the implementation of Athena along with tests is described in detail in Stone et al. (2008). Athena is a finite-volume code, which uses the Godunov method. We use the directionally unsplit corner transport upwind method along with constrained transport (CTU + CT), which is the recommended setting. We furthermore use the anisotropic heat conduction module that was implemented in Athena by Parrish & Stone (2005) using operator splitting.

Appendix A explains the implementation of a spatially varying mean molecular weight, μ , the anisotropic diffusion of helium and tests cases, in Athena. In Appendix B we discuss in detail the boundary conditions used in the simulations.

APPENDIX A IMPLEMENTATION OF ANISOTROPIC DIFFUSION OF COMPOSITION IN ATHENA

Let us consider the equation describing the evolution of the helium mass concentration, $c = \rho_{\text{He}}/\rho$, given by⁶

$$\frac{\partial c}{\partial t} + (\mathbf{v} \cdot \nabla)c = -\nabla \cdot \mathbf{Q}_c. \quad (25)$$

Athena has an option for adding passive scalars, which we use for adding the helium mass concentration. This option turns on an extra equation,

$$\frac{\partial(\rho c_n)}{\partial t} + \nabla \cdot (\rho c_n \mathbf{v}) = 0, \quad (26)$$

where ρ is the total density and c_n is the mass concentration of the n th scalar. We only add a single scalar, namely, the helium mass concentration, c . This built-in function takes care of the Lagrangian part of Equation (25). The diffusion term is then solved using a finite-difference scheme and operator splitting.

⁶ We do not consider the effects of thermo-diffusion and baro-diffusion, which makes our current model unable to describe the slow sedimentation of helium (Bahcall & Loeb 1990) that can give rise to a composition gradient.

Anisotropic diffusion of helium is described by the right-hand side of Equation (25), which, when $\nu = 0$, reduces to

$$\frac{\partial c}{\partial t} = -\nabla \cdot \mathbf{Q}_c = D \nabla \cdot (\hat{\mathbf{b}} \hat{\mathbf{b}} \cdot \nabla c). \quad (27)$$

The composition flux for anisotropic helium diffusion has the same form as the heat flux for anisotropic heat conduction, as seen by comparing Equations (12) and (11), respectively. We can therefore use the same method to calculate the two physically different anisotropic fluxes. The original implementation of anisotropic heat conduction was done by Parrish & Stone (2005) using an asymmetric finite-difference scheme (Sharma & Hammett 2007; van Es et al. 2014).

Nonideal effects are computationally expensive because they are generally described by parabolic operators that cannot be added to the hyperbolic fluxes used in the Godunov scheme. The parabolic operators can be shown to have a very prohibitive time-step constraint (Durran 2010) for heat conduction and concentration diffusion as given by, respectively,

$$\Delta t_{\chi_{\parallel}} < \frac{b (\Delta x)^2}{\kappa_{\parallel} \gamma - 1}, \quad (28)$$

$$\Delta t_D < b \frac{(\Delta x)^2}{D}. \quad (29)$$

Here $\kappa_{\parallel} = \chi_{\parallel} T/P$ is the heat diffusivity, the parameter b is $b = 1/2, 1/4, 1/6$ in one, two, and three dimensions, respectively, and Δx is the grid size.

The Courant number, C , is defined to be the ratio of the applied time step to the allowed time step. We use $C = 0.4$ in all our simulations. Because $\Delta t_{\text{MHD}} \propto \Delta x$, the very prohibitive constraints on the time step for the parabolic operators will generally lead to $\Delta t_{\text{MHD}} \gg \Delta t_{\chi} \sim \Delta t_D$. In order to partially circumvent this problem, we use subcycling, taking up to 10 diffusion steps for each MHD step, as suggested in Kunz et al. (2012).

Sharma & Hammett (2007) found that the finite-difference approximation can lead to unphysical behavior with diffusion in the wrong direction. In the context of heat diffusion this problem can lead to negative temperatures and therefore an imaginary sound speed. The same problem arises when considering helium diffusion, and we use van Leer limiters on the derivatives to circumvent it (Sharma & Hammett 2007).

The publicly available version of Athena works with constant viscosity, ν_{\parallel} , and heat diffusivity, $\kappa_{\parallel} = \chi_{\parallel} T/P$. However, these coefficients, as well as the diffusion coefficient D , do in general depend on temperature, density, and composition; see, for instance, the discussion in the appendix of Berlok & Pessah (2015). Accounting for this dependence is not crucial in local simulations, but it becomes essential in global simulations. We have modified Athena to use spatially varying coefficients by using a harmonic average of the coefficients (Sharma & Hammett 2007). This makes the time step computed from Equations (28) and (29) spatially dependent. We therefore calculate the time step at each cell and use the minimum value. This implementation will be useful in future global studies.

A.1. Tests of the Implementation of Anisotropic Diffusion

In order to verify the implementation of anisotropic diffusion of helium, we performed three different test problems with a known analytical solution. These tests were carried out with the MHD solver turned off.

A.1.1. One-dimensional Diffusion

We consider the diffusion of a step function as in Rasera & Chandran (2008) using a one-dimensional grid with 100 cells on the domain $x = [0, 1]$ with $D = 1$ and run the simulation up to $t = 0.0028$. The analytical solution to the diffusion of a step function is

$$c(x, t) = c_0 + \frac{\Delta c}{2} \operatorname{erf}\left(\pm \frac{x - x_0}{\sqrt{4Dt}}\right), \quad (30)$$

where $c_0 = 3/2$ and $\Delta c = 1$. The “+” sign is used with $x_0 = 0.25$ for $x < 0.5$ and the “-” sign is used with $x_0 = 0.75$ for $x > 0.5$. The numerical result matches the analytical solution, as seen in Figure 11, implying that the method works well in one dimension.

A.1.2. Diffusion of a 2D Gaussian

A more challenging test can be posed by considering the magnetic field to be inclined at an angle, θ , with respect to the grid. We consider an initially isotropic, 2D Gaussian distribution of helium diffusing out along an inclined magnetic field. The analytical solution is⁷

$$c(x, y, t) = \frac{1}{2\pi a(t)a_0} \exp\left\{-\frac{(x \cos \theta + y \sin \theta)^2}{2a(t)^2}\right\} \times \exp\left\{-\frac{(y \cos \theta - x \sin \theta)^2}{2a_0^2}\right\}, \quad (31)$$

where $a(t)^2 = a_0^2 + 2Dt$ and a_0 is the initial standard deviation of the Gaussian.

The computational domain is a $[-1, 1] \times [-1, 1]$ Cartesian box. We use $a_0 = 1/8$ and $D = 0.001$. The errors at $t = 4$ are compared to the analytical solution in Figure 12. In the left panel the L_2 errors are shown as a function of the magnetic field inclination and resolution. These errors are smallest when $\theta = 0$ or $\theta = \pi/2$, corresponding to the grid and the magnetic field being aligned. In the right panel we show that the solution for $\theta = 40^\circ$ converges as $L_2 \propto (\Delta x)^m$, where Δx is the (uniform) grid spacing and $m = 1.9$ is the order of convergence.

A.1.3. Diffusion of a High-concentration Patch in a Circular Magnetic Field

The final and most challenging test that we carry out for anisotropic transport was introduced in Parrish & Stone (2005). We consider a Cartesian box of size $[-1, 1] \times [-1, 1]$ with a patch with higher concentration c , specifically⁸

$$c = \begin{cases} 12 & \text{if } 0.5 < r < 0.7 \text{ and } -\pi/12 < \theta < \pi/12, \\ 10 & \text{otherwise.} \end{cases} \quad (32)$$

⁷ This result can be derived by solving the one-dimensional diffusion equation for a Gaussian initial distribution followed by a rotation of the coordinate system. The one-dimensional problem is solved by using a Fourier transform in space and a Laplace transform in time.

⁸ This test was constructed for the anisotropic heat conduction. We are using the same initial values (10 and 12) as in the literature, making it easier to compare the results. These values are of course not meaningful values for c , but it still serves as a test of the implementation of anisotropic diffusion. The same considerations apply to the step function test.

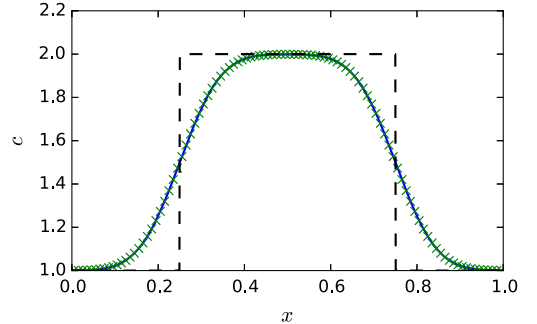


Figure 11. Diffusion of a step function. The initial condition is shown with a dashed line. The green crosses correspond to data from the simulation, and the solid blue line is the analytical solution at $t = 0.0028$.

The density is uniform with $\rho = 1$, and the magnetic field is circular. In order to ensure $\nabla \cdot \mathbf{B} = 0$, the magnetic field was initialized with a vector potential satisfying $\nabla \times \mathbf{A} = \mathbf{B}$.

We considered the value $D = 0.01$ and run the simulation until $t = 200$. The overconcentration diffuses out along the magnetic field lines, as observed in Figure 13. We have run this test problem with the same resolutions as Sharma & Hammett (2007) and obtain the exact same values quoted there for the error norms associated with the resolutions 200×200 and 400×400 . For instance, for a resolution of 200×200 , we obtain $L_1 = 0.0264$, $L_2 = 0.0407$, $L_\infty = 0.0928$, $c_{\min} = 10$, and $c_{\max} = 10.1016$ at $t = 200$ as stated in Sharma & Hammett (2007).

It is evident from Figure 13 that, even though only anisotropic diffusion is explicitly turned on, there is still a small amount of numerical, perpendicular diffusion. This is undesired in simulations of instabilities because isotropic diffusion will lower the growth rates or even quench the instabilities. This was investigated by Parrish & Stone (2005) for the MTI, who found that it is, however, insensitive to perpendicular diffusion provided that $|\chi_\perp/\chi_\parallel| < 10^{-3}$. The fact that we find the correct analytical growth rates for all simulations discussed in Section 4 shows that the numerical perpendicular diffusion is not a problem for our present purposes.

APPENDIX B BOUNDARY CONDITIONS

In the horizontal direction we use the periodic boundary conditions that Athena provides as a standard option. In the vertical direction, boundary conditions that maintain hydrostatic equilibrium are required. In this section we describe the conventional, reflective boundary conditions, as well as the quasi-periodic boundary conditions alluded to in Section 3.2.

B.1. Reflective Boundary Conditions

Our implementation of reflective boundary conditions follows the description in Zingale et al. (2002). Hydrostatic equilibrium requires that Equation (13) is satisfied. This requirement can be approximated by

$$P_i - P_{i+1} = \frac{ag \Delta z}{12} (5\rho_{i+1} + 8\rho_i - 2\rho_{i-1}), \quad (33)$$

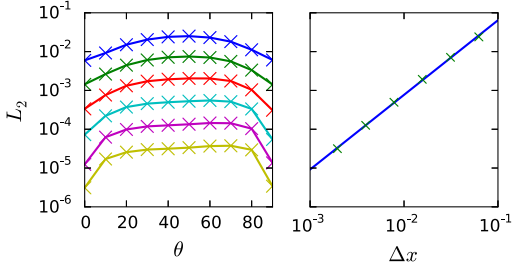


Figure 12. Left: L_2 error as a function of magnetic field inclination. Resolutions of $N \times N$ with $N = 32, 64, 128, 256, 512,$ and 1024 were used with monotonically decreasing L_2 at all angles. As expected, the asymmetric finite-difference scheme gives the best result when the magnetic field is aligned with the grid. Right: convergence to the exact solution with decreasing Δx for a magnetic field inclined at 40° from the x -axis.

where $a = 1$ ($a = -1$) at the top (bottom) of the domain. In this notation, i refers to cell i and $i + 1$ refers to one cell further up (down) when $a = 1$ ($a = -1$). This equation is then solved for ρ_{i+1} using that

$$\rho_{i+1} = \frac{\rho_{i+1} T_{i+1}}{\mu_{i+1}}, \quad (34)$$

along with an assumption on μ_{i+1} and T_{i+1} . Either one can assume $\mu_i = \mu_{i+1}$ and $T_i = T_{i+1}$, or one can prescribe the values at the boundaries to be equal to their initial values, i.e., $\mu_{i+1} = \mu_0$ and $T_{i+1} = T_0$. In the case where the mean molecular weight μ is not included, Parrish & Stone (2005) refer to these boundary conditions as adiabatic and conductive, respectively. A combination of these two boundary conditions is also possible (i.e., fixing μ and varying T or vice versa). We have implemented all four combinations but will only discuss the conducting boundary conditions ($\mu_{i+1} = \mu_0$ and $T_{i+1} = T_0$) in the following, since these are the boundary conditions used in Section 5.

Solving Equations (33) and (34) for ρ_{i+1} and P_{i+1} , we find

$$\rho_{i+1} = \frac{P_i + \alpha(8\rho_i - \rho_{i-1})}{T_0/\mu_0 - 5\alpha} \quad (35)$$

and $P_{i+1} = \rho_{i+1} T_0/\mu_0$, where

$$\alpha = \frac{a \Delta z g}{12}. \quad (36)$$

These relations are used to calculate the density and pressure of the four ghost zones at the top and bottom of the computational domain. At the same time, velocity is reflected symmetrically around $z = 0$ and $z = L_z$. The magnetic field components are also mirrored. In the case of an initially vertical magnetic field, we let the B_x component change sign, whereas in the case of an initially horizontal magnetic field, we let the B_z component change sign. This forces the field to remain vertical (horizontal) at the boundary in the case of an initially vertical (horizontal) field.

Athena uses the Godunov scheme, which is known not to be optimal at maintaining hydrostatic equilibrium (Zingale et al. 2002). The reason is that the pressure term in the momentum equation is not solved simultaneously with the

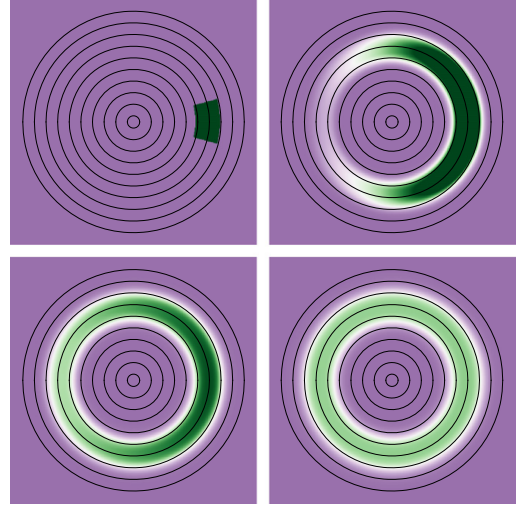


Figure 13. The patch with a high concentration of c diffuses out along the circular magnetic field. Snapshots at $t = 0, 25, 75,$ and 200 . The color scale is from 10 to 10.2, and the perpendicular diffusion is small. The resolution in this numerical experiment is 400×400 .

gravity term. There are ways to modify a Godunov scheme such that this problem is circumvented; see, for instance, Zingale et al. (2002) and Käppeli & Mishra (2014). We use a high numerical resolution and a low Courant number ($C = 0.4$) in order to maintain hydrostatic equilibrium as well as possible. The minimum amplitude we can use for perturbations in \mathbf{v} is, however, limited by the numerical noise caused by the inability of the code to perfectly maintain hydrostatic equilibrium, in agreement with the findings of Parrish et al. (2012b).

B.2. Quasi-periodic Boundary Conditions

A key assumption in standard local linear mode analysis, such as presented in Pessah & Chakraborty (2013) and Berlok & Pessah (2015), is that the perturbations have the spatial dependence $\exp(i\mathbf{k} \cdot \mathbf{x})$. This assumption is not fulfilled for the reflective boundary conditions, and it is thus impossible to cleanly excite a single eigenmode, the problem being that the boundary conditions excite other modes in an uncontrolled way. We originally realized this problem when we studied the HBI, but it persists in the case of the HPBI and its diffusive variant. The problem is not present for the MTI and the MTCI in the case $k_z = 0$ because the boundaries are periodic in x .

We have developed special boundary conditions that are consistent with the assumptions used in the local mode analysis. One of the key assumptions here is that the perturbed quantities $\delta v_x, \delta v_z, \delta B_x, \delta B_z, \delta \rho/\rho, \delta \mu/\mu,$ and $\delta T/T$ are periodic. In the following, the values outside the computational domain (the ghost zones) are denoted by a subscript g , and the values on the inside are denoted by a subscript i . The subscript “eq” refers to the value of the equilibrium background (as given in Sections 3.1.1 or 3.1.2). The mapping from interior to ghost zones ($i \rightarrow g$) is the same as for periodic boundary conditions. Instead of directly mapping the interior values to the ghost zones, we let the ghost zones depend on the change in the interior values with respect to the equilibrium background. The

quasi-periodic boundary conditions are then defined as

$$\rho_g = \rho_{g,\text{eq}} \left(1 + \frac{\rho_i - \rho_{i,\text{eq}}}{\rho_{i,\text{eq}}} \right), \quad (37)$$

$$T_g = T_{g,\text{eq}} \left(1 + \frac{T_i - T_{i,\text{eq}}}{T_{i,\text{eq}}} \right), \quad (38)$$

$$\mu_g = \mu_{g,\text{eq}} \left(1 + \frac{\mu_i - \mu_{i,\text{eq}}}{\mu_{i,\text{eq}}} \right), \quad (39)$$

with the pressure given by $P_g = \rho_g T_g / \mu_g$. The equilibrium magnetic field and velocity do not have a gradient, and so their boundary conditions are simply periodic, i.e., $v_g = v_i$ and $B_g = B_i$. These are the boundary conditions we used in Section 4.

REFERENCES

- Bahcall, J. N., & Loeb, A. 1990, *ApJ*, **360**, 267
 Balbus, S. A. 2000, *ApJ*, **534**, 420
 Balbus, S. A. 2001, *ApJ*, **562**, 909
 Berlok, T., & Pessah, M. E. 2015, *ApJ*, **813**, 22
 Bogdanović, T., Reynolds, C. S., Balbus, S. A., & Parrish, I. J. 2009, *ApJ*, **704**, 211
 Braginskii, S. 1965, in Review of Plasma Physics, Vol. 1, ed. M. A. Leontovich, (trans. H. Lashinsky; New York: Consultants Bureau), 205
 Chuzhoy, L., & Loeb, A. 2004, *MNRAS*, **349**, L13
 Chuzhoy, L., & Nusser, A. 2003, *MNRAS*, **342**, L5
 Durran, D. R. 2010, Numerical Methods for Fluid Dynamics (Berlin: Springer)
 Fabian, A. C. 1994, *ARA&A*, **32**, 277
 Fabian, A. C., & Pringle, J. E. 1977, *MNRAS*, **181**, 5
 Gardiner, T. A., & Stone, J. M. 2005, *JCoPh*, **205**, 509
 Gilfanov, M. R., & Syunyaev, R. A. 1984, *SvAL*, **10**, 137
 Käppeli, R., & Mishra, S. 2014, *JCoPh*, **259**, 199
 Kunz, M. W. 2011, *MNRAS*, **417**, 602
 Kunz, M. W., Bogdanović, T., Reynolds, C. S., & Stone, J. M. 2012, *ApJ*, **754**, 122
 Latter, H. N., & Kunz, M. W. 2012, *MNRAS*, **423**, 1964
 Markevitch, M. 2007, arXiv:0705.3289
 McCourt, M., Parrish, I. J., Sharma, P., & Quataert, E. 2011, *MNRAS*, **413**, 1295
 McCourt, M., Sharma, P., Quataert, E., & Parrish, I. J. 2012, *MNRAS*, **419**, 3319
 Parrish, I. J., McCourt, M., Quataert, E., & Sharma, P. 2012a, *MNRAS*, **419**, L29
 Parrish, I. J., McCourt, M., Quataert, E., & Sharma, P. 2012b, *MNRAS*, **422**, 704
 Parrish, I. J., & Quataert, E. 2008, *ApJL*, **677**, L9
 Parrish, I. J., Quataert, E., & Sharma, P. 2009, *ApJ*, **703**, 96
 Parrish, I. J., Quataert, E., & Sharma, P. 2010, *ApJL*, **712**, L194
 Parrish, I. J., & Stone, J. M. 2005, *ApJ*, **633**, 334
 Parrish, I. J., & Stone, J. M. 2007, *ApJ*, **664**, 135
 Parrish, I. J., Stone, J. M., & Lemaster, N. 2008, *ApJ*, **688**, 905
 Peng, F., & Nagai, D. 2009, *ApJ*, **693**, 839
 Pessah, M. E., & Chakraborty, S. 2013, *ApJ*, **764**, 13
 Quataert, E. 2008, *ApJ*, **673**, 758
 Rasera, Y., & Chandran, B. 2008, *ApJ*, **685**, 105
 Ruszkowski, M., & Oh, S. P. 2010, *ApJ*, **713**, 1332
 Schekochihin, A. A., & Cowley, S. C. 2006, *AN*, **327**, 599
 Schekochihin, A. A., Cowley, S. C., Kulsrud, R. M., Hammett, G. W., & Sharma, P. 2005, *ApJ*, **629**, 139
 Schekochihin, A. A., Cowley, S. C., Rincon, F., & Rosin, M. S. 2010, *MNRAS*, **405**, 291
 Sharma, P., & Hammett, G. W. 2007, *JCoPh*, **227**, 123
 Shtykovskiy, P., & Gilfanov, M. 2010, *MNRAS*, **401**, 1360
 Spitzer, L. 1962, Physics of Fully Ionized Gases (2nd ed.; New York: Interscience)
 Stone, J. M., & Gardiner, T. 2009, *NewA*, **14**, 139
 Stone, J. M., Gardiner, T. A., Teuben, P., Hawley, J. F., & Simon, J. B. 2008, *ApJS*, **178**, 137
 van Es, B., Koren, B., & de Blank, H. J. 2014, *JCoPh*, **272**, 526
 Zingale, M., Dursi, L. J., Zuhone, J., et al. 2002, *ApJS*, **143**, 539

Paper III

On Helium Mixing in Quasi-global Simulations of the Intracluster Medium.

Reprinted from

The Astrophysical Journal, Volume 833, August 2016

doi:10.3847/1538-4357/833/2/164

with the permission of IOP Publishing.



ON HELIUM MIXING IN QUASI-GLOBAL SIMULATIONS OF THE INTRACLUSTER MEDIUM

THOMAS BERLOK AND MARTIN E. PESSAH

Niels Bohr International Academy, Niels Bohr Institute, Blegdamsvej 17, DK-2100 Copenhagen Ø, Denmark; berlok@nbi.dk, mpessah@nbi.dk
Received 2016 August 10; revised 2016 October 16; accepted 2016 October 17; published 2016 December 15

ABSTRACT

The assumption of a spatially uniform helium distribution in the intracluster medium (ICM) can lead to biases in the estimates of key cluster parameters if composition gradients are present. The helium concentration profile in galaxy clusters is unfortunately not directly observable. Current models addressing the putative sedimentation are one-dimensional and parametrize the presence of magnetic fields in a crude way, ignoring the weakly collisional, magnetized nature of the medium. When these effects are considered, a wide variety of instabilities can play an important role in the plasma dynamics. In a series of recent papers, we have developed the local, linear theory of these instabilities and addressed their nonlinear development with a modified version of Athena. Here, we extend our study by developing a quasi-global approach that we use to simulate the mixing of helium as induced by generalizations of the heat-flux-driven buoyancy instability (HBI) and the magnetothermal instability, which feed off thermal and composition gradients. In the inner region of the ICM, mixing can occur over a few gigayears, after which the average magnetic field inclination angle is $\sim 30^\circ$ – 50° , resulting in an averaged Spitzer parameter higher by about 20% than the value obtained in homogeneous simulations. In the cluster outskirts the instabilities are rather inefficient, due to the shallow gradients. This suggests that composition gradients in cluster cores might be shallower than one-dimensional models predict. More quantitative statements demand more refined models that can incorporate the physics driving the sedimentation process and simultaneously account for the weakly collisional nature of the plasma.

Key words: diffusion – galaxies: clusters: intracluster medium – instabilities – magnetohydrodynamics (MHD)

1. INTRODUCTION

The intracluster medium (ICM) of galaxy clusters is comprised of a very high-temperature and low-density gas in which charged particles are bound to the magnetic field with gyroradii that are much smaller than the mean-free path of particle collisions. In this weakly collisional medium, the weak ($\sim \mu\text{G}$) magnetic field (Carilli & Taylor 2002) channels the transport of heat and momentum, as well as the diffusion of particles. The anisotropic character of the weakly collisional ICM has been found to significantly alter its dynamical properties. Whereas the stability of a stratified gas in the presence of a gravitational field is governed by its entropy gradient (Ledoux 1947; Schwarzschild 1958), Balbus (2000, 2001) and Quataert (2008) found that temperature gradients can have an important impact on the stability properties if the plasma is weakly collisional. Two distinct instabilities were found to feed off temperature gradients in weakly collisional plane-parallel atmospheres, even when their entropy increases with height. The discovery of the magnetothermal instability (MTI, Balbus 2000, 2001), which is maximally unstable when the magnetic field is perpendicular to gravity and the temperature decreases with height, and the heat-flux-driven buoyancy instability (HBI, Quataert 2008), which is maximally unstable when the magnetic field is parallel to gravity and the temperature increases with height, led to a surge in research on the stability properties of the ICM during the last decade.

These investigations considered both two- and three-dimensional simulations in local, quasi-global, and even global settings including a variety of physical effects, for instance, anisotropic heat conduction, Braginskii viscosity, radiative cooling, and imposed turbulence (Parrish & Stone 2005, 2007; Parrish & Quataert 2008; Parrish et al. 2008, 2009, 2010, 2012a, 2012b; Bogdanović et al. 2009; Ruszkowski &

Oh 2010; McCourt et al. 2011, 2012; Kunz et al. 2012). This collection of studies have led to a better understanding of a number of fundamental issues governing ICM plasma dynamics (see Balbus & Potter 2016 for a recent review of the physics of the MTI and HBI). In particular, Kunz (2011) pointed out that Braginskii viscosity makes the fastest growing wavelengths for the HBI very long in the direction parallel to gravity (see also Gupta et al. 2016). This limited the validity of the local approaches employed thus far and ultimately led to quasi-global studies of the HBI (Kunz et al. 2012; Latter & Kunz 2012).

While the temperature distribution of the ICM is observable (Vikhlinin et al. 2006), the fact that most elements are completely ionized makes it difficult to constrain the composition of the plasma. If present, composition gradients, as envisioned, for example, by the sedimentation of helium over a Hubble time, can lead to biases in the estimates of key cluster properties with important implications for cosmology (Markovitch 2007; Peng & Nagai 2009). This has motivated the study of the long-term dynamics of heavy elements in the ICM. As an example, the models in Peng & Nagai (2009) predict that composition gradients can lead to a bias of up to 20% in the Hubble constant if the total mass of the cluster is estimated assuming a uniform, primordial composition (see Figure 4 in Peng & Nagai 2009). The models for the evolution of the radial distribution of elements are one-dimensional (Fabian & Pringle 1977; Gilfanov & Syunyaev 1984; Chuzhoy & Nusser 2003; Chuzhoy & Loeb 2004; Peng & Nagai 2009; Shtykovskiy & Gilfanov 2010) and consider the effects of magnetic fields in rather simplified form, or ignore it altogether.

Motivated by the need for a more fundamental approach to understand the role of magnetic fields in the dynamics of weakly collisional media, Pessah & Chakraborty (2013) and Berlok & Pessah (2015) extended the works carried out in

homogeneous settings by Balbus (2000, 2001), Quataert (2008), and Kunz (2011) to include composition gradients. They showed that a host of instabilities feeding off composition gradients can have an important impact on the stability properties of the ICM. Two of these instabilities are the generalizations of the MTI and HBI, namely the magneto-thermo-compositional instability (MTCI) and the heat- and particle-flux-driven buoyancy instability (HPBI). Both instabilities can be active even for isothermal atmospheres if the mean molecular weight increases with height, even if the entropy gradient increases with height.

In order to understand how the new instabilities driven by composition gradients saturate, Berlok & Pessah (2016) considered the nonlinear evolution of the MTCI and the HPBI in local, isothermal settings, using a modified version of the magnetohydrodynamics (MHD) code Athena (Stone et al. 2008). These simplifying assumptions made it possible to understand some of the differences observed in the saturated state of instabilities that are driven by either thermal or composition gradients alone. A notable difference is that the instabilities driven exclusively by composition gradients saturate with an average magnetic field inclination of 45° . This is in contrast with the thermal instabilities, where the MTI drives the magnetic field to be almost parallel to gravity (Parrish & Stone 2005) and the HBI drives the magnetic field to be almost perpendicular to gravity (Parrish & Quataert 2008).

In this paper, we present the first two-dimensional (2D) quasi-global simulations of plane-parallel atmospheres with initial equilibrium structures inspired by the models of Peng & Nagai (2009), that we use to model the inner and outer regions of the ICM. We show that the HPBI leads to mixing of the helium content in the inner regions of the ICM and, as a consequence, diminishes the initial gradient in composition. The inclusion of a composition gradient leads to an $\sim 20\%$ increase in heat flux to the core at late times compared to a simulation of a homogeneous ICM.

The paper is organized as follows. In Section 2, we introduce the equations of Braginskii-MHD that we employ to model a completely ionized plasma composed of hydrogen and helium. In Section 3, we present an equilibrium atmosphere for the inner regions of the ICM, which is based on the helium sedimentation model of Peng & Nagai (2009). This atmosphere is then studied in Section 4 by using a quasi-global linear theory and in Section 5 by performing a suite of simulations using a modified version of the MHD code Athena (Stone et al. 2008; Berlok & Pessah 2016). We also present in Section 6 simulations of the outer region of the ICM, where the MTCI could be active. We conclude in Section 7 by discussing the consequences of plasma instabilities on the long-term evolution of composition gradients in the ICM as well as the limitations of our present approach.

2. BRAGINSKII-MHD FOR A BINARY MIXTURE

We model the ICM by solving equations that evolve the total mass density, ρ , momentum density, $\rho\mathbf{v}$, magnetic field, \mathbf{B} , total energy density, E , and composition, c , for a weakly collisional binary mixture of hydrogen and helium. Here, \mathbf{v} is the fluid velocity and the total energy density of the plasma is given by

$$E = \frac{1}{2}\rho v^2 + \frac{B^2}{8\pi} + \frac{P}{\gamma - 1}, \quad (1)$$

where $\gamma = 5/3$ is the adiabatic index and P is the thermal gas pressure. We assume the magnetic field to have the direction $\hat{\mathbf{b}} = (b_x, 0, b_z)$ and define the composition of the plasma as

$$c \equiv \frac{\rho_{\text{He}}}{\rho}. \quad (2)$$

The plasma is assumed to obey the ideal gas law

$$P = \frac{\rho k_B T}{\mu m_H}, \quad (3)$$

where T is the temperature, m_H is the proton mass, and k_B is Boltzmann's constant. The mean molecular weight, μ , which enters in Equation (3), can be shown to be related to the composition by

$$\mu = \frac{4}{8 - 5c}, \quad (4)$$

for a completely ionized mixture of hydrogen and helium.

The equations of motion are (Pessah & Chakraborty 2013; Berlok & Pessah 2016) the continuity equation for the total mass

$$\frac{\partial \rho}{\partial t} + \nabla \cdot (\rho \mathbf{v}) = 0, \quad (5)$$

the momentum equation

$$\frac{\partial (\rho \mathbf{v})}{\partial t} + \nabla \cdot \left(\rho \mathbf{v} \mathbf{v} + P_{\text{T}} \mathbf{I} - \frac{B^2}{4\pi} \hat{\mathbf{b}} \hat{\mathbf{b}} \right) = -\nabla \cdot \Pi + \rho \mathbf{g}, \quad (6)$$

the energy equation

$$\begin{aligned} \frac{\partial E}{\partial t} + \nabla \cdot \left[(E + P_{\text{T}}) \mathbf{v} - \frac{\mathbf{B}(\mathbf{B} \cdot \mathbf{v})}{4\pi} \right] \\ = -\nabla \cdot \mathbf{Q}_s - \nabla \cdot (\Pi \cdot \mathbf{v}) + \rho \mathbf{g} \cdot \mathbf{v}, \end{aligned} \quad (7)$$

the induction equation for the magnetic field

$$\frac{\partial \mathbf{B}}{\partial t} = \nabla \times (\mathbf{v} \times \mathbf{B}), \quad (8)$$

and the continuity equation for the helium mass

$$\frac{\partial (c\rho)}{\partial t} + \nabla \cdot (c\rho \mathbf{v}) = -\nabla \cdot \mathbf{Q}_c. \quad (9)$$

In these equations, P_{T} is the total pressure (gas + magnetic) and $\mathbf{g} = (0, 0, -g)$ is the gravitational acceleration, which we assume to be constant.

The equations include terms that take into account the influence of three anisotropic effects. These anisotropic effects arise because the plasma is weakly collisional and weakly magnetized. In this regime, the charged particles are effectively bound to the magnetic field and collisions occur primarily along the magnetic field. This causes the associated transport phenomena to be directed along the magnetic field.

Electrons, which are responsible for heat conduction, can in this way create a heat flux along the magnetic field given by

$$\mathbf{Q}_s = -\chi_{\parallel} \hat{\mathbf{b}} \hat{\mathbf{b}} \cdot \nabla T, \quad (10)$$

where χ_{\parallel} is the Spitzer heat conductivity (Spitzer 1962).

Similarly, the continuity equation for the helium density includes a flux of composition along the magnetic field given

by (Bahcall & Loeb 1990; Pessah & Chakraborty 2013)

$$\mathbf{Q}_c = -D\hat{\mathbf{b}}\hat{\mathbf{b}} \cdot \nabla c, \quad (11)$$

where D is the diffusion coefficient.

Finally, the conservation of the first adiabatic invariant of the ions can lead to anisotropy in the pressure tensor with differences in the parallel (p_{\parallel}) and perpendicular (p_{\perp}) pressures. This pressure difference results in gradients in velocity components along the magnetic field being viscously damped. This effect, called Braginskii viscosity (Braginskii 1965), is described by the viscosity tensor

$$\Pi = -3\rho\nu_{\parallel}\left(\hat{\mathbf{b}}\hat{\mathbf{b}} - \frac{1}{3}\mathbf{I}\right)\left(\hat{\mathbf{b}}\hat{\mathbf{b}} - \frac{1}{3}\mathbf{I}\right) : \nabla\mathbf{v}, \quad (12)$$

where ν_{\parallel} is the viscosity coefficient and \mathbf{I} is a unit tensor.

Expressions for the dependence of χ_{\parallel} , D , and ν_{\parallel} for an ionized mixture of hydrogen and helium can be found in the appendix of Berlok & Pessah (2015). More details about the utility of Braginskii MHD and its range of applicability can be found in Schekochihin et al. (2005), Kunz et al. (2012), Pessah & Chakraborty (2013), and references therein.

For future reference, we also define the plasma- $\beta = 8\pi P/B^2 = 2v_{\text{th}}^2/v_A^2$, where $v_A = B/\sqrt{4\pi\rho}$ is the Alfvén speed and $v_{\text{th}} = \sqrt{P/\rho}$ is the thermal speed.

3. EQUILIBRIUM PROFILE

In order to understand the quasi-global linear dynamics arising from Equations (5)–(9), we derive an equilibrium profile for a model plane-parallel atmosphere, which has proven to be useful for capturing key aspects of the plasma dynamics in galaxy clusters. We assume that gravity can be modeled locally via a constant acceleration, g , and that the magnetic field is purely vertical, i.e., $b_x = 0$ and $b_z = 1$. The magnetic field is assumed to be weak enough that we can neglect its contribution to the total pressure gradient responsible for hydrostatic equilibrium. Nevertheless, the vertical weak magnetic field can enable a background heat flux in the vertical direction. Therefore, in order for the model atmosphere to be in equilibrium, we require $\nabla \cdot \mathbf{Q}_c = 0$ and $\nabla \cdot \mathbf{Q} = 0$. In what follows, we ignore helium diffusion and assume $D = 0$ such that the second condition is trivially satisfied.

Motivated by the models considered in Peng & Nagai (2009), which result in helium concentration profiles that peak off-center, we consider a situation where the composition of the plasma increases linearly outward from the bottom of the atmosphere, i.e., center of the cluster, as

$$c(z) = c_0 + s_c z, \quad (13)$$

where $s_c = (c_z - c_0)/L_Z$ is the slope in composition. Notice that the mass concentration of helium, $c(z)$, is related to the mean molecular weight, $\mu(z)$, by

$$\mu(z) = \frac{4}{8 - 5c(z)}, \quad (14)$$

for a completely ionized plasma of hydrogen and helium. The equilibrium needs to fulfill

$$\frac{d}{dz}\left(\chi_{\parallel}\frac{dT}{dz}\right) = 0, \quad (15)$$

where χ_{\parallel} is a function of temperature $T(z)$ and composition, $c(z)$. We will for simplicity assume that χ_{\parallel} depends only on temperature as $\chi_{\parallel} = \chi_{\parallel,0}(T/T_0)^{5/2}$, i.e., we assume that this dependence on composition can be neglected.¹ With this assumption, Equation (15) is identical to the one derived in Latter & Kunz (2012) and it decouples from the rest of the equations yielding the solution

$$T(z) = T_0(1 + \zeta z)^{2/7}, \quad (16)$$

where $\zeta_{L_Z} = (T_Z/T_0)^{7/2} - 1$ and $T_Z(T_0)$ is the temperature at the top (bottom) of the atmosphere. Using the equation of state

$$P(z) = \frac{\rho(z)k_B T(z)}{\mu(z)m_H}, \quad (17)$$

we solve the equation for hydrostatic equilibrium

$$\frac{\partial P}{\partial z} = -\rho g, \quad (18)$$

and find

$$P(z) = P_0 e^{h(0) - h(z)}, \quad (19)$$

where the function $h(z)$ is related to a Gauss hypergeometric function, ${}_2F_1$, as

$$h(z) = \frac{28(1 + \zeta z)^{5/7}}{5H_0\alpha} {}_2F_1\left(\frac{5}{7}, 1; \frac{12}{7}; \frac{5s_c\mu_0}{\alpha}(1 + \zeta z)\right). \quad (20)$$

In deriving the above result, we have introduced the scale height at the bottom of the atmosphere

$$H_0 = \frac{k_B T_0}{\mu_0 m_H g}, \quad (21)$$

and the parameter

$$\alpha = 5s_c\mu_0 + 4\zeta. \quad (22)$$

The density, $\rho(z)$, can be found from Equation (3).

The values of the constants used for this equilibrium atmosphere are inspired by the model of Peng & Nagai (2009). In physical units, the model atmosphere has a height of $L_Z = 2H_0 = 80$ kpc, corresponding to the region between $r/r_{500} = 0.01$ and $r/r_{500} = 0.06$ with $r_{500} = 1.63$ Mpc in their model. The values for the temperature and composition of the plasma at the top and bottom of the atmosphere are given by $T_Z = 9.6$ keV, $T_0 = 5.8$ keV, $c_Z = 0.62$, and $c_0 = 0.52$, respectively. In Figure 1, we show $P(z)/P_0$, $\rho(z)/\rho_0$, $T(z)/T_0$, $\mu(z)/\mu_0$, and $(2H_0 m_H / 3k_B)(ds/dz)$, where the entropy per unit mass is defined by

$$s = \frac{3k_B}{2m_H} \ln\left[\left(\frac{P}{P_0}\right)\left(\frac{\rho}{\rho_0}\right)^{-5/3}\right]. \quad (23)$$

Note that, even though the composition increases with height, the Ledoux criterion for stability (Ledoux 1947; which is the generalization of the Schwarzschild criterion, Schwarzschild 1958, valid for a heterogeneous collisional medium) is

¹ For the profiles employed here, the dependence on composition is much weaker than the dependence on temperature (Pessah & Chakraborty 2013). The maximum error incurred by using this approximation is less than 5% on the value of χ_{\parallel} at the top of the atmosphere.

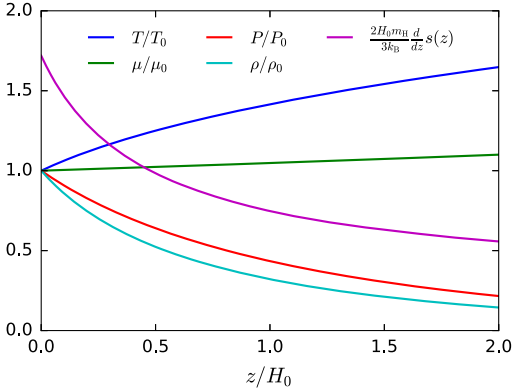


Figure 1. Equilibrium atmosphere inspired by the sedimentation model of Peng & Nagai (2009) and the radial temperature profile of Vikhlinin et al. (2006). The temperature (blue) and the mean molecular weight (green) increase with radius while pressure (red) and density (magenta) decrease with radius at this radial distance in the cluster model. The derivative of the entropy (purple) is positive, indicating stability according to Equation (24).

not violated. Indeed, for this model atmosphere, the entropy is an increasing function of height, i.e.,

$$\frac{ds}{dz} > 0, \quad (24)$$

as illustrated in Figure 1. As we will discuss next, the instabilities present in the linear theory and in the simulations are due to the weakly collisional nature of the plasma.

4. QUASI-GLOBAL LINEAR THEORY

The HPBI has its fastest growth rates on radial scales longer than a scale height when Braginskii viscosity is included in the analysis (Berlok & Pessah 2015). The local linear mode analysis is therefore not strictly valid because it assumes that the radial scales are much shorter than a scale height. This problem has previously been found for the HBI in Kunz (2011) and solved by introducing a quasi-global linear theory for the HBI in Latter & Kunz (2012). In the same vein, in this section, we develop a quasi-global linear theory for the HPBI by considering a model atmosphere with a non-uniform mean molecular weight.

The purpose of deriving a quasi-global theory is to predict the growth rates of the instability as a function of perpendicular wavenumber, k_x , in order to understand whether the instability will grow on astrophysically relevant timescales. Furthermore, the eigenmodes obtained from linear theory can also be used to compare with the linear stage of simulations using Athena. Such a comparison will serve as a test of our modified version of Athena in Section 4.3.

4.1. Equations of Motion and Relevant Parameters

The equations governing the quasi-global, linear dynamics for the perturbations are obtained from the equations of Braginskii-MHD for a binary mixture (Pessah & Chakraborty 2013; Berlok & Pessah 2015) by using a Fourier transform along the x -coordinate but retaining the z -derivatives explicitly in order to relax the local approximation. Therefore, the perturbations are calculated in terms of the complex Fourier

coefficients, $\tilde{f}(k_x, z)$, which we assume to have a time dependence, $\exp(\sigma t)$, where σ is the (in general complex) eigenvalue. We assume that $\chi_{\parallel} = \chi_{\parallel,0} (T/T_0)^{5/2}$ and $\nu_{\parallel} = \nu_{\parallel,0} \rho_0/\rho (T/T_0)^{5/2}$, i.e., χ_{\parallel} and ν_{\parallel} only depend on the composition through the constants $\chi_{\parallel,0}$ and $\nu_{\parallel,0}$. We also introduce a flux function such that $\mathbf{B} = \nabla \times (A\hat{y})$. The initial condition is $A = Bx$ which is equivalent to $\mathbf{B} = B\hat{z}$. In the present work, we only consider the case of $D = 0$. In this case, and with the above caveats, the quasi-global linearized equations are the continuity equation

$$\sigma \frac{\delta \rho}{\rho} = -ik_x \delta v_x - \left(\frac{d \ln \rho}{dz} + \frac{\partial}{\partial z} \right) \delta v_z, \quad (25)$$

the x -component of the momentum equation

$$\begin{aligned} \sigma \delta v_x = & -ik_x \frac{T}{\mu} \left(\frac{\delta \rho}{\rho} + \frac{\delta T}{T} - \frac{\delta \mu}{\mu} \right) + \frac{2}{\rho \beta_0} \left(k_x^2 - \frac{\partial^2}{\partial z^2} \right) \delta A \\ & - \frac{ik_x T^{5/2}}{3\rho \text{Re}_0} \left(2 \frac{\partial \delta v_z}{\partial z} - ik_x \delta v_x \right), \end{aligned} \quad (26)$$

the z -component of the momentum equation

$$\begin{aligned} \sigma \delta v_z = & -\frac{T}{\mu} \left(\frac{\delta T}{T} - \frac{\delta \mu}{\mu} \right) \frac{d \ln P}{dz} - \frac{T}{\mu} \frac{\partial}{\partial z} \left(\frac{\delta \rho}{\rho} + \frac{\delta T}{T} - \frac{\delta \mu}{\mu} \right) \\ & + \frac{2T^{5/2}}{3\rho \text{Re}_0} \left(\frac{5}{2} \frac{d \ln T}{dz} + \frac{\partial}{\partial z} \right) \left(2 \frac{\partial \delta v_z}{\partial z} - ik_x \delta v_x \right), \end{aligned} \quad (27)$$

the entropy equation (with $\gamma = 5/3$)

$$\begin{aligned} \frac{3}{2} \sigma \frac{\delta T}{T} = & -ik_x \delta v_x - \left(\frac{3}{2} \frac{d \ln T}{dz} + \frac{\partial}{\partial z} \right) \delta v_z \\ & + \frac{1}{P \text{Pe}_0} \left(\frac{\partial^2}{\partial z^2} \left(T^{7/2} \frac{\delta T}{T} \right) + q_0 ik_x \frac{\partial \delta A}{\partial z} \right), \end{aligned} \quad (28)$$

the induction equation

$$\sigma \delta A = -\delta v_x, \quad (29)$$

and the equation for the mean molecular weight, μ ,

$$\sigma \frac{\delta \mu}{\mu} = -\delta v_z \frac{d \ln \mu}{dz}. \quad (30)$$

Here, the perturbation to the flux function is related to the perturbation to the magnetic field by $\delta \mathbf{B} = \nabla \times (\delta A \hat{y})$.

Equations (25)–(30) have been written in dimensionless variables by scaling μ with μ_0 , T with T_0 , the velocities with $v_{\text{th},0}$, σ with $\sigma_0 = \tau_0^{-1} = v_{\text{th},0}/H_0$, δA with $B_0 H_0$, and z with H_0 such that k_x is scaled with $1/H_0$. The background heat flux parameter q_0 , is given by

$$q_0 = -T^{7/2} \frac{d \ln T}{dz}, \quad (31)$$

in dimensionless variables. At the bottom of the atmosphere, $z = 0$, the Peclet number is given by

$$\text{Pe}_0 = \frac{v_{\text{th},0} P_0 H_0}{\chi_{\parallel,0} T_0} \approx 70, \quad (32)$$

and the Reynolds number is given by

$$\text{Re}_0 = \frac{v_{\text{th},0} \rho_0 H_0}{\nu_{\parallel,0}} \approx 3800. \quad (33)$$

These parameters were found by using Equations (B6) and (B7) in Berlok & Pessah (2015) to estimate the values of $\chi_{\parallel,0}$ and $\nu_{\parallel,0}$. Following Latter & Kunz (2012) and Kunz et al. (2012) we furthermore take the plasma- β at the bottom of the atmosphere to be

$$\beta_0 = 10^5. \quad (34)$$

4.2. Solutions Obtained with a Pseudo-spectral Method

The linearized quasi-global equations (Equations (25)–(30)) are solved using a pseudo-spectral method, in a manner similar to the analysis presented in Latter & Kunz (2012), see also Boyd (2000). We discretize the six equations on a Chebyshev-Gauss–Lobatto roots grid transformed onto the domain $z = [0, 2]$. The grid has N grid points, where $N = 200$, and the resulting algebraic equations constitute a generalized eigenvalue problem of size $6N$. We use the same boundary conditions as Latter & Kunz (2012), which means that δv_z , $\delta T/T$, and $\partial_z \delta A$ are set to zero at the boundaries. The latter condition corresponds to $\delta B_x = 0$ at the boundaries, which implies that the field remains vertical there. We furthermore impose $\delta \mu / \mu = 0$ at the boundaries.

Equations (25)–(30) only depend on the value of $k_x H_0 = 2\pi n$, where n is the horizontal mode number. All other parameters are set by our model. For each value of k_x , there are a number of modes that we designate with the vertical mode number m , where $m = 1$ is the fastest growing mode, $m = 2$ labels the second fastest growing mode, and so on. We show the solution for $n = 5$ in Figure 2, where the left panel shows the $m = 1$ mode, which is confined to the lower region of the domain. The right panel shows the $m = 2$ mode, which has a slower growth rate but a larger vertical extent than the $m = 1$ mode. A general property of the solutions is that the vertical extent of the perturbations increases with the mode number m , while it does not depend on the mode number n . Therefore, in a simulation where the instability is excited using Gaussian noise, we expect the perturbations to grow fastest in the lower region of the computational domain. This is indeed the case, as we will see in Section 5.

The growth rates as a function of the wavenumber, k_x , are shown in Figure 3, where the solid lines are obtained using the pseudo-spectral method and the crosses are obtained from Athena simulations (see the next subsection). The maximum growth rate is $\sigma_{\text{max}} \approx 10 \text{ Gyr}^{-1}$ implying that the instability can develop significantly on relevant timescales. The gradient in the mean molecular weight acts to increase the growth rate with respect to the homogeneous case. The maximum growth rate found for the HPBI is, however, still smaller than the one found for the HBI in Latter & Kunz (2012) due to the shallower temperature gradient that we use in this work, which is inspired by the models in Peng & Nagai (2009) as detailed above. The temperature ratio, T_z/T_0 , is 2.5 in the model of Latter & Kunz (2012) while it is only ~ 1.65 in our model. The growth rate is proportional to the gradient in temperature in the local, weak magnetic field and fast heat conduction limit. A rough estimate is therefore that their growth rate should be higher by a factor

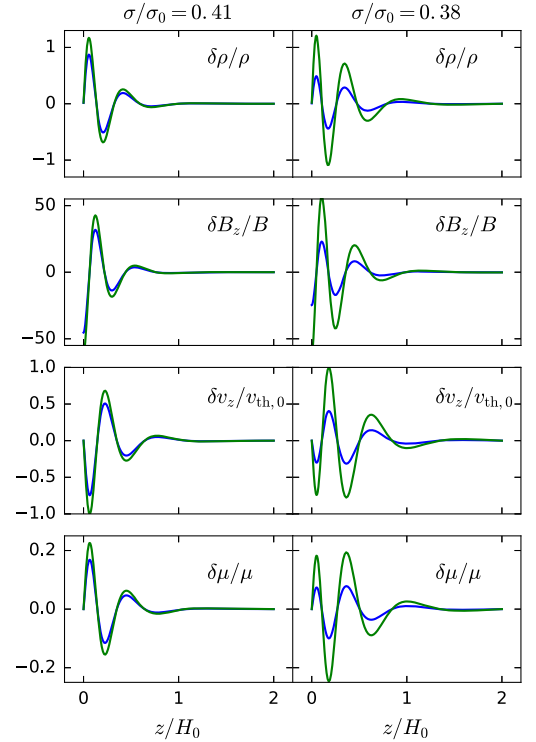


Figure 2. Select components of the eigenmode for the fastest (left, $m = 1$) and second fastest (right, $m = 2$) eigenmode with $n = 5$ and the real (imaginary) part of the eigenmode shown in blue (green). A general rule seems to be that the fastest growing modes have a small vertical extent while slower growing modes have a larger vertical extent. This trend also appears in the homogeneous setting (Latter & Kunz 2012) and it is consistent with the simulations presented in Section 5.

of roughly 1.5, which we confirmed with the results of the full quasi-global analysis.

4.3. Solutions Obtained with Athena

We have modified the publicly available MHD code Athena (Stone et al. 2008) in order to be able to describe the nonlinear evolution of weakly collisional atmospheres with non-uniform composition. Our modified version of the code has anisotropic heat conduction and diffusion of composition with spatially dependent transport coefficients. These modifications, along with tests, were described in detail in Berlok & Pessah (2016) and applied to local settings, where the vertical extent of the simulation domains considered was small compared to the relevant scale height.

We use a pseudo-spectral method in order to test the numerical solutions obtained with Athena in a quasi-global setting. This is done by exciting the HPBI in the Athena simulations using an exact eigenmode found in the quasi-global linear theory. An example is shown in Figure 4, where four of the components of the perturbation are shown for the $n = 5$ and $m = 4$ mode at $t = 3$ in units of $t_0 = H_0/v_{0,\text{th}} = 45 \text{ Myr}$. The growth rate can be measured in the simulations by

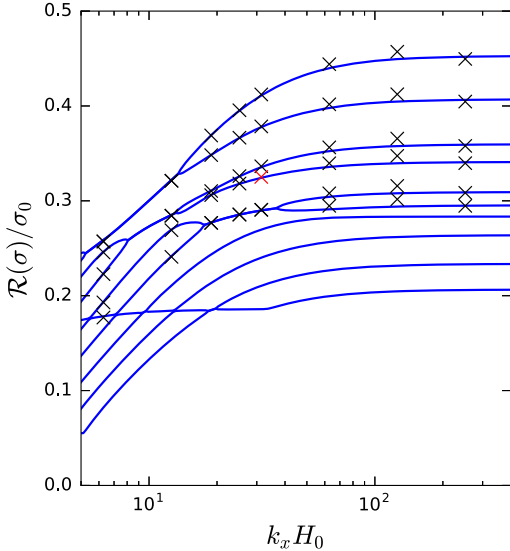


Figure 3. Growth rates as a function of the horizontal wavenumber, k_x , for the 10 fastest growing modes. The solid blue lines were obtained using the pseudo-spectral method. Each cross corresponds to a simulation where the eigenmodes were used for initial conditions. The numerical growth rate was found from the subsequent exponential evolution.

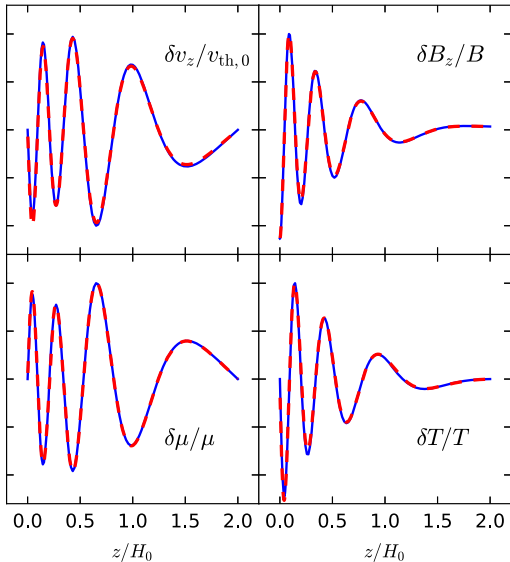


Figure 4. Comparison between a simulation using Athena and the pseudo-spectral method. A slice in the x -direction at $t = 3$ is shown in dashed red and the pseudo-spectral solution is shown in blue. The growth rate is $\sigma/\sigma_0 = 0.324$ according to the pseudo-spectral method and $\sigma/\sigma_0 = 0.325$ according to the simulation, the error is less than a percent. This mode has $n = 5$ and $m = 4$ and it is also indicated with a red cross in Figure 3.

following the evolution of the amplitude of the perturbations. We find that the error in the growth rate for this simulation is less than a percent compared to the pseudo-spectral linear theory. We have thoroughly tested this by running a suite of simulations where we vary the n and m mode numbers. A total of 42 simulations were run with $n = 1-8$ and $m = 1-6$ with six of the simulations being degenerate² in m . A comparison between the growth rates obtained using the pseudo-spectral method and the simulations is shown in Figure 3. In this figure, each cross corresponds to an individual simulation, where the eigenmode was excited exactly. The results shown in the figure were obtained by fitting an exponential function to the time evolution of the volume average of $\delta B_x^2/8\pi$ for each simulation. We have checked that the other components of the perturbation (such as δv_x and $\delta\mu/\mu$) also grow at the correct rate. Due to the exact excitation of the modes the evolution is exponential from the onset.

The simulations were run at half the resolution, 256×512 , of the simulations presented in Section 5 in order to expedite the numerical simulations. As noted already by Latter & Kunz (2012), the low resolution causes some discrepancy at the highest wavenumbers. These tests illustrate the generally good agreement between the numerical implementation in Athena and our quasi-global linear theory using pseudo-spectral methods.

5. INNER REGIONS OF THE ICM

In this section, we consider the long time evolution of plasma instabilities in the inner regions of the ICM by performing fully nonlinear simulations of the HPBI using Athena. We describe the details of the numerical setup in Section 5.1, the evolution of key quantities in Section 5.2 and conclude by comparing a simulation of the HPBI with a simulation of the HBI in Section 5.3.

Some of the simulations include Braginskii viscosity, which is a numerical and theoretical challenge (Schekochihin et al. 2005; Kunz et al. 2012). The reason is that microscale instabilities are triggered if the magnitude of the pressure anisotropy grows too large. The pressure tensor can become anisotropic due to conservation of the first adiabatic invariant of the ions. Specifically, when the pressure anisotropy exceeds the limits given by

$$-\frac{B^2}{4\pi} < p_{\perp} - p_{\parallel} < \frac{B^2}{8\pi}. \quad (35)$$

the firehose or mirror instabilities are triggered (Parker 1958). This is an issue for the kind of simulations we consider because the microscale instabilities are not correctly described by Braginskii-MHD (Schekochihin et al. 2005).

Two different approaches used to handle this problem are described in Kunz et al. (2012). The first approach is to use high resolution and hope that the firehose instability grows sufficiently fast in order to regulate the pressure anisotropy. The second approach is to artificially limit the pressure anisotropy to the interval given by Equation (35). The latter approach is motivated by studies showing that the microscale instabilities will likely saturate by driving the pressure anisotropy back to marginal stability (Schekochihin et al. 2008; Bale et al. 2009; Rosin et al. 2011) and a similar

² They are complex conjugate solutions so the eigenvalues do differ in their imaginary part, which is very small.

approach has been used for the magnetorotational instability in local studies of weakly collisional disks (Sharma et al. 2006). A recent study of the solar wind showed that the firehose and mirror thresholds also provide good constraints for the pressure anisotropy in a multispecies plasma with electrons, hydrogen, and helium ions (Chen et al. 2016). We have used both of these approaches in our simulations.

5.1. Description of Numerical Setup and Overview of Results

We perform a suite of three simulations of the HPBI: one without Braginskii viscosity (HPBI_isoP), one with Braginskii viscosity where the pressure anisotropy is limited (HPBI_Blim) by Equation (35) and one with Braginskii viscosity without limiters (HPBI_Brag). We furthermore consider a simulation where the atmosphere has uniform composition ($c_0 = c_Z = 0.62$) in order to compare the simulations with the homogeneous case (HBI_Brag) in Section 5.3.

The initial condition is the plane-parallel atmosphere introduced in Section 3. The instability is triggered by adding Gaussian, subsonic noise in the velocity components with a magnitude of 10^{-4} . This initial condition, together with the imposed perturbations, ensures an initial evolution, where all the quantities evolve exponentially in time. In reality, the agents driving the ICM dynamics are more complex and involve, for example, the stirring by mergers in the outskirts of the cluster and outflows from active galactic nuclei in the cluster core. All simulations have a spatial extent of $H_0 \times 2H_0$ (with $H_0 = 1$ in code units). The resolution used is 512×1024 . In terms of the dimensionless units introduced above, the coefficients for anisotropic heat diffusivity and Braginskii viscosity are $\kappa_{\parallel} = 1.4 \times 10^{-2} T^{5/2} \mu \rho^{-1}$ and $\nu_{\parallel} = 2.6 \times 10^{-4} T^{5/2} \rho^{-1}$.

The three simulations of the HPBI are shown in Figure 5, where the evolution of the mean molecular weight and the magnetic field lines is followed as a function of time with snapshots at $t/t_0 = 0, 25, 40, 100,$ and 200 , with $t_0 = H_0/v_{0,\text{th}} = 45$ Myr. In this figure, a high (low) concentration of helium is indicated with green (purple) and the magnetic field lines are shown as solid black lines. The top row of panels was created from HPBI_isoP which did not include Braginskii viscosity, while the middle row (HPBI_Blim) and bottom row (HPBI_Brag) of panels did include Braginskii viscosity.

The various panels in Figure 5 illustrate how the magnetic field, which is initially vertical, becomes rapidly tangled. The temperature profile, which is not shown here does not vary significantly as time progresses. The composition evolves rapidly with bubbles of helium sinking down to the center of the core. By the end of the simulation, the helium content has been very well mixed in HPBI_isoP. In HPBI_Brag, blobs of gas with a high helium content have sunk toward the center of the cluster, but they have retained their structure and have not mixed with their new environment. This lack of mixing can be understood from the ability of Braginskii viscosity to make the magnetic field retain a coherent structure over larger distances than one would find for a simulation with isotropic pressure (see the discussion of the MTI in Kunz et al. 2012). This feature, along with the fact that the magnetic field is tied to the gas, suppresses small-scale mixing of the helium content. This implies that the spatial distribution of helium might be more patchy in a viscous ICM than in a non-viscous ICM.

5.2. Evolution of Composition, Temperature, Magnetic Field Inclination, and Energy Densities

The evolution of the composition gradient can be illustrated by taking averages along the x -direction, designated by the brackets $\langle \rangle_x$. This is shown in the top row of panels in Figure 6, which have been produced at the same times as the snapshots shown in Figure 5. We see that on very long timescales of the order of 9 Gyr ($t/t_0 = 200$) the instability, on average, acts to remove the gradient in composition that originally gave rise to it. Note, however, that the gradient in composition is rather long-lived as its profile remains rather unaltered until about 4.5 Gyr ($t/t_0 = 100$).

We have limited our study to a binary mixture of hydrogen and helium, the latter being the most important element leading to potential biases in X-ray measurements (Markevitch 2007). Our approach has the advantage that enrichment from galaxies can be ignored in our simulations because the mass of helium in the ICM is much greater than the stellar component (see, e.g., Andreon 2010). This is not the case for heavier metals for which enrichment becomes important. A systematic study of mixing in the presence of imposed MHD turbulence including the injection of pollutants can be found in Sur et al. (2014) along with a detailed analysis of the mixing process.

The evolution of the temperature gradient is less dramatic, as illustrated in the middle row of panels in Figure 6. Changes in the temperature profile are also modest when the composition is uniform, as seen in, for instance, Kunz et al. (2012) and Figure 8.

It is already evident from Figure 5 that the magnetic field changes its inclination with respect to the direction perpendicular to gravity as time progresses. This can be further studied by considering the average inclination angle defined by (Parrish & Quataert 2008)

$$\langle \theta_B \rangle_x = \langle \sin^{-1}(|b_z|) \rangle_x. \quad (36)$$

The evolution of this quantity is shown in the bottom row of panels in Figure 6. We see that the instability grows fastest at the bottom of the atmosphere but increases its region of influence as time progresses. The evolution of $\langle \theta_B \rangle_x$ is initially fast compared to the changes in either composition or temperature and the average angle has changed significantly at most heights by 1.8 Gyr ($t/t_0 = 40$).³ However, on timescales of the order of 4.5 Gyr ($t/t_0 = 100$), $\langle \theta_B \rangle_x$ seems to settle at around $\sim 30^\circ$ – 50° and the overall distribution of angles shows little evolution until the end of the run at 9 Gyr ($t/t_0 = 200$). The change in average inclination angle might have consequences for the cooling flow problem (Fabian 1994) because heat transport is primarily along magnetic field lines. We discuss this in more detail in terms of the Spitzer parameter below.

We consider the evolution of the the kinetic and magnetic energy densities by calculating volume averages, designated by the brackets $\langle \rangle$, and shown in Figure 7 as a function of time. Braginskii viscosity acts to inhibit the growth rate of the instability and we therefore see the highest growth rate in HPBI_isoP, followed by HPBI_Blim (which is less viscous than HPBI_Brag due to the limiters) and then HPBI_Brag. All of the simulations saturate with magnetic and kinetic energy density components in rough equipartition with $B_z^2/8\pi$ having increased by a factor of about 10.

³ In the second panel of the bottom row, it is evident that Braginskii viscosity slows down the instability.

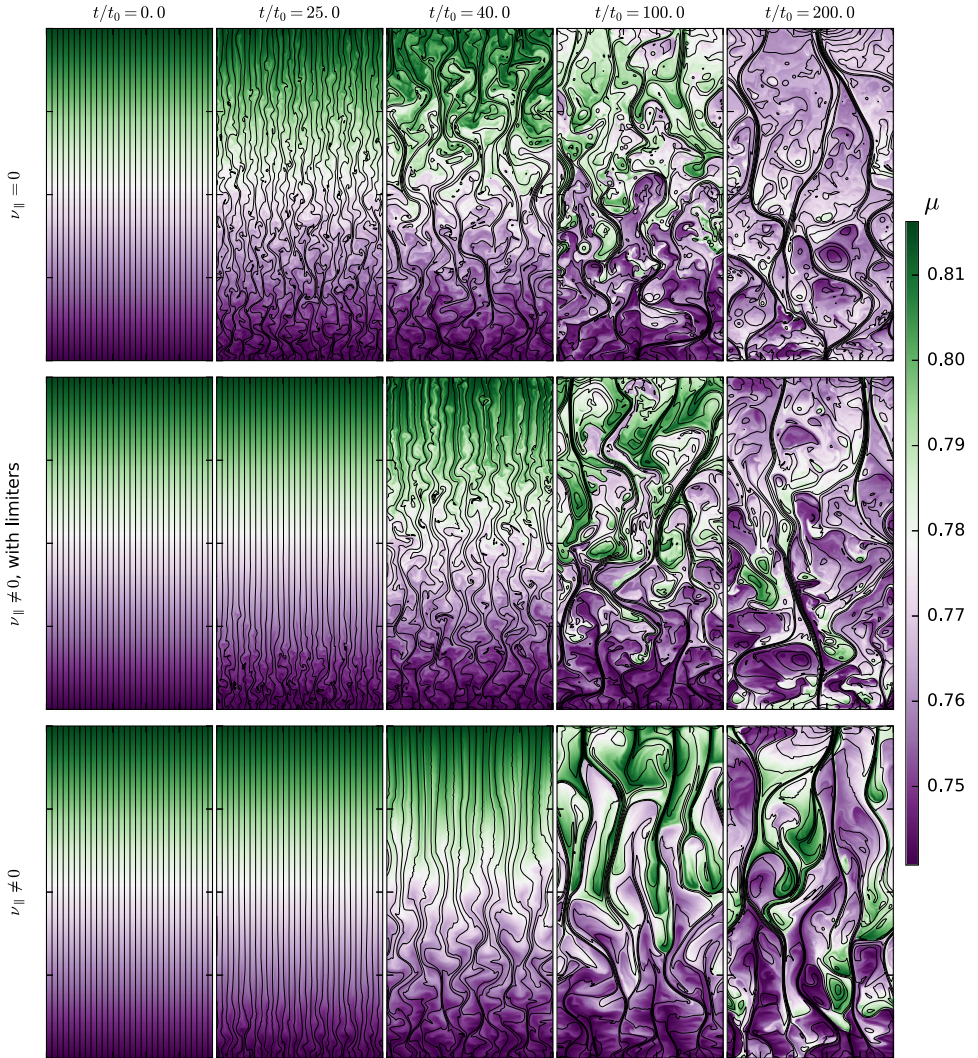


Figure 5. Evolution of the HPBI as a function of time in units of $t_0 = H_0/v_{0,\text{th}} = 45$ Myr. The size of the box is $H_0 \times 2H_0$ with $H_0 = 40$ kpc. The bottom of the atmosphere has $T_0 = 5.8$ keV and $c_0 = 0.52$ while the top of the atmosphere has $T = 9.6$ keV and $c = 0.62$, values found at $r_0 = 160$ kpc and $r = r_0 + 2H_0 = 240$ kpc in the model of Peng & Nagai (2009). The top row of panels includes anisotropic heat conduction and the middle and bottom rows also include Braginskii viscosity. The middle row uses limiters. An animated version is available at http://www.nbi.dk/~berlok/movies/icm_quasi_global.html.

5.3. Comparison between HBI and HPBI

In order to compare our results with previous work on the HBI, where the plasma is assumed to be of uniform composition, we performed a simulation (HBI_Brag) using the same atmosphere as for the HPBI but with $c_0 = c_Z$. All other aspects of this simulation are identical to run HPBI_Brag. The evolution of the temperature and the magnetic field is shown in Figure 8. The gradient in composition leads to a slightly faster growth rate with respect to the homogeneous case, as predicted by linear theory (Pessah & Chakraborty 2013; Berlok & Pessah 2015).

We see that both instabilities reorient the magnetic field, driving the average inclination of the magnetic field to be more horizontal (azimuthal). This feature of the HBI has been argued to be of importance for the cooling flow problem because a magnetic field that is predominantly perpendicular to gravity tends to insulate the core from heat transport from the outskirts of the cluster (Parrish & Quataert 2008; Bogdanović et al. 2009; Parrish et al. 2009). For a vertical (radial) magnetic field the heat flux is given by the Spitzer value

$$\bar{Q} = -\chi_{\parallel} \frac{\partial T}{\partial z}, \quad (37)$$

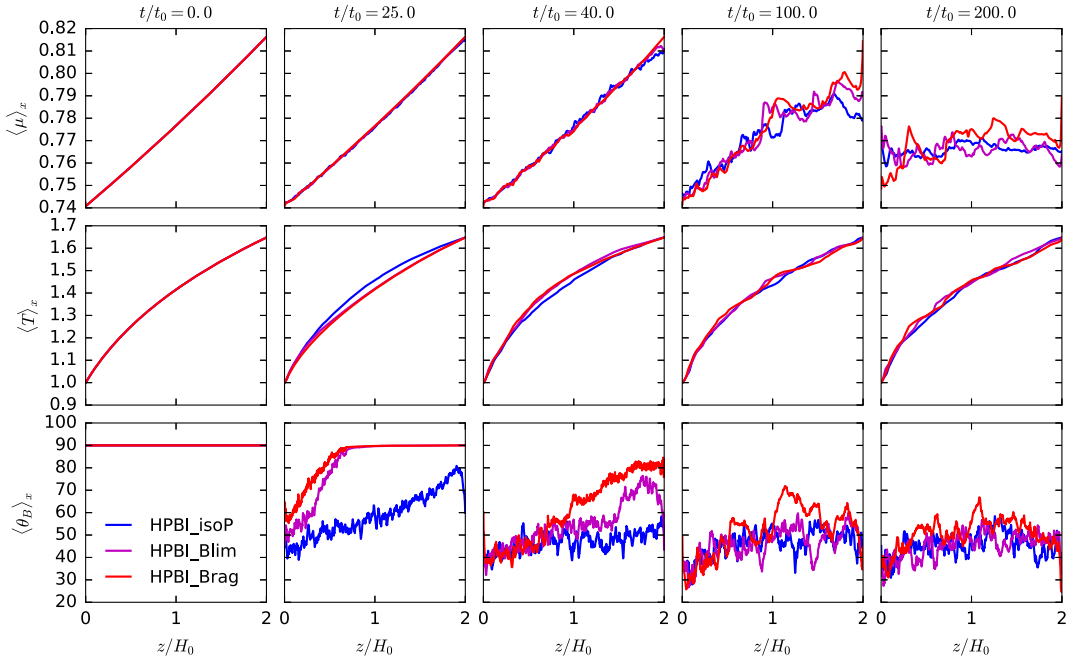


Figure 6. Key quantities averaged along x as a function of height z scaled by $H_0 = 40$ kpc, at times $t/t_0 = 0, 25, 40, 100,$ and 200 , with $t_0 = 45$ Myr, for the simulation without viscosity (blue), with viscosity and limiters (magenta) and with viscosity but without limiters (red). Top: average mean molecular weight. Middle: average temperature. Bottom: average inclination angle of the magnetic field.

while the heat flux is zero for a horizontal (azimuthal) field. In Berlok & Pessah (2016), we showed that when considering a local domain in an isothermal atmosphere, the HPBI drives the magnetic field to have an average inclination angle of 45° . This is in contrast to the uniform case, where the HBI drives the magnetic field toward 0° (Parrish & Quataert 2008). This feature of the HPBI led us to speculate that a composition gradient might be able to alleviate the cooling flow problem by limiting the average magnetic field inclination. We can now test this idea in our quasi-global simulations where the temperature gradient has been obtained from Vikhlinin et al. (2006).

We consider the evolution of the volume-averaged Spitzer parameter (Parrish & Quataert 2008)

$$f_S = \langle \hat{z} \cdot \mathbf{Q}_c / \bar{Q} \rangle, \quad (38)$$

as a function of time. This quantity shows how effective heat conduction is at transporting heat in the radial direction in the cluster compared to the case of a vertical (radial) magnetic field (or unmagnetized heat conduction). The same parameter was used to parameterize the effectiveness of helium sedimentation in the model of Peng & Nagai (2009). We show the evolution of f_S in the fifth panel of Figure 7 with the HBI simulation ($\nabla\mu=0$) indicated with a blue solid line and the HPBI simulation ($\nabla\mu \neq 0$) indicated with a red solid line. Initially, the volume-averaged Spitzer parameter decreases more rapidly in the HPBI simulation than in the HBI simulation, the reason being the slower growth rate in the absence of a composition

gradient. The inclusion of a composition gradient, however, leads to an increase in the volume-averaged Spitzer parameter at late times compared to the homogeneous case. We find that $f_S \approx 0.20$ ($f_S \approx 0.17$) for the HPBI (HBI) at $t/t_0 = 200$. This corresponds to an increase in heat flux by $\sim 20\%$ with respect to the homogeneous case.

6. OUTER REGIONS OF THE ICM

In this section, we consider two simulations of the outer parts of the ICM, where we assume that the initial magnetic field is perpendicular to gravity, i.e., horizontal. In one of these simulations, labeled MTI_Brag, the plasma is assumed to have uniform composition and in the other one, labeled MTI_Blim, the composition is assumed to decrease with height (radius). The bottom of the model plane-parallel atmosphere is located at $r = 0.65$ Mpc, corresponding roughly to the radius indicated with an A in Figure 8 in Berlok & Pessah (2015).

As in Section 5, we use reflecting boundary conditions at the top and bottom of the domain. The MTI creates vertical motions that will eventually reach the top and bottom of the domain, potentially influencing the nonlinear evolution of the instability. In order to circumvent this problem, we implement a procedure that has successfully been applied to the MTI by Parrish & Stone (2007) and Kunz et al. (2012). We sandwich the unstable layer between two buffer zones in which we add isotropic heat conduction and viscosity in order to damp any motions making their way into these regions. This results in two stable layers at the top and bottom, where the density decreases exponentially away from the mid-plane and the

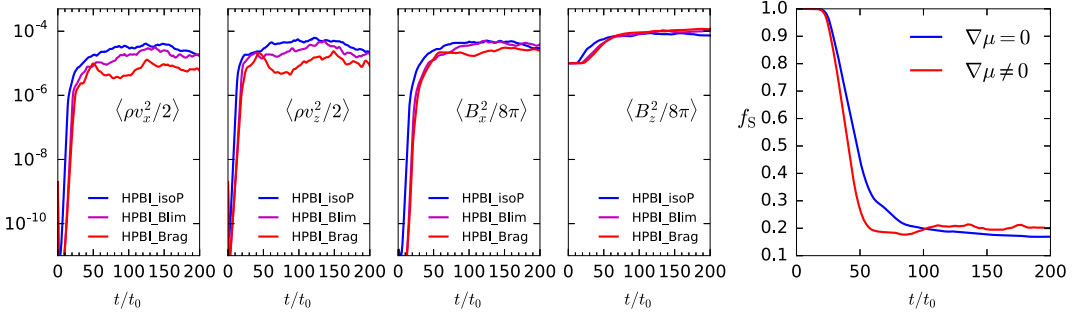


Figure 7. Evolution of the magnetic and kinetic energies in the simulations of the HPBI with blue (HPBI_isoP), red (HPBI_Blim), and magenta (HPBI_Brag) with spatial averages of $\langle \rho v_x^2/2 \rangle$ (first panel), $\langle \rho v_z^2/2 \rangle$ (second panel), $\langle B_x^2/8\pi \rangle$ (third panel), and $\langle B_z^2/8\pi \rangle$ (fourth panel). In the fifth panel, we show the evolution of the volume-averaged Spitzer parameter, $f_S = \langle Q_z/\tilde{Q} \rangle$ for the HBI and the HPBI. The initial growth of the HPBI is faster than for the HBI, but the final state of the simulation with a composition gradient has a heat flux that is roughly 20% higher than for the uniform simulation. More information about this panel can be found in Section 5.3.

temperature and composition are constant, with values T_0 and c_0 (T_Z and c_Z) in the lower (upper) stable layer.

We use the equilibrium for an initially horizontal magnetic field given in Berlok & Pessah (2016), i.e., the temperature and composition profiles given by

$$T(z) = T_0 + s_T z', \quad (39)$$

$$c(z) = c_0 + s_c z', \quad (40)$$

in the middle of the computational domain ($z' = z - H_0/4$ and $H_0/4 < z < 3H_0/4$), where $s_T = (T_Z - T_0)/H_0$ is the slope in temperature and $s_c = (c_Z - c_0)/H_0$ is the slope in composition. The pressure in the unstable region is given by

$$P(z') = P_0 \left(\frac{T(z')\mu(z')}{T_0\mu_0} \right)^\alpha, \quad (41)$$

where $\mu(z)$ is related to $c(z)$ by Equation (4) and the constant coefficient α is given by

$$\alpha = -\frac{T_0}{H_0} \left(\frac{4}{4s_T + 5\mu_0 T_0 s_c} \right). \quad (42)$$

Due to the very strong time-step constraint arising from the non-ideal terms, we have, however, opted to use significantly reduced values of χ_{\parallel} and ν_{\parallel} , by dividing the expected values by a factor of 10. The dimensionless values used in the simulations are therefore $\kappa_{\parallel} = 0.12 T^{5/2} \mu \rho^{-1}$ and $\nu_{\parallel} = 3.3 \times 10^{-3} T^{5/2} \rho^{-1}$. Both temperature and composition decrease with radius with $T_0 = 10.2$ keV and $c_0 = 0.32$ at the bottom of the unstable domain and $T = 9$ keV and $c = 0.27$ at the top for the non-uniform simulation ($c_0 = c_Z = 0.32$ for the uniform simulation). Furthermore, we use $\beta = 10^5$ and include Braginskii viscosity without limiters. As for the inner region, these simulations start from hydrostatic equilibrium with a subsonic velocity perturbation. In real clusters, the turbulence caused by accretion of material onto the cluster can contribute to a significant fraction of the pressure support needed to counteract gravity (Lau et al. 2009; Nelson et al. 2014).

The evolution of the initial horizontal magnetic field and the temperature is shown in Figure 9 for MTI_Brag (top row) and MTCI_Brag (bottom row). In these simulations, the unit of time is $t_0 = H_0/v_{0,\text{th}} = 230$ Myr. Note that because this is

roughly a factor of five longer than the t_0 characterizing the inner cluster it is only necessary to evolve the simulations up to $50 t_0$ to cover timescales of the order of $10+$ Gyr. For the MTI (top row) the evolution is very similar to the one presented for the MTI with Braginskii viscosity in Figure 17 in Kunz et al. (2012) except that the growth rate is significantly slower in the simulation presented here. This is simply due to the much shallower temperature gradient that we are using (Vikhlinin et al. 2006). As predicted by theory (Pessah & Chakraborty 2013; Berlok & Pessah 2015), we observe that the instability grows at an even slower rate when a gradient in composition is included (bottom row of Figure 9). For these parameters, linear theory predicts that the maximum growth rate⁴ of the MTI is $\sigma = 1.42 \text{ Gyr}^{-1}$, while the MTCI only has a maximum growth rate of $\sigma = 1.09 \text{ Gyr}^{-1}$. The maximum growth rate is only $\sim 20\%$ slower but this difference is able to significantly alter the final state of the system in this case. The instabilities are still in the exponential phase and have not reached saturation at the end of the simulation.

7. DISCUSSION

Understanding the distribution of helium in the ICM is an open problem with important implications for astrophysics and cosmology (Markevitch 2007; Peng & Nagai 2009).

The assumption of a spatially uniform composition of helium in the ICM is routinely applied when interpreting X-ray observations of galaxy clusters. This can lead to biases in the estimates of various key cluster parameters if a composition gradient is present, which can in turn propagate into estimates of the inferred cosmological constants (Markevitch 2007; Peng & Nagai 2009).

Current models to address this problem are one-dimensional and treat the turbulent, magnetized nature of the medium in a very crude way (Fabian & Pringle 1977; Gilfanov & Syunyaev 1984; Chuzhoy & Nusser 2003; Chuzhoy & Loeb 2004; Peng & Nagai 2009; Shtykovskiy & Gilfanov 2010). This usually amounts to parameterizing the presence of magnetic fields so that its main effect is to slow down the sedimentation process at the same rate at all radii. The advantage of these kinds of models is that they can be evolved for long timescales. In general terms, they predict

⁴ Found by solving the dispersion relation for a grid of values in k -space and taking the maximum value.

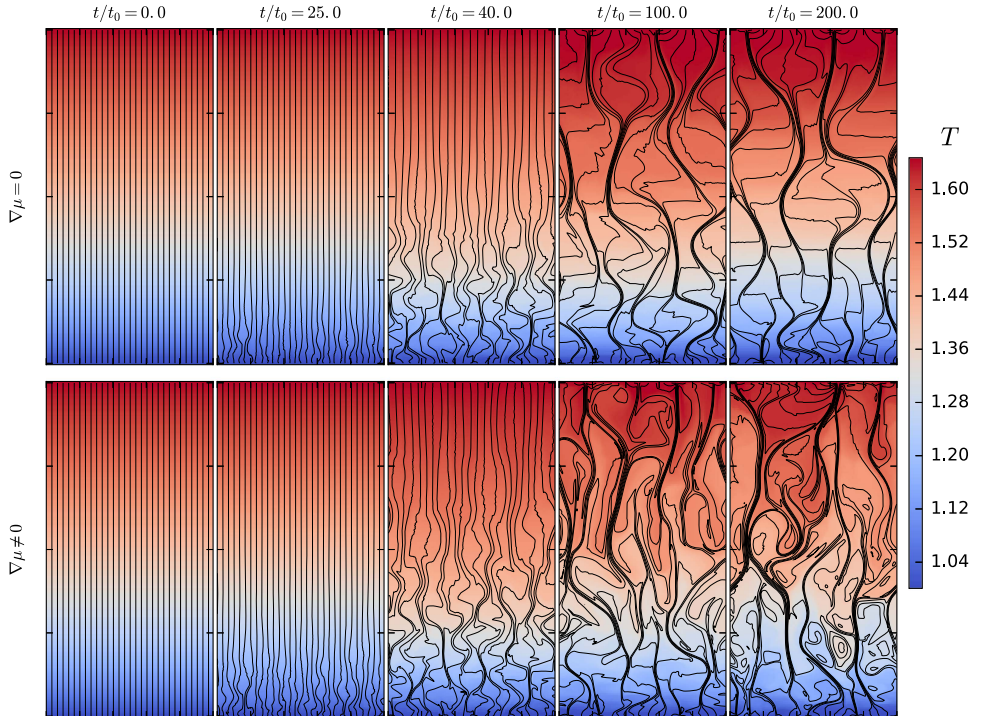


Figure 8. Temperature and magnetic field evolution as function of time for the HBI (HBI_Brag, upper row) and the HPBI (HPBI_Brag, lower row) in units of $t_0 = H_0/v_{0,th} = 45$ Myr. The size of the box is $H_0 \times 2H_0$ with $H_0 = 40$ kpc. The evolution of the composition for HPBI_Brag is shown in the bottom row of Figure 5, while HBI_Brag has uniform composition at all times. Both simulations included anisotropic heat conduction and Braginskii viscosity without limiters.

helium profiles that peak off-center when the (fixed) temperature profile is typical of cool-core clusters (Peng & Nagai 2009).

The approach employed, however, does not allow us to take into consideration the fact that the weakly collisional nature of the ICM renders its properties anisotropic due to inefficient transport across the magnetic field. When the effects of anisotropic heat conduction, viscosity, and particle diffusion are considered, with given initial thermal and composition profiles, a wide variety of instabilities, which are absent in one-dimensional settings, can play an important role in the plasma dynamics (Balbus 2000, 2001; Quataert 2008; Kunz 2011; Pessah & Chakraborty 2013).

Ideally, it would be desirable to evolve, in a global setting, the system of equations that describes the evolution of the thermal and composition gradients of a weakly collisional plasma (with initial cosmic composition) in the potential well of a dark-matter halo. In lieu of pursuing this arguably daunting task at once, we have opted to analyze this problem by developing a better understanding of the plasma dynamics using a number of approximations, which can, in principle, be relaxed in future studies:

(1) We have adopted as a working model a binary mixture composed of hydrogen and helium in the Braginskii-MHD approximation with Braginskii viscosity (Braginskii 1965; Pessah & Chakraborty 2013). This approach is known to be subject to small-scale instabilities that need to be dealt with

appropriately in numerical simulations (Schekochihin et al. 2005; Kunz et al. 2012). The firehose and mirror instabilities can be more accurately captured using hybrid particle-in-cell codes where the ions are treated as particles and the electrons are treated as a fluid (see, for instance, Kunz et al. 2014). Studies of the firehose and mirror instabilities normally assume a hydrogen plasma. Extending such simulations in order to study the kinetics of a multispecies plasma might therefore give new insights on how to incorporate microscale instabilities in Braginskii-MHD simulations of binary mixtures.

Particle-in-cell simulations have shown that the heat conductivity, χ_{\parallel} , can be significantly reduced by the action of the ion mirror instability (Komarov et al. 2016; Riquelme et al. 2016), the latter study also finding a reduction due to the electron whistler instability. The suppression of conductivity is found by Komarov et al. (2016) to be due to a combination of trapping of electrons in $\delta B/B \sim 1$ magnetic traps and a decreased mean-free path of collisions due to pitch-angle scattering off microscale fluctuations. The suppression of heat flux with respect to the Spitzer value in the simulations we present in Section 5.3 is due to the change in magnetic field orientation. Both of these effects yield a suppression of the heat flux by a factor of ~ 5 , a result that has also been found in magnetic turbulence (Narayan & Medvedev 2001; Chandran & Maron 2004). If a large fraction of the plasma is mirror unstable, the two effects could in principle act in unison to give

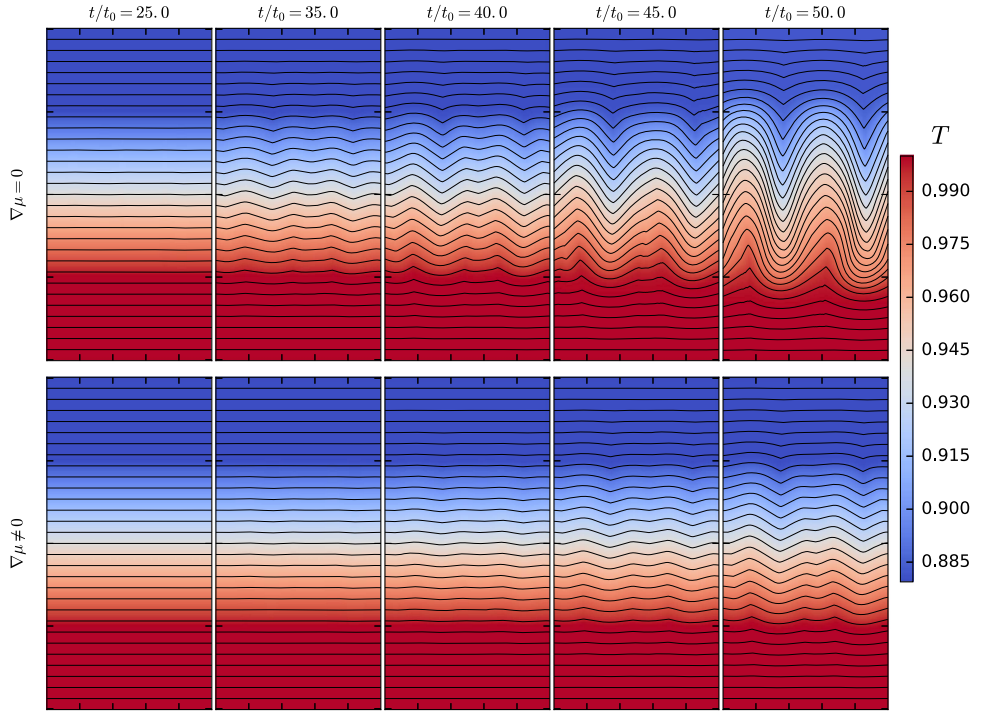


Figure 9. Evolution of the MTI (upper row) and the MTCI (lower row) as a function of time in units of $t_0 = H_0/v_{0,\text{th}} = 230$ Myr. The size of the unstable part of the box is $H_0 \times H_0$ with $H_0 = 300$ Mpc. The bottom of the unstable region has $T_0 = 10.2$ keV, while the top of the unstable region has $T = 9$ keV, values found at $r_0 = 0.65$ Mpc and $r = r_0 + H_0 = 0.95$ Mpc in the model of Peng & Nagai (2009). The MTI (upper row) has a uniform composition, while the MTCI (lower row) has $c_0 = 0.32$ at the bottom and $c = 0.27$ at the top.

a total reduction by a factor of ~ 25 . A reduction of χ_{\parallel} due to microscale instabilities could, however, also have consequences for the importance of the HBPI and the MTCI, given that their growth rates depend on fast heat conduction along magnetic field lines.

More recently, Xu & Kunz (2016) studied the stability of a collisionless, thermally stratified plasma by using linear Vlasov theory and described the kinetic version of the MTI. Moreover, an electron version of the MTI, the eMTI, was found to operate at sub-ion-Larmor scales and have a faster growth rate than the long wavelength kinetic MTI. The dispersion relation derived in Xu & Kunz (2016) can, in principle, be used to determine whether the MTCI also carries over to the collisionless regime. Subsequent particle-in-cell simulations could then be used to assess the differences with respect to the Braginskii-MHD framework employed in this paper. At present, such comparisons have yet to be done in homogeneous settings. The nonlinear outcome of the combined presence of the long wavelength kinetic MTI and the eMTI has yet to be explored by dedicated particle-in-cell in simulations.

(2) We have simplified the geometry of the problem by considering a plane-parallel atmosphere. This approach has been applied with success in a wide variety of astrophysical settings. Its accuracy depends on the phenomena under study having radial scales that are smaller than the fiducial radius at which the model is adopted. We have improved on our previous work (Pessah & Chakraborty 2013; Berlok &

Pessah 2015, 2016), in which the domains under consideration were local in both radius and azimuth, and developed a quasi-global approach, extending previous work in homogeneous settings (Kunz et al. 2012; Latter & Kunz 2012). This enabled us to consider domains that are not necessarily small compared to the thermal scale height at the fiducial radius.

(3) The helium concentration profile in galaxy clusters is, unfortunately, not directly observable (Markevitch 2007). In order to construct our model atmospheres, we relied on current one-dimensional helium sedimentation models (Peng & Nagai 2009). By considering these as initial conditions, we investigated the evolution of a number of instabilities that feed off the gradients in temperature and composition in the inner regions as well as the outskirts of the ICM. This approach assumes that the timescales for the evolution of the temperature and composition profiles are long compared to the timescales for the instabilities to grow significantly (Berlok & Pessah 2015). While this seems to be a reasonable assumption, the fact that the large-scale gradients, from which the instabilities feed off, are unable to evolve prevents us from understanding how the instabilities interact with the processes that drive their evolution at a more fundamental level (Burgers 1969; Bahcall & Loeb 1990).

While our approach cannot directly predict the evolution of the helium distribution in the ICM, we have been able to learn a few interesting things about how composition gradients can influence the dynamics of the weakly collisional medium.

In the inner region of the ICM, the nonlinear evolution of our model shows that helium rich material, initially at the top of the atmosphere, will fall down onto the inner core of the cluster. The relevant timescale for mixing to occur is of the order of a few gigayears. It is important to emphasize that this process cannot be attributed to standard convection driven by composition gradients since the Ledoux criterion (Ledoux 1947) is fulfilled in the model atmospheres we employed. The driving mechanism is the generalization of the heat-flux-driven buoyancy instability HBI, which we have termed the heat- and particle-flux-driven buoyancy instability (HPBI). We analyzed in some detail the effects that the evolution of the magnetic fields has on the thermal conductivity of the plasma to assess whether composition gradients can alleviate the core insulation observed in homogeneous settings (Parrish & Quataert 2008). Beyond a few gigayears the average inclination angle of the magnetic field is close to $\sim 30^\circ$ – 50° resulting in an averaged Spitzer parameter higher by about 20% than the value obtained in a corresponding homogeneous simulation. The distribution of composition is more patchy in the simulations where Braginskii viscosity is included because it can inhibit mixing at smaller scales. The main conclusions described here, however, seem to be rather insensitive to Braginskii viscosity when the composition is averaged along the azimuthal direction.

We also investigated the dynamics of the outskirts of the ICM, where both the temperature and the composition are expected to decrease with increasing radius (Vikhlinin et al. 2006; Peng & Nagai 2009). In this case, the mechanism driving instabilities is the generalization of the MTI, which we have termed the MTCI. The shallower gradients characterizing current models imply that the instabilities evolve slowly and there is not enough time for them to evolve in the strong nonlinear regime even after several gigayears. Therefore, in the outskirts of the cluster, the instabilities are rather inefficient at erasing the composition gradients.

This mismatch between fast growing instabilities in the inner core and rather slow instabilities in the outskirts could imply that compositions gradients in cluster cores might be shallower than predicted by one-dimensional models. One could speculate about the long-term outcome of the interplay between the various competing processes, but it seems to be safer to develop more self-consistent models in which the instabilities can develop in a global setting where the physics driving helium sedimentation is accounted for. One alternative, intermediate step in developing these models could consist of using the type of numerical simulations we have employed here to develop more physically motivated effective models for mixing that can be incorporated in improved one-dimensional models.

The weakly collisional, magnetized nature of the ICM is likely to have an impact on the long-term evolution of the gas dynamics, including the issue of whether helium can sediment efficiently. Our work constitutes the first few steps in this direction. More quantitative statements will demand improved models that incorporate the physics driving the sedimentation process, while simultaneously accounting for the anisotropic transport properties of the medium.

We acknowledge useful discussions with Daisuke Nagai, Matthew Kunz, Prateek Sharma, Ellen Zweibel, and Ian Parrish during the 3rd ICM Theory and Computation Workshop held at

the Niels Bohr Institute in 2014. We would like to thank Matthew Kunz for sharing with us the Athena files used to run the simulations presented in Kunz et al. (2012). Furthermore, we thank him and Henrik Latter for providing us with a copy of the script they used in Latter & Kunz (2012) and that we used as a starting point to build the code used in this paper. We are grateful to Daisuke Nagai and Fang Peng for sharing with us the Fortran program used to calculate the mean molecular weight profile used as inspiration for the simulations presented in this paper. We also acknowledge useful discussions with Gopakumar Mohandas and Sagar Chakraborty. We thank the anonymous referee for helpful comments that helped improve the final version of the manuscript. The research leading to these results has received funding from the European Research Council under the European Union's Seventh Framework Programme (FP/2007-2013) under ERC grant agreement 306614. T.B. also acknowledges support provided by a Lørup Scholar Stipend and M.E.P. also acknowledges support from the Young Investigator Programme of the Villum Foundation.

REFERENCES

- Andreon, S. 2010, *MNRAS*, 407, 263
 Bahecall, J. N., & Loeb, A. 1990, *ApJ*, 360, 267
 Balbus, S. A. 2000, *ApJ*, 534, 420
 Balbus, S. A. 2001, *ApJ*, 562, 909
 Balbus, S. A., & Potter, W. J. 2016, *RPPH*, 79, 066901
 Bale, S. D., Kasper, J. C., Howes, G. G., et al. 2009, *PhRvL*, 103, 211101
 Berlok, T., & Pessah, M. E. 2015, *ApJ*, 813, 22
 Berlok, T., & Pessah, M. E. 2016, *ApJ*, 824, 32
 Bogdanović, T., Reynolds, C. S., Balbus, S. A., & Parrish, I. J. 2009, *ApJ*, 704, 211
 Boyd, J. P. 2000, Chebyshev and Fourier Spectral Methods (New York: Dover)
 Braginskii, S. I. 1965, *RvPP*, 1, 205
 Burgers, J. M. 1969, Flow Equations for Composite Gases (New York: Academic)
 Carilli, C. L., & Taylor, G. B. 2002, *ARA&A*, 40, 319
 Chandran, B. D. G., & Maron, J. L. 2004, *ApJ*, 602, 170
 Chen, C. H. K., Matteini, L., Schekochihin, A. A., et al. 2016, *ApJL*, 825, L26
 Chuzhoy, L., & Loeb, A. 2004, *MNRAS*, 349, L13
 Chuzhoy, L., & Nusser, A. 2003, *MNRAS*, 342, L5
 Fabian, A. C. 1994, *ARA&A*, 32, 277
 Fabian, A. C., & Pringle, J. E. 1977, *MNRAS*, 181, 5
 Gilfanov, M. R., & Syunayev, R. A. 1984, *SvAL*, 10, 137
 Gupta, H., Rathor, S. K., Pessah, M. E., & Chakraborty, S. 2016, *PhLA*, 380, 2407
 Komarov, S. V., Churazov, E. M., Kunz, M. W., & Schekochihin, A. A. 2016, *MNRAS*, 460, 467
 Kunz, M. W. 2011, *MNRAS*, 417, 602
 Kunz, M. W., Bogdanović, T., Reynolds, C. S., & Stone, J. M. 2012, *ApJ*, 754, 122
 Kunz, M. W., Schekochihin, A. A., & Stone, J. M. 2014, *PhRvL*, 112, 205003
 Latter, H. N., & Kunz, M. W. 2012, *MNRAS*, 423, 1964
 Lau, E. T., Kravtsov, A. V., & Nagai, D. 2009, *ApJ*, 705, 1129
 Ledoux, P. 1947, *ApJ*, 105, 305
 Markevitch, M. 2007, arXiv:0705.3289
 McCourt, M., Parrish, I. J., Sharma, P., & Quataert, E. 2011, *MNRAS*, 413, 1295
 McCourt, M., Sharma, P., Quataert, E., & Parrish, I. J. 2012, *MNRAS*, 419, 3319
 Narayan, R., & Medvedev, M. V. 2001, *ApJL*, 562, L129
 Nelson, K., Lau, E. T., & Nagai, D. 2014, *ApJ*, 792, 25
 Parker, E. N. 1958, *PhRv*, 109, 1874
 Parrish, I. J., McCourt, M., Quataert, E., & Sharma, P. 2012a, *MNRAS*, 422, 704
 Parrish, I. J., McCourt, M., Quataert, E., & Sharma, P. 2012b, *MNRAS*, 419, L29
 Parrish, I. J., & Quataert, E. 2008, *ApJL*, 677, L9
 Parrish, I. J., Quataert, E., & Sharma, P. 2009, *ApJ*, 703, 96
 Parrish, I. J., Quataert, E., & Sharma, P. 2010, *ApJL*, 712, L194
 Parrish, I. J., & Stone, J. M. 2005, *ApJ*, 633, 334
 Parrish, I. J., & Stone, J. M. 2007, *ApJ*, 664, 135
 Parrish, I. J., Stone, J. M., & Lemaster, N. 2008, *ApJ*, 688, 905

- Peng, F., & Nagai, D. 2009, *ApJ*, 693, 839
- Pessah, M. E., & Chakraborty, S. 2013, *ApJ*, 764, 13
- Quataert, E. 2008, *ApJ*, 673, 758
- Riquelme, M. A., Quataert, E., & Verscharen, D. 2016, *ApJ*, 824, 123
- Rosin, M. S., Schekochihin, A. A., Rincon, F., & Cowley, S. C. 2011, *MNRAS*, 413, 7
- Ruszkowski, M., & Oh, S. P. 2010, *ApJ*, 713, 1332
- Schekochihin, A. A., Cowley, S. C., Kulsrud, R. M., Hammett, G. W., & Sharma, P. 2005, *ApJ*, 629, 139
- Schekochihin, A. A., Cowley, S. C., Kulsrud, R. M., Rosin, M. S., & Heinemann, T. 2008, *PhRvL*, 100, 081301
- Schwarzschild, M. 1958, *Structure and Evolution of the Stars* (Princeton, NJ: Princeton Univ. Press)
- Sharma, P., Hammett, G. W., Quataert, E., & Stone, J. M. 2006, *ApJ*, 637, 952
- Shtykovskiy, P., & Gilfanov, M. 2010, *MNRAS*, 401, 1360
- Spitzer, L. 1962, *Physics of Fully Ionized Gases* (New York: Interscience)
- Stone, J. M., Gardiner, T. A., Teuben, P., Hawley, J. F., & Simon, J. B. 2008, *ApJS*, 178, 137
- Sur, S., Pan, L., & Scannapieco, E. 2014, *ApJ*, 784, 94
- Vikhlinin, A., Kravtsov, A., Forman, W., et al. 2006, *ApJ*, 640, 691
- Xu, R., & Kunz, M. W. 2016, arXiv:1608.05316